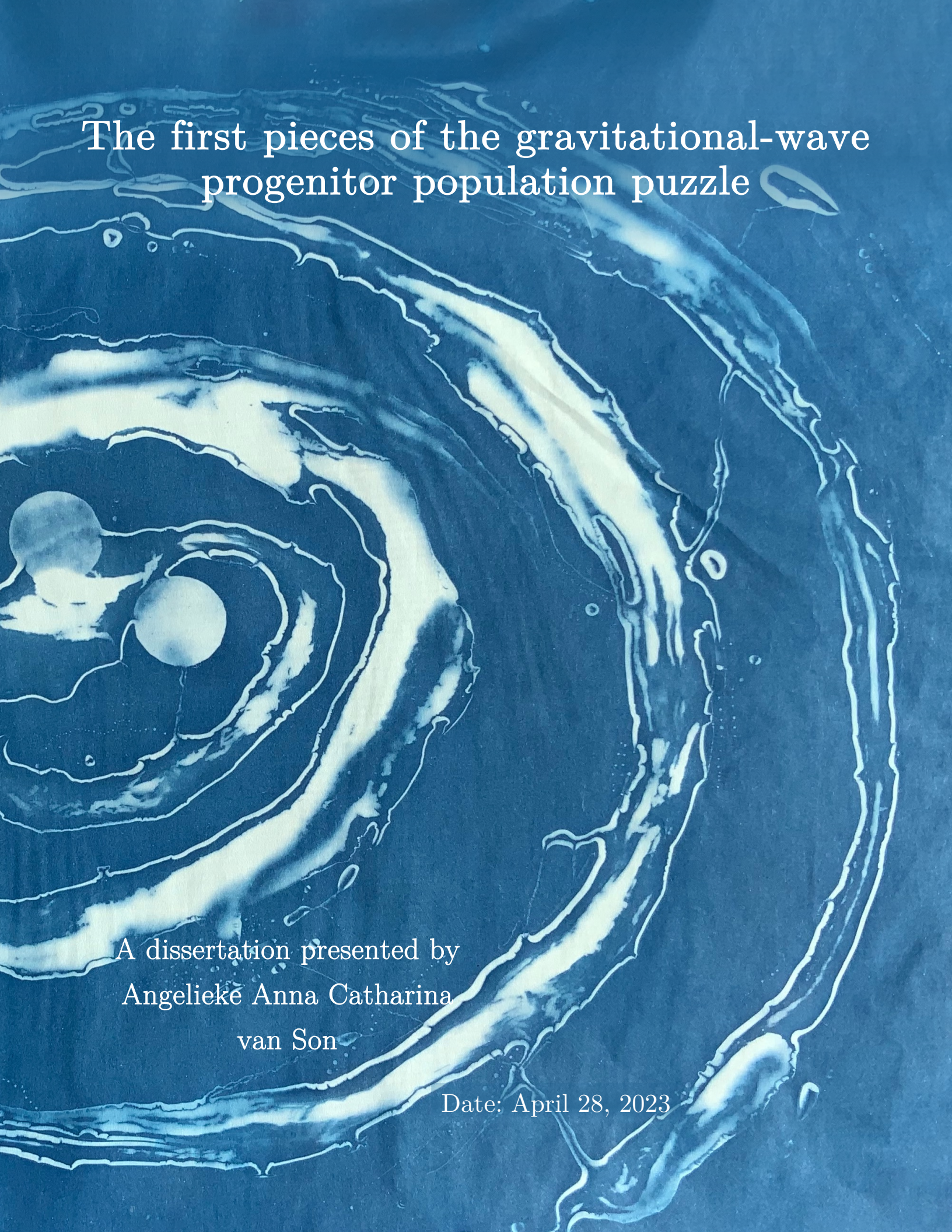


Date: April 28, 2023



The first pieces of the gravitational-wave progenitor population puzzle

A dissertation presented by
Angелиke Anna Catharina
van Son

Date: April 28, 2023

HARVARD UNIVERSITY
Graduate School of Arts and Sciences



DISSERTATION ACCEPTANCE CERTIFICATE

The undersigned, appointed by the

Department of Astronomy

have examined a dissertation entitled

The first pieces of the gravitational-wave progenitor population puzzle

presented by Angelieke Anna Catharina van Son

candidate for the degree of Doctor of Philosophy, and hereby

certify that it is worthy of acceptance.

Signature

A handwritten signature in black ink, appearing to read "Lars Hernquist".

Typed name: Prof. Lars Hernquist, Chair

Signature

A handwritten signature in black ink, appearing to read "Charlie Conroy".

Typed name: Prof. Charlie Conroy

Signature

A handwritten signature in black ink, appearing to read "R. Narayan".

Typed name: Prof. Ramesh Narayan

Signature

A handwritten signature in black ink, appearing to read "Selma de Mink".

Typed name: Prof. Selma de Mink

Date: April 28, 2023

The first pieces of the gravitational-wave progenitor population puzzle

A dissertation presented

by

Angелиke Anna Catharina van Son

to

The Department of Astronomy

in partial fulfillment of the requirements

for the degree of

Doctor of Philosophy

in the subject of

Astronomy & Astrophysics

Harvard University

Cambridge, Massachusetts

April 2023

© 2023 — Angeliuke Anna Catharina van Son

All rights reserved.

The first pieces of the gravitational-wave progenitor population puzzle

Abstract

The first gravitational wave (GW) observation marked a monumental moment in science and heralded the birth of a new field: GW astronomy. Since then, the field has rapidly developed, with about 90 mergers of binary black Hole (BBH), black hole neutron star (BHNS), and binary neutron star (NSNS) mergers observed to date. This number is set to triple in the next few years, with millions of detections anticipated in the following decade. How do these merging double compact objects form? Each detection adds a new piece to the puzzle of their origins, moving us from a phase of initial discovery into an era of population studies. Many different formation channels have been proposed to solve this ‘progenitor population puzzle’, but all depend crucially on their direct ancestors: massive stars. Massive binary stars impact nearly *every* part of modern astrophysics, as they shape our Universe through the elements and ionizing radiation they emit. However, these stars are challenging to study while alive as they are intrinsically rare and live short lives. This raises a second question: (what) can GW sources teach us about the lives and deaths of their stellar progenitors?

In this thesis, we aim to shed light on this question by analyzing the early population results of GW sources that make up the first pieces of the progenitor puzzle. We apply a combination of numerical population synthesis models and analytical models to develop an intuitive understanding of the complex phenomena that govern the evolution of

massive stars, and ultimately lead to the formation of double compact objects.

The first puzzle piece is the notable structure that emerged in the mass distribution of merging BBHs. Observations have revealed a ‘bump’, followed by a low but non-zero rate of mergers with components $\gtrsim 35 M_{\odot}$. This has been linked to the theoretical prediction of a ‘mass gap’ caused by Pair Instability Supernovae (PISN). We show that the contribution of isolated binaries to form BBH mergers in this mass gap is negligible, even under extreme assumptions about mass accretion. This points towards dynamical formation channels for BBHs in this mass range. We furthermore provide the first quantitative study into the origin of the global peak of the BBH mass distribution, and find that it results naturally from the stable Roche-lobe overflow channel. The reason behind this lies in a characteristic of this channel: it cannot form BBH mergers below a certain mass. This also provides an alternative explanation for the much disputed ‘neutron star-black hole mass gap’ if observed in GW sources. More clues follow from the evolution of the BBH merger rate with redshift, which is determined by the delay-time distribution of its formation channel. We identify unique delay time-mass relationships for the two main isolated binary evolution channels and provide testable predictions for the redshift evolution for the BBH merger rates from each channel. Lastly, we investigate how our model predictions are affected by the metallicity-dependent cosmic star formation history. We present a new functional form for the latter and determine that it will not shift the location of features such as those discussed above. This is exciting as it suggests that these features indeed have the potential to reveal the underlying physics of their stellar progenitors.

Contents

Title page

Copyright

Abstract	iii
----------	-----

Contents	ix
----------	----

Acknowledgments	x
-----------------	---

Thesis Propositions	xvii
---------------------	------

1 Introduction	1
1.1 The advent of gravitational-wave astronomy	3
1.2 Formation channels of merging DCO	5
1.3 Massive (binary) stars	9
1.4 The emerging progenitor population puzzle	15
1.5 Thesis outline	21
2 Polluting the pair-instability mass gap for binary black holes through super-Eddington accretion in isolated binaries	23
2.1 Introduction	25
2.1.1 The scope of this work	27
2.2 Forming PISN mass gap events	28
2.2.1 Forming PISN mass gap events through the classic isolated binary channel	28
2.2.2 Pathways to pollute the PISN mass gap requiring dynamical interaction	30
2.3 Method	33

CONTENTS

2.3.1	Initial parameters	33
2.3.2	Evolution and mass loss	34
2.3.3	Treatment of black hole accretion in this study	36
2.4	Results	37
2.4.1	Component masses	38
2.4.2	Total mass distribution	46
2.4.3	Mass ratios	51
2.4.4	BBH merger rates	52
2.5	Distinguishing between different pathways to PISN mass gap events	56
2.5.1	The shape of the BBH mass distribution	57
2.5.2	Predictions for masses, mass ratios and spins	62
2.6	Discussion	68
2.6.1	Variations in mass transfer	68
2.6.2	Effects of super-Eddington accretion on the lower mass gap	72
2.6.3	Caveats	73
2.7	Conclusions and summary	74
2.8	acknowledgments	76
2.9	Appendix: Angular momentum loss during (non) conservative mass transfer	76
2.9.1	Varying the mass conservation	78
2.9.2	Varying the specific angular momentum lost	80
2.10	Appendix: BH Formation yields and merger rates	81
2.11	Appendix: Remnant mass prescription	84
2.12	Appendix: Additional material	85
3	The redshift evolution of the binary black hole merger rate: a weighty matter	86
3.1	Introduction	88
3.2	Method (I) : Simulating merging BBH populations	93

CONTENTS

3.2.1	Binary evolution	93
3.2.2	Sampling	97
3.3	BH mass-delay time relations	100
3.3.1	Why the CE channel does not produce high-mass black holes	101
3.3.2	Why the stable RLOF channel does not produce short delay times .	104
3.4	Method (II) : Calculating Intrinsic merger rates	106
3.4.1	Estimating the intrinsic BBH merger rate	106
3.5	The merger rates and mass function at different redshifts	108
3.5.1	The role of the two formation channels	108
3.5.2	The shape of the mass function at different redshifts.	112
3.6	Prospects for observing trends with redshift in the intrinsic merger rate density	115
3.6.1	The slope of the intrinsic rates per mass bin at low redshift	116
3.6.2	Observing the different slopes in GWTC-2	120
3.7	Discussion	123
3.7.1	The relative contribution of the CE and stable RLOF channel	124
3.7.2	Are the delay time and mass distributions of the two channels dis- tinguishable?	125
3.7.3	Alternative observables to distinguish the two channels	126
3.7.4	The uncertain metallicity dependent cosmic star formation history	130
3.7.5	Further caveats of rapid population synthesis	131
3.7.6	Contribution from other formation channels	133
3.8	Conclusions and summary	136
3.9	Appendix: Inspecting mass ratios	140
3.9.1	First mass transfer: from the primary to the secondary	140
3.9.2	Second mass transfer: from the secondary to the primary	141
3.9.3	Final mass ratio	142

CONTENTS

3.10 Appendix: Delay time distributions	143
3.11 Appendix: Metallicity-dependent star formation rate $\mathcal{S}(Z, z)$	143
3.12 Appendix: The redshift dependence of the merger rate as a function of chirp mass	147
3.13 Appendix: Mass distribution split by formation channel and metallicity .	147
3.14 Appendix: Physics variations	148
4 The locations of features in the mass distribution of merging binary black holes are robust against uncertainties in the metallicity-dependent cosmic star formation history.	155
4.1 Introduction	157
4.2 A convenient analytic expression for the metallicity-dependent cosmic star formation history	160
4.2.1 The cosmic metallicity density distribution	161
4.2.2 The overall cosmic star formation rate density	164
4.3 Fit against Cosmological simulation	164
4.3.1 IllustrisTNG Cosmological simulations	164
4.3.2 Choices and binning of the data	167
4.3.3 Optimisation function	167
4.3.4 Resulting $\mathcal{S}(Z, z)$	168
4.4 Application: systematic variations of $\mathcal{S}(Z, z)$ and the effect on the mass distribution of merging BBHs	172
4.4.1 Determining reasonable variations of $\mathcal{S}(Z, z)$	173
4.4.2 The effect of the $\mathcal{S}(Z, z)$ on the primary masses of merging BBH .	176
4.5 Discussion & Summary	184
4.6 Appendix: Evaluating our fit; the squared residuals	187
4.7 Appendix: Determining reasonable variations of the $\mathcal{S}(Z, z)$	189
5 No peaks without valleys: The stable mass transfer channel for gravitational-wave sources in light of the neutron star–black hole mass gap.	192

CONTENTS

5.1	Introduction	194
5.1.1	Motivation for this work	199
5.2	Analytic approximation of the stable mass transfer channel	201
5.2.1	The evolutionary steps of the stable channel	202
5.2.2	Derivation of low-mass cutoff for primary components	205
5.3	Results: Effect of the minimum mass for the stable channel	209
5.3.1	Comparison to numerical data	212
5.3.2	Effect of minimum mass on mass distributions	214
5.3.3	Variations in the SN mass loss and angular momentum loss	217
5.4	Discussion	222
5.4.1	Remnant mass function or binary physics effect?	223
5.4.2	NSNS and binary white dwarf mergers	224
5.4.3	Results in context of X-ray binary observations	225
5.4.4	Filling the low-mass gap from below	228
5.4.5	Caveats	228
5.5	Conclusions	230
5.6	Appendix: The dependence of mass transfer stability on the mass ratio and the mass transfer accretion fraction	233
5.7	Appendix: Mass dependent core mass fraction	234
5.8	Appendix: Chirp mass and final mass ratios	236
5.9	Appendix: Overview of rates	237
6	Summary and Outlook	239
6.1	Summary of this thesis	241
6.2	The observational landscape of the next 20 years	243
A	Cover and Chapter Images	248
References		250

Acknowledgments

‘No man is an island’, and this thesis, along with the science it presents, is no exception. In particular, the road to this thesis has been a journey that involved multiple moves, resulting in an accumulation of affiliations and a network of collaborators and friends that stretches across the Atlantic. As a result, it would be impossible for me to truly do justice to all the people that helped me shape this thesis over the past 4+ years. I hope that even if your name is not explicitly stated, you are aware of your role, and know that I am deeply grateful for your support.

To Selma, I remember meeting you in the Starbucks of Amsterdam central, when you were recruiting me to the BinCosmos group. Little did I know what the coming years would have in store, but I could sense from the sparkle in your eye that you were determined to make this an exciting scientific journey, no matter where it took us. And it has been an incredible journey indeed! You have seen me at both my highest and lowest moments, and I want to thank you for your unwavering support, your care, and the countless hours you have put into advising me!

Charlie, thank you for accepting me in your group and for creating an environment where I felt included and like I belonged, which I think meant more to me than you might have known at the time. You have always been a steady hand on the tiller of my thesis, and your light and cheerful approach to mentoring and supporting have helped me surpass my own expectations, thank you for that.

I would also like to thank the remaining members of my thesis advisory committee: Josh Grindlay, Ramesh Narayan, and Lars Hernquist. Thank you for your advise and support over the years! Lars, thank you for welcoming me at your group and wine

meetings, they were often the highlight of my week, especially during the darker times of this PhD. In general, thanks to the many lovely members of the Hernquist group, both past and present. To Lex, thank you for supporting me throughout the years, and making me feel welcome at the API. Your calm and kind demeanor always left me feeling reassured after our meetings. Thank you for helping me to zoom out and see the bigger picture.

I have been fortunate enough to be involved in multiple exceptional research groups around the world. Firstly, I am deeply grateful for all the past and present members of the BinCosmos group; Stephen Justham, Rob Farmer, Eva Laplace, Ylva Götberg, Mathieu Renzo, Floor Broekgaarden, Floris Kummer, Lokesh Khandelwal, Tom Wagg, Katie Sharpe, Jing-Ze Ma, Ruggero Valli, Martyna Chruścińska, Jakub Klencki, Julia Bodensteiner, Chen Wang, and Earl Bellinger. Every one of you is a warm and lovely person, and I feel privileged to count myself amongst the likes of you. Special thanks to Stephen for your advice and guidance, which is always much more useful than you yourself think it is. To my older PhD brothers and sisters, Eva, Ylva, Mathieu, and Manos: It is hard to fill the shoes of such smart and kind people. Mathieu, it has truly been a pleasure to not just discuss science, but also politics/ethics/whatever is on the table with you! Ylva, your excitement and support made me feel valued and strengthened in the steps I took. Eva, my friend, and mentor in disguise. Our weekly chats during the pandemic were invaluable to me. Thank you for believing in me when I did not, and for being the incredibly strong and supportive person that you are. I hope we continue our chats in one way or another until we are old and well-retired.

I am further grateful, to the members from the Conroy Group, including Ana Bonaca, Ben Johnson, Evan Bauer, Jesse Han, Kareem El-Badry, MJ Park, Vedant,

Chandra, Phill Cargile, Rohan Naidu, Turner Woody, Katie Sharpe and Harshil Kamdar. Thank you all for making group meeting fun and lighthearted. Katie, thank you for trusting me to be your advisor at some point, I wish you all the best during grad school, though I have no doubt you will be great! I would also like to thank the members of the gravitational wave group at the CCA. Will Farr, Katie Breivik, Tom Callister, Mathieu Renzo, Harrison Siegel, Kaze Wong, Barry McKernan, Saavik Ford, Chiara Mingarelli, Deborah Good, and Max Isi, thank you for creating such an exciting and invigorating atmosphere. I enjoyed every moment of every visit, and I am keen to continue the legacy of your kindness in the coming years! Lastly, I would like to thank the members of the COMPAS group, including but not limited to Ilya Mandel, Reinhold Willcox, Alejandro Vigna-Gómez, Jeff Riley, Mike Lau, and Ryo Hirai. It has been a great honor for me to even be a small part of the team.

To my fellow grad students both from the years before and after me. Thank you for helping to transform the CfA into the much more social and supportive place that it is today. In particular, Magda, your legacy of the CfA garden is something for which the entire CfA community is grateful! To all the Gooney Tunes members: Claire, Harshil, Floor, Daniel, Ian, Kait, Gus, Madison, Magda, Mike, Ned, Chris, Eliška, Holly, Olga, Ralf ,Sandy, Tanveer, Alexia, Cadence, Chelsea, Chima, and Sarah. Our hikes, snow-adventures, cook-outs, and movie nights are what made my time here a blast! Most importantly, I owe both my physical and mental health to Body by Covid – to date the best fitness class I have ever attended.

Gus, my roommate/office mate/peer/group mate(?), and lifelong friend. You have been my go-to American for every one of the many occasions that I didn't understand this country. Thank you for putting up with me as a snobby European. You might be

surprised to learn that I did in fact ‘fancy seeing you’, every time I said it, and I hope we keep running into each other in the indefinite future! Floor, your endless optimism (even during the hardest times), your profound morals, and your all-round kindness make you are a source of inspiration, not just to me, but to everyone you know. I am truly honored to be able to call you my friend. Sarah, our friendship just clicked from the first moment we had that mid-covid thanksgiving dinner together. I can’t wait for you to come visit me in NYC. Alexia, thank you for being my friend and office mate. I hope we will have many more wine nights and parties together. Tanveer, thank you for our candid discussions about life and happiness, especially during application season. To Fabio, our coffees and drinks were a welcome relief during the pandemic. One day, we’ll write that paper, but until then we will have to continue getting drinks together for more inspiration. Elishka, thank you for always keeping our house cheerful, know that Nymeria misses you. Poorna, thank you for helping me out in these last miles of the run. Hanging out and having dinner together after a long day of work is what makes Beacon street feel like home! Thanks to the Bunch of Avengers, that made me feel welcome from the moment I stepped foot in the API. Special cheers to Frank and Ben, for continuing the borrel legacy. Also, a shout-out to everyone at “the Coolest office “at API, which I am sure will never be this cool again.

Everyone knows that there are a few staff members that are the real and only reason that departments don’t collapse. Thank you Peg Herlihy, Lisa Catella, and Robb Scholten for all your help and support over the years. Thanks also to Milena, Susan, and Martin for being the heart and soul of the API. I would further like to thank Thom Burns for introducing me to some of the amazing stories of pioneering women behind the Harvard Plate Stacks Collection, and to cyanotypes. Thank you for helping me create

awesome cover and chapter title images in this thesis (see also Appendix A).

To my many friends from home, whom I have often missed so dearly during my PhD endeavor abroad. Marlous, m'n lievelingsbanaan en langstdurende vriendin, bedankt voor de steun en toeverlaat die je me hebt geboden door de jaren heen. Van Almere Muziek wijk tot New York, met jou is alles een feestje! Job, Marco, en Robbie, de echte harde kern. Ik heb er alle vertrouwen in dat we nog samen kaasjes eten, koehandel spelen en diepe/belachelijke discussies voeren tot we er bij neervallen in een bejaardentehuis. Nina, bedankt voor alle avonturen die we samen hebben beleefd, van Leiden tot in Boston. Aan de 'kornuiten van de Langebrug': Mart, Tom, Jos, Kim, Aj, Tim, Skull, Simone, Marc, Coen en Rox. Zonder onze geestverruimende gesprekken had ik het behaupt niet door mijn bachelor sterrenkunde gehaald. Aan alle Scyllias leden, bedankt voor alle duiken, borrels en nieuwjaarsdiners, ik hoop dat we snel weer een port-proeverij kunnen houden! Gwen, Saar, Row, thanks for keeping me real. Het voelt alsof er de afgelopen 10 (!) jaar niets is veranderd als we over de wereld praten terwijl ik van jullie geweldige kookkunsten mag genieten.

This thesis would never have been possible without the support of my family. Dana, my favorite sister, and best friend. I don't have the words to express how much you mean to me. All I will say is how excited I am for the life you and Joeri are building together. To my mom, Sylvia, your strong role model is what has driven me to pursue my ambitions in life. To my dad, Rob, your bottomless reserve of knowledge is what sourced my love for science, I would not have been here without you.

Finally, Tom, your love and encouragement are what got me through this PhD. Whenever I was about to give up, you brought me back to earth, cared for my happiness and health, and ultimately pulled me through each one of the difficult times. I can't

believe how lucky I am to have you in my life, and I can't wait for our next adventure, and the one after that, and so forth.

“I haven’t been everywhere but it is on my list”

- Susan Sontag

Thesis Propositions

In keeping with Dutch tradition, I will summarize what I have learned during my time as a graduate student in a set of ‘propositions’. These propositions concern insights I have gained on the topic of this dissertation, on science in general, and on our community as a whole.

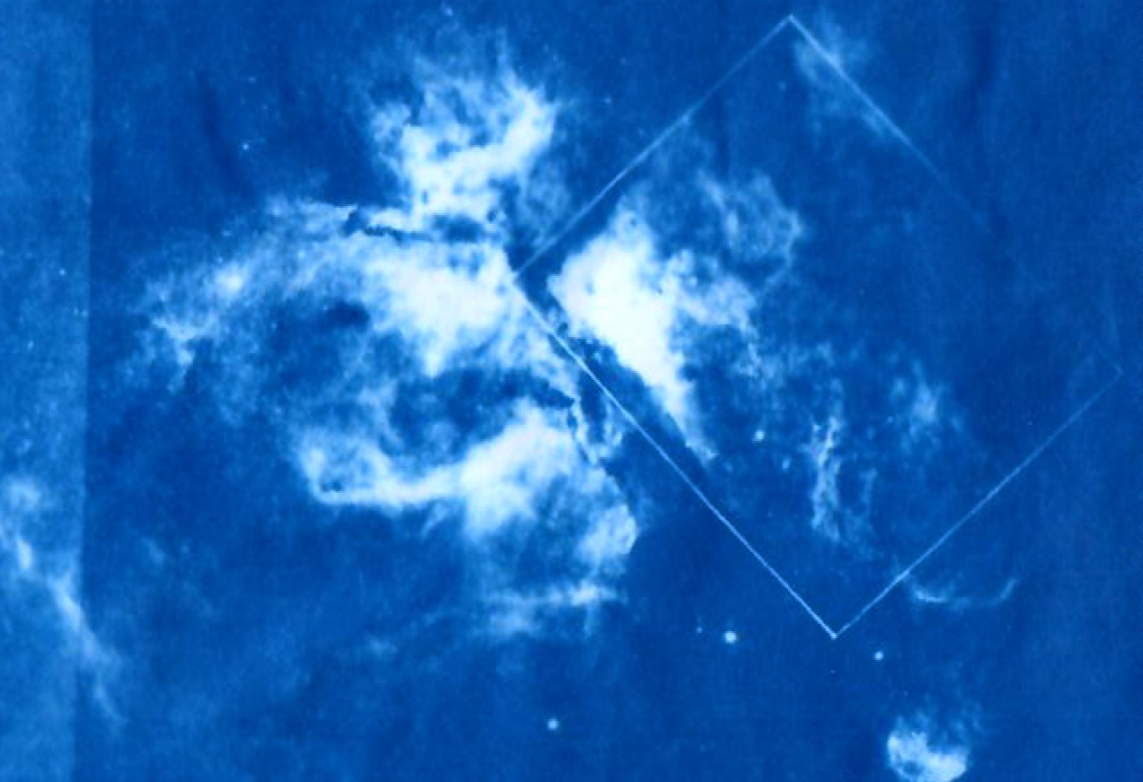
1. Super-Eddington mass transfer in binary stars cannot explain binary black hole mergers with masses in the so-called ‘Pair Instability Supernova’ mass gap.
2. The classic ‘common-envelope channel’ to merging double compact object formation leads to lower masses, and shorter delay times compared to the ‘stable mass transfer channel’.
3. As a result of the previous proposition, high and low-mass compact objects are predicted to exhibit a distinct rate evolution with redshift.
4. The metallicity-dependent cosmic star formation history does not affect the location of features in the mass distribution of merging binary black holes.
5. The global peak of the mass distribution of merging binary black holes currently offers the highest potential for using gravitational-wave sources to constrain the physics of isolated binary systems.
6. A characteristic of the stable mass transfer channel is that it is unable to form binary black hole mergers below a certain primary mass. This property results in a dearth of low-mass black hole mergers that provides an alternative explanation for the much disputed ‘neutron star - black hole mass gap’ if observed in the mass distribution of merging double compact objects.

7. A prediction is only as strong as the weakest underlying assumption.
8. The names of flagship telescopes reflect a small but significant shift towards more gender-diverse leadership in astronomy that has occurred over the past two decades (e.g., from the Very Large Telescope to the Vera C. Rubin Observatory).
9. Shared spaces and communal breaks are an integral part of any scientific institution.
The informal interactions that they foster I) promote scientific discussions in a nonthreatening environment, II) reduce stress and thereby can help increase productivity, and most importantly III) increase a sense of belonging among community members.

Chapter 1

Introduction

bridge photograph



1.1 The advent of gravitational-wave astronomy

The field of GW astronomy is rapidly unfolding; since the first detection in 2015 (Abbott et al., 2016) we have observed ~ 90 GW events. The growth of the GW catalog has been accompanied by a multitude of scientific discoveries. GW observations have been used to I) test the theory of general relativity (see review by Krishnendu & Ohme, 2021), II) constrain the abundance of primordial black holes (BHs, e.g., Mandic et al., 2016; Wang et al., 2018), and III) provided an independent measurement of the Hubble constant (Schutz, 1986; Holz & Hughes, 2005; Farr et al., 2019a; María Ezquiaga & Holz, 2022). The inferred rates of binary black hole (BBH) black hole-neutron star (BHNS) and NSNS mergers prompted a flood of studies to the formation channels of merging double compact objects (see reviews by Mandel & Farmer, 2022a; Mapelli, 2021; Mandel & Broekgaarden, 2022). For BBH mergers, we have made significant progress towards measuring the mass and spin distributions, and evolution of the merger rate with redshift (e.g., Fishbach et al., 2018; Abbott et al., 2021f; Tiwari, 2022; Edelman et al., 2023). The first NSNS merger (Abbott et al., 2017b) placed new constraints on the neutron star (NS) equation of state (see review by Raithel, 2019), while also confirming that NSNS mergers are a source of r-process elements (Arcones & Thielemann, 2023), and short gamma-ray bursts (Abbott et al., 2017c).

This is only just the beginning. As the sensitivity of current and upcoming detectors improves, we can expect millions of detections in the coming decades (see Figure 1.1¹). The driving force behind the growing catalog is the detector horizon that expands with sensitivity. For stellar BBHs (with $M_{\text{tot}} \approx 10 - 100 M_{\odot}$), the Einstein

¹The code to reproduce this Figure can be found here: <https://github.com/LiekeVanSon/ThesisFigures>

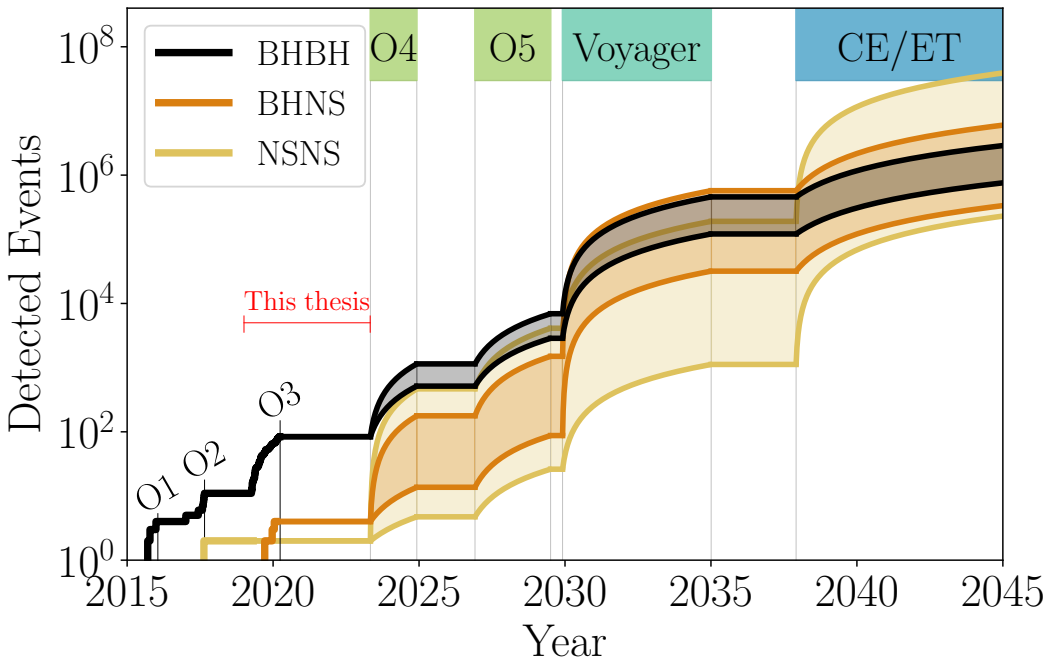


Figure 1.1: The current and projected size of the GW-source catalog. Detection rates and mission times for observing run O4 and O5 are taken from Abbott et al. (2018b) and the ligo doc pages. Detection rates for Voyager, Cosmic explorer (CE) and the Einstein telescope (ET) follow from Borhanian & Sathyaprakash (2022), and Gupta et al. (2023). Mission times are only indicative for the latter detectors. The minimum and maximum number were calculated using the redshift-independent rates from Abbott et al. (2021e).

telescope (ET) and Cosmic explorer (CE) will detect more than 50% of *all* BBHs out to $z = 10$. Additionally, a tail of BBH mergers is expected to be detected out to $z = 100$ (e.g., Maggiore et al., 2020), i.e., before the time of first star formation (Naoz et al., 2006), thereby directly probing primordial BHs. Lastly, current detections are merely scratching the surface of the GW spectrum. Planned third generation GW detectors will expose other GW frequencies, unveiling completely new sources (see Section 6.2). As GW astronomy blooms, and the catalog grows, a fundamental question arises:

How do merging double compact object form?

1.2 Formation channels of merging DCO

Many different formation channels have been proposed (see Figure 1.2). These formation channels aim to explain how to get two compact objects close enough to merge within a Hubble time through GW emission, as GWs quickly become inefficient at larger separations. For a circular system² the time to inspiral (or coalescence time, Peters, 1964) scales as: $T_c \propto a_0^4/(m_1 m_2(m_1 + m_2))$. Here a_0 is the initial separation, and $m_1 > m_2$ are the component masses. Separation thus typically dominates the coalescence time due to its higher power (fourth instead of third for masses). Moreover, the separations of interest ($\sim 10 R_\odot - 10^4 R_\odot$) span more decades than the range of relevant masses ($1 - 100 M_\odot$ for stellar objects). This means that a circular BBH of two $30 M_\odot$ components would need to be brought to separations $\lesssim 35 R_\odot$ to merge within a Hubble time. However, stars of $M_{\text{ZAMS}} = 10 - 100 M_\odot$ will typically extend beyond $100 - 1000 R_\odot$ at one point during their evolution. This discrepancy between the sizes of massive stars and the small separations required for double compact object mergers is sometimes referred to as the *separation challenge*. The way that formation channels overcome this ‘separation challenge’ can broadly be subdivided in two groups: I) isolated binary channels, and II) dynamical formation channels.

- *Isolated binary channels* consider stars that were born together in pairs and bring their cores to small orbits through binary interactions. Partially driven by the observed Hulse–Taylor binary pulsar (see e.g., Flannery & van den Heuvel, 1975), predictions for double compact object formation from this channel long predate the

²In case of an eccentric binary, the relevant integral from Peters (1964) can be approximated with $T_{\text{coalescence}} \approx T_c(1 + 0.27e_0^{10} + 0.33e_0^{20} + 0.2e_0^{1000})(1 - e_0^2)^{7/2}$ (Mandel, 2021)

CHAPTER 1. INTRODUCTION

first observation of GW (e.g., Smarr & Blandford, 1976; Tutukov & Yungelson, 1993; Lipunov et al., 1997; Bethe & Brown, 1998; Nelemans et al., 2001a; Belczynski et al., 2002; Voss & Tauris, 2003, and many others) The isolated binary channels can be further subdivided based on the stability of the mass transfer involved into the ‘stable mass transfer channel’, and the ‘common envelope channel’ (see 1.3 below). Furthermore, the chemically homogeneous evolution channel is an isolated binary channel that solves the separation challenge by staying compact due to efficient chemical mixing (e.g., de Mink & Mandel, 2016; Mandel & de Mink, 2016; Marchant et al., 2016; Song et al., 2016a; du Buisson et al., 2020; Riley et al., 2021).

- *Dynamical formation channels* on the other hand assume that the compact objects are brought together through dynamical interactions in dense environments. The idea of forming BBH mergers in (young stellar and globular) cluster environments also predates the first GW observations, since such mergers have long been proposed as the foundations of intermediate-mass and super-massive black hole (BH) formation (e.g., Kulkarni et al., 1993; Portegies Zwart & McMillan, 2000a; Wen, 2003; Banerjee et al., 2010; Downing et al., 2011; Morscher et al., 2015). Typically the BHs involved are of astrophysical origin, but primordial BHs have been proposed as well (Sigurdsson & Hernquist, 1993; O’Leary et al., 2006; Bird et al., 2016). More recently, the disks of active galaxy nuclei (AGN) have been suggested as an additional dynamical environment (McKernan et al., 2012, 2014a; Bellovary et al., 2016; Bartos et al., 2017; Stone et al., 2017; McKernan et al., 2018a; Tagawa et al., 2020). Stars in triple systems are an edge case between isolated and dynamical formation channels. Much of their evolution is dominated

by stellar interactions like mass transfer, but the third companion adds secular dynamics to the evolution (Lidov-Kozai cycles, e.g. Thompson, 2011; Antonini & Perets, 2012; Toonen et al., 2016; Kimpson et al., 2016; Antonini et al., 2017a; Vynatheya & Hamers, 2022; Stegmann et al., 2022).

In reality, these two camps of formation channels are not strictly disparate, in particular, there are observational hints that the formation of close pairs of ‘isolated’ binary stars requires dynamical interactions (e.g., Ramírez-Tannus et al., 2021; Stoop et al., 2023).

Source properties and their distinguishing power

The source properties of double compact objects (i.e., the total mass, mass ratio, spin properties, and eccentricity) shape the waveform of the GW signal they emit. The leading contribution to the waveform comes from the mass of the system, which determines the frequency at which the merger occurs (more massive mergers occur at lower frequencies). The component masses do not follow directly from the waveform, instead we measure the chirp mass $M_{\text{chirp}} = (m_1 m_2)^{3/5} / (m_1 + m_2)^{1/5}$, where $m_1 > m_2$ are the component masses. Because higher-mass systems are louder, they can be detected out to larger distances. For this reason current GW detectors are biased in favor of more massive systems (e.g., Fishbach & Holz, 2017), but next-generation detectors will not be bothered by this selection bias (see Section 6.1, and Vitale, 2016). Estimates of the mass ratio and spins are complicated due to a well-known degeneracy between the two (a large spin produces the same waveform as an unequal mass ratio e.g., Baird et al., 2013). Spins are better constrained for more unequal mass ratios (Vitale et al., 2014, 2017), in part because unequal mass ratios excite higher order harmonics, which helps

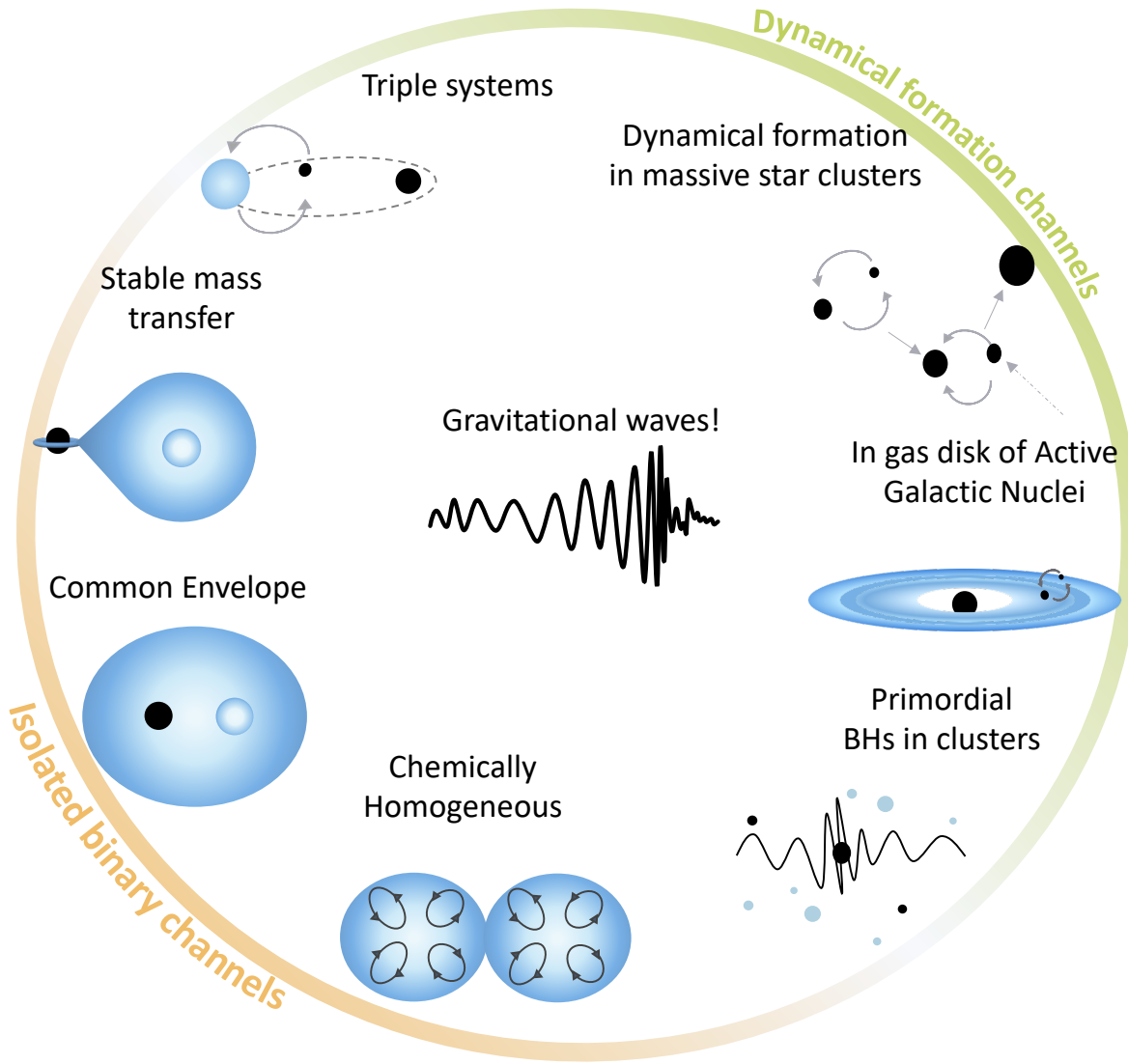


Figure 1.2: Cartoon depictions of the many channels that have been proposed to lead to merging double compact object formation. See text for details.

to break the degeneracy. As double compact objects lose angular momentum through GWs they circularize. Their eccentricity is typically small by the time they enter the LIGO-Virgo-KAGRA (LVK) frequency band. Ground-based detectors are thus not effective at measuring eccentricity, and it is necessary to move to lower frequencies (like those accessible with LISA Robson et al., 2019, see also Section 6.2).

The precision to which source properties can be estimated depends largely on the signal to noise ratio S/N, which is set by the signal amplitude, and the detector sensitivity. As detectors improve, so will the number of systems measured with high S/N. These improvements will be particularly significant for properties that leave weaker imprints on the waveform, such as the mass ratio and spin distributions (e.g. [Knee et al., 2022](#)).

Formation channels can potentially be distinguished by the imprints they leave on the source properties of merging double compact objects. Identifying the dominant formation channel is currently a major focus in the field of GW astronomy (e.g. [Rodriguez et al., 2016](#); [Arca Sedda, 2020](#); [Wong et al., 2021a](#); [Zevin et al., 2021](#); [Bouffanais et al., 2021](#); [Stevenson & Clarke, 2022](#); [Godfrey et al., 2023](#)). The myriad of physical processes involved in different formation channels indicate that GW astronomy has great potential to provide new insights on a broad range of topics, including the physics of binary interactions, the rate of massive star formation throughout cosmic history, and the structure and abundance of nuclear and globular clusters, as well as AGN disks. Despite the large number of formations channels that have been proposed, virtually *all*³ channels depend crucially on their direct ancestors: **massive stars**.

1.3 Massive (binary) stars

Massive stars (defined as stars with zero age main sequence (ZAMS) masses $\geq 10 M_{\odot}$) impact nearly *every* part of modern astrophysics; they shape our Universe through the ionizing radiation that they emit, and drive the chemical evolution of the Universe that enables the formation of complex molecules, ultimately facilitating the

³with the exception of primordial BH

CHAPTER 1. INTRODUCTION

formation of all complex molecules we encounter in our every-day life.

- The first stars were massive and metal poor (see review by [Bromm & Larson, 2004](#)), and are thought to be responsible for the reionization of the Universe (see reviews by [Barkana & Loeb, 2001](#); [Loeb & Barkana, 2001](#)). The hard ionizing emission from the stripped-star descendants of massive stars further help ionize the intergalactic medium (see [Götberg et al., 2020](#), and references therein).
- Massive stars furthermore play a crucial role in the chemical evolution of the Universe, as they are responsible for the production of the vast majority of elements more massive than boron (see review by [Arcones & Thielemann, 2023](#)). Elements up to iron are created through nuclear burning processes in the cores of massive stars, though only a small fraction of this material is ejected into the circum-stellar medium through winds and mass-transfer outflows (see e.g., [Smith, 2014](#)). S-processes in late burning phases can form elements heavier than iron. They primarily occur in low-mass Asymptotic Giant Branch stars, but also to some degree in WR stars (and even in chemically homogeneous stars [Banerjee, 2021](#)). Most of the chemical enrichment from massive stars occurs postmortem; through their explosive deaths known as supernova (SNe), and the merger event of their remnant neutron stars.
- Massive stars also play a key role in the formation and evolution of galaxies. The light from the first galaxies that are now being observed by the recently launched James Webb space Telescope (JWST [Gardner et al., 2006](#)) is dominated by the radiation from massive stars. SNe are furthermore a key driver of galactic winds, which can quench star formation (e.g., [Dekel & Silk, 1986](#); [Springel & Hernquist,](#)

2003; Faucher-Giguère et al., 2011) and enrich the circum-galactic medium (e.g., Aguirre et al., 2001; Oppenheimer & Davé, 2006; Fielding et al., 2017)

- Lastly, the compact-object remnants that they leave behind are interesting in their own right. Neutron stars and stellar-mass black holes result in a myriad of astronomical phenomena ranging from jets to tests of general relativity. (Lattimer & Prakash, 2004; Vidaña, 2018; Bambi, 2018; Krishnendu & Ohme, 2021). Their mergers have recently led to the discovery of GW, which is the central topic of this thesis.

The cosmic star-formation rate of massive stars

The time spanned between the birth of a binary star system and the moment of double compact object merger is known as the delay time, and can range from Myr to many Gyr. The mergers we observe today can thus originate from stars that formed at very high redshift. Hence, in order to make predictions for the merger rates of double compact objects, we need to account for the star-formation rate throughout cosmic history. Moreover, birth metallicity plays an important role in the evolution of massive stars (e.g. Maeder, 1992; Vink et al., 2001a; Vink & de Koter, 2005; Mokiem et al., 2007; Gräfener & Hamann, 2008; Vink & Sander, 2021). These effects propagate to the yield of double compact object formation, which is a strong function of metallicity (in particular more massive systems can only be formed at low metallicity Belczynski et al., 2010a; Mapelli et al., 2010; Giacobbo et al., 2018). Consequently, models of double compact object formation are sensitive to the *metallicity-dependent* cosmic star formation history (see Chapter 4, and the review by Chruścińska, 2022).

Massive stars are not alone

Over the past decade, it has become increasingly clear that virtually all massive stars (observationally classified as O- or early B-type stars) are born with at least one companion (e.g., Chini et al., 2012; Kobulnicky et al., 2014; Moe & Di Stefano, 2017; Almeida et al., 2017; Price-Whelan et al., 2020; Kounkel et al., 2021; Daher et al., 2022). Moreover, about 70% of O-type stars is part of a close binary system (with $a < 10$ AU) that will at some point interact with their companion (Sana et al., 2012; Offner et al., 2022). The closest binary stars (with orbital periods less than a few days) will interact through tidal forces. Moreover, the majority of binary systems on separations smaller than about $1000 R_{\odot}$ (or orbital periods less than about a few years), will at one point interact with their companion through mass transfer. As stars evolve and swell up, they can expand beyond the gravitational equipotential surface (the so-called ‘Roche Lobe’), causing mass to flow toward its companion (known as Roche-lobe overflow, RLOF). Such mass transfer events are ubiquitous, and the outcome of the interaction is decisive for the evolution and fate of the stars involved.

Mass transfer can broadly be classified as dynamically stable or unstable. Although the details of mass-transfer stability are complex (e.g., Woods & Ivanova, 2011; Pavlovskii et al., 2017; Klencki et al., 2021), this distinction is commonly made based on the response to mass loss of the Roche lobe radius ($\zeta_{RL} = d \log R_{RL} / d \log M$) and the radius of the donor star ($\zeta_{\star} = d \log R_{\star} / d \log M$). Mass transfer is dynamically stable if $\zeta_{\star} \geq \zeta_{RL}$, and unstable otherwise. During stable mass transfer or RLOF, the companion star has time to possibly accrete (part of) the donated companion envelope. How much of the donated mass is accreted by its companion, and the specific angular momentum carried by the transferred mass, determine the orbital evolution (e.g., Soberman et al.,

1997). On the other hand, unstable mass transfer is expected to lead to a ‘common envelope’ phase (see e.g., reviews by Ivanova et al., 2013a; Ivanova et al., 2020). This will dramatically shrink the binary orbit, and lead to very close orbit systems, or even stellar mergers.

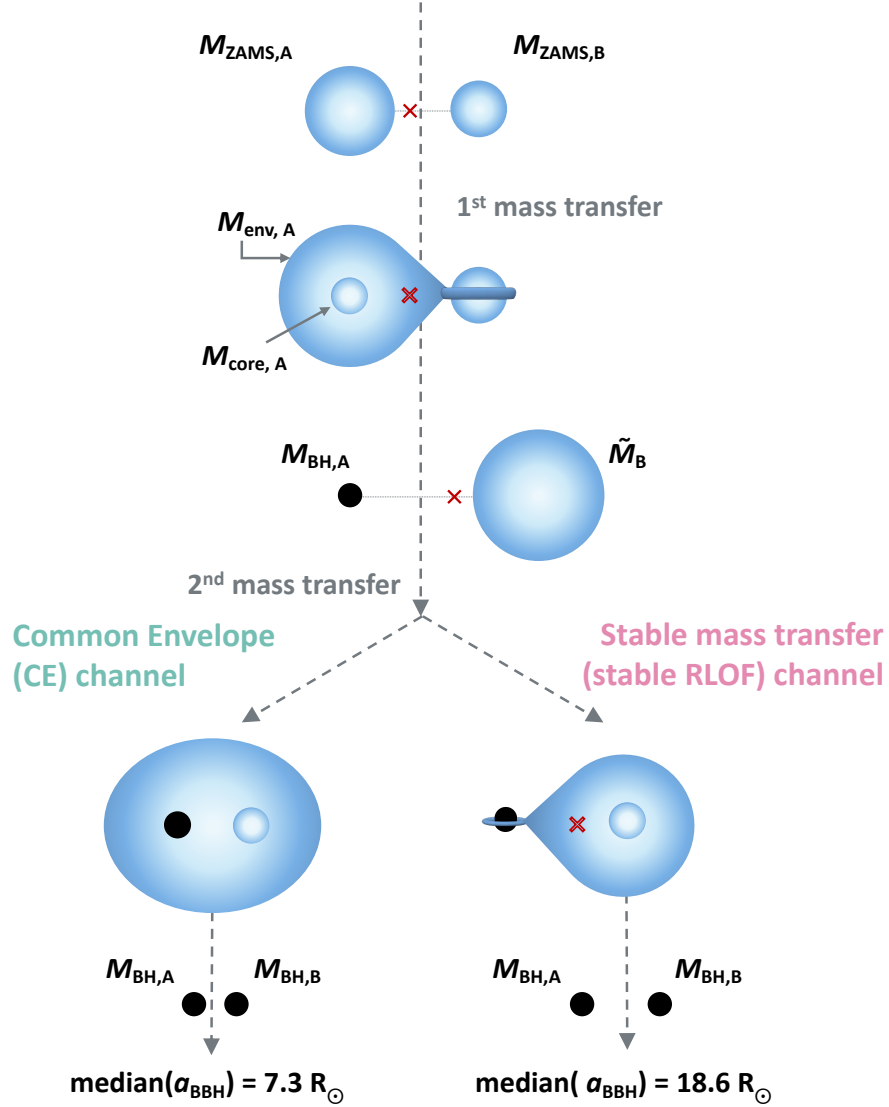


Figure 1.3: Isolated binary channels can broadly be separated based on the stability of mass transfer. Systems that experience *only* stable mass transfer are part of the ‘stable mass transfer channel’, or stable RLOF channel. Systems that experience unstable mass transfer and a following common envelope (CE) phase are considered part of the ‘common envelope channel’. Figure adapted from van Son et al. (2022b)

The dynamical stability of mass transfer has a significant impact on the final masses, separations, and expected delay times for double compact objects (see also Chapter 3). As a result, it plays a crucial role in the main subdivision of isolated binary formation channels that lead to merging double compact objects (see Figure 1.3). Specifically, isolated binary channels can broadly be divided between 1) the common envelope channel (or CE channel, e.g. Belczynski et al., 2007a; Postnov & Yungelson, 2014a; Belczynski et al., 2016a; Vigna-Gómez et al., 2018a), including BBH systems where the progenitor system has experienced at least one phase of unstable mass transfer, leading to a common envelope event, and 2) the stable Roche-lobe overflow channel (or stable RLOF channel, e.g. van den Heuvel et al., 2017; Inayoshi et al., 2017; Pavlovskii et al., 2017; Neijssel et al., 2019; van Son et al., 2022a; Briel et al., 2022b). The stable RLOF channel contains all BBH systems that experience *only* stable mass transfer (i.e., that *do not* experience CE events, and so it is the complement set of the CE channel). The relative contribution of the CE and the stable RLOF channel to the observed population of merging double compact objects is an active area of research (see e.g. Neijssel et al., 2019; Bavera et al., 2021a; Marchant et al., 2021; Gallegos-Garcia et al., 2021).

The challenge of understanding massive stars

Though impactful, massive stars are difficult to observe while alive. Firstly, massive stars are intrinsically rare as they are disfavored by the initial mass function (e.g., Kroupa, 2001). Second, massive stars live fast and die young: the more massive a star is, the faster it will burn through its fuel (e.g., Pols, 2011). Because of their elusive nature, only about a handful of stars with masses of more than $100 M_{\odot}$ have been detected so far (e.g., Crowther et al., 2010; Bestenlehner et al., 2011). Massive stars are furthermore difficult to model theoretically due to the enormous spatial and temporal range that

they cover: the relevant densities span from about $\rho = 10^{-9}\text{g/cm}^3$ in the envelope to $\rho = 10^1\text{g/cm}^3$ in the core. Similarly, the timescales involved range from Myr during H-burning, to sub-second timescales during SNe.

Due to the challenges in both observing and modeling massive stars, many open questions remain about their birth, lives and deaths. These questions range from the highly uncertain observed mass-loss rates that do not match theoretical predictions (e.g., [Brands et al., 2022](#)), to the final evolutionary stages of massive stars such as luminous blue variables (e.g., [Smith, 2017](#); [Weis & Bomans, 2020](#)), core-collapse supernovae ([Janka, 2012](#); [Burrows & Vartanyan, 2021](#); [Mezzacappa, 2023](#)) and gamma-ray bursts ([D'Avanzo, 2015](#); [Mészáros, 2019](#)). Binary interactions most likely play a fundamental role in each of these phenomena.

The new field of GW-astronomy is revealing a fossil record of these otherwise elusive massive stars, leading to a second fundamental question:

What can gravitational-wave sources teach us about their stellar progenitors?

1.4 The emerging progenitor population puzzle

The early stages of GW astronomy have been packed with surprises and discoveries. The first detection itself (GW150914 [Abbott et al., 2016](#); [Abbott et al., 2016a](#)). was a surprise for the scientific community since the existence of stellar-mass BHs with masses exceeding $15 M_\odot$ had not been anticipated. As we move from the excitement about individual sources to an era of ‘big data’, we can start to infer properties of the underlying population. The first ~ 90 observations of GW sources represent just the starting pieces of a much larger puzzle that will continue to be unveiled in the coming

decades. The hope is that different formation channels leave distinct imprints on the observed population of GW sources, that will help us uncover their origins. In particular, isolated binary channels are expected to carry signatures of the physical processes that governed the lives of their massive stellar ancestors. The observed properties of merging double compact objects, such as the overall merging rate, and the shape of the mass, mass ratio, and spin distributions, can thus provide crucial clues about the underlying physics. Below are two examples where observed features in the mass distribution of binary black holes have been linked to the underlying stellar and binary physics, leading to interesting new insights.

example 1: The Pair-Instability SN mass gap: Stellar theory predicts a gap in the black hole mass function between approximately $45 - 80 M_{\odot}$ and $135 - 160 M_{\odot}$, known as the pair-instability supernova mass gap (PISN mass gap, e.g., Heger & Woosley, 2002; Woosley et al., 2002a; Woosley, 2017). The progenitor stars of these BHs reach temperatures and densities in their centers that allow for electron-pair production, triggering a premature collapse of the carbon-oxygen core that results in an explosion that completely disintegrates the star (Fowler & Hoyle, 1964; Rakavy & Shaviv, 1967; Barkat et al., 1967; Fraley, 1968). For helium cores of $M_{\text{He}} \gtrsim 130 M_{\odot}$, photo disintegration prevents the premature collapse of the core and we expect BHs to form again (e.g. Bond et al., 1982; Heger & Woosley, 2002). PISN theory thus predicts a mass gap in the distribution of BH masses. The expected location of this gap is remarkably robust against most uncertainties in stellar evolution, but is only sensitive to the $^{12}\text{C}(\alpha, \gamma)^{16}\text{O}$ reaction rate (Takahashi et al., 2018; Farmer et al., 2019; Farmer et al., 2020; Renzo et al., 2020; Marchant & Moriya, 2020a). This has renewed interest in constraining this rate (Mehta et al., 2021; Farag et al., 2022;

Shen et al., 2023), and it has conversely been suggested that an observed mass gap in GW sources can be used to assess its value (Farmer et al., 2020). Initial GW-detections supported a dearth of BHs with masses above $45 M_{\odot}$ (Fishbach & Holz, 2017; Abbott et al., 2019b), but more recent observations have shown that this ‘gap’ is not empty (Abbott et al., 2021f). Since PISN theory predicts that isolated binaries cannot form BHs in this mass range, other formation channels have been suggested to explain the low but non-zero rate of mergers in the gap (see Chapter 2). This is one of the key assumptions in studies that aim to constrain the contribution of different formation channels to the overall population of merging BBHs (e.g., Arca Sedda et al., 2020a; Baibhav et al., 2020; Zevin et al., 2021; Wong et al., 2021a). It remains an open question whether the PISN mass gap has been observed in the population of merging BBHs, but near-future observations, such as those in O4, will help address this question.

example 2: The NS-BH mass gap: Early studies on the mass distribution of BHs based on X-ray binary observations suggested an absence of black holes in the $2\text{--}5 M_{\odot}$ range (e.g., Bailyn et al., 1998; Fryer & Kalogera, 2001; Özel et al., 2010; Farr et al., 2011). However, this idea of a gap between the most massive neutron stars and the least massive black holes, also known as the ‘NS–BH mass gap,’ has been a topic of active debate ever since it was first suggested due to expected observational and evolutionary selection biases (e.g., Kreidberg et al., 2012; Wyrzykowski & Mandel, 2020; Jonker et al., 2021; Siegel et al., 2022). Nonetheless, multiple theoretical models have been proposed to explain this gap as the result of a discontinuous remnant-mass distribution, driven by either the supernova engine (Fryer et al., 2012, 2022) or the progenitors’ density profile which determines if a supernova

fails (Kochanek, 2014, 2015). Recent GW observations show tentative evidence for a relative dearth of merging BBHs with component masses between $3 - 5 M_{\odot}$ (Farah et al., 2022; Ye & Fishbach, 2022; Biscoveanu et al., 2022). Some studies have linked this observed dearth of low-mass BHs observed in GWs to the underlying supernova engine (e.g., Zevin et al., 2020; Olejak et al., 2022). However, it is important to note that the population of GW sources is also a biased population and should receive equal, if not more scrutiny over its evolutionary selection effects as X-ray bright sources. In Chapter 5 we show how binary evolution alone can produce a dearth of low-mass BHs without invoking a discontinuous remnant-mass distribution, underlining the importance of understanding the effects of binary evolution.

To achieve our goal of using GW-sources to learn about their stellar ancestors, we must simulate populations of double compact objects that can be compared to observations. However, modeling their progenitor stars is challenging given the significant uncertainties associated with the evolution of massive stars. Assumptions about physical processes like stellar winds, SN physics, and mass transfer stability can vary greatly, and the large range of temporal and spatial scales involved makes it impossible to model many binary-star systems from first principles without incurring computational costs that are currently out of reach (see Section 1.3). To efficiently explore the uncertainties of massive binary star physics, we require a tool for rapidly simulating a range of assumptions. This is precisely the objective of rapid population synthesis simulations.

Rapid binary population synthesis simulations

The essence of rapid population synthesis simulations is to model large populations of binary stars by combining prescriptions for the evolution of single stars with prescriptions

CHAPTER 1. INTRODUCTION

for binary interactions. These simulations aim to produce predictions that can be compared to observations, ranging from expectations for stellar populations (such as the number of wide binaries) to transient event rates (like types of SNe or GW sources). Observationally motivated distributions are used to sample the initial conditions of binary stars such as masses, period, and metallicity (although adaptive importance sampling can be used to improve computational efficiency, see e.g., Broekgaarden et al., 2019). Some of the earliest works that follow this approach are; the Scenario Machine Lipunov et al. (1996a,b, 2009), IBiS (Tutukov & Yungelson, 1996), SeBa (Portegies Zwart & Verbunt, 1996; Portegies Zwart & Yungelson, 1998; Nelemans et al., 2001b; Toonen et al., 2012), and the Brussels population number synthesis code (Vanbeveren et al., 1998; De Donder & Vanbeveren, 2004).

Today, the most commonly used analytical formulae for single-star evolution are those from Hurley et al. (2000), which are based on evolutionary models by Pols et al. (1998). Combined with the binary evolution models from Hurley et al. (2002), this forms the basis for the majority of contemporary binary population synthesis codes, including BSE itself (Hurley et al., 2000, 2002), StarTrack (Belczynski et al., 2002, 2008, 2020), binary_c (Izzard et al., 2004, 2006, 2009), MOBSE(Giacobbo & Mapelli, 2018; Giacobbo et al., 2018), COSMIC (Breivik et al., 2020), and COMPAS (Riley et al., 2022a). Codes such as BPASS (Eldridge et al., 2017; Stanway & Eldridge, 2018) take a similar approach as the aforementioned codes, but base their single-star evolution on a grid of detailed stellar evolution tracks, that is computed using the STARS code (Eggleton, 1971; Pols et al., 1995; Eldridge & Tout, 2004). Other approaches similarly include generating large libraries of evolutionary tracks to that can be interpolated, such as is done in ComBinE (Kruckow et al., 2018), SEVN (Spera et al., 2015; Mapelli, 2020; Iorio et al., 2022), and

CHAPTER 1. INTRODUCTION

METISSE (Agrawal et al., 2020, 2023). Lastly, POSYDON (Fragos et al., 2022) incorporates full single-stellar and binary evolution modeling, using MESA evolutionary models, but this requires a lot more input, and is currently only available at one metallicity.

The main code applied in this thesis is COMPAS (Riley et al., 2022a). In addition to its binary evolution models, COMPAS also includes post-processing tools to study the evolution of populations over cosmic time (i.e., ‘cosmic integration’, see Chapter 4 and Neijssel et al., 2019). These tools can place binaries in a cosmological framework by linking birth metallicities to a metallicity-dependent cosmic star formation history, enabling us to make predictions for the double compact object merger rate distributions at different redshifts.

When is population synthesis an appropriate tool?

“All models are wrong but some are useful.” - George E. P. Box

It is important to keep in mind that *all* rapid population synthesis models heavily rely on crude assumptions for the underlying stellar physics. These uncertainties lead to many degeneracies in the results, and as a consequence, rate predictions can vary widely between studies (see Mandel & Broekgaarden, 2022). This implies that population synthesis can lead to ‘the right answer for the wrong reasons’, much like how some puzzle pieces can fit into several places, even if they do not make sense in the overall picture.. Therefore, population synthesis models are poorly equipped to measure an isolated parameter, and they will not answer questions like “what is the value of α_{CE} ”? (a parameter that is commonly used to estimate the outcome of a CE event). While population synthesis simulations may not provide ‘the one true solution’, they can be valuable for exploring the effect of certain physics assumptions on observable predictions.

In particular, it can be an extremely useful tool to I) isolate the effects of the certain assumptions in a way that is similar to a controlled laboratory setting, and II) tease out universal truths that are valid *regardless* of all the model uncertainties. In this thesis we aim to use both of these methods to gain insight into massive binary star evolution through GW observations.

1.5 Thesis outline

This thesis aims to assemble the first pieces of the progenitor population puzzle, as laid out by the the first three catalogs of GW sources. We apply a combination of numerical population synthesis models (using **COMPAS** as our main tool), and analytical models to build intuition for the complex phenomena involved.

Chapter 2 *Polluting the pair-instability mass gap for binary black holes*

through super-Eddington accretion in isolated binaries - in this chapter we examine whether BHs in isolated binaries can pollute the PISN mass gap by accreting a significant fraction of their stellar companion's envelope. We explore extreme assumptions about the accretion physics and allow for significantly super-Eddington accretion. We show how the classical isolated binary formation scenario does not contribute significantly to the pollution of the pair-instability mass gap, despite these extreme assumptions.

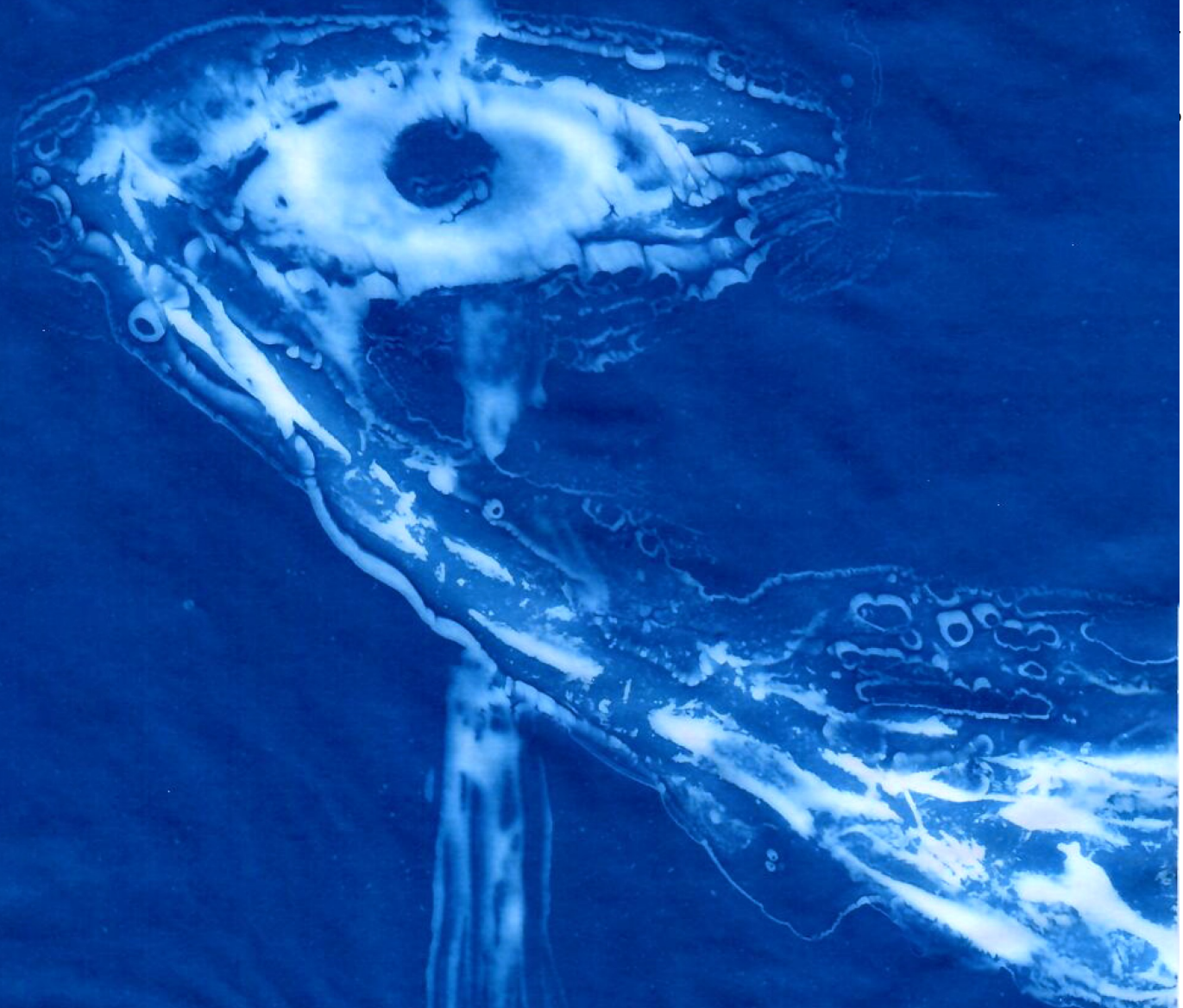
Chapter 3 *The redshift evolution of the binary black hole merger rate: a weighty matter* - aims to link delay times of merging BBHs to observables, such as the mass distribution. We distinguish between the CE channel and the stable RLOF channel, and find that each channel forms distinct mass and delay time distributions. Namely, the CE channel primarily forms lower mass BBHs (with primary masses $\lesssim 30 M_\odot$), and

CHAPTER 1. INTRODUCTION

shorter delay times ($t_{\text{delay}} \lesssim 1 \text{ Gyr}$), while the stable RLOF channel can also form more massive systems, and skews towards longer delay times. We use these findings to make predictions for the redshift evolution of the mass distribution for each formation channel.

Chapter 4 *The locations of features in the mass distribution of merging binary black holes are robust against uncertainties in the metallicity-dependent cosmic star formation history.* - In this chapter we introduce a simple analytical function for the metallicity-dependent cosmic star formation history ($\mathcal{S}(Z, z)$). The advantage of this function is that the parameters link to its shape in an intuitive way, which makes it easy to interpret variations. We use this function to systematically explore the effect of the $\mathcal{S}(Z, z)$ parameters on the mass distribution of merging BBH, and find that it does not affect the location of peaks in the mass distribution. This is promising as it implies that the locations of features can help constrain physics of their stellar progenitors.

Chapter 5 *No peaks without valleys: The stable mass transfer channel for gravitational-wave sources in light of the neutron star–black hole mass gap.* - In this chapter we explore the origin of the global peak of the merging BBH mass distribution at $\sim 9 M_\odot$. The location of this peak is tied to a dearth of BHs with masses just below $9 M_\odot$, reminiscent of the NS–BH mass gap. We show how binary-evolution effects alone are sufficient to explain the location of this peak. In particular we show that the stable mass transfer channel is inefficient at forming BBH mergers with more massive components below about $6 M_\odot$. This results in a dearth of low-mass BHs without the need for a discontinuous remnant-mass distribution.

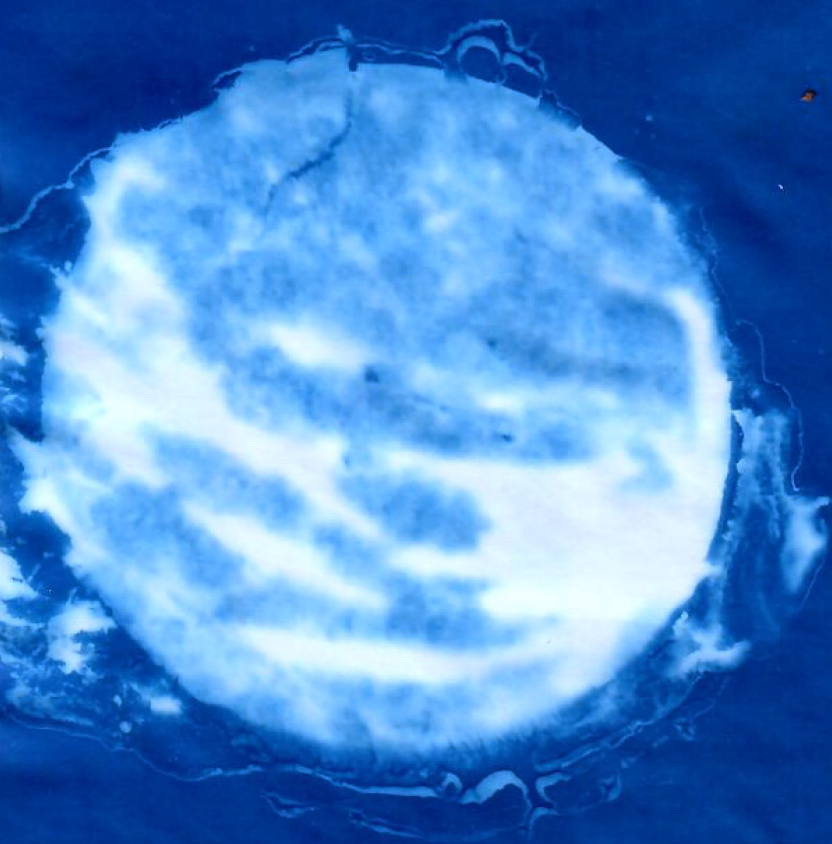


Chapter 2

Polluting the pair-instability mass gap for binary black holes through super-Eddington accretion in isolated binaries

This thesis chapter originally appeared in the literature as

L.A.C. van Son, S. E. de Mink, F. S. Broekgaarden, M. Renzo, S. Justham,
E. Laplace, J. Mor an-Fraile, D. D. Hendriks & R. Farmer,
The Astrophysical Journal, 2020, Vol. 897, Issue 1, Article id. 100



Abstract

The theory for single stellar evolution predicts a gap in the mass distribution of black holes (BHs) between approximately $45\text{--}130 M_{\odot}$, the so-called “pair-instability mass gap”. We examine whether BHs can pollute the gap after accreting from a stellar companion. To this end, we simulate the evolution of isolated binaries using a population synthesis code, where we allow for super-Eddington accretion. Under our most extreme assumptions, we find that at most about 2% of all merging binary BH systems contains a BH with a mass in the pair-instability mass gap, and we find that less than 0.5% of the merging systems has a total mass larger than $90 M_{\odot}$. We find no merging binary BH systems with a total mass exceeding $100 M_{\odot}$. We compare our results to predictions from several dynamical pathways to pair-instability mass gap events and discuss the distinguishable features. We conclude that the classical isolated binary formation scenario will not significantly contribute to the pollution of the pair-instability mass gap. The robustness of the predicted mass gap for the isolated binary channel is promising for the prospective of placing constraints on (i) the relative contribution of different formation channels, (ii) the physics of the progenitors including nuclear reaction rates, and (iii), tentatively, the Hubble parameter.

2.1 Introduction

Gravitational-wave detections are starting to reveal the properties of the population of merging binary black holes (BBHs). From the first gravitational-wave detections we learned that heavy black holes with masses $\gtrsim 30 M_{\odot}$ exist (Abbott et al., 2016b; Abbott et al., 2019a,b), which is well above the typical mass for BHs found in X-ray binaries in our galaxy (e.g. Özel et al., 2010; Farr et al., 2011).

These gravitational-wave detections yield unique information about the physics that governed the lives and deaths of their massive stellar progenitors. The first ten gravitational-wave detections already support a dearth of BBH mergers with component masses greater than $45 M_{\odot}$ (Fishbach & Holz, 2017; Abbott et al., 2019b). It has been suggested that this dearth can be attributed to so-called Pair-instability supernova (or PISN, Belczynski et al., 2016e; Woosley, 2017; Stevenson et al., 2019).

The theory of stellar evolution predicts that massive stars can end their lives as BHs with masses up to about $M_{\text{BH,max}} \approx 45 M_{\odot}$ (e.g. Heger & Woosley, 2002; Woosley et al., 2002a; Woosley, 2017; Farmer et al., 2019; Renzo et al., 2020). Progenitor stars with initial masses between $100 M_{\odot}$ and $140 M_{\odot}$ which potentially produce BHs with masses above $M_{\text{BH,max}} \approx 45 M_{\odot}$, become unstable due to the production of electron-positron pairs in their cores. This leads to the explosive ignition of oxygen, resulting in complete disintegration of the star in a pair-instability supernova (PISN, Fowler & Hoyle, 1964; Rakavy & Shaviv, 1967; Barkat et al., 1967; Fraley, 1968). Photodisintegration prevents the explosion of the most massive progenitors, with final helium cores of $M_{\text{He}} \gtrsim 130 M_{\odot}$, thus allowing for BH formation with masses in excess of $130 M_{\odot}$ (e.g. Bond et al., 1982; Heger & Woosley, 2002). Stellar theory thus predicts a gap in the black hole mass function between approximately 45 and $130 M_{\odot}$, referred to as the pair-instability supernova mass gap (or PISN mass gap).

Farmer et al. (2019) and Renzo et al. (2020) show that the predictions for the existence and the location of the pair-instability mass gap are remarkably robust. However, uncertainties in the nuclear reaction rates have a significant effect on $M_{\text{BH,max}}$, though they merely shift the location of the gap, and do not affect its existence. The fact that a robust and quantitative prediction exists for the final remnant masses of very mas-

sive stars is remarkable given how little is known about the lives of the most massive stars.

This prediction of a gap leads to many applications of $M_{\text{BH},\text{max}}$. For example, [Farr et al. \(2019b\)](#) (following [Schutz, 1986](#); [Holz & Hughes, 2005](#)) argue that if the BH mass distribution is truly shaped by PISN, $M_{\text{BH},\text{max}}$ could be used as a standard siren for cosmology. [Farmer et al. \(2020, in prep.\)](#) show that the location of $M_{\text{BH},\text{max}}$ can be used to constrain stellar physics, in particular the uncertain nuclear reaction rate of $^{12}\text{C}(\alpha, \gamma)^{16}\text{O}$. It has also been suggested that the existence of a mass gap can help to determine the relative contribution of different formation channels to the overall population of BBHs ([Arca Sedda et al., 2020a](#); [Baibhav et al., 2020](#)).

2.1.1 The scope of this work

In this work, we consider the possibility of forming BBH mergers where at least one of the components has a mass within the PISN mass gap, which we will refer to as “PISN mass gap events” hereafter, via the classic isolated binary channel. The classical isolated binary evolution channel for BBH mergers considers the evolution of stars that are born as members of an isolated binary system and experience a common-envelope (CE) phase ([Postnov & Yungelson, 2014a](#); [Belczynski et al., 2016a](#); [Eldridge & Maund, 2016](#); [Lipunov et al., 2017](#)).

We compare our results to predictions from dynamical pathways to PISN mass gap events. For this purpose, we adapt an existing population synthesis code, and we allow BHs to accrete mass from a stellar companion assuming the Eddington accretion rate can be exceeded during either a stable mass-transfer phase or during a common envelope event. We investigate the implications for the final masses of the merging BBH population.

This paper is structured as follows: we give an overview of different pathways to PISN mass gap events in Section 2.2. We describe our simulations in Section 2.3. The resulting predictions for populations of BHs are presented in Section 2.4. We compare our results to predictions from dynamical pathways to PISN mass gap events and discuss the distinguishable features in Section 2.5. We then discuss the robustness of our results in Section 2.6, and provide a summary of our conclusions in Section 2.7.

2.2 Forming PISN mass gap events

The formation of BBH mergers can be broadly divided into two channels, those originating from isolated binary evolution, and those that require dynamical interaction. We provide a brief overview of how each channel may contribute to the pollution of the PISN mass gap.

2.2.1 Forming PISN mass gap events through the classic isolated binary channel

In this paper we investigate whether the classical isolated binary evolution channel can contribute to the rate of PISN mass gap events. The first born BH in the classical isolated binary evolution channel may accrete mass from its companion star as this star evolves and swells to fill its Roche lobe.

In most population synthesis simulations of compact object mergers, accretion onto the compact object is assumed to be limited by the Eddington rate (e.g. Belczynski et al., 2002; Vigna-Gómez et al., 2018a; Neijssel et al., 2019; Spera et al., 2019a). Though exceptions exist, see for example Belczynski et al. (2008) and Mondal et al. (2019).

The Eddington rate is defined as the threshold where radiation pressure from the accretion luminosity halts the inflow of material in the case of spherical accretion.

Assuming pure hydrogen accretion;

$$\dot{M}_{\text{Edd}} = \frac{4\pi G m_p M}{\epsilon c \sigma_T} \approx 10^{-8} \left(\frac{M}{M_{\odot}} \right) \left[\frac{M_{\odot}}{\text{yr}} \right], \quad (2.1)$$

with G the gravitational constant, m_p the proton mass, M the mass of the accreting object, c the speed of light, and σ_T the Thompson scattering cross section (Eddington, 1926). We have assumed an accretion efficiency of $\epsilon = 0.1$ (Frank et al., 2002).

When considering BHs that can accrete from a companion star, the duration of the mass transfer phase is typically short (at most of the order of the thermal timescale of the donor star in the case of stable mass transfer and of the order of the dynamical timescale during a common envelope inspiral) and never longer than about 10 Myr, which is longer than the typical lifetime of massive stars. For these short durations the Eddington limit poses a very severe restriction on the amount of mass that a BH can accrete, as Eq. 2.1 shows. For example, a typical BH of $M_{\text{BH}} \approx 10 M_{\odot}$ cannot accrete more than a solar mass in 10 Myr if its accretion is limited at the Eddington rate.

Whether or not the Eddington rate poses an absolute limit to the rate at which BHs can accrete is matter of debate. First of all, it is based on several idealized assumptions, such as spherical accretion, that are typically not valid. If a BH accretes through a ‘slim’ accretion disk, the photons may escape without preventing accretion onto the BH (e.g. Abramowicz et al., 1988; Jiang et al., 2014; Madau et al., 2014; Volonteri et al., 2015). At high accretion rates, larger than approximately $10 \times \dot{M}_{\text{edd}}$, photons may be trapped, and advected into the black hole (e.g. Popham et al., 1999; Wyithe & Loeb,

2012; Sadowski & Narayan, 2015; Inayoshi et al., 2016). It is uncertain how accretion proceeds in such cases, but Inayoshi et al. (2016) argue that mass accretion in excess of 5000 times the Eddington accretion rate could occur, and can proceed stably.

Secondly, super-Eddington accretion has been suggested as the most natural explanation for a wide range of astronomical phenomena. For example in the context of the rapid growth of super-massive BHs in galactic nuclei (e.g. Volonteri & Rees, 2005; Pezzulli et al., 2016; Johnson & Haardt, 2016, and references therein). But also in the case of ultra luminous X-ray pulsars (Bachetti et al., 2014; Israel et al., 2017) and the galactic source SS 433 (see Fabrika, 2004, for a review).

The uncertainties related to the applicability of the Eddington rate pose an uncertainty on the predictions for binary black hole populations and therefore on the robustness of the prediction of the existence of the PISN mass gap. In this work we consider whether and how the possibility of super-Eddington accretion can lead to PISN mass gap events.

2.2.2 Pathways to pollute the PISN mass gap requiring dynamical interaction

Various other pathways have been proposed to create PISN mass gap events. Here, we provide a brief overview of these potential alternative pathways.

Consecutive mergers of BHs

The pathway that has been most extensively studied so far with regards to PISN mass gap events involves multiple consecutive mergers of BHs. These may occur in very dense environments where the escape velocities are large, and BBH

can form dynamically. High escape velocities are required to retain the BBH-merger product within the formation environment, thereby enabling a consecutive BH merger (Schnittman & Buonanno, 2007; Baker et al., 2007). Gerosa & Berti (2019) estimate that an escape speed of about $\gtrsim 50 \text{ km s}^{-1}$ is required to produce PISN mass gap events through consecutive BH mergers. Promising sites are nuclear star clusters (Antonini et al., 2019a) and the disks of active galactic nuclei (McKernan et al., 2014b, 2018b; Secunda et al., 2019; Secunda et al., 2020), where BHs may assemble in migration traps (Bellovary et al., 2016; Yang et al., 2019b; McKernan et al., 2020b).

Globular clusters have also been proposed as sites to create PISN mass gap events through consecutive mergers (Rodriguez et al., 2019a). However, their contribution may be low due to their low escape velocities. Globular clusters can only contribute significantly to the production of PISN mass gap events if the BHs are born with low spin (Rodriguez et al., 2019a), which minimizes the BBH merger-recoil.

Fallback of a H-rich envelope

An alternative idea involves a star with a final He core mass just below the limit for pulsational pair-instability, i.e. with $M_{\text{He}} \lesssim 35 M_{\odot}$, and an overmassive hydrogen-rich envelope (Woosley et al., 2007; Spera et al., 2019a). If such a star would (i) retain a hydrogen envelope that is substantially more massive than $10 M_{\odot}$ until its final stages, and (ii) the envelope of this star would fall onto the BH, then the total mass of the resulting BH could exceed the PISN limit.

Woosley et al. (2007) find BH masses of up to $65 M_{\odot}$ in their models for single stars, when assuming strongly reduced stellar winds and complete fallback of the hydrogen envelope. Di Carlo et al. (2020a) propose to produce hydrogen-rich progenitors with core

masses near the PISN limit through the merger of two stars in a binary system (see also Di Carlo et al., 2019; Vigna-Gómez et al., 2019; Mapelli et al., 2020). They argue that such stellar mergers may be prevalent in globular clusters as the result of dynamical encounters.

To be detectable as a PISN mass gap event, these BHs need to pair up with another BH, which may be possible inside young stellar clusters (Di Carlo et al., 2019, 2020a). The predictions for this channel are considered to be uncertain because these stellar mergers are not well understood (Justham et al., 2014; Menon & Heger, 2017) and since it is unclear whether the hydrogen envelope will fall back onto the BH (e.g. Nadezhin, 1980; Lovegrove & Woosley, 2013; Wu et al., 2018).

Accretion from the interstellar medium

Roupaas & Kazanas (2019) explore the limits of BHs fed by the interstellar medium (ISM), based on earlier work from Leigh et al. (2013). They assume that BHs in young stellar clusters accrete all the gas from their formation environment. These BHs subsequently form BBH pairs in the cluster through dynamical interactions. Their simulations suggest that it is possible to populate the PISN mass gap through this pathway, although their results depend heavily on the assumed cluster mass and gas density, as well as the gas depletion time-scale.

Primordial BHs

So far we have implicitly assumed the BHs to be of stellar origin. BHs have been hypothesized to be of primordial nature, in which case they are formed as a result of fluctuations in the early Universe (Zel'dovich & Novikov, 1966; Hawking, 1971). In principle, such BHs could populate the PISN mass gap, since there is no reason to expect

a sudden absence or reduction of BHs in this mass range (Carr, 1975; Bird et al., 2016; Sasaki et al., 2016; Raidal et al., 2017; Dvorkin et al., 2018). Primordial BHs also have to dynamically find a companion BH to form a PISN mass gap event.

2.3 Method

For this study we use the rapid population synthesis code that is part of the [COMPAS](#) suite. A full description of the code can be found in Stevenson et al. (2017); Vigna-Gómez et al. (2018a); Broekgaarden et al. (2019). Here we give a brief summary with an emphasis on the physics relevant for this study.

2.3.1 Initial parameters

We assume the masses of the initially more massive stellar components (the primary M_1) are distributed following a Kroupa (2001) initial mass function and draw masses in the range $20 - 150 \text{ M}_\odot$. The binary systems are assumed to follow a uniform distribution of mass ratios ($0.001 \lesssim q = M_2/M_1 < 1.0$) where the lower limit is set by the minimum mass of the initially less massive component (the secondary component, $M_2 \geq 0.1 \text{ M}_\odot$). The initial binary separations are furthermore assumed to follow a distribution of orbital separations that is flat in the logarithm (Öpik, 1924) in the range $0.01 - 1000 \text{ AU}$. Binary systems that fill their Roche lobe at zero age main sequence are discarded. All simulations assume a metallicity of $Z = 0.001$, chosen to represent a typical low metallicity environment in which heavy black holes can form (Belczynski et al., 2010b; Stevenson et al., 2017) and to be consistent with Farmer et al. (2019). In Section 2.4.4, we discuss why adopting a single metallicity is sufficient for the purposes of this study.

To optimize computing time, we use the adaptive sampling algorithm [STROOPWAFEL](#)

([Broekgaarden et al., 2019](#)) to draw the initial parameters of the binaries. This algorithm consists of an exploration phase to draw massive binaries directly from their initial birth distributions. After this, systems are drawn from reweighted distributions to optimize for the number of systems that end as a BBH that will merge within a Hubble time. In total we evolve 10^6 binaries for each considered model variation. This results in approximately 1.4×10^5 BBH systems in each model.

2.3.2 Evolution and mass loss

We model the evolution of individual binary systems with the algorithms by [Hurley et al. \(2000, 2002\)](#) based on evolutionary models by [Pols et al. \(1995\)](#). We account for stellar wind mass loss following [Vink et al. \(2000, 2001b\)](#), [Hamann & Koesterke \(1998\)](#) and [Vink & de Koter \(2005\)](#), and we assume enhanced mass loss rates in the regime of luminous blue variables following [Belczynski et al. \(2010a\)](#).

Compact objects and supernova kicks

The remnant mass is modeled as a function of the estimated carbon-oxygen (CO) core mass at the moment of core collapse (M_{CO}). For $M_{\text{CO}} < 30 M_{\odot}$ we use the delayed model from [Fryer et al. \(2012\)](#) to determine the remnant masses. For $M_{\text{CO}} > 30 M_{\odot}$ we use the remnant mass prescription from [Farmer et al. \(2019\)](#) to account for the effects of pair pulsations and pair-instability supernovae (see Appendix 2.11 for a comparison of these two prescriptions). With this implementation the lower edge of the pair-instability mass gap is located at $M_{\text{BH,max}} \approx 43.5 M_{\odot}$, for a metallicity $Z = 0.001$.

To model supernova kicks, we draw kick velocities with random isotropic orientations and kick magnitudes from a Maxwellian distribution ([Hobbs et al., 2005](#)). BH kicks are subsequently reduced. For BHs resulting from progenitors with $M_{\text{CO}} < 30 M_{\odot}$ at

the moment of core-collapse, BH kicks are reduced by the amount of mass falling back onto them during the explosion mechanism, following Fryer et al. (2012). Since the most massive BHs are thought to form without a supernova explosion, we assume no supernova kick occurs for BHs resulting from progenitors with $M_{\text{CO}} > 30 M_{\odot}$.

Mass transfer

We account for mass transfer when a star overflows its Roche lobe, where the Roche-lobe radius is approximated following Eggleton (1983). To determine whether Roche-lobe overflow is stable we use an estimate for the response of the radius of the donor star and its Roche lobe as a result of mass transfer (see e.g. Vigna-Gómez et al., 2018a, and references therein).

During stable mass transfer onto a stellar companion we assume that the accretion rate is limited to at most ten times the thermal rate of the accreting star (Neo et al., 1977; Hurley et al., 2002). Material lost from the system is assumed to carry the specific orbital angular momentum of the accreting star (e.g. Soberman et al., 1997; van den Heuvel et al., 2017).

Unstable mass transfer is assumed to result in CE evolution (Paczyński, 1970; Ivanova et al., 2013b). Successful CE ejection is allowed for donor stars that are in the Hertzsprung gap (the optimistic approach to CE, following Belczynski et al., 2020). This is consistent with Stevenson et al. (2019). We assume this shrinks the orbit following the α, λ formalism as proposed by Webbink (1984) and de Kool (1990), using the fits provided by Xu & Li (2010b,a) that account for the internal energy of the envelope. If the donor star overflows its Roche lobe directly following a CE event, we assume the binary was not able to eject its envelope and presume the system ends as a stellar

merger.

2.3.3 Treatment of black hole accretion in this study

Here we consider different modes where we allow for the possibility of super-Eddington accretion onto BHs, as we describe below. We adopt the assumption of Eddington limited accretion in what we will refer to as our fiducial simulation (model 0). Specifically, we limit the accretion onto compact objects to the Eddington rate as given in Eq. 2.1.

In our first model variation (model 1) we allow for super-Eddington accretion during phases of stable mass transfer when the accretor is a BH. We consider the extreme limit where the black hole accretes all the mass provided by the donor star.

In our second model variation (model 2), we consider the accretion of mass onto BHs during the inspiral phase of a CE event. Following the arguments first presented in Chevalier (1993); Brown (1995); Bethe & Brown (1998) and later MacLeod & Ramirez-Ruiz (2015), the mass accreted by the BH, ΔM_{acc} , can be estimated as Hoyle-Littleton accretion rate \dot{M}_{HL} times the duration of the inspiral time, Δt_{insp} . This gives

$$\Delta M_{\text{acc}} \approx \dot{M}_{\text{HL}} \Delta t_{\text{insp}} \approx \frac{M_{\text{BH,birth}} \cdot M_{\text{comp}}}{2(M_{\text{BH,birth}} + M_{\text{comp}})}, \quad (2.2)$$

where $M_{\text{BH,birth}}$ is the birth mass of the BH and M_{comp} is the mass of the companion. Equation 2.2 approximates the inspiral time as the ratio of the orbital energy to the drag luminosity (i.e. Iben & Livio, 1993). Unlike MacLeod & Ramirez-Ruiz (2015), we do not restrict the accreted mass due to microphysics or the envelope structure, implying that our estimates for the final BH masses can be taken as extreme upper limits.

Lastly, we also run a combined model (model 3) which allows for super-Eddington accretion onto BHs during both stable mass-transfer phases and CE phases.

The assumptions adopted in our model variations are extreme by design. This allows us to place an upper limit on the masses that stellar-mass BHs can reach. These assumptions are intended to provide upper limits to the contribution of the isolated binary evolutionary channel to PISN gap merger events.

We refer to our first model variation as model 1: ‘stable accretion model’, and to our second model variation as model 2: ‘CE accretion model’. The combined model variation is referred to as model 3: ‘combined model’.

Throughout this paper we will use ‘PISN mass gap systems’ as a shorthand for BBH systems with at least one component with $M_{\text{BH}} > M_{\text{BH,max}}$. If a PISN gap system will merge within a Hubble time due to gravitational waves, we refer to it as a ‘PISN mass gap event’.

We adopt $M_{\text{BH,max}} = 45 \text{ M}_{\odot}$ for the lower edge of the PISN mass gap. This value is slightly higher than the $M_{\text{BH,max}}$ resulting from the simulations by Farmer et al. (2019) at $Z = 0.001$, whose prescriptions we adopt to model the final remnant masses. $M_{\text{BH,max}} = 45 \text{ M}_{\odot}$ is thus chosen to represent a conservative limit for the lower edge of the PISN mass gap. This value is also consistent with the limit used by Fishbach et al. (2020).

2.4 Results

We describe our results for the individual component masses of BBH systems in Section 2.4.1, and the effect on the mass ratios in Section 2.4.3. The distribution of total

BBH masses is discussed in Section 2.4.2, and the estimated merger rates in Section 2.4.4.

2.4.1 Component masses

Figure 2.1 shows the distribution of individual BH masses for our fiducial (model variation 0), stable accretion (model variation 1) and CE accretion model (model variation 2). The top row of Figure 2.1 shows a cartoon depiction of the model variations considered here. The primary BH mass, $M_{\text{BH},1}$, refers to the mass of the BH that originates from the initially more massive star in the binary system. Similarly the secondary BH mass, $M_{\text{BH},2}$, refers to the mass of the BH that originates from the initially less massive star. The middle row displays all BBHs resulting from our simulations, while the bottom row focuses on BBH systems that merge within a Hubble time due to gravitational-wave emission.

Figure 2.1 (following page): **Top:** Cartoon depictions of the BH accretion phase of binary evolution that is varied between the simulations. **Middle:** The final component masses of the simulated BBH systems for the fiducial population (left column), the BH population that accretes at super-Eddington rates during stable mass transfer (middle column), and the BH population that accretes during CE events (right column). The light blue shaded region bordered by dotted blue lines indicates the approximate location of the PISN mass gap. Colors indicate the amount of mass accreted by one of the BH components. Gray dots are systems where the BHs did not accrete any mass. The black dotted line shows where $M_{\text{BH},1} = M_{\text{BH},2}$. **Bottom:** same as middle, but only including the BHs that merge within a Hubble time. Note that the BHs as shown are all those that occur in our simulations; they are not weighted by their formation probability.

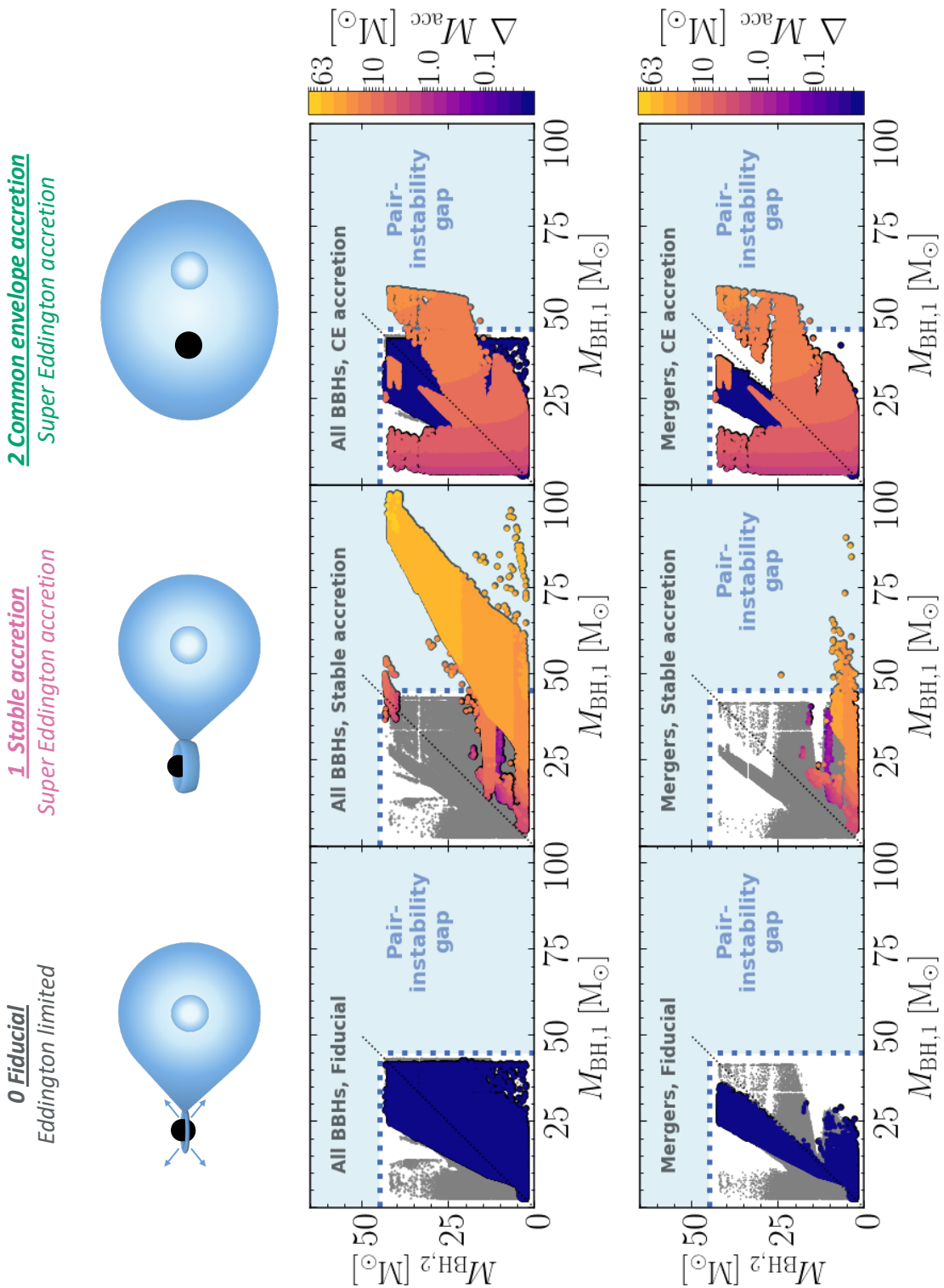


Table 2.1.: Comparison of the full population of BBH (All) and the subset of those that merge within a Hubble time (Merging). We provide the maximum BH ($M_{\text{BH,max}}$) for individual BHs and the fractions of BBHs with at least one component more massive than $30 M_{\odot}$ and $45 M_{\odot}$ (f_{30} and f_{45} , respectively). The errors shown are an estimate of the $1-\sigma$ errors that result from the statistical sampling uncertainty , see Appendix 2.10 for the derivation.

Model	All			Merging		
	f_{30}	f_{45}	$M_{\text{BH,max}}$	f_{30}	f_{45}	$M_{\text{BH,max}}$
	%	%	(M_{\odot})	%	%	(M_{\odot})
0. Fiducial	35.5 ± 0.4	0.0	43	10.7 ± 0.1	0.0	42
1. Stable super-Eddington	44.0 ± 0.5	20.3 ± 0.2	103	7.89 ± 0.1	0.13 ± 0.03	90
2. Common envelope accretion	36.6 ± 0.4	0.63 ± 0.01	57	14.8 ± 0.1	1.33 ± 0.05	57
3. Combined	46.1 ± 0.4	20.7 ± 0.2	103	16.8 ± 0.1	2.35 ± 0.06	90

BBH systems are shown as gray points unless the first born BH accreted from its companion. For the latter systems, the colors indicate the amount of mass that is accreted by the first born BH through accretion from its stellar companion, ΔM_{acc} .

We furthermore estimate the fraction of BBHs with at least one component more massive than $30 M_{\odot}$ and $45 M_{\odot}$, denoted as f_{30} and f_{45} respectively. We also quote the maximum mass for individual BHs ($M_{\text{BH,max}}$) created in our simulations. The results for all three model variations as discussed below are summarized in Table 2.1.

Fiducial model

The fiducial population does not produce any BBH systems with component masses above $M_{\text{BH,max}} = 45 M_{\odot}$ (i.e. $f_{45} = 0\%$), in agreement with earlier studies (e.g. Belczynski et al., 2016e; Stevenson et al., 2019). This can be seen in the left-most column of Figure 2.1 and in Table 2.1. In practice we find no BHs more massive than

$M_{\text{BH}} \approx 43 M_{\odot}$, which is the limit set by the remnant mass function as adopted in this work (see Appendix 2.11).

We see that BBHs that have accreted mass (blue points in the left column of Figure 2.1) span the whole mass range, but have a slight preference for equal mass ratios. BHs that are part of a merging BBH system prefer lower primary BH masses, $M_{\text{BH},1}$. The BBH systems with the lowest mass $M_{\text{BH},1}$ primarily result from systems that interacted early on in their stellar evolution. Further substructure in the $M_{\text{BH},1}$, $M_{\text{BH},2}$ distribution is caused by their origin from different evolutionary channels (see e.g. Dominik et al., 2012, for a discussion of different evolutionary channels).

The fraction systems containing a heavy BH, f_{30} , is about a third for the full population and one tenth for the population that merges. These values are relatively large, this results from the fact that we have assumed a low value for the metallicity $Z = 0.001$, which leads to reduced mass loss through stellar winds and the formation of heavier black holes. This has been pointed out in earlier studies (e.g. Belczynski et al., 2010a; Stevenson et al., 2017).

The Eddington limit severely restricts the amount of mass that is accreted, ΔM_{acc} , and BHs accrete less than about $0.01 M_{\odot}$ in this model. This confirms that accretion cannot lead to PISN mass gap systems in the fiducial model.

The results obtained with our fiducial model are very similar to those presented in Stevenson et al. (2019), who also used the COMPAS suite, with very similar assumptions and initial conditions. Small differences arise from the different treatment of pulsational mass loss and PISNe, which are discussed in Section 2.3 and Appendix 2.11).

Model variation 1: Stable Accretion

Our first model variation, where we allow for super-Eddington accretion rates during stable mass transfer, is shown in the central column of Figure 2.1. The population of BHs experiencing stable mass accretion accretes between 0.1 and approximately $63 M_{\odot}$, placing many BHs in the PISN mass gap. Note that the progenitors of accreting BHs are commonly the initially more massive stars, since these typically evolve on a shorter timescale. We find that approximately one fifth of all systems have at least one BH more massive than $45 M_{\odot}$, i.e. $f_{45} \approx 20\%$.

The maximum amount of mass that BHs can accrete is limited by the available matter rather than the accretion rate in this model. In practice the available matter equals the mass of the donor’s envelope. The theoretical maximum for the most massive BH in this model variation is therefore the maximum mass of a BH at birth, plus the maximum envelope mass of the companion. The most massive BH formed in this simulation is just over $100 M_{\odot}$ (i.e., $M_{\text{BH,max}} \approx 103 M_{\odot}$), but we note that for the most extreme masses, our simulations are affected by uncertainties resulting from sampling effects.

The distribution shows a clear upward diagonal trend, similar to the fiducial simulation but shifted to higher masses for $M_{\text{BH},1}$. This can be understood when considering that higher-mass BHs generally come from higher-mass progenitors, which typically have higher-mass companions. Higher-mass companions typically have more massive envelopes and thus have more mass available to donate to the first born BH, leading to a larger amount of accreted mass, ΔM_{acc} , and a higher-mass primary BH, $M_{\text{BH},1}$. At the same time, the higher-mass companions have larger cores and result in higher-mass secondary BHs, $M_{\text{BH},2}$. Thus, the accreted mass (ΔM_{acc}) scales with the

final mass of the secondary BH, $M_{\text{BH},2}$.

Outliers to this main trend exist, as can be seen in the central column, middle row of Figure 2.1 around $M_{\text{BH},1} \approx M_{\text{BH},2} \approx 50 M_{\odot}$, and around $M_{\text{BH},1} \approx 75 M_{\odot}$ with $M_{\text{BH},2} \leq 25 M_{\odot}$. In these cases, the massive stellar progenitor of the BH has already lost most of its envelope due to winds. This occurs in systems where the mass transfer happens at a later evolutionary stage of the donor star (i.e., case C mass transfer, Lauterborn, 1970).

For conservative mass transfer, as we assume for accreting BHs in this model variation, mass and angular momentum conservation dictate that the binary orbit widens when the donor is less massive than the accretor, i.e. when the mass ratio is reversed (e.g. Soberman et al., 1997). This is also true when we consider lower accretion efficiencies and assume that the mass that is not accreted is lost with the specific orbital angular momentum of the BH (see Appendix 2.9 and Section 2.6.1 for a discussion). We find that the mass ratio is almost always reversed by the super-Eddington accretion in this model variation, and thus also that the binary orbit widens in almost all cases.

Stable mass transfer thus widens BBH systems. Moreover, the more mass is transferred, the wider the system becomes and therefore stable super-Eddington accretion widens BBH systems significantly. Widening the orbit has a strong effect on the gravitational-wave merger time, since it scales with the binary separation to the fourth power (Peters, 1964). Sufficiently wide BBH systems cannot merge within a Hubble time through gravitational waves alone.

The most massive BH that is part of a BBH system that still merges within a Hubble time has a mass of $M_{\text{BH}} \approx 90 M_{\odot}$. The most massive systems ($M_{\text{BH},1} \geq 70 M_{\odot}$) in the stable accretion model that still merge within a Hubble time experience a similar evolution. Merging BBH systems after a long phase of stable super Eddington accretion is only possible through a BH-kick from the secondary BH. A ‘lucky’ BH-kick can increase the binary eccentricity to nearly 1, which radically reduces the gravitational wave inspiral time (Peters, 1964). Significant BH-kicks are only implemented in our simulations for relatively low mass CO cores ($\leq 15 M_{\odot}$). Therefore this evolutionary pathway is only possible for relatively extreme mass ratio BBHs. Whether such BBH systems exist in nature furthermore depends on the physics of BH-kicks, which is a matter of debate.

The vast majority of the affected systems do not merge within a Hubble time (central column, bottom row of Figure 2.1). Only 0.1% of the merging BBH systems in this model variation contain a BH with $M_{\text{BH}} \geq 45 M_{\odot}$ ($f_{45} = 0.1 \pm 0.03\%$). Moreover, the bulk of PISN mass gap systems created in this model variation is not only too wide to merge within a Hubble time, but is also too wide to be detectable through all planned gravitational-wave detectors such as LISA (based on values from Ni, 2018).

Model variation 2: common envelope accretion

Our second model variation, which allows super-Eddington accretion onto BHs during the inspiral phase of a CE event, is displayed in the right-most column of Figure 2.1. This model does produce BHs with masses in the PISN gap, but the BHs are not as massive as those resulting from our stable super-Eddington accretion model.

The amount that BHs can accrete in this model, ΔM_{acc} , is regulated by Equation 2.2,

which effectively limits the maximum mass that a BH can accrete to about $20 M_{\odot}$. We illustrate this in Figure 2.2, where we plot $M_{\text{BH}} = M_{\text{BH,birth}} + \Delta M_{\text{acc}}$ as a function of the companion mass at the onset of the CE, for different values of $M_{\text{BH,birth}}$. The figure shows that only BHs with high birth masses can produce BHs with masses in the PISN gap. The maximum potential BH mass is about $60 M_{\odot}$, but this mass can only be achieved under optimal and idealized circumstances. In practice this limit is never reached, both because of sampling effects, and because of stellar winds, which eject part of the envelope before it can be transferred to the BH companion. In our numerical simulations, the most massive BH formed is $M_{\text{BH,max}} \approx 57 M_{\odot}$.

While this model does not favor the formation of extremely massive systems as found in model variation 1, it does favor the formation of BBHs in tight orbits. A larger number of affected systems can thus merge within a Hubble time through the emission of gravitational waves with respect to the affected systems in model variation 1, as can be seen in the bottom row of Figure 2.1.

Model variation 3: Combined

Our combined model variation leads to the combined effects of model variations 1 and 2, the stable accretion and CE accretion models respectively. More BBH systems are affected by accretion in the combined model, and the fraction of PISN gap mergers increases. However, it does not lead to a significantly larger $M_{\text{BH,max}} \approx 103$ nor a larger BH mass among the merging BBH population, $M_{\text{BH,max}} \approx 90 M_{\odot}$, than in our second model variation. We find only about 2% PISN gap mergers where one of the BHs is more massive than $45 M_{\odot}$, i.e. $f_{45} \approx 2.4\%$.

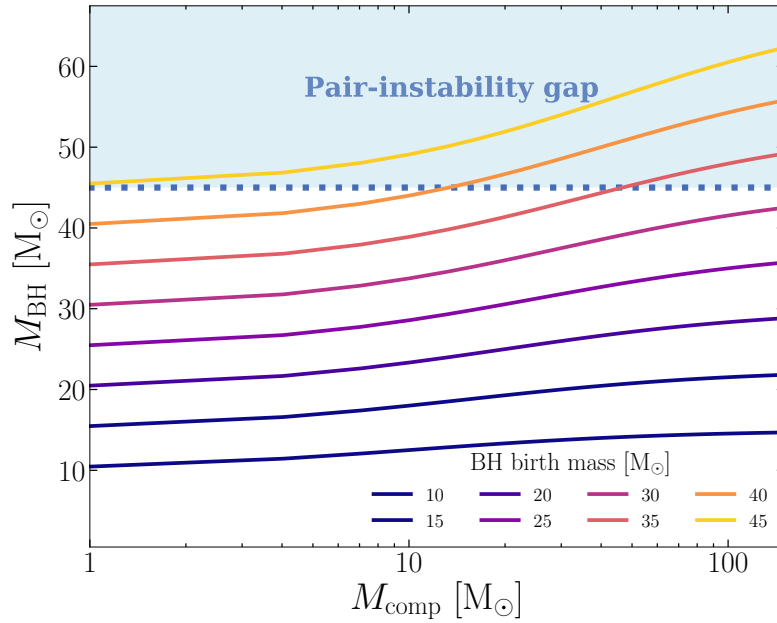


Figure 2.2: The maximum mass for accreting BHs in model variation two, the CE accretion model, following Equation 2.2 as a function of the companion mass at the moment of Roche-lobe overflow. This illustrates that only BHs with a birth mass close to the PISN gap can potentially accrete enough to end with a final mass in the gap.

2.4.2 Total mass distribution

Analysis of gravitational wave merger signals provides a more accurate determination for the total mass of BBH mergers than for the individual BH masses. We therefore show the distribution of the total BBH masses ($M_{\text{BBH}} = M_{\text{BH},1} + M_{\text{BH},2}$) in Figure 2.3. The distributions are normalized and the individual BHs are weighted according to the distributions of their initial parameters. We have checked that the $1-\sigma$ statistical sampling error is less than 0.001 for all bins. The blue-shaded region marks the location of the PINS mass gap for equal mass systems.

We furthermore provide the maximum total BBH mass ($M_{\text{BBH},\text{max}}$) and the fractions of BBHs with a total mass M_{BBH} higher than 60 M_\odot and 90 M_\odot ($f_{\text{BBH},60}$ and $f_{\text{BBH},90}$) respectively, in Table 2.2.

All BBHs

The top panel of Figure 2.3 shows the distribution for all BBHs formed in our simulations, including those that are too wide to merge.

The assumptions we make in the second model variation (super-Eddington accretion during CE) appear to have limited effect on the overall population of BBHs, and the shape of the BBH mass distribution varies little between the fiducial and CE accretion model (models 0 and 2).

Both the fiducial and CE accretion model avoid the PISN mass gap. For the fiducial model $M_{\text{BBH,max}} \approx 86 M_\odot$ and $f_{\text{BBH},90} = 0\%$. Although the maximum BBH system mass $M_{\text{BBH,max}} \approx 99$ for the CE accretion model, $f_{\text{BBH},90}$ is only 0.1%.

As discussed in Section 2.4.1, the CE accretion model only produces BBH mergers

Figure 2.3 (following page): **Top:** Weighted distribution of the total BBH masses (M_{BBH}) from our fiducial simulation (filled gray), the stable super-Eddington accretion (dashed pink line), the simulation allowing super-Eddington accretion during a CE phase (dotted green line) and the combined model (solid orange line). All distributions are normalized. The light blue region bordered by dotted lines indicates the approximate location of the PISN gap assuming BHs of equal mass. **Middle:** The same as the top panel, but restricted to BBH systems that are close enough to merge within a Hubble time. **Bottom:** The same as the middle panel, but the population is re-weighted by the detection bias from LIGO/Virgo (Fishbach & Holz, 2017). The 90% confidence intervals of the observed M_{BBH} values from Abbott et al. (2019a) are also shown as grey horizontal lines, at arbitrary heights.

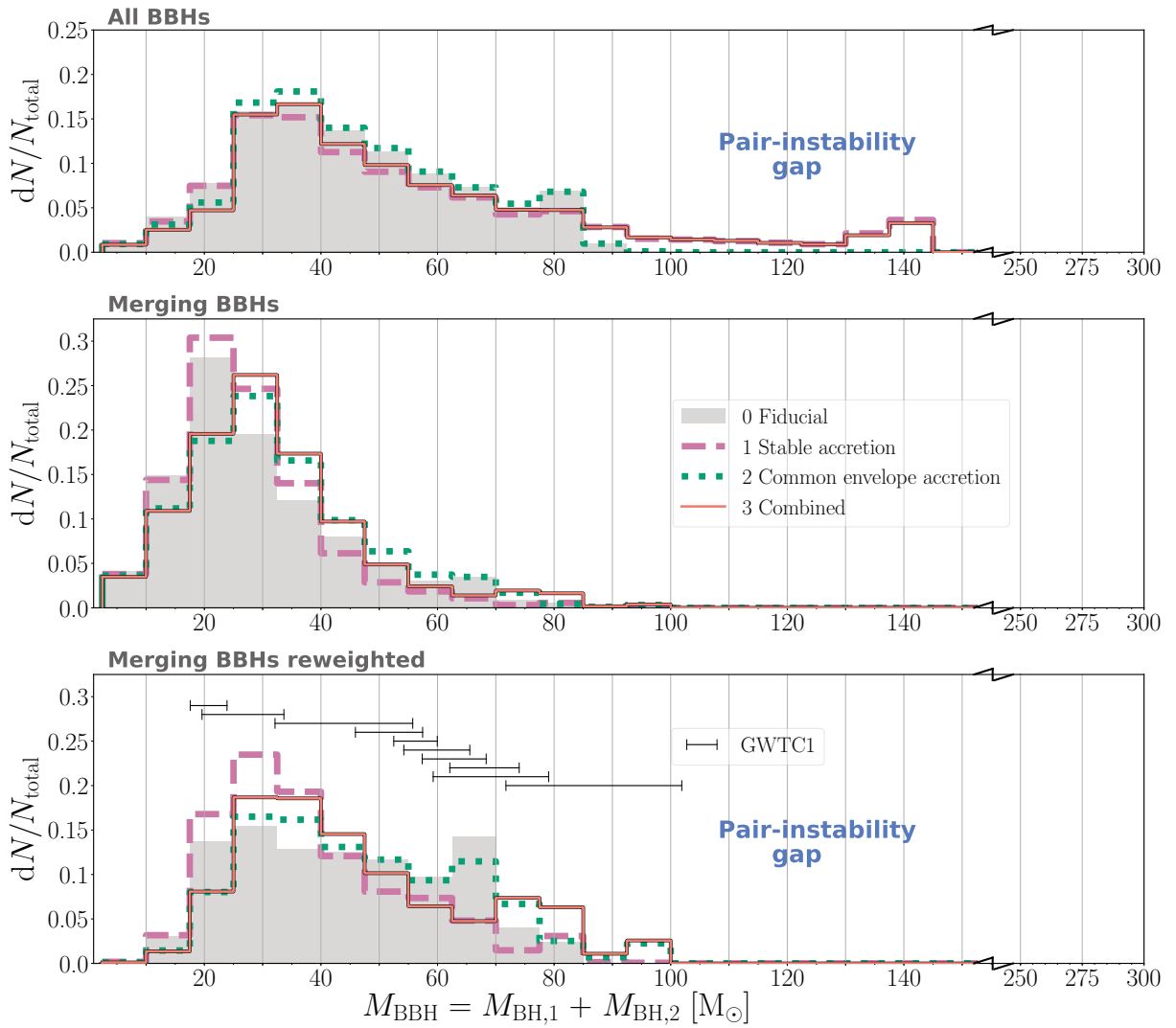


Table 2.2.: The fractions of BBHs with a total mass M_{BBH} higher than 60 and 90 M_{\odot} ($f_{\text{BBH},60}$ and $f_{\text{BBH},90}$, respectively), and the maximum total BBH mass ($M_{\text{BBH},\text{max}}$). The errors shown are the $1-\sigma$ estimate of the statistical sampling uncertainty.

Model	All			Merging		
	$f_{\text{BBH},60}$	$f_{\text{BBH},90}$	$M_{\text{BBH},\text{max}}$ (M_{\odot})	$f_{\text{BBH},60}$	$f_{\text{BBH},90}$	$M_{\text{BBH},\text{max}}$ (M_{\odot})
	%	%		%	%	
0. Fiducial	23.1 ± 0.3	0.0	86	5.8 ± 0.1	0.0	84
1. Stable super-Eddington	32.2 ± 0.4	12.7 ± 0.2	144	2.6 ± 0.1	0.01 ± 0.00	95
2. Common envelope accretion	23.4 ± 0.3	0.11 ± 0.01	99	7.1 ± 0.1	0.36 ± 0.03	99
3. Combined	32.6 ± 0.3	12.2 ± 0.2	146	6.2 ± 0.1	0.45 ± 0.03	99

that are marginally in the PISN mass gap. Figure 2.3 shows that such marginal BBH mergers do not stand out as PISN mass gap systems when M_{BBH} is evaluated.

The stable accretion and combined model variations (models 1 and 3) both display a clear tail of massive systems. The maximum total BBH mass extends to $M_{\text{BBH},\text{max}} \approx 144 M_{\odot}$ in both models. We find that approximately 12.7% and 12.2% of the BBH systems has a mass of $M_{\text{BBH}} \geq 90 M_{\odot}$ for model variation 1 and 3, respectively.

All model variations peak in M_{BBH} at approximately 30 to 40 M_{\odot} .

Merging BBHs

The middle panel of Figure 2.3 only shows BBH systems that merge within a Hubble time. The tail of massive systems from the stable accretion and combined model variations is absent in the merging populations, since nearly all of these systems are too wide to merge (as discussed in Section 2.4.1). We see that the subset of merging BBHs from the first model variation (super-Eddington accretion during stable mass transfer) is not significantly different from the fiducial population of merging BBHs. For both the

fiducial and the first model variation $f_{\text{BBH},90} = 0\%$ and $M_{\text{BBH},\text{max}} \approx 84 M_\odot$.

The second model variation (super-Eddington accretion during CE) affects the subset of BBHs that merges more strongly than the first model variation. We see that the peak of the merging distribution is shifted to higher masses with respect to the fiducial population, which is reflected in the higher value of $f_{\text{BBH},60} \approx 7.1\%$. In other words, mass distribution of merging BBHs is shifted to higher masses in the CE accretion model with respect to the fiducial distribution. This effect is also visible in the combined model variation, which closely follows the merging BBH distribution of the CE accretion model. Although the peak of the merging distribution is shifted to higher masses for our second and third model variations, they do not produce a significant amount of PISN mass gap events in terms of M_{BBH} . Only about 0.36% and 0.45% of the merging populations has a $M_{\text{BBH}} > 90 M_\odot$ for model variation 2 and 3.

Merging BBHs reweighted

In the bottom panel of Figure 2.3 we apply a simple re-weighting to the merging distribution to account for the detection probability which scales approximately as $(M_{\text{BH},1})^{2.2}$, following [Fishbach & Holz \(2017\)](#). In this panel, we show the 90% confidence intervals of the observed M_{BBH} values from [Abbott et al. \(2019a\)](#) at arbitrary heights with horizontal grey lines. This shows that the total mass distribution as produced by our fiducial model is able to form BBHs with total masses similar to the detections from LIGO and Virgo’s first and second observing runs.

Re-weighting the distribution results in the largest deviations from the fiducial simulation. In general the re-weighting has a flattening effect on the distribution of BBH masses, since the massive end ($M_{\text{BBH}} > 60 M_\odot$) of the distribution is boosted, while the

intrinsic BBH distributions peak at low masses (approximately between 20 and $30 M_{\odot}$). The small fraction of BBHs with masses in the PISN mass gap from the second and third model variation becomes visible due to the re-weighting. However, we see that BBH mergers with masses in the range $90 M_{\odot} \leq M_{\text{BBH}} < 100 M_{\odot}$ only constitute a few percent of the re-weighted distribution. Moreover, none of the model variations produces a merging BBH system with a mass of $M_{\text{BBH}} \geq 100 M_{\odot}$.

We conclude that, despite our extreme assumptions regarding accretion onto BHs, none of our model variations is able to significantly populate the PISN mass gap with systems that merge in a Hubble time. Under our most extreme assumptions, we find that in only about 0.45% of all cases, the BBH mass M_{BBH} exceeds $90 M_{\odot}$.

2.4.3 Mass ratios

Figure 2.4 displays the cumulative distribution function of the mass ratio, q , defined as the ratio of the less massive over the more massive BH. Figure 2.4 shows that the CE accretion model leads to similar mass ratios as the fiducial model, but results in a slightly larger fraction of mass ratios with $q \leq 0.35$ when considering the merging population (dash-dotted gray, and dotted green lines in Figure 2.4).

The stable accretion model and combined model (dashed pink, and solid orange line in Figure 2.4) lead to a higher fraction of low mass ratio systems than the fiducial model. For the combined model, we find that about 40% (50%) of all (merging) BBHs have a mass ratio of $q \leq 0.5$. For the fiducial model, we find that about 20% (40%) of all (merging) BBHs have a mass ratio of $q \leq 0.5$. Moreover, the stable accretion model and combined model allow for more extreme mass ratios with respect to the fiducial population, down to $q \approx 0.1$. These low mass ratios are caused by accretion onto

the first-born BH in the models where we allow for super-Eddington accretion. This accretion increases the mass of the first-born BH, and thus leads to BBHs with lower mass ratios.

The 90% confidence interval of observed mass ratios from LIGO/Virgo’s first and second observing run are shown at the bottom right of Figure 2.4 ([Abbott et al., 2016](#)). For most detections, the mass ratios are relatively poorly constrained. Of special interest is the recently announced GW190412, which is the only system published so far with significantly unequal masses, ($q = 0.28^{+0.13}_{-0.07}$, [Abbott et al., 2020](#), blue line in Figure 2.4). The formation of systems with such mass ratios is more common in our models that allow for super Eddington accretion. We find that about 30% of the merging fiducial population has a mass ratio of $q \leq 0.41$, which is the upper limit of the 90% confidence interval for the mass ratio of GW190412. This fraction increases to 40% of the merging BBH population for the combined model variation.

If we consider systems for which the individual masses coincide with the component masses inferred for GW190412 ($M_{\text{BH},1} = 29.7^{+5.0}_{-5.3} M_{\odot}$, $M_{\text{BH},2} = 8.4^{+1.7}_{-1.0} M_{\odot}$, [Abbott et al., 2020](#)), we find that 0.5% of the merging fiducial population coincides with GW190412. This fraction increases to 3.6% for the merging population of the Combined model. We further note that GW190412 shows evidence for spin, which may be expected for the accreting BH. However, see Section 2.5.2 for a more in depth discussion of the spins.

2.4.4 BBH merger rates

We briefly discuss simple estimates for the merger rates that can be obtained directly from our simulations. For this we closely follow the procedure outlined by [Dominik](#)

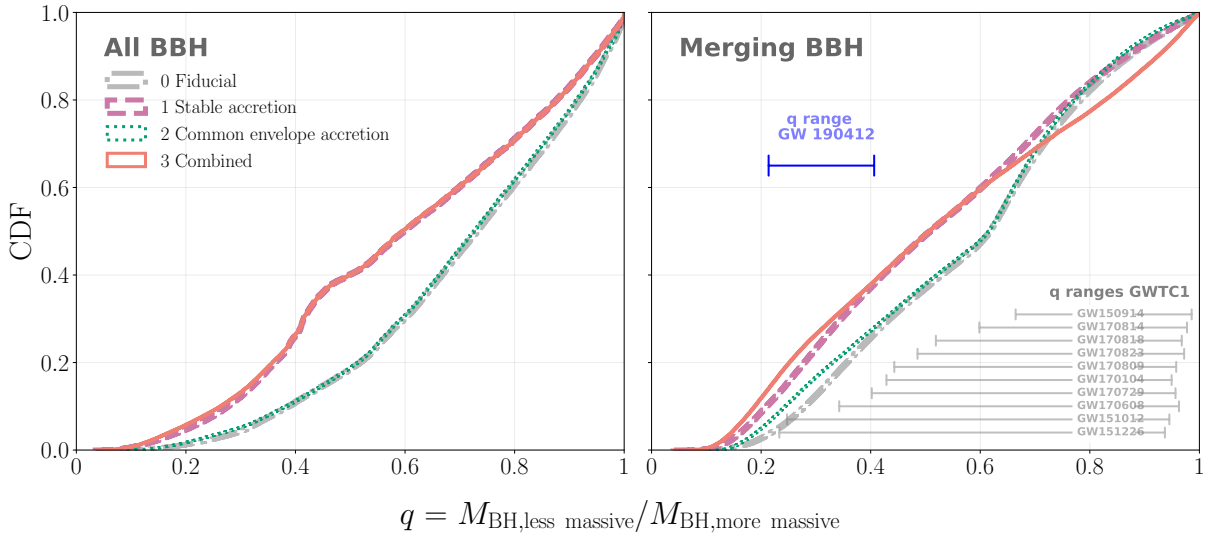


Figure 2.4: Cumulative distribution function of the mass ratio q , defined as the ratio of the less massive over the more massive BH. The left panel shows all BBHs, while the right panels displays only the BBH population that merges within a Hubble time. The 90% confidence interval of observed mass ratios are shown as gray lines for observations from LIGO/Virgo’s first and second observing run (Abbott et al., 2019a), and as a blue line for GW190412. The CE accretion model has little effect on the mass ratio distribution of BBHs. The stable accretion model variation and combined model variation shift the mass ratios to lower values.

et al. (2012), detailed in Appendix 2.10. Table 2.3 provides an overview of the quantities discussed here.

In this work, we consider simulations at a fixed metallicity of $Z=0.001$, representative for the low metallicity environments in which heavy BBHs are believed to form (e.g. Abbott et al., 2016b). By choosing a fixed low metallicity, we overestimate the BBH formation rate and BBH merger rate. We furthermore assume the optimistic CE model as discussed in Belczynski et al. (2020). The optimistic CE model tends to lead to an overprediction of the BBH merger rate (e.g. Dominik et al., 2012). Stevenson et al. (2017) find merger rates which are approximately 3 times lower for the pessimistic model with respect to the optimistic model at $Z = 0.001$. Assuming the optimistic model, their

Table 2.3.: Estimate of the BBH merger rates for our chosen fixed metallicity. We provide the total number of BBHs formed per unit star-forming mass that merge within a Hubble time, dN_{t_H}/dM_{SFR} , and within 10 Gyr, N_{10}/M_{SFR} , respectively. The BBH merger rate for a synthetic Milky Way-like galaxy (\mathcal{R}_{MWG}), the volumetric BBH merger rate \mathcal{R}_{vol} , and the volumetric merger rate for BBHs with a component $M_{\text{BH}} > 45 M_{\odot}$. The $1-\sigma$ estimate of the statistical sampling uncertainty is shown whenever it exceeds 0.5% of the relevant value.

Model	N_{t_H}/M_{SFR} ($M_{\odot} \cdot 10^{-5}$)	N_{10}/M_{SFR} ($M_{\odot} \cdot 10^{-5}$)	\mathcal{R}_{MWG} (Myr $^{-1}$)	\mathcal{R}_{vol} (Gpc $^{-3}$ yr $^{-1}$)	$\mathcal{R}_{\text{vol},45}$ (Gpc $^{-3}$ yr $^{-1}$)
0. Fiducial	2.3	2.2	77 ± 0.3	897 ± 4	0.0
1. Stable super-Eddington	2.4	2.3	81 ± 0.3	937 ± 4	1.2
2. Common envelope accretion	2.2	2.0	72 ± 0.3	832 ± 3	11
3. Combined	2.1	2.0	71 ± 0.3	825 ± 3	19

BBH merger rates at $Z = 0.001$ are comparable to the rate estimate we find for our Fiducial model.

Our estimates of the BBH merger rates should be considered as rough upper limits that enable comparison to other work. For a more careful treatment we refer to [Neijssel et al. \(2019\)](#) and [Stevenson et al. \(2019\)](#), who consider different metallicities and account for the abundance evolution through cosmic time. They also both use the [COMPAS](#) suite, while assuming initial conditions that are very similar to those adopted in our fiducial model. They indeed find merger rates that are consistent with the rates from [Abbott et al. \(2019a\)](#).

We first estimate the number of BBHs formed per unit star forming mass that merge within a Hubble time, dN_{t_H}/dM_{SFR} and the number of BBHs formed per unit star forming mass that merge within 10 Gyr dN_{10}/dM_{SFR} . We find that both quantities

vary only slightly across our model variations, as can be seen in Table 2.3. The physical assumptions we varied primarily affect the amount of mass that BHs accrete and therefore their masses, but these assumptions do not significantly affect the rate of BBH mergers.

We also estimate the total merger rates for a synthetic Milky Way-like galaxy, \mathcal{R}_{MWG} and the consequential total volumetric merger rates \mathcal{R}_{vol} . As stated above, these rates are higher than the current estimates from Abbott et al. (2019a) due to the fixed low metallicity, however they are consistent with estimates from Stevenson et al. (2017) and de Mink & Belczynski (2015a). \mathcal{R}_{MWG} (and consequently \mathcal{R}_{vol}) are comparable for the fiducial and first model variation. However, they are slightly lower for the second and third model variation, which implies that allowing for accretion during a CE leads to slightly fewer BBH mergers. This can be understood as our CE accretion model leading to more ‘failed’ common envelopes that end in a stellar merger instead of a BBH.

Applying the fractional rates, f_{45} , to the volumetric merger rate for BBHs (\mathcal{R}_{vol}), results in our estimates of the PISN mass gap event rate, $\mathcal{R}_{\text{vol},45}$. For our first model variation, the estimates of the PISN mass-gap-event rates $\mathcal{R}_{\text{vol},45}$, are consistent with the rates inferred by Fishbach et al. (2020) for gravitational wave events in the first and second observing run. They find $\mathcal{R}_{\text{vol},45} = 3.02^{+12.97}_{-2.28} \text{ Gpc}^{-3} \text{ yr}^{-1}$ under the assumption of a flat-in-log prior for the mean merger rate per bin. Assuming a power-law prior, Fishbach et al. (2020) constrain the PISN mass gap merger rates to $\mathcal{R}_{\text{vol},45} = 1.79^{+2.30}_{-1.23} \text{ Gpc}^{-3} \text{ yr}^{-1}$. The second and third model variation lead to estimates of the PISN mass-gap-event rates that are higher than the current estimates from Fishbach et al. (2020).

The uncertainties quoted in Table 2.3 result from the sampling procedure. We note

that the model uncertainties are much larger, by orders of magnitude (e.g. Dominik et al., 2012; de Mink & Belczynski, 2015a; Chruslinska et al., 2018a) and that the rates are affected by the choice of a constant metallicity $Z = 0.001$.

2.5 Distinguishing between different pathways to PISN mass gap events

In this paper we consider the possibility to form PISN mass gap events through the isolated binary evolutionary channel. Various other pathways have been proposed to produce PISN mass gap events, see Section 2.2.2 for a brief overview. In this Section, we compare our results to the findings for other pathways that have been proposed in the literature to create PISN mass gap events.

This comparison is not straightforward. Different studies have adopted different input assumptions, for example concerning the location of the PISN mass gap. Moreover, the few quantitative predictions that exist to date often rely on relatively crude assumptions for complex physical processes. It is to be expected that these predictions will change with time as the models become more sophisticated. The comparison we present here reflects what is available in the literature to date.

We first briefly compare different pathways and their predictions for the shape of the BBH mass distribution (Section 2.5.1 and Figure 2.5), followed by predictions for the maximum masses (Sect. 2.5.2), mass ratios (Section 2.5.2) and BH spins (Section 2.5.2). A schematic overview is provided in Figure 2.6.

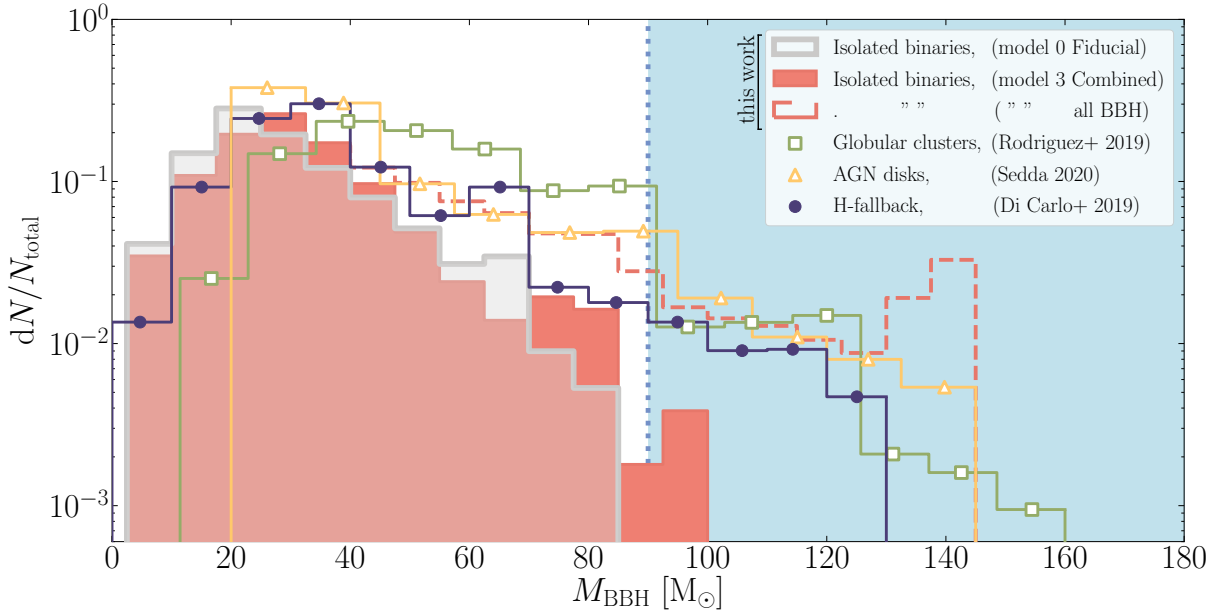


Figure 2.5: M_{BBH} distribution for BBH systems from different pathways into the PISN mass gap. We compare the distribution of total BBH masses, M_{BBH} , of multiple generations of BH-mergers in globular clusters (green open squares, Rodriguez et al., 2019a), multiple generations of BH-mergers in AGN disks (yellow open triangles, Sedda, 2020) and stellar mergers in young stellar clusters assuming full H-fallback during BH formation (closed dark blue circles, Di Carlo et al., 2019) to the effect of super-Eddington accretion in isolated binaries as discussed in this work. The grey line displays the merging population of BBH systems from our Fiducial model (model 0). The dashed and filled orange distributions respectively show the total and merging population of BBH systems from our most optimistic model variation (model 3 combined). The light blue region bordered by dotted lines indicates the approximate location of the PISN gap assuming BHs of equal mass. All distributions are normalized to their respective population of merging BBHs. This is therefore *not* a prediction for the number of PISN mass gap events.

2.5.1 The shape of the BBH mass distribution

In Figure 2.5, we compare various predictions for the distribution of total BBH masses, M_{BBH} , for systems that merge within a Hubble time. This figure is similar to the middle panel of Figure 2.3 except for the use of a logarithmic y-axis, to highlight the differences in the tail of the distribution. We consider BBHs with total masses above

$90 M_{\odot}$ to be PISN mass gap events. All distributions are normalized to their respective population of BBHs. This figure thus allows us to compare the shape of the distributions but, at present, cannot be used to infer which pathway contributes most significantly to PISN mass gap since the relative contribution from each pathway is unknown.

[Arca Sedda et al. \(2020a\)](#) argue that with enough detections, the fraction of mergers with masses falling in the low or high mass end of the BBH mass distribution can be used to place constraints on the relative contribution of different pathways to the overall population.

Isolated binaries

Our most optimistic simulation for super-Eddington accretion in isolated binaries, which allows for accretion onto BHs during both stable mass transfer, and CE events is shown in filled red in Figure 2.3. We find that isolated binaries will contribute less than 0.45% of mergers with $M_{\text{BBH}} \geq 90 M_{\odot}$. As discussed in Section 2.4, although the maximum value of M_{BBH} , i.e. $M_{\text{BBH},\text{max}}$, increases with respect to our fiducial simulation (model 0, shown in grey for reference), isolated binary evolutionary does not significantly populate the PISN mass gap.

Our results show that super-Eddington accretion in interacting binaries can produce BBHs with total masses larger than $90 M_{\odot}$, but due to their typically large orbital periods (of approximately 100 days), we do not expect these systems to merge as a result of isolated binary interaction alone. It is conceivable that a fraction of these binaries experience a decay of their orbits due to external factors. For example, a significant number of massive binary systems are born as part of a triple system or even higher order multiple (e.g. [Sana et al., 2014](#)). Secular interactions with a third companion such

as Lidov-Kozai cycles have been proposed to increase the merger rate (Toonen et al., 2016; Kimpson et al., 2016; Antonini et al., 2017a).

Furthermore, a fraction of massive binaries is born in dense stellar environments, such as a globular or nuclear star cluster. These binaries and their BH remnants can be affected by a sequence of dynamical encounters and exchanges (Rodriguez et al., 2016). The heavy BHs in our models are good candidates for dynamical interactions since they will be among the most massive BHs formed in the cluster. As these sink to the center of the cluster they will be prone to interact and take part in dynamically-assisted mergers.

Simulating the combined effects of super-Eddington accretion and external effects is beyond the scope of this paper. However, we can explore the upper limits of the contribution from super-Eddington accretion by considering the distribution of total masses for our full BBH population including those that are too wide to merge due to gravitational waves alone (model 3 “al”, dashed red line in Figure 2.5). About 12% of the BBHs in this distribution have a total mass M_{BBH} , that exceeds $2 \times 45 = 90 M_{\odot}$. This should be considered as an extreme upper limit that we do not believe to be realistic. The distribution of all BBH systems in our combined model extends up to $145 M_{\odot}$, showing a rise around 130 – $145 M_{\odot}$. This pile up results from BBH systems where the first born BH gained mass through stable accretion from its companion. This distinguishes this distribution from other pathways, which all decline at high masses.

Globular clusters

We show results for globular clusters from Rodriguez et al. 2019a (green open squares). In their simulations, close BBHs form and tighten as a result of dynamical interactions in the dense core of a globular star cluster. Massive BHs that form as the

result of an earlier BBH merger may stay bound to the cluster if the merger recoil is sufficiently small. These so-called second generation BHs can have masses in the PISN gap. They can give rise to PISN mass gap events if they pair and merge with a third BH. We show the results from the most optimistic model for all redshifts by Rodriguez et al. 2019a (as shown in the top left panel of their figure 3). This model assumes zero birth spin for all black holes. Low birth spin minimizes the BBH merger recoil during the first merger event, enabling the resulting BH to take part in a second merger.

Their distribution displays a significant drop around $90 M_{\odot}$, which corresponds to two times the maximum value for first generation mergers. For total masses between 90 and $125 M_{\odot}$ the distribution is dominated by 1st + 2nd generation mergers. A second drop exist, near $125 M_{\odot}$, which is close to three times $M_{\text{BH,max}}$. Events with masses in excess of $125 M_{\odot}$ are primarily the result of 2nd + 2nd generation BHs, which very rare. Their distribution extends to $M_{\text{BBH}} \approx 150 M_{\odot}$.

Rodriguez et al. (2019a) find that about 4% of the detected BBHs will have $M_{\text{BBH}} \geq 100 M_{\odot}$ for their most optimistic model assuming zero birth spin for all BHs. This pathway is the most efficient at producing very massive events among all those we consider, at least in relative terms. The fraction of events where the total mass exceeds $90 M_{\odot}$ is about 5% in their simulations. However, when a less optimistic model is assumed, i.e. when the birth spin for BHs is assumed to be non-zero, the rate of PISN mass gap events drops significantly. For example, when assuming a birth spin of $\chi_{\text{birth}} = 0.5$ for all BHs, they find that less than 0.1% of all BBH mergers will have a total mass $M_{\text{BBH}} \geq 100 M_{\odot}$ (as shown in the bottom left panel of figure 3 from Rodriguez et al., 2019a).

AGN disks

AGN disks have been proposed as promising sites that allow for a sequence of multiple mergers and thus the creation of PISN gap mergers in a similar way as globular clusters. The difference between these two pathways arises from the larger escape speeds in AGN disks due to a deeper potential well. This opens the possibility for higher generations of BHs in AGN disks, while the contribution from 2nd + 2nd and > 3rd generation BHs is expected to be negligible in globular clusters ([Gerosa & Berti, 2019](#)). We compare our mass distribution to predictions from [Sedda \(2020\)](#), extracted from the top panel of their figure 19, shown as yellow open triangles in Fig. 2.5. Their distribution extends to about $140 M_{\odot}$. The fraction of events where the total mass exceeds $M_{\text{BBH}} > 2 \times 45 = 90 M_{\odot}$ is about 4% in their simulations, which is comparable to the predictions by [Rodriguez et al. \(2019a\)](#) for globular clusters when BHs are born with zero spin.

Fallback of a hydrogen-rich envelope

Finally, we compare to a pathway studied by [Di Carlo et al. \(2019\)](#). They consider stellar mergers occurring in young star clusters, involving at least one evolved star. Such mergers are poorly understood, but they may produce stars with overmassive hydrogen envelopes and relatively small cores ([Vigna-Gómez et al., 2019](#)). If the core mass of such a merger product is below the limit for pair pulsations, it is expected to collapse directly to a BH. If it is assumed that the massive hydrogen envelope is entirely accreted onto the forming BH, this can result in a BH with a mass in the PISN mass gap. Dynamical interactions within the cluster could later pair such a BH with another BH, possibly facilitating a BBH merger. We compare to the simulations from [Di Carlo et al. \(2019\)](#), their Figure 5), shown as closed dark blue circles in Figure 2.5. They find BBH mergers

with total masses up about $130 M_{\odot}$. This is higher than what we expect from isolated binaries, but lower than what is claimed for globular clusters and AGN disks. The fraction of events where the total mass exceeds $M_{\text{BBH}} > 2 \times 45 = 90 M_{\odot}$ is about 3% in their simulations, which is also slightly below the predictions for globular clusters and AGN disks.

2.5.2 Predictions for masses, mass ratios and spins

The overview of predicted BBH mass distributions as displayed in Figure 2.5 show that the BBH population cannot be explained by the isolated binary evolution channel alone if more than 1% of all BBH mergers has a mass higher than $90 M_{\odot}$. We will now discuss other observables that might help distinguish between the different pathways considered in this work.

Maximum masses

In all our model variations, the amount of mass that a BH can accrete is ultimately capped by the envelope mass of the donor star. The most massive BBH system that merges within a Hubble time has a mass $99 M_{\odot}$, though this is for extreme assumptions. We do find more massive systems, up to about $144 M_{\odot}$, but for those we would need to invoke an external mechanism to merge the system.

Figure 2.6 (following page): Predicted characteristics of PISN mass gap events from different pathways. We compare the maximum BBH mass, $M_{\text{BBH},\text{max}}$, the mass ratio q of the system defined as the ratio less massive over the more massive BH mass, the dimensionless spin parameters of the BHs χ_1 and χ_2 , the effective spin parameter, χ_{eff} , the expected spin orientation and the fraction of BH systems with $M_{\text{BBH}} > 90 M_{\odot}$.

a. Isolated binaries		b. Multiple BH mergers in clusters	c. Multiple BH mergers in AGN disks	d. Overmassive envelope + fallback	e. Primordial
All BBH	Merging BBH	Globular clusters	AGN disk	Fall back	Primordial
Reference	This work, model 3, Combined	Rodriguez et al. 2019	Yang et al. 2019, Sedda 2020	Di Carlo et al. 2019a, Di Carlo et al. 2019b	Mirbabayi et al. 2019 Postnov et al. 2019
$M_{BBH,\max} [M_\odot]$	146	99	≈ 160	No maximum?	No maximum
q of PISN gap system lower mass/higher mass	≈ 0.4	$0.2\text{--}0.7$	≈ 0.5	$0.2\text{--}0.97$, possibility to ~ 0.1	$\approx 0.4\text{--}0.5$
χ_1	Possibly spun up?	Possibly spun up?	≈ 0.69	≈ 0.69	Spinning progenitor? ≈ 0
χ_2	natal	natal	≈ 0	natal	≈ 0
$\chi_{\text{eff}} = \frac{M_{\text{BH}}\chi_1 + M_{\text{BH}}\chi_2}{M_{\text{BH}}} \hat{\mathbf{l}}_{\mathbf{N}}$	$\approx 0.45, \approx 0.75$	≈ 0.47	≈ 0.46	≈ 0.4	
Spin orientation	aligned	aligned	isotropic	isotropic	isotropic
$f_{\text{BH},90}$ [$M_{\text{BH}} > 90 M_\odot$]	$12.2 \pm 0.2\%$	$0.45 \pm 0.03\%$	4.6%	4.4%	3.2%

This maximum mass distinguishes this channel from predictions by other proposed pathways. Simulations of multiple BH mergers in massive globular clusters and AGN disks are found to result in maximum BBH masses of about $160 M_{\odot}$ (Rodriguez et al., 2019a) and about $145 M_{\odot}$ (Sedda, 2020) respectively. However, as long as the merger product remains bound to the merger environment, there is no reason to believe that these pathways have to adhere to any maximum value of M_{BBH} .

[Di Carlo et al. \(2019\)](#) find a maximum of $130 M_{\odot}$ for a metallicity of $Z = 0.02$. The maximum mass resulting from PISN mass gap events as discussed in [Di Carlo et al. \(2019\)](#) and [Di Carlo et al. \(2020a\)](#) are in essence the sum of the maximum BH mass and the envelope mass of the progenitor at the moment of BH formation (i.e. $M_{\text{BH,max}} + M_{\text{env}}$). When complete fallback of the overmassive envelope is assumed, the maximum BBH system mass is thus capped by the maximum possible envelope mass prior to BH formation.

Mass ratios

PISN mass gap events resulting from the classical binary evolutionary channel may also be distinguished by their mass ratios. Here we define q to be the mass ratio of the less massive over the more massive BH. As discussed in Section 2.4.3, accretion onto the first born BH increases its mass, leading to events with more extreme mass ratios. Figure 2.4 displays the mass ratios for all BBH systems. When we focus on the mass ratios of PISN mass gap systems, we find that our Combined model predicts BBH systems that peak strongly at $q \approx 0.4$.

The merging population of PISN mass gap systems from our Combined model

predicts a wider range of mass ratios: $0.2 < q < 0.7$. These mass ratios are comparable but slightly lower than those for PISN gap events from stellar and globular clusters, which are expected to peak around $q \sim 0.4 - 0.6$ and $q \sim 0.5$, respectively (Rodriguez et al., 2019a; Di Carlo et al., 2019).

Mass ratios from BBH mergers in AGN disks are still highly uncertain, but McKernan et al. (2020a) predict that the median mass ratios of BBH mergers in AGN disks will range from 0.20 to 0.97. However, when a higher generation BH is involved (i.e. a BH formed through multiple consecutive BBH mergers), mass ratios can be expected to drop to very small values of q . This could possibly push q down to values lower than $q \sim 0.1$ when around 10 consecutive mergers or more are allowed.

Spins

Bardeen (1970) argues that spin-up is expected as a result of accretion in the case of a thin disk (see also King & Kolb, 1999; O'Shaughnessy et al., 2008). However, the (significantly) super-Eddington accretion rates considered in this work are expected to result in thick accretion disks or even near-radial inflow (Volonteri & Rees, 2005; Begelman et al., 2006; Pezzulli et al., 2016; Johnson & Haardt, 2016). It is not clear whether this accretion geometry will lead to significant spin up. For example, Tchekhovskoy et al. (2012) show that accumulation of magnetic flux around the central regions of the accreting BHs might cause the BH to spin down instead of spinning up. Therefore we cannot, at present, confidently predict the final spins of BHs.

Nevertheless, we attempt to provide an upper limit using the expression in Eq. 4 of Bardeen (1970) for thin accretion disks. Using this and the assumption of zero natal spins, we find that the vast majority ($> 75\%$) of the accreting BHs are spun up to the

maximum possible spin value in our first model variation for stable mass transfer. This results in effective spins of $0.65 < \chi_{\text{eff}} < 0.8$. In our second model variation for CE accretion, we find effective spins of $0.2 < \chi_{\text{eff}} < 0.6$. Our combined model spans the whole range of effective spins and results in $0.2 < \chi_{\text{eff}} < 0.85$, with two distinct peaks, one around $\chi_{\text{eff}} \approx 0.45$ and one around $\chi_{\text{eff}} \approx 0.75$. The merging population of the combined model is dominated by the effective spins of the CE accretion model and spans the range $\chi_{\text{eff}} \approx 0.2\text{--}0.6$, with a peak around $\chi_{\text{eff}} \approx 0.47$.

We expect PISN mass gap events created through super-Eddington accretion in isolated binaries to result in relative alignment of the BH-spin with the orbit. The spin of the first-born BH will likely align with the orbit during the mass transfer phase. However, a natal kick of the second born BH could possibly tilt the orbit. Given the uncertainties in the spin itself we have chosen not to model this, but we expect no, or very low velocity, natal kicks for the most massive BHs.

For globular clusters, the optimal conditions for PISN mass gap events as discussed in Rodriguez et al. (2019a) require two non-spinning BH for the first generation of BHs, which are expected to produce BHs with spins strongly peaked at $\chi \approx 0.69$. This implies that one of the BHs involved in the PISN mass gap event is expected to have a spin of $\chi_1 \approx 0.69$, while its companion is expected to have its natal spin of $\chi_2 \approx 0$.

Yang et al. (2019b) predict that the effective spin distribution of BBHs is dominated by 1st + 2nd generation BHs. This suggests that the spin of the incoming second generation BH will be strongly peaked around $\chi_1 \approx 0.69$, as explained above. Assuming all first generation BHs have the same mass, they find that due to the random alignment of spins, this results in an effective spin distribution that is peaked strongly around $\chi_{\text{eff}} \approx 0.4$.

Furthermore, it is highly uncertain what BH spin is expected for BBHs in stellar clusters when the BH-progenitor is the end product of a stellar merger (as suggested in Di Carlo et al., 2019). One might intuitively argue that such a stellar merger would lead to a spinning BH progenitor, however Schneider et al. (2019) show that stellar mergers can result in a slowly spinning merger product. In any case, the connection between BH spin and its progenitor is highly uncertain, even more so when an overmassive envelope is speculated to fall back during BH formation (see e.g. Heger et al., 2005; Lovegrove & Woosley, 2013; Belczynski et al., 2020).

The BBH systems leading to PISN mass gap events formed in globular clusters, AGN disks, and stellar clusters are all dynamically assembled. For such dynamically-assembled BBHs, the angle between the orbital angular momentum and the BH spins is expected to be distributed isotropically (Rodriguez et al., 2016). This results in misaligned spin orientation in the majority of cases and suggests that the distribution of χ_{eff} is also symmetric and centered on zero (Rodriguez et al., 2019a).

Lastly, the spin of primordial BHs is conventionally believed to be small (Mirbabayi et al., 2020; Luca et al., 2019). BBHs consisting of primordial BHs are expected to be dynamically assembled and thus have isotropically distributed spins (Rodriguez et al., 2016).

In conclusion, it is extremely difficult to distinguish between the different pathways to PISN mass gap events. At the time of writing, predictions from different pathways for the maximum masses, mass ratios, and BH spins are not sufficiently constrained to decisively differentiate between pathways.

In light of the above discussions, we find that the combination of extreme mass

ratios and an aligned spin orientation in a BBH system with $M_{\text{BBH}} \leq 100 M_{\odot}$ could be indicative of BHs that underwent super-Eddington accretion from a companion star (Figure 2.6). We expect that our ability to distinguish between the different pathways will be improved with upcoming gravitational-wave surveys which will enhance constraints on both the rates and properties of (PISN mass gap) mergers.

2.6 Discussion

This work examines whether the classical isolated binary evolutionary channel can produce BBH mergers with a component in the pair instability mass gap (a PISN mass gap event). Under our most extreme assumptions (i.e., those that favor the mass growth of black holes most strongly) we find about 2% of all BBH mergers at $Z = 0.001$ to be PISN mass gap events and we find a maximum mass for a BH involved in a PISN mass gap event of $M_{\text{BH,max}} = 90 M_{\odot}$. Moreover, under these assumptions, we find only about 0.45% of the merging BBH systems have a total mass $M_{\text{BBH}} \geq 90 M_{\odot}$, and we find no merging BBH systems with masses of $M_{\text{BBH}} \geq 100 M_{\odot}$.

We discuss how robust these main findings are against variations in the assumptions about mass transfer in Sections 2.6.1 and 2.6.1, and consider further caveats in Section 2.6.3. We conclude by speculating on the effects of super-Eddington accretion in binaries to the lower mass gap in Section 2.6.2.

2.6.1 Variations in mass transfer

Most of the heavy BBHs in our simulations are too wide to merge within a Hubble time (see Section 2.4). The BBHs that do merge as PISN mass gap events are only marginally in the PISN mass gap since they have accreted less mass than their

non-merging counterparts. We first discuss additional mechanisms that could shrink the BBH orbits and whether this could increase the rate of PISN mass gap events in Section 2.6.1. This is followed by a discussion on whether there are any possibilities left to accrete more mass onto the BHs in Section 2.6.1.

Shrinking the binary orbit

In our first model variation, we have assumed that BHs can accept all the mass that is available from their donor star. We thus assume that the total mass and angular momentum is conserved. If instead a fraction of the mass is lost, this lost mass will carry away angular momentum, which leads to a different orbital evolution.

Observations of X-ray binary systems show evidence for outflows resulting from the accretion disk around a black hole (e.g. [Blundell & Bowler, 2005](#); [Remillard & McClintock, 2006](#)). The effect of such an outflow on the binary orbit can be modeled assuming that a fraction of the transferred mass (β) is accreted and the remainder is lost from the system carrying away the specific angular momentum of the accretor ([Soberman et al., 1997](#)). It can be shown that under these assumptions the orbit widens irrespective of the chosen mass transfer efficiency (value of β), as long as the mass of the accreting black hole becomes large relative to the donor mass (M_d). For low β this implies the orbit widens as soon as $M_{\text{BH}} \gtrsim 0.76$ times the mass of the donor (see Appendix 2.9 for the derivation). This condition is typically met for the progenitors of systems that can form PISN mass gap systems. This is a robust result that is also valid for other binaries that do not evolve into BHs ([Renzo et al., 2019](#)).

We thus conclude that lowering the mass transfer efficiency under these assumptions does not increase the number of PISN mass gap mergers.

We can furthermore consider what happens when mass is lost with a higher specific angular momentum. For example, mass lost from the outer Lagrangian point may be ejected to form a circumbinary disk. This mode of mass loss leads to rapid shrinking of the orbit for almost all variations of mass transfer efficiency (see Appendix 2.9 for details). Test simulations show that most BHs plunge into the companion’s envelope, unless the mass transfer efficiency is highly fine-tuned. It is unclear what is the fate of such systems.

In conclusion, we do not expect that variations in the mass transfer efficiency can significantly increase the number of PISN gap mergers.

Can we accrete even more?

The most massive black hole involved in a BBH merger in our simulations has a mass of $M_{\text{BH,max}} \approx 90 M_{\odot}$. Can $M_{\text{BH,max}}$ be taken as a robust upper limit or are there uncertainties that allow us to increase $M_{\text{BH,max}}$ further?

During stable mass transfer we already assume a mass transfer efficiency of 100%. However, in our CE accretion model, the BHs typically accrete less than 20% of the companions mass (see also Figure 2.2). While the assumptions in our second model variation are already extreme, it is worthwhile to consider what happens if BHs are allowed to accrete even more during the CE inspiral phase.

To investigate this, we ran a grid of 17 additional simulations with the same setup as for our second model variation (as described in Section 2.3), but now assuming that a fixed fraction f_{acc} of the envelope is accreted onto the BH. We vary f_{acc} between 0.0 and 0.99. We still estimate the final separations by considering the binding energy of the envelope, after subtracting the mass accreted by the BH. These additional simulations

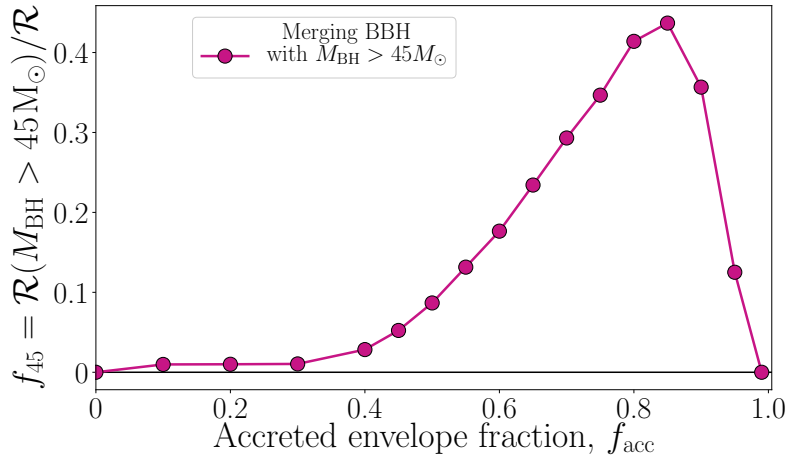


Figure 2.7: The fraction of BBH mergers with a component mass $M_{\text{BH}} > 45 M_{\odot}$ (i.e. f_{45}), as a function of the fraction of the companion’s envelope that is accreted during each CE mass transfer episode. Each point represents one simulation from the additional exploratory grid of 17 simulations discussed in Section 2.6.1.

are run at a lower resolution of 10^5 systems per simulation.

Figure 2.7 shows the fractional rate of PISN gap mergers, $f_{\text{gal},45}$ as a function of f_{acc} . We see that the rate of PISN gap mergers increases with f_{acc} and peaks when BHs are assumed to accrete about 85% of their companions envelope. This simulation predicts as many as 42% of BBH mergers from PISN mass gap systems. For even higher values of f_{acc} , we see that there is not enough of the envelope left to sufficiently shrink the orbit. We note that such high rates for PISN gap mergers are already contradicted by first and second LIGO and Virgo observing run (Abbott et al., 2019b).

These simulations further show that we can only obtain a significant fraction of PISN gap mergers ($> 2\%$) when BHs accrete at least 35% of their companion’s envelope mass during the envelope inspiral. This would suggest accretion rates that significantly surpass the Hoyle-Lyttleton accretion rate (MacLeod & Ramirez-Ruiz, 2015) during every CE event. We consider it unlikely that such high rates are physical.

We thus consider it very unlikely that $M_{\text{BH,max}}$ can be significantly increased beyond the values as quoted in Tables 2.1 and 2.2 for systems originating from isolated binary evolution.

2.6.2 Effects of super-Eddington accretion on the lower mass gap

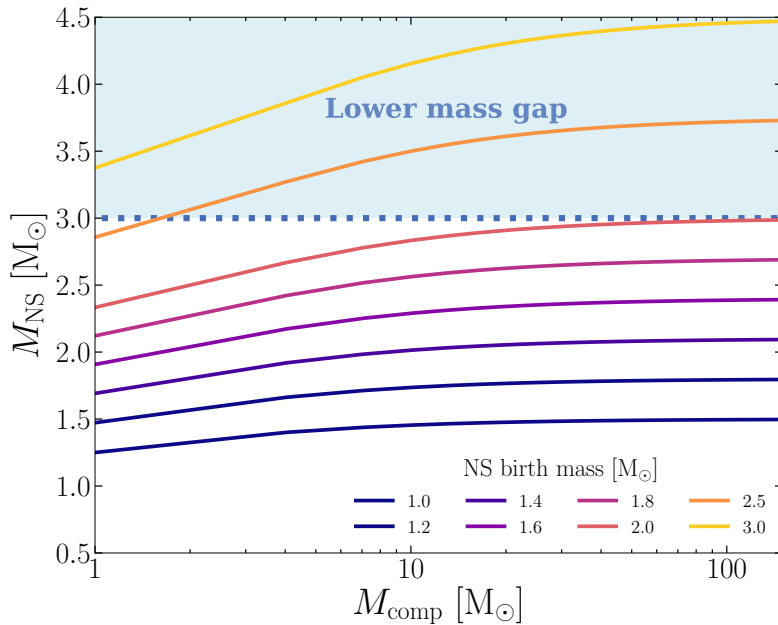


Figure 2.8: The maximum mass for an accreting NS according to Equation 2.2 as a function of the companion mass at the moment of Roche-lobe overflow. This illustrates that only neutron stars that are born close to the lower mass gap will be able to accrete enough to end with a final mass in the lower mass gap.

If all BHs that enter a CE-phase are allowed to accrete at a super-Eddington rate, we could hypothesize that the same accretion model would apply to neutron stars, as was originally suggested by [Houck & Chevalier \(1991\)](#) [Fryer et al. \(1996\)](#) and [Popham et al. \(1999\)](#). Allowing for accretion onto neutron stars during every CE event following Eq. 2.2 could create an overabundance of BHs and possibly leads to BH neutron star and binary neutron star rates that are inconsistent with the current estimates from [Abbott](#)

et al. (2019b).

We consider the consequences of super-Eddington accretion onto NS stars and whether this can populate the lower mass gap between neutron stars and BHs (between 3 and $5 M_{\odot}$) by evaluating the effect of applying Equation 2.2 to mass ranges that are relevant for neutron stars.

In Figure 2.8 we show the maximum mass for accreting NS according to Equation 2.2 as a function of the companion mass at the moment of Roche-lobe overflow. This illustrates that only neutron stars that are born close to the lower mass gap will be able to accrete enough to end with a final mass in the gap. We thus expect that extending our model variation 2 to mass ranges relevant for neutron stars, would not significantly pollute the lower mass gap, which is in accordance with the findings in MacLeod & Ramirez-Ruiz (2015).

2.6.3 Caveats

We emphasize that the simulations presented in this paper are extreme by design. We do not consider them realistic, but they are chosen to constrain the maximum amount by which the isolated binary evolutionary channel can pollute the PISN mass gap.

Our results are subject to all caveats that apply to population synthesis simulations that make use of approximate evolutionary algorithms (see e.g., Langer et al., 2020). Of primary concern is the treatment of the common-envelope phase, which is one of the least understood phases of binary interaction. A specific example is the stability of mass transfer in cases where the donor star evolves to become a convective red giant (e.g., Pavlovskii & Ivanova, 2015; Pavlovskii et al., 2016, and references therein).

The treatment we adopt in our second model variation is inspired by the results of hydro-dynamical simulations by MacLeod & Ramirez-Ruiz (2015) and uses very simple scaling arguments as a recipe for accretion onto the compact object. The predictions for the final separation after the common envelope phase are based on simple energy arguments (Webbink, 1984). The treatment of this process is simplistic, and we hope this will be reconsidered carefully in future work as the understanding of the common-envelope phase increases.

We are further affected by uncertainties in massive star evolution. The main open questions concern the role of stellar wind mass loss (e.g., Smith, 2014; Renzo et al., 2017), and interior mixing (e.g., Maeder & Meynet, 2000), which affect the final core masses and radial evolution. The algorithms used in our simulations are based on detailed evolutionary simulations for single stars with masses up to $50 M_{\odot}$. Above $50 M_{\odot}$ we rely on extrapolations of fits.

2.7 Conclusions and summary

In this work we investigate the BBH population in the pair-instability mass gap due to isolated binaries, by allowing for accretion onto BHs at a super-Eddington rate from their stellar companions. We accomplish this by means of the population synthesis code **COMPAS**.

We place an upper limit on the contribution of isolated binaries to creating PISN mass gap events, defined as BBH mergers that contain a component with $M_{\text{BH}} > 45 M_{\odot}$. We find that a substantial population of BBH systems with a component in the PISN mass gap can be formed via stable super-Eddington accretion onto BHs (see Figure 2.1). However, these systems will not contribute to the BBH merger rate since their binary

orbits are typically too wide to merge within a Hubble time (Table 2.3).

In our most optimistic model, which allows for accretion onto BHs during both stable mass transfer and during a CE phase (model 3, combined), we find that less than about 2% of all BBH mergers are expected to contain one component in the PISN mass gap (see Table 2.1). Moreover, only about 0.5% of the merging BBH systems in this model variation have a total mass $M_{\text{BBH}} \geq 90 M_{\odot}$ (see Figure 2.3 and Table 2.2). By design this model includes extreme assumptions about the accretion physics. More conventional assumptions significantly lower these fractions.

Our results show that the classical isolated binary formation scenario of BBHs is not expected to significantly pollute the pair-instability mass gap when compared to other pathways proposed in the literature (see Figure 2.5). None of our simulations produce a merging BBH system with a total mass $M_{\text{BBH}} \geq 100 M_{\odot}$ (Table 2.2).

We argue that BBH systems with $M_{\text{BBH}} \leq 100 M_{\odot}$ and extreme mass ratios, combined with an aligned spin orientation could be indicative of BHs that underwent super-Eddington accretion from a companion star (Figure 2.6). However, at the time of writing, predictions from different pathways for the maximum masses, mass ratios and BH spins are not sufficiently constrained to decisively differentiate between pathways.

We predict that the BBH population cannot be explained by the isolated binary evolution channel alone if more than 1% of all BBH mergers has a mass higher than $90 M_{\odot}$. Future detections of PISN mass gap events will enable us to determine the relative contribution of different channels to the overall population of BBHs.

Our finding that the isolated binary evolutionary scenario does not introduce significant uncertainties for the existence and location of the PISN mass gap are promising. This strengthens the predictive power that can be drawn from $M_{\text{BH,max}}$ for constraining the relative contribution of different formation scenarios (Arca Sedda et al., 2020a), the physics of the progenitors including nuclear reaction rates (Farmer et al., 2019), and possibly even the Hubble constant (e.g. Farr et al., 2019b).

2.8 acknowledgments

We thank Y. Götberg, M. MacLeod, E. Ramirez-Ruiz, R. Narayan, C. Rodriguez, N. Ivanova and the members of the [COMPAS](#) collaboration for insightful discussions. This project was funded in part by the European Union’s Horizon 2020 research and innovation program from the European Research Council (ERC, Grant agreement No. 715063), and by the Netherlands Organization for Scientific Research (NWO) as part of the Vidi research program BinWaves with project number 639.042.728. RF is supported by an NWO top grant (PI: de Mink) with project number 614.001.501.

2.9 Appendix: Angular momentum loss during (non) conservative mass transfer

To evaluate the evolution of the binary separation during mass transfer, we need to quantify the angular momentum that is lost from the system. For this purpose we follow classical arguments describing the details of mass transfer in binaries, (e.g. those presented in van den Heuvel 1994 and similarly Section 4 from Renzo et al. 2019, and references therein).

The orbital evolution of binaries is well constrained by the change in total orbital angular momentum, J :

$$J^2 = G \frac{M_d^2 M_a^2}{M_d + M_a} a(1 - e^2) \quad (2.3)$$

with G the gravitational constant, a the orbital separation, e the eccentricity and M_d the mass of the donor star, and M_{BH} the mass of the accreting BH.

We parametrise the amount of mass lost from the system with a conservativeness parameter β , defining $\dot{M}_{BH} = -\beta \dot{M}_d$ where \dot{M}_{BH} and $-\dot{M}_d$ are the mass accretion and donation rates respectively. We furthermore approximate the specific orbital angular momentum of the ejected matter as γ times the specific angular momentum of the binary. The specific angular momentum of the ejected matter, h_{loss} , can then be rewritten in terms of γ and β :

$$\begin{aligned} h_{loss} &= \gamma \frac{J}{M_1 + M_2} = \frac{J}{\dot{M}_1 + \dot{M}_2}, \\ &\rightarrow \frac{J}{J} = \frac{\gamma(1 - \beta)\dot{M}_d}{M_d + M_a}. \end{aligned} \quad (2.4)$$

Using Eq. 2.3 we can derive a very general formula for the change in angular momentum:

$$2 \frac{\dot{J}}{J} = 2 \frac{\dot{M}_d}{M_d} + 2 \frac{\dot{M}_a}{M_a} - \frac{\dot{M}_d + \dot{M}_a}{M_d + M_a} + \frac{\dot{a}}{a} + \frac{(-2e\dot{e})}{(1 - e^2)} \quad (2.5)$$

In the case of Roche-lobe overflow we assume the orbit is fully circularised, and thus the last term is zero (see e.g. Soberman et al., 1997, for an expression of the orbital evolution including eccentricity). Substituting the result from Eq. 2.4 and the definition

of β , we can write this for the orbital evolution;

$$\frac{\dot{a}}{a} = -2 \frac{\dot{M}_d}{M_d} \left\{ 1 - \beta \frac{M_d}{M_{BH}} - (\gamma + \frac{1}{2})(1 - \beta) \frac{M_d}{M_d + M_{BH}} \right\} \quad (2.6)$$

or, rewriting to explicitly show the dependence on our different parametrisation parameters:

$$\frac{\dot{a}}{a} = -2 \frac{\dot{M}_d}{M_d} \{ 1 - f(\beta, M_{BH}, M_d, \gamma) \} \quad (2.7)$$

Since $\dot{M}_d < 0$, we see that the orbit shrinks ($\dot{a} < 0$) as soon as $f(\beta, q, \gamma)$ is larger than one.

It is now a matter of specifying γ and β .

2.9.1 Varying the mass conservation

In this work we assume isotropic reemission of the ejected matter. This assumes that the mass is ejected from the vicinity of the accretor, e.g. when mass is lost via bipolar outflows from a compact object. In this case we can approximate $\gamma_1 = M_d/M_{BH}$ (e.g. [Soberman et al., 1997](#)). We can rewrite Equation 2.7 as

$$f(\beta, q, \gamma_1) = \frac{\beta}{q} + \left(\frac{1}{q} + \frac{1}{2} \right) (1 - \beta) \frac{1}{q + 1} \begin{cases} > 1 & \text{orbit shrinks, } (\dot{a} < 0) \\ < 1 & \text{orbit widens, } (\dot{a} > 0) \end{cases}, \quad (2.8)$$

where we have used $q \equiv M_{BH}/M_d$ to describe the mass ratio.

Figure 2.9 displays the condition for widening or shrinking the orbit (Eq. 2.8) as a function of the mass ratio and the conservativeness parameter. In the case of stable mass

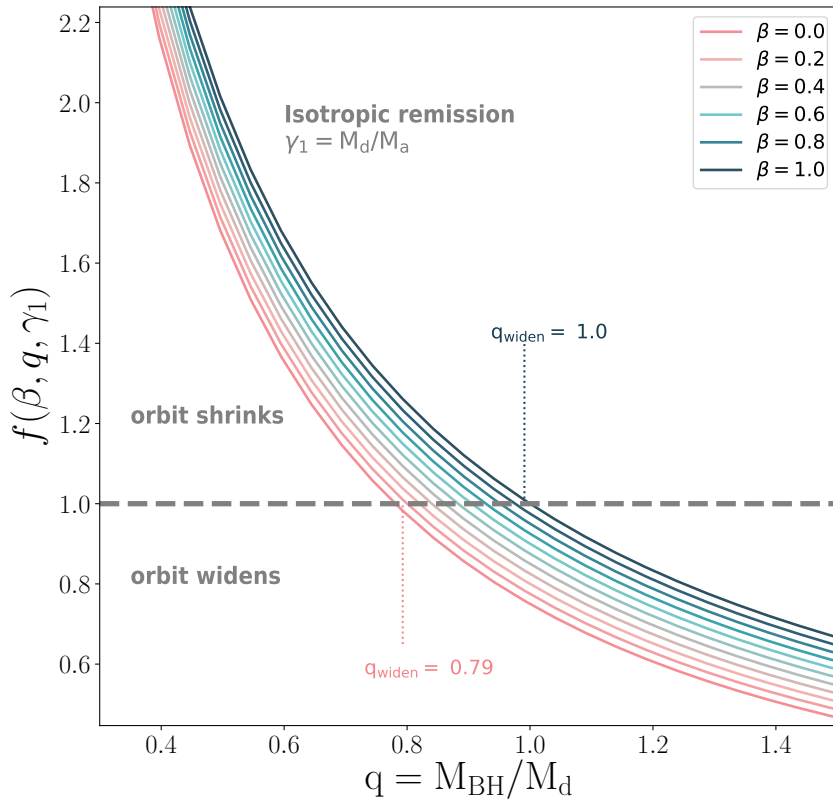


Figure 2.9: Parametrisation of the specific orbital angular momentum evolution that determines whether mass transfer will shrink (above the dashed black line) or widen (below the dashed black line) the binary orbit. The conservativeness parameter β varies from completely non-conservative ($\beta = 0$) to completely conservative ($\beta = 1$). This assumes isotropic reemission of the ejected matter, i.e., assuming the ejected matter carries the specific angular momentum of the accretor.

transfer from a star onto a BH, the binary typically starts with $q \leq 1$ and then moves to higher q . For fully non-conservative mass transfer ($\beta = 0.0$) the system will widen as soon as the mass ratio $q > q_{\text{widen}} = 0.76$. For fully conservative mass transfer ($\beta = 1.0$) the system will widen as soon as the mass ratio $q > q_{\text{widen}} = 1.0$. Systems where the accreting BH is more massive than the donor at the start of the stable mass transfer will always widen.

Figure 2.9 shows that mass transfer *will always widen the orbit* when the mass ratio q is larger than some mass ratio q_{widen} , as long as the lost mass is presumed to carry the specific angular momentum of the accretor. We therefore expect high amounts of mass transfer to always lead to significant widening of the binary system, regardless of the conservativeness of the mass transfer, and thus prevent the BBH from merging within a Hubble time.

In model 1, allowing for stable super Eddington accretion onto BHs, we assume the mass transfer is completely conservative ($\beta = 1$). Based on Figure 2.9 we conclude that varying the mass conservation in model 1 would still lead to significant widening of the BBHs and thus would not change our main conclusions.

2.9.2 Varying the specific angular momentum lost

If the mass that is lost from the system carries sufficiently high specific angular momentum, the orbit will shrink. If the lost mass ends up in a Keplerian orbit around the binary, it is called a circumbinary ring. This may occur when mass escapes through the outer Lagrangian point, L2. The angular momentum of such a ring would correspond to (Artymowicz & Lubow, 1994b):

$$\gamma_2 = \frac{(M_d + M_{\text{BH}})^2}{M_d M_{\text{BH}}} \sqrt{\alpha}, \quad (2.9)$$

where $\alpha = a_{\text{ring}}/a$ is the ratio of the orbital separation of the binary over the distance between the circumbinary ring and the center of mass. For typical parameter of viscous disks, the location of the inner edge of a circumbinary disk varies between $1.8a$ and $2.6a$ (Artymowicz & Lubow, 1994a).

Equation 2.7 can then be rewritten as:

$$f(\beta, q, \gamma_2) = \frac{\beta}{q} + \frac{(1+q)(1-\beta)}{q}\sqrt{\alpha} + \frac{1-\beta}{2(q+1)}\sqrt{\alpha} \begin{cases} > 1 & \text{orbit shrinks, } (\dot{a} < 0) \\ < 1 & \text{orbit widens, } (\dot{a} > 0) \end{cases}. \quad (2.10)$$

We have calculated the effect of this mode of non-conservative mass transfer for $\alpha = 2$. Larger α lead to higher \dot{a} , though varying between $1.8a$ and $2.6a$ has little effect. We find that non-conservative mass transfer ($\beta \leq 0.3$) in combination with high mass-transfer rates leads to shrinking of the binary orbit in a runaway fashion, which leads to a stellar merger. The orbit will shrink with increasing speeds (increasing $f(\beta, q, \gamma_2)$) as the mass ratio q increases.

For mass transfer with slightly to highly conservative mass transfer ($\beta \geq 0.3$) it is unclear what the fate of the systems will be. Test simulations using $\alpha = 2$, indicate that most BHs in this situation will plunge into their companion's envelope, unless the mass transfer efficiency is highly fine-tuned. More detailed simulations of this specific scenario are needed to determine its plausibility.

2.10 Appendix: BH Formation yields and merger rates

Our calculation of the BH formation yields follow [Dominik et al. \(2012\)](#) and [Neijssel et al. \(2019\)](#) but includes the weights from the adaptive sampling (as described in [Broekgaarden et al., 2019](#)).

We start by calculating the total stellar mass contained in a synthetic galaxy ($M_{*,\text{gal}}$), assuming a [Kroupa \(2001\)](#) initial mass function with initial masses in the range

$0.08 - 200 M_{\odot}$. We compute the subset of this synthetic galaxy that is spanned by our set of initial parameters ($M_{\star, \text{sub-gal}}$) by integrating over the volume of initial parameter space. In our simulations, we adopt a binary fraction $f_{\text{bin}} = 0.5$ (e.g. Sana et al., 2013) and draw initial masses in the range $20 - 150 M_{\odot}$. The fraction of the synthetic Universe that is spanned by our initial parameter space is now computed as follows:

$$f_{\text{sim}} = \frac{M_{\star, \text{sub-gal}}}{M_{\star, \text{gal}}}. \quad (2.11)$$

The total star forming mass that our simulation represents is given by:

$$M_{\text{SF}} = M_{\text{sim}} \cdot f_{\text{sim}}^{-1}, \quad (2.12)$$

where M_{sim} is the total initial mass that is evolved in COMPAS. This is used to calculate the number of merging BBHs formed per unit of star forming mass:

$$\frac{N_{\text{BBH}, t_H}}{M_{\text{SFR}}} = \frac{\sum_i^N \delta_{t_H, i} w_i}{M_{\text{SF}}}, \quad \text{with } \delta_{t_H, i} = \begin{cases} 1, & \text{if } \text{type}(i) = \text{BBH}, \text{ and } t_{\text{delay}, i} < t_H \\ 0, & \text{otherwise} \end{cases}. \quad (2.13)$$

Here N_{BBH, t_H} is the total number of BBHs formed with a coalescence time that is less than the Hubble time, $\delta_{t_H, i}$ is the Dirac delta function that equals 1 for a BBH system with a coalescence time that is less than the Hubble time, i.e. if it merges within the age of the Universe, and N is the total number of samples in the simulation $N = 1 \times 10^6$.

Finally, w_i is the formation weight of the binary based on the adaptive importance sampling algorithm as described in Broekgaarden et al. (2019). We estimate the absolute $1-\sigma$ statistical sampling uncertainty on the number of BBHs that merge in a Hubble

time N_{BBH,t_H} by computing the variance about the mean, that is

$$\sigma^2 \approx \sum_i^N (\delta_{t_H,i}^2 w_i^2) - \frac{[\sum_i^N (\delta_{t_H,i} w_i)]^2}{N}, \quad (2.14)$$

We calculate merger rates for a synthetic galaxy following the same procedure as Belczynski et al. (2016a) and de Mink & Belczynski (2015a). For this purpose, we calculate the number of coalescing BBHs occurring in a synthetic galaxy, observed per Myr today;

$$N_{BBH,gal} = \frac{N_{BBH,10}}{M_{SFR}} \cdot SFR_{gal} \cdot t_{gal}, \quad (2.15)$$

with a constant star formation rate, $SFR_{gal} = 3.5 M_\odot \text{ yr}^{-1}$, and a galaxy lifetime $t_{gal} = 10 \text{ Gyr}$. These properties are chosen to resemble the Milky Way (following estimates from Flynn et al., 2006; McMillan, 2011). The number of merging BBH systems per unit star forming mass, $N_{BBH,10}/M_{SFR}$, is defined in a similar way as in Equation 2.13, but we now require the BBHs to merge in less than the age of the galaxy, $t_{gal} = 10 \text{ Gyr}$. The statistical sampling uncertainty on $N_{BBH,10}$ is estimated analogous to equation 2.14.

The merger rate per synthetic galaxy is then calculated as

$$\mathcal{R}_{MWG} = \frac{N_{BBH,gal}}{t_{gal}} [\text{Myr}^{-1}], \quad (2.16)$$

note that the age of the synthetic galaxy t_{gal} , cancels out in this equation. t_{gal} only appears in the equivalent of Equation 2.13, when calculating the number of merging BBH systems per unit star forming mass.

The merger rate per synthetic galaxy can be converted into an approximate volumetric rate following:

$$\mathcal{R}_{vol} = 10^3 \left[\frac{\rho_{gal}}{\text{Mpc}^{-3}} \right] \left[\frac{\mathcal{R}_{MWG}}{\text{Myr}^{-1}} \right] \text{ yr}^{-1} \text{Gpc}^{-3} \quad (2.17)$$

where $\rho_{\text{gal}} = 0.0116 \text{ Mpc}^{-3}$ is the local density of Milky Way-like galaxies (e.g. Kopparapu et al., 2008).

All uncertainty ranges on the formation yields and merger rates as quoted in this work are estimates of the $1-\sigma$ statistical sampling uncertainty following from Equation 2.14.

2.11 Appendix: Remnant mass prescription

To calculate the remnant masses we adopt the delayed model from Fryer et al. (2012) for estimated CO core masses at the moment of core collapse $M_{\text{CO}} < 30 \text{ M}_{\odot}$, while we follow Farmer et al. (2019) for $M_{\text{CO}} > 30 \text{ M}_{\odot}$.

Previous works studying the PISN gap (Stevenson et al., 2017; Belczynski et al., 2016a) use Fryer et al. (2012) for $M_{\text{CO}} > 30 \text{ M}_{\odot}$. Fryer et al. (2012) compute the remnant mass based on the estimated helium core masses at the moment of core collapse while Farmer et al. (2019) account for a PISN and compute the remnant mass based on the estimated CO core masses at the moment of core collapse. Mapping between the helium core masses and PISN depends on uncertain physics such as the efficiency and extent of mixing (overshooting) which varies between models and with wind mass loss. The CO core mass at the moment of supernova is therefore a more robust parameter than the helium core mass at the moment of supernova to map the pre-supernova stellar properties to the final remnant mass (Farmer et al., 2019).

For $M_{\text{CO}} > 30 \text{ M}_{\odot}$ the prescription from Farmer et al. (2019) results in lower remnant masses with respect to the prescriptions from Fryer et al. (2012). This is because Fryer et al. (2012) does not account for pulsational pair-instability supernovae.

The maximum BH mass formed in our simulation at $Z = 0.001$ for Farmer et al. (2019) is $M_{\text{BH,max}} = 43.4 \text{ M}_{\odot}$, while $M_{\text{BH,max}} = 54 \text{ M}_{\odot}$ for Fryer et al. (2012).

2.12 Appendix: Additional material

For each model variation, we provide a `python` file describing the initial conditions as used in each of our 4 model variations described in Section 2.3, and a HDF file containing i.a. a list of compact object properties as resulting from our COMPAS simulations at <https://doi.org/10.5281/zenodo.3746936> and https://liekevanson.github.io/IsolatedBinaries_PISNgap.html.

Chapter 3

The redshift evolution of the binary black hole merger rate: a weighty matter

This thesis chapter originally appeared in the literature as

L.A.C. van Son, S. E. de Mink, T. Callister, S. Justham, M. Renzo, T. Wagg,
F. S. Broekgaarden, F. Kummer, R. Pakmor & I. Mandel,
The Astrophysical Journal, 2022, Vol. 931, Issue 1, Article id. 17, 24 pp.

Abstract

Gravitational wave detectors are starting to reveal the redshift evolution of the binary black hole (BBH) merger rate, $R_{\text{BBH}}(z)$. We make predictions for $R_{\text{BBH}}(z)$ as a function of black hole mass for systems originating from isolated binaries. To this end, we investigate correlations between the delay time and black hole mass by means of the suite of binary population synthesis simulations, [COMPAS](#). We distinguish two channels: the common envelope (CE), and the stable Roche-lobe overflow (RLOF) channel, characterised by whether the system has experienced a common envelope or not. We find that the CE channel preferentially produces BHs with masses below about $30 M_\odot$ and short delay times ($t_{\text{delay}} \lesssim 1 \text{ Gyr}$), while the stable RLOF channel primarily forms systems with BH masses above $30 M_\odot$ and long delay times ($t_{\text{delay}} \gtrsim 1 \text{ Gyr}$). We provide a new fit for the metallicity specific star-formation rate density based on the Illustris TNG simulations, and use this to convert the delay time distributions into a prediction of $R_{\text{BBH}}(z)$. This leads to a distinct redshift evolution of $R_{\text{BBH}}(z)$ for high and low primary BH masses. We furthermore find that, at high redshift, $R_{\text{BBH}}(z)$ is dominated by the CE channel, while at low redshift it contains a large contribution ($\sim 40\%$) from the stable RLOF channel. Our results predict that, for increasing redshifts, BBHs with component masses above $30 M_\odot$ will become increasingly scarce relative to less massive BBH systems. Evidence of this distinct evolution of $R_{\text{BBH}}(z)$ for different BH masses can be tested with future detectors.

3.1 Introduction

The Advanced LIGO ([LIGO Scientific Collaboration et al., 2015](#)), Advanced Virgo ([Acernese et al., 2015](#)) and KAGRA ([Akutsu et al., 2021](#)) gravitational wave detectors

are revealing gravitational wave events that probe a progressively larger fraction of the Universe (Abbott et al., 2018a, 2021b,g,c). As the number of gravitational wave detections increases, they unveil the evolution of the binary black hole (BBH) merger rate with redshift. Current gravitational wave detectors already probe black holes (BHs) with component masses of about $30 M_{\odot}$ out to redshifts $z \sim 1$ (Fishbach et al., 2018; Callister et al., 2020; Abbott et al., 2021c,f,a). Third-generation detectors, scheduled to start observations in the 2030s, promise to observe stellar mass BBH mergers with component masses in the range $\sim 5 - 350 M_{\odot}$ out to $z > 10$ (e.g. Sathyaprakash et al., 2019a,b; Maggiore et al., 2020). This means that we are rapidly moving towards a complete picture of both the redshift evolution of the stellar-mass BBHs merger rate, and the redshift evolution of source property distributions.

The redshift evolution of the BBH merger rate contains information on the origin of these BBHs, however, a direct interpretation is complicated. To infer the birth-time and environment of the observed merging BBHs we first need to understand the difference between the time at which the progenitor stars formed and the time of merger of the BBH. This is what we define as the delay time t_{delay} . It is the sum of two independent timescales: I) the lifetime of the binary stars up to the moment that both have become compact objects, and II) the inspiral time of the two BHs up to the BBH merger event. The former timescale, i.e. the lifetime of massive stars, is typically a few Myr. The latter timescale depends primarily on the separation between the two BHs at BBH formation (Peters, 1964). To interpret the BBH merger rate, we first need to understand the impact of the delay time distribution on the observed rate at each redshift.

The delay time of BBHs from isolated binaries of interest can range from Myr to more than a Hubble time (see e.g. Neijssel et al., 2019; Giacobbo & Mapelli, 2018). This

implies that BBH mergers observed to merge at a given redshift, z_{merge} , formed Myr to Gyr earlier. Hence, these mergers are comprised of a mixture of systems that originate from different formation redshifts, and likely probe a range of different formation environments.

The delay time is thus a very important quantity, which, unfortunately, cannot be observed directly for an individual system. It is possible to make statistical inferences about the delay time distribution using the detections available so far (see e.g. [Fishbach & Kalogera, 2021](#)). However, inference of the time delay distribution is difficult because it is degenerate with the progenitor formation rate. Moreover, we are currently still limited by the low number of sources that are detected out to higher redshifts.

Although the delay time is not directly observable, we will observe the redshift evolution of the source properties, i.e. the BH-mass, spin and mass ratio distributions at different redshifts. Several earlier studies have investigated the evolution of the BBH merger rate with redshift for the total population of merging BBHs, (e.g. [Rodriguez & Loeb, 2018](#); [Mapelli & Giacobbo, 2018](#); [Choksi et al., 2019](#); [Santoliquido et al., 2021a](#)). The redshift evolution of source property distributions remains relatively obscured, though it is actively being studied (see e.g. [Neijssel et al., 2019](#); [Mapelli et al., 2022](#)). Recent work hints towards relations between source properties and redshift evolution. [Mapelli et al. \(2019\)](#) for example, find that massive BBHs tend to have longer delay times in their models. An important step to move forward, is thus to associate possible trends in delay time distribution to observable characteristics, while understanding their physical origin.

Here, we inspect the delay time-mass relation for BHs coming from isolated binaries, as predicted by the rapid population synthesis code [COMPAS](#). We consider two main

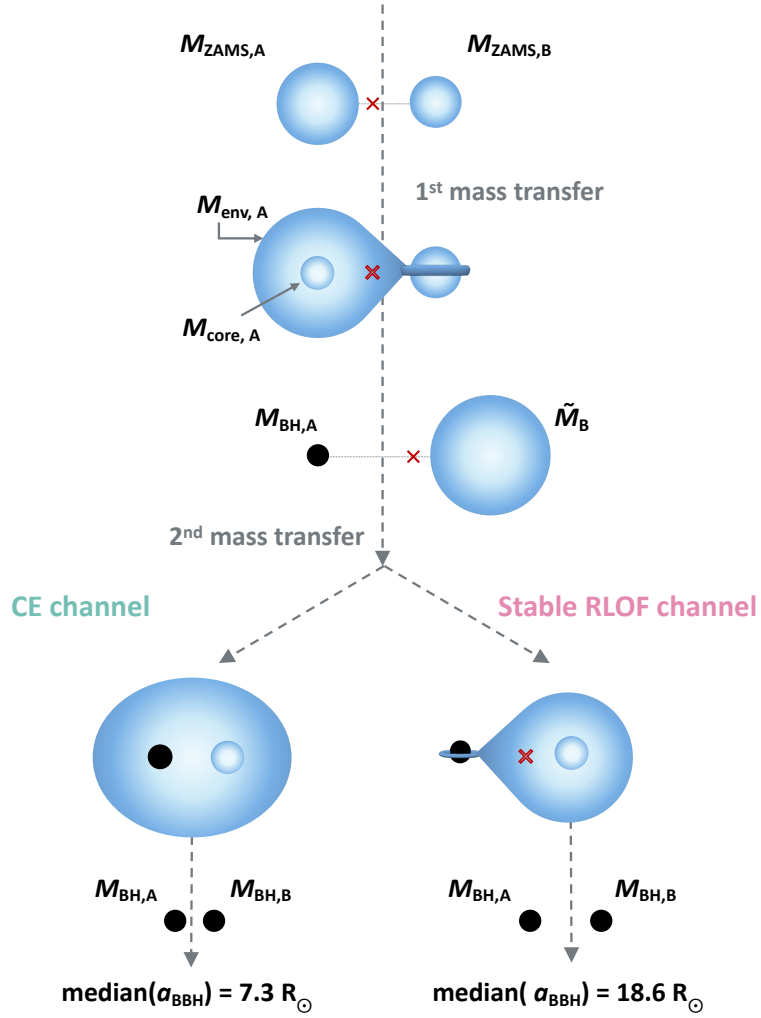


Figure 3.1: Cartoon depiction of the *typical* evolution of a BBH progenitor system through the stable RLOF and CE channel. Annotations refer to masses at zero age main sequence (M_{ZAMS}), the envelope mass (M_{env}), the core mass (M_{core}), mass post mass transfer (\tilde{M}_B) and BH mass (M_{BH}). The subscript A (B) denotes the initially more (less) massive star. The red cross gives an impression of the location of the centre of mass at the onset of the evolutionary phase depicted (not to scale). The median separation is annotated for each channel, considering BBH mergers that can be observed by a ‘perfect detector’ (see text).

channels: 1) the common envelope channel (or CE channel, e.g. Belczynski et al., 2007a; Postnov & Yungelson, 2014a; Belczynski et al., 2016a; Vigna-Gómez et al., 2018a), including BBH systems where the progenitor system has experienced at least one common envelope, and 2) the stable Roche-lobe overflow channel (or stable RLOF channel, e.g. van den Heuvel et al., 2017; Inayoshi et al., 2017). The stable RLOF channel contains all BBH systems that experience *only* stable mass transfer (i.e. all systems that *do not* experience CE events, and so it is the complement set of the CE channel). See also Figure 3.1 for a cartoon depiction of the most common evolution of these two channels. Note that this does not display all possible variations of the CE and stable RLOF channel. However, other sub-channels are rare. For example, the sub-channel where both the first and second mass transfer are unstable (which is one of the mos common sub-channels), contributes only 0.6% to the total rate of BBH mergers as observed by a perfect detector (equation 3.6). The respective contribution of the CE and the stable RLOF channel to the observed population of merging double compact objects is an active area of research (see e.g. Neijssel et al., 2019; Bavera et al., 2021a; Marchant et al., 2021; Gallegos-Garcia et al., 2021). In this work we aim to use characteristic delay time-mass distributions from each channel to make predictions for observables in the gravitational wave distributions.

This paper is structured as follows: in Section 3.2 we describe the population synthesis code **COMPAS** used in this work. We find that massive BHs ($M_{\text{BH},1} > 30 M_\odot$, where we define $M_{\text{BH},1}$ as the more massive BH at BBH merger) predominantly form in BBHs with long delay times ($t_{\text{delay}} > 1 \text{ Gyr}$). We show that this can be explained by differences between the CE channel and the stable RLOF channel in Section 3.3. In Section 3.4 we describe how we calculate cosmic BBH merger rates. We then discuss how

the distinct delay times and mass distributions arising from CE and stable RLOF affect the observed merger rate evolution of BBHs in Section 3.5. In Section 3.6 we discuss the prospect of observing trends in the BBH merger rate with current and near-future gravitational wave detectors. Specifically, our models predict that the slope of the intrinsic BBH merger rate density with redshift is more shallow and starts decreasing at lower redshift for higher $M_{\text{BH},1}$. We discuss the robustness of our main findings and caveats that apply to a population synthesis approach in Section 3.7, and summarise our main results in Section 3.8.

3.2 Method (I) : Simulating merging BBH populations

To simulate the evolution of isolated massive binary star progenitors that lead to merging BBH, we use the rapid population synthesis code that is part of the [COMPAS](#) suite¹ (version v02.19.04, Riley et al., 2022b; Stevenson et al., 2017; Vigna-Gómez et al., 2018a). We simulate a total of 10^7 binaries. To check that our results are converged, we have repeated all analyses for an independent set of 10^6 binaries, and we found no significant differences. In this section we discuss the treatment of stellar evolution and binary interaction processes (Sec. 3.2.1) and sampling of the initial parameters (Sec 3.2.2).

3.2.1 Binary evolution

We model the evolution of massive stars in binary systems using fast algorithms following Hurley et al. (2000, 2002), based on detailed evolutionary models by [Pols](#)

¹see also <https://compas.science/>

et al. (1998). Here we summarise the treatment of the physical processes that are most relevant for this study. For a full description of the code we refer to the references mentioned above.

Winds For hot O and B type stars (with effective temperatures $T_{\text{eff}} \geq 12500\text{K}$), we follow Vink et al. (2000, 2001b) to account for metallicity-dependent stellar wind mass loss. For cooler, more evolved stars ($T_{\text{eff}} \leq 12500\text{K}$) the mass-loss prescription from Kudritzki & Reimers (1978) and the prescription from Nieuwenhuijzen & de Jager (1990), modified by a metallicity dependent factor from Kudritzki et al. (1989), are compared and the maximum is adopted. The latter mass-loss prescription is only assumed to be non-zero for stars with luminosity $L > 4000 L_{\odot}$. For low mass stars that evolve towards the asymptotic giant branch, the prescription from Vassiliadis & Wood (1993) is added to this comparison. For hot Wolf-Rayet-like stars, we use the empirical mass loss prescription from Belczynski et al. (2010a), that is adapted from Hamann & Koesterke (1998) but scaled by metallicity following Vink & de Koter (2005). For very luminous stars, that lie above the Humphreys-Davidson limit, i.e. if the luminosities L and stellar radii R fulfil the condition $L > 6 \times 10^5 L_{\odot}$ and $(R/R_{\odot})(L/L_{\odot})^{1/2} > 10^5$ (Humphreys & Davidson, 1979), we assume enhanced mass loss rates following Hurley et al. (2000), motivated by the scarcity of observed stars in this regime and the observed Luminous Blue Variables (LBV) phenomenon. This additional mass loss is metallicity independent (in line with recent results from, e.g. Davies & Beasor, 2020), and is meant to mimic eruptive mass loss.

Stable mass transfer and common envelope phases We account for mass transfer when a star overflows its Roche lobe (Eggleton, 1983). To determine whether

Roche-lobe overflow is stable we use an estimate for the response of the radius of the donor star, R and its Roche lobe, R_{RL} as a result of mass transfer. **COMPAS** determines stability by comparing estimates of the adiabatic response of the donors radius and the response of the donors Roche-lobe radius (see e.g. Vigna-Gómez et al., 2018a, 2020, and references therein). This procedure depends crucially on the assumed value of $\zeta_* \equiv (\partial \log R / \partial \log M)_{\text{ad}}$, with R and M the radius and mass of the donor star, for different types of donor stars (e.g. Soberman et al., 1997). We assume $\zeta_{\text{ad}} = 2$ for main sequence donors, $\zeta_{\text{ad}} = 6.5$ for Hertzsprung gap donor stars (Ge et al., 2015) and follow Soberman et al. (1997) for donor stars post helium ignition.

During stable mass transfer onto a stellar companion we assume that the accretion rate is limited to ten times the thermal rate of the accreting star (Neo et al., 1977; Hurley et al., 2002). If the accreting component is a BH, the accretion is assumed to be Eddington limited. Material lost from the system during non conservative mass transfer, is assumed to carry away the specific orbital angular momentum of the accreting component (e.g. Soberman et al., 1997; van den Heuvel et al., 2017). This reduces the orbital angular momentum and can lead to either shrinking or widening of the orbit, depending on the fraction of mass that is accreted and the binary's mass ratio (e.g. van Son et al., 2020, Appendix A).

Unstable mass transfer is assumed to result in CE evolution (Paczynski, 1976; Ivanova et al., 2013b; Ivanova et al., 2020). We assume that ejecting the envelope shrinks the binary orbit following the energy considerations proposed by Webbink (1984) and de Kool (1990). Here, the pre-CE binding energy of the donor's envelope is equated to the orbital energy that becomes available by shrinking the orbit. How efficiently this orbital energy can be used to eject the envelope is parameterized by the α_{CE} parameter, which

is set to one in this work. For the binding (and internal) energy of the envelope, we use the “Nanjing” prescription (Dominik et al., 2012), based on fits provided by Xu & Li (2010b,a). We adopt the *pessimistic* CE scenario from Dominik et al. (2012), that is, we assume that Hertzsprung Gap donor stars do not survive a CE event.

Supernovae, kicks and compact remnants To model natal supernova kicks, we draw kick velocities with random isotropic orientations and draw the kick magnitudes from a Maxwellian distribution (Hobbs et al., 2005). BH kicks are reduced by the amount of mass falling back onto the newly-formed BH during the explosion mechanism, following the ‘delayed’ prescription from (Fryer et al., 2012). This prescription assumes full fallback for BHs resulting from progenitors with a carbon oxygen core mass $M_{\text{CO}} > 11 M_{\odot}$, and hence these BHs receive no supernova kick.

The remnant mass is modelled as a function of the estimated M_{CO} at the moment of core collapse following Fryer et al. (2012). Stars with helium cores above $35 M_{\odot}$ at the moment of core collapse are assumed to experience pulsational-pair instability following Farmer et al. (2019). Stars with helium core masses between $60 - 135 M_{\odot}$ at the moment of core collapse are expected to be completely disrupted by pair instability, and therefore leave no remnant BH. With this implementation the lower edge of the pair-instability mass gap is located at about $45 M_{\odot}$ (Stevenson et al. 2017; Marchant et al. 2019; Farmer et al. 2019; Farmer et al. 2020; Woosley & Heger 2021, but see e.g. Mehta et al. 2021). Due to the metallicity dependence of stellar winds and the adopted pulsational-pair instability prescription, the maximum BH mass is also metallicity dependent. The upper limit of about $45 M_{\odot}$ is only reached for the lowest metallicity systems (with $Z \lesssim 0.001$). For reference, systems with metallicities of about $Z \sim 0.01$ and $Z \sim 0.0032$ can maximally achieve a BH mass of about $18 M_{\odot}$ and $32 M_{\odot}$ respectively in our simulations

(see Figure 3.7 for a decomposition of the BH mass distribution by metallicity).

3.2.2 Sampling

The evolution of a binary system is mainly a function of its initial metallicity Z , initial primary and secondary mass M_1 and M_2 , and the initial separation a .

We sample birth metallicities with a probability distribution that is flat-in-log in the range $10^{-4} \leq Z \leq 0.03$. Sampling metallicities from a smooth probability distribution is an improvement over discrete sets of metallicity, which is the most common technique in binary population synthesis studies (but see, for example, Riley et al. 2021 for an exception). Smoothly sampling birth metallicity avoids artificial peaks in the BH mass distribution (e.g. Dominik et al., 2015a; Kummer, 2020). The flat-in-log distribution ensures that we sample ample binaries at the low metallicities that are favoured for BBH formation. Later in this paper, when we calculate cosmic merger rates, we re-weight systems to account for the metallicity-dependent star formation (see Section 3.4). We adjust the normalisation of this re-weighting over the metallicity range of our simulations to preserve the correct total star-formation rate, i.e., star formation at more extreme metallicities is not discarded.

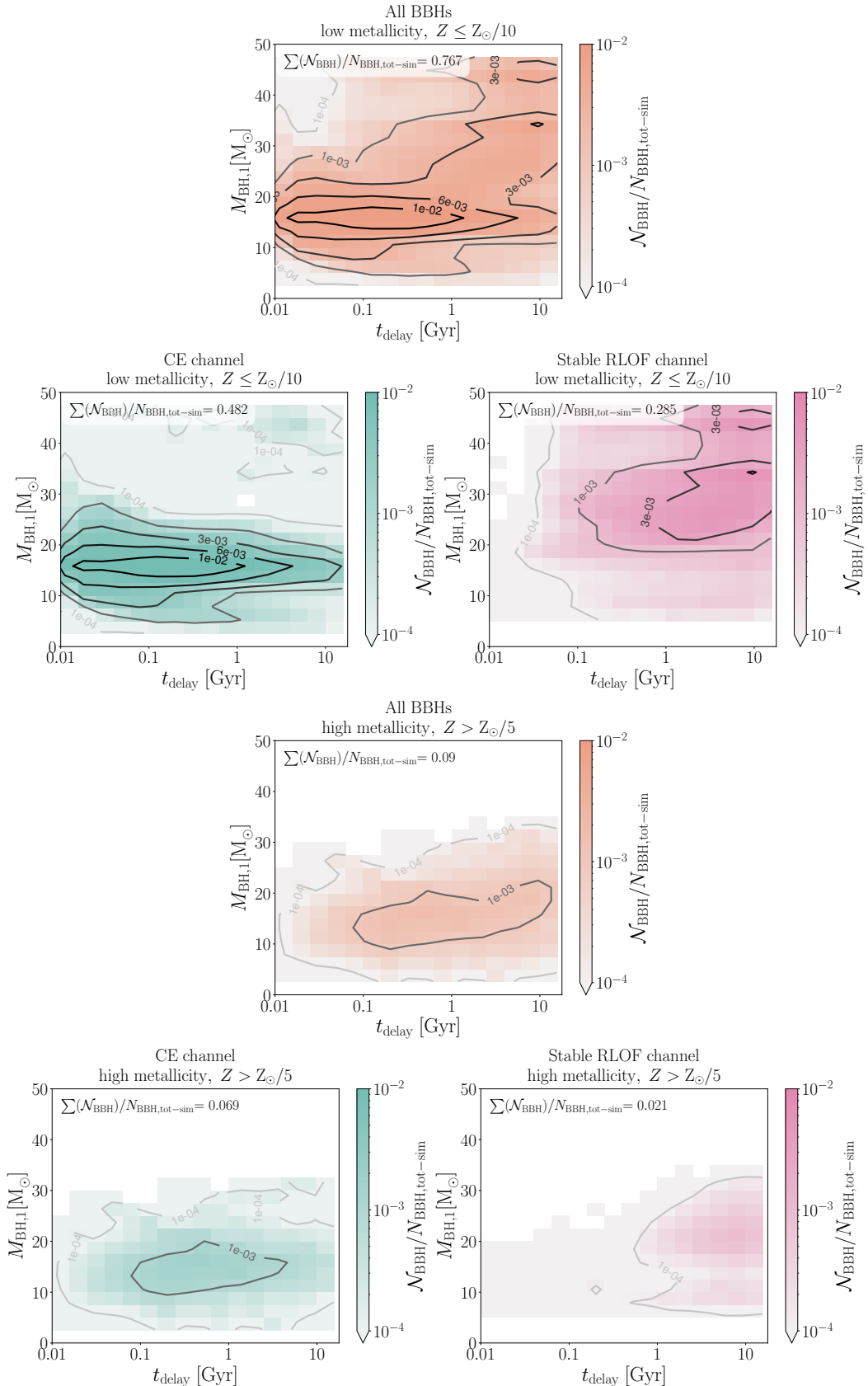
We assume the masses of the initially more massive stellar components (the primary, M_1) are universally distributed following a Kroupa (2001) initial mass function and draw masses in the range $10 - 150 M_\odot$, in order to focus on stars that evolve into BHs. The binary systems are assumed to follow a uniform distribution of mass ratios ($0.01 \lesssim q \equiv M_2/M_1 < 1.0$, with M_2 , the mass of the secondary star). We require $M_2 \geq 0.1 M_\odot$. The initial binary separations are assumed to follow a distribution of orbital separations that is flat in the logarithm (Öpik, 1924) in the range $0.01 - 1000$ AU.

Binary systems that fill their Roche lobe at zero age main sequence are discarded. All binary orbits are assumed to be circular at birth.

If a zero age main sequence (ZAMS) star is rotating faster than the metallicity-dependent rotational frequency threshold described in Riley et al. (2021), the binary is assumed to evolve chemically homogeneously. In this work, we focus on the ‘classical’ pathway of isolated binaries towards merging BBHs and thus we exclude chemically homogeneously evolving stars from our sample.

Because BBH mergers are intrinsically very rare events, direct sampling of the birth distributions is very inefficient and time consuming. We therefore make use of the adaptive importance sampling code STROOPWAFEL. This algorithm consists of an initial exploration phase to find regions of interest in the binary parameter space. In a subsequent adaptive refinement phase we optimise the simulations by sampling near the regions of interest (see Broekgaarden et al., 2019, for details).

Figure 3.2 (following page): Two-dimensional histograms of the distribution of delay times and primary masses for BBHs in our simulation. The top two and bottom two rows show results for low ($\leq Z_{\odot}/10$) and high ($> Z_{\odot}/5$) metallicity, respectively. The first and third rows show all BBHs, while the second and last rows are split by formation channel. All histograms are normalized relative to the total simulation including all simulated metallicities. The colour-bar and contours thus indicate the relative frequency of occurrence in our simulations. We use bin sizes of $\Delta \log_{10}(t_{\text{delay}}) = 0.2$ and $\Delta M_{\text{BH},1} = 2.5 M_{\odot}$. All panels reveal a lack of BBH systems with high mass ($M_{\text{BH},1} \gtrsim 30 M_{\odot}$) and short delay time ($t_{\text{delay}} \lesssim 0.1 \text{ Gyr}$).



3.3 BH mass-delay time relations

In this section, we first explore the type of BBHs that can be produced by the isolated channel according to our simulations. We aim to find links between the delay time t_{delay} and observable properties, such as BH masses and spins. Of these, the BH mass is observationally the best constrained source property. Hence our main focus is on the BH mass. While we do not discuss BH spins here, previous studies have argued that tidal spin-up is most likely in close binaries with short delay times (e.g. [Kushnir et al., 2016](#); [Zaldarriaga et al., 2018](#); [Bavera et al., 2020](#)). In appendix 3.9, we additionally investigate the correlations between BBH mass ratios and t_{delay} .

In Figure 3.2 we show two-dimensional histograms of t_{delay} , and the mass of the heavier BH, $M_{\text{BH},1}$, for BBHs in our simulations. In the first and second row, we show results for low metallicity, which is representative for the majority of BBH formation (defined as $Z \leq Z_{\odot}/10$, with solar metallicity $Z_{\odot} = 0.014$, [Asplund et al., 2009](#)). To elucidate the impact of metallicity, we show results for the highest metallicities ($Z > Z_{\odot}/5$) in the bottom two rows. The first and third row show the result for all BBHs in the selected metallicity range. The second and bottom row show the separate contributions of the CE and stable RLOF channel in green and pink respectively. All histograms shown are normalized relative to the number of merging BBHs in our full simulation, combining all metallicities. The color shading and contours thus indicate the relative frequency with which these combinations of primary mass and delay time occur in our full set of simulations. We refer to Sect 3.2 for how the progenitors are sampled and weighed in our simulation. We note that the underlying distribution in metallicity that is implicitly assumed here, is not representative for star formation in the Universe. Nevertheless, these diagrams are useful to understand trends in the delay times and

primary BH masses at low and high metallicity.

When inspecting the results for all BBH in our simulations for low-metallicity (top panel of Figure 3.2), we observe two main components. Firstly, we see that the histogram peaks at delay times of $\sim 0.1\text{--}1$ Gyr and primary BH masses of $\sim 18 M_{\odot}$. This peak comes predominantly from systems formed through the CE channel (as can be seen in green). Secondly, we see a noticeable tail of more massive systems $M_{\text{BH}} \gtrsim 20 M_{\odot}$ with longer delay times around ~ 10 Gyr, which predominantly come from the stable RLOF channel (as can be seen in pink). Finally, we see a dearth of BBH systems with high masses ($M_{\text{BH},1} \geq 30 M_{\odot}$) and short delay times ($t_{\text{delay}} \leq 0.1$ Gyr), which are not formed by either of the channels considered here.

Comparing low and high metallicity, we see that the same two components are present, but the systems with highest mass are absent at high metallicity. This result is understood as the effect of the metallicity dependent stellar winds, which are stronger for higher metallicity (e.g. Vink & de Koter, 2005). The high metallicity systems thus also display a lack of BH systems with high masses ($M_{\text{BH},1} \geq 30 M_{\odot}$) and short delay times ($t_{\text{delay}} \leq 0.1$ Gyr).

In the following subsections we discuss the origin for these features.

3.3.1 Why the CE channel does not produce high-mass black holes

We find that the massive progenitor stars that lead to BHs with masses $M_{\text{BH},1} > 30 M_{\odot}$ are disfavoured from engaging in, and surviving, CE events in our simulations because of a variety of effects. To form such BHs, we need stars that form

helium cores of at least $M_{\text{He}} \gtrsim 30 M_{\odot}$. Such cores can only be formed in the most massive stars in our simulations, typically with zero-age main sequence masses of $60 M_{\odot}$ and higher, although we note that the exact value is considerably uncertain. Such massive stars are unlikely to engage in, and survive a CE for several reasons.

First of all, the massive progenitors of heavy black holes are thought to experience heavy mass loss, which can remove a large part of the hydrogen envelope before the stars initiates interaction with its companion. Although mass loss by radiatively driven winds is thought to be reduced at low metallicity, mass loss by LBV eruptions is likely to still be very significant also at low metallicity (e.g. Smith, 2014; Sanyal et al., 2017; Kalari et al., 2018; Davies et al., 2018; Higgins & Vink, 2020; Sabhahit et al., 2021; Gilkis et al., 2021). In fact, such heavy mass loss can prevent massive stars in wider binaries from ever filling their Roche lobe (Mennekens & Vanbeveren, 2014a; Belczynski et al., 2016c). In our simulations this is the dominant reason for the suppression of the CE channel at higher masses.

Secondly, even if a massive progenitor would fill its Roche lobe, it is unlikely to do so while it has a convective envelope. It is generally thought that donor stars with extended convective envelopes are favoured for successful ejection of a common envelope. This is mainly because convective stars have large dimensions, and a relatively large fraction of the mass is located at large radii. The binding energy of the envelopes of such stars is thus low with respect to radiative counterparts, and it is thought that the envelope can therefore more easily be removed by an inspiraling companion, as recently emphasised by Klencki et al. (2021) and Marchant et al. (2021). Very massive stars typically do not grow to the dimensions needed to cool their envelope sufficiently to become unstable against convection. Even though some massive stars may manage develop a deep convective

envelope, they do not significantly expand further in radius (in contrast to less massive stars that will ascend the giant branch). Hence very massive stars generally fill their Roche lobe at an earlier point in their evolution, when the envelope was still radiative. Overall, the occurrence of successful CE is therefore very rare for such massive stars.

Thirdly, closely related to the second effect, mass transfer from high-mass donor stars is preferentially stable and hence it does not initiate a CE phase. This is especially true for radiative donors, as the early adiabatic response of radiative envelopes to mass loss is contraction (see, e.g. Hjellming & Webbink, 1987b). Recent studies, based on simulations with a more sophisticated treatment of the physics, tend to emphasize this finding, also for convective donors (e.g. Pavlovskii & Ivanova, 2015; Pavlovskii et al., 2017; Marchant et al., 2021). In addition, albeit more speculatively, this effect may be enhanced by the role of envelope inflation. This occurs in massive stars that are close to the Eddington limit. They can develop extended halos (e.g. Sanyal et al., 2015; Jiang et al., 2015, 2018). This can likely cause stable mass exchange before the star has really filled its Roche lobe. Although our simulations treat the stability criteria in a very simplified way, the recent studies mentioned above tend to strengthen our findings that mergers involving more massive BHs are unlikely from the CE channel.

We remind the reader that, in the CE channel, it is normally the second phase of mass transfer where the common envelope phase occurs, see Fig. 3.1. The considerations above thus primarily concern the initially less massive star in the binary system. In principle, it is possible to form BBH mergers with at least one heavy BH from binary systems with a very massive primary ($\gtrsim 60 M_{\odot}$) and significantly less massive secondary ($\lesssim 40 M_{\odot}$). The heavy BH then originates from the primary star, while the secondary star is of low enough mass to initiate a CE phase in which the envelope is ejected

successfully. However, we find that such systems are extremely rare. The secondary typically accretes during the first mass transfer phase and becomes massive enough to be subject to the first two effects mentioned above. This scenario thus only works for systems with extreme initial mass ratios. Such systems tend to merge upon the first mass transfer phase and will thus not be able to form BBHs that merge within a Hubble time.

Overall we find that the formation of BBHs with at least one heavy BH is not impossible through the CE channel, but very unlikely in our simulations. More detailed recent studies on partial aspects of the problem strengthen this finding.

3.3.2 Why the stable RLOF channel does not produce short delay times

We find that the stable RLOF channel leads to longer delay times than the CE channel, due to longer inspiral times. These longer inspiral times are caused by wider separations (larger semi-major axis) at BBH formation. We find that the median separation at BBH formation is about $7 R_{\odot}$ for systems that came from the CE channel, and about $20 R_{\odot}$ for systems that come from the stable RLOF channel, when considering all systems that can be observed by a ‘perfect detector’ (see Eq. 3.6). Wider separations lead to longer inspiral times because the orbital decay time from gravitational-wave emission scales with the fourth power of the separation (Peters, 1964). We find that the effect of the component masses and eccentricity of BBH systems are typically subdominant to the effect of the separation.

To understand why the CE channel produces shorter separations we consider the difference in orbital evolution for both channels. For stable mass transfer, whether the

orbit widens or shrinks depends on the mass ratio, the amount of mass lost from the system, and the assumed angular momentum that is carried away by the mass that is lost (e.g. Soberman et al., 1997). To produce merging BBH systems through stable RLOF we typically need to considerably shrink the orbit during reverse mass transfer (van den Heuvel et al., 2017). The accretor is already a BH at this time and its accretion is assumed to be limited to the Eddington accretion rate. This means that most of the mass that is transferred is lost from the system. For highly non-conservative mass transfer, the orbit shrinks (when $M_{\text{acc}}/M_{\text{donor}} \leq 0.79$, for which see e.g. Appendix A from van Son et al. 2020) under the assumption that mass is lost from the vicinity of the accreting companion and has the specific angular momentum of the accretor’s orbit. This criterion may be fulfilled when the secondary star fills its Roche lobe at first and lead to shrinking of the orbit, but as more mass is lost, the orbital evolution can reverse from shrinking to widening. In contrast, CE evolution exclusively shrinks the orbit in our simulations, in agreement with general expectation (e.g. Paczynski 1976, Ivanova et al. 2013b).

Even though many of the details regarding orbital shrinking are uncertain in both scenarios, these mechanisms are so different that we can robustly expect substantial differences in the resulting final separations. Since the separation is the dominant term in the expression for the inspiral time, we are confident that our finding that the two channels lead to a difference in their delay times is robust, at least qualitatively. For completeness, we show the delay times distributions, similar to Figure 3.2, but for all metallicities and integrated over $M_{\text{BH},1}$ in Appendix 3.10.

3.4 Method (II) : Calculating Intrinsic merger rates

To place our results into cosmological context we need to integrate over the metallicity-dependent star formation rate density, $\mathcal{S}(Z, z)$ (see also Dominik et al., 2013a, 2015a; Belczynski et al., 2016c; Mandel & de Mink, 2016; Chruslinska et al., 2018a). This results in an intrinsic BBH merger rate density, $R_{\text{BBH}}(z)$, that we will discuss in Sections 3.5.1 and 3.6. Throughout this work we adopt cosmological parameters consistent with the WMAP9–cosmology (Hinshaw et al., 2013) including $h = H_0 / (100 \text{ km s}^{-1} \text{ Mpc}^{-1}) = 0.693$, where H_0 is the Hubble constant.

3.4.1 Estimating the intrinsic BBH merger rate

We follow the method described in Neijssel et al. (2019) and Broekgaarden et al. (2021a) to calculate the BBH merger rate².

The number of detections that occur during the active observing time (T_{obs} , measured in the detector frame at $z = 0$) of an infinitely sensitive gravitational-wave detector is given by

$$\frac{d^2N_{\text{det}}}{d\zeta dz} = \frac{R_{\text{BBH}}(z, \zeta)}{d\zeta} \left[\frac{dV_c}{dz}(z) \right] \frac{T_{\text{obs}}}{1+z}, \quad (3.1)$$

where N_{det} is the number of detectable BBH mergers, ζ is the set of parameters that describe a BBH, and $\frac{dV_c}{dz}(z)$ is the differential co-moving volume per redshift (see e.g. Abbott et al., 2019c).

Our goal is to estimate the intrinsic merger rate density of all BBHs in the source

²The scripts to compute the rates are available as part of the COMPAS suite <https://github.com/TeamCOMPAS/COMPAS>.

frame, $R_{\text{BBH}}(z)$:

$$R_{\text{BBH}}(z) = \int d\zeta R_{\text{BBH}}(z, \zeta) = \frac{d^2 N_{\text{BBH}}}{dV_c dt}(z) [\text{cGpc}^{-3}\text{yr}^{-1}], \quad (3.2)$$

which is the number of mergers N_{BBH} per co-moving volume V_c in co-moving gigaparsec, cGpc^{-3} per year, with t the time in the source frame.

Often, we would like to evaluate the intrinsic rate density over larger redshift bins.

For that purpose, we define the volume averaged intrinsic merger rate density:

$$\bar{R}_{\text{BBH}}(z) = \frac{\int_{z_{\min}}^{z_{\max}} R_{\text{BBH}}(z) \frac{dV_c}{dz} dz}{\int_{z_{\min}}^{z_{\max}} \frac{dV_c}{dz} dz} [\text{cGpc}^{-3}\text{yr}^{-1}], \quad (3.3)$$

To approximate the intrinsic merger rate density at redshift z , we convolve the number of BBH mergers per unit star-forming mass with the star-formation rate density over the merger time $t_m(z)$, and integrate this over all metallicities:

$$R_{\text{BBH}}(z, \zeta) = \underbrace{\int dZ' \int_0^{t_{m(z)}} dt'_{\text{delay}}}_{\text{BBH formation rate}} \underbrace{\frac{d^2 N_{\text{form}}}{dM_{\text{SF}} dt_{\text{delay}}}(Z', t'_{\text{delay}}, \zeta) * \mathcal{S}(Z', z(t_{\text{form}}))}_{\text{Z-dependent SFRD}}, \quad (3.4)$$

where the time of merger, $t_m(z)$, delay time, t_{delay} , and formation time, t_{form} , are related by $t_{\text{form}} = t_m - t_{\text{delay}}$. We adopt the redshift of first star-formation $z_{\text{first SF}} = 10$ in our work. Equation 3.4 is evaluated at redshift steps of $dz = 0.001$.

Our choice for the metallicity-dependent star formation rate at the formation redshift, $\mathcal{S}(Z, z_{\text{form}}(t_{\text{form}}))$ is detailed and discussed in Appendix 3.11. $d^2 N_{\text{form}} / (dM_{\text{SF}} dt_{\text{delay}})$ is the number of BBH systems that form with delay times in the interval dt_{delay} per unit of star forming mass dM_{SF} . Because we model only a small fraction of the total

star forming mass, we need to re-normalise our results, given the initial distributions of primary masses and mass ratios (see §3.2.2). In our simulations we neglect single stars, only draw primary masses in the range $10 - 150 M_{\odot}$ and apply adaptive importance sampling. When re-normalising, we assume that the Universe has a constant binary fraction of $f_{\text{bin}} = 0.7$ (Sana et al., 2012), and stars are formed with initial masses in the range $0.1 - 200 M_{\odot}$.

3.5 The merger rates and mass function at different redshifts

3.5.1 The role of the two formation channels

In Figure 3.3 we show the averaged intrinsic merger rate density $\bar{R}_{\text{BBH}}(z)$, as a function of redshift, z , and per primary BH mass, $M_{\text{BH},1}$. We split the rate by channel, showing the CE and stable RLOF channel in the bottom row.

In the top panel, we see that the overall BBH merger rate density peaks around redshift $2 - 3$, and at a mass of about $15 M_{\odot}$ for the most massive BH. The merger rate decreases towards higher mass and higher redshift. Comparing the bottom two panels, we see that the CE channel and RLOF channel contribute to the rate in distinct ways.

We would like to quantify the relative contribution of each channel to the production of $M_{\text{BH},1}$. For this purpose we define the total rate of BBH mergers in the detector frame as:

$$\mathcal{R}^{\text{det}}(z, \zeta) = \frac{R_{\text{BBH}}(z, \zeta)}{1+z} \frac{dV_c}{dz}. \quad (3.5)$$

Integrating this from redshift zero to the redshift of first star formation, we obtain the

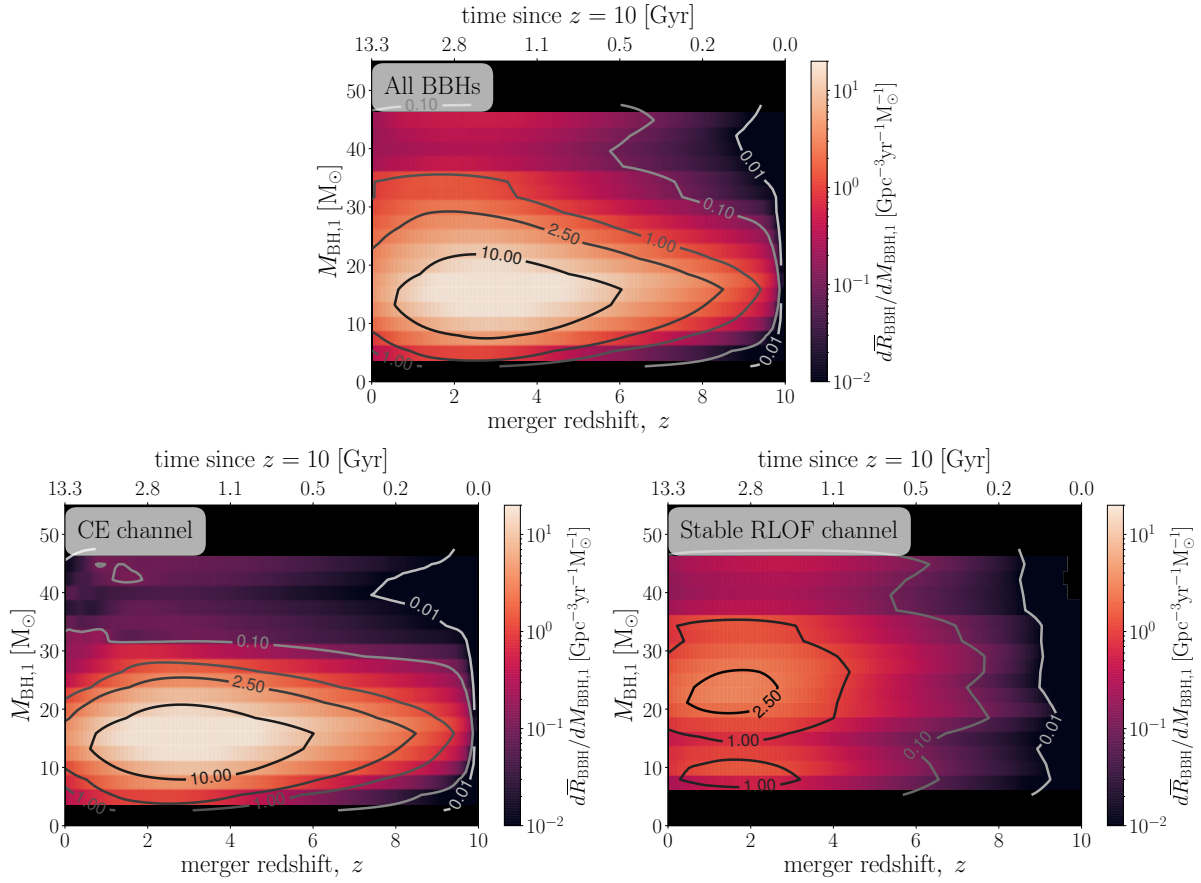


Figure 3.3: The averaged intrinsic merger rate density $\bar{R}_{\text{BBH}}(z)$, for redshift bins of $dz = 0.2$, and primary BH mass bins of $dM_{\text{BH},1} = 2.5 M_{\odot}$. The top axis shows the time passed since $z = 10$, which we have chosen as the redshift of first star formation. The top panel shows the full distribution. The bottom left panel shows mergers of systems that have experienced at least one CE during their evolution, while the bottom right shows mergers of systems that formed through the stable RLOF channel. All panels show a dearth of high mass BHs ($M_{\text{BH},1} \gtrsim 30 M_{\odot}$) merging at higher redshifts ($z > 6$).

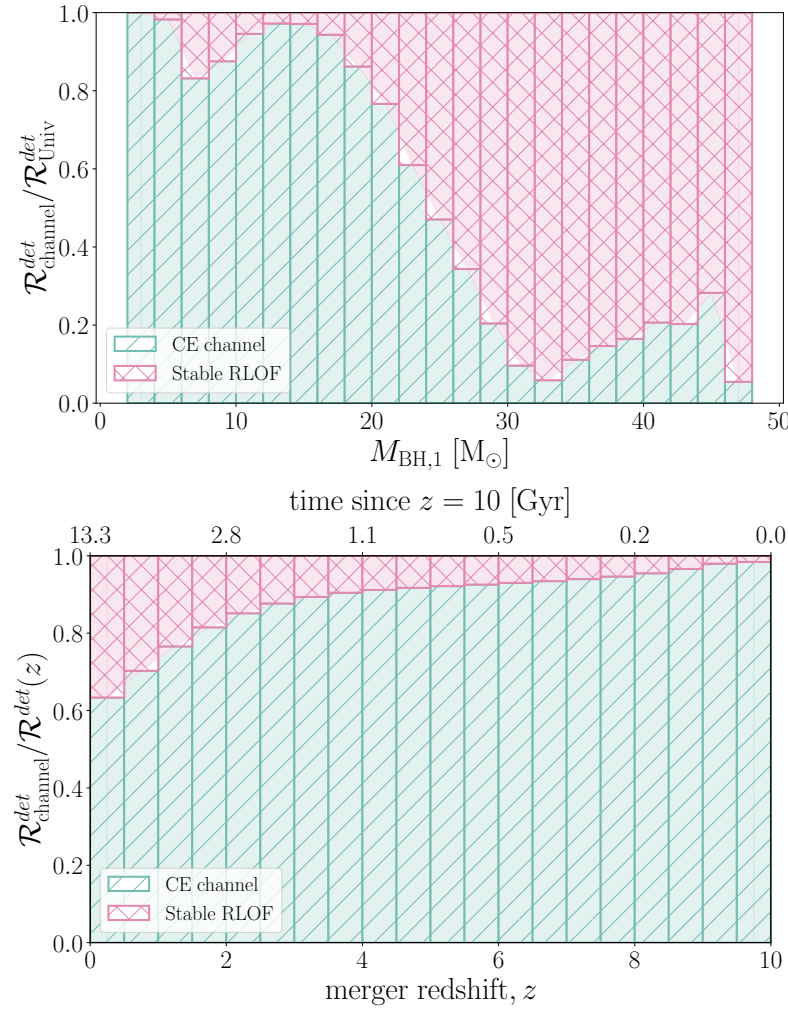


Figure 3.4: Fractional contribution of the CE channel (green hatched) and the stable RLOF channel (pink cross hatched) to $\mathcal{R}^{\text{det}}(z, \zeta)$. Top panel shows the relative contributions to $\mathcal{R}^{\text{det}}(z, \zeta)$ per mass bin after integrating over all redshifts. Bottom panel shows the fractional contribution to $\mathcal{R}^{\text{det}}(z, \zeta)$ integrated over all $M_{\text{BH},1}$, as a function of redshift.

total rate of BBH mergers throughout the Universe:

$$\mathcal{R}_{\text{Univ}}^{\text{det}}(\zeta) = \int_0^{z_{\text{first SF}}} dz \mathcal{R}^{\text{det}}(z, \zeta) \quad (3.6)$$

This is the same as the BBH merger rate as observed by an infinitely sensitive detector at redshift zero. In the top panel of Figure 3.4 we show what fraction of $\mathcal{R}_{\text{Univ}}^{\text{det}}(\zeta)$ derives from which channel for different values of $M_{\text{BH},1}$. This emphasizes how the stable RLOF channel dominates $\mathcal{R}_{\text{Univ}}^{\text{det}}(\zeta)$ at higher masses, while the CE channel dominates for primary BH masses below $25 M_{\odot}$.

The formation channels differ in how they contribute to the intrinsic merger rate density as a function of redshift. Specifically, the contribution of the stable RLOF channel decreases faster towards higher redshifts than the CE channel. As a result, the CE channel becomes increasingly dominant towards higher redshifts. To show this more clearly, we again integrate $\mathcal{R}^{\text{det}}(z, \zeta)$, but now over all $M_{\text{BH},1}$ to obtain $\mathcal{R}^{\text{det}}(z)$. We show what fraction of $\mathcal{R}^{\text{det}}(z)$ derives from which channel for different redshift bins in the bottom panel of Figure 3.4. Overall the CE channel is dominant, but the stable RLOF channel becomes more important at low redshift, and is responsible for about 40% of BBHs merging in the local Universe.

The reduced contribution of the stable RLOF channel at higher redshifts is a result of the scarcity of short delay times in this channel, as shown in Fig 3.2. Systems coming from the stable RLOF channel generally have delay times $\gtrsim 1$ Gyr. At redshift 6, only 0.5 Gyr has passed since our adopted redshift of first star formation ($z = 10$). This means that systems coming from the stable RLOF channel have typically not had enough time to merge at these high redshifts. For completeness, we show the distributions similar to Figure 3.3, but for chirp mass M_{chirp} in Appendix 3.12.

In Figure 3.5 we display the distribution of $M_{\text{BH},1}$ split by formation channel, for merger redshifts between 0 and 0.5 (see equation 3.3).

The results in Figure 3.5 imply that the high-mass merger events that have been detected so far at relatively low redshift, primarily come from the stable RLOF channel (assuming that the observed BBH merger rate is dominated by these two channels). This is in contrast to the results in, e.g., Belczynski et al. (2016a) and Stevenson et al. (2017), but agrees with findings in more recent work from e.g. Neijssel et al. (2019) and Gallegos-Garcia et al. (2021).

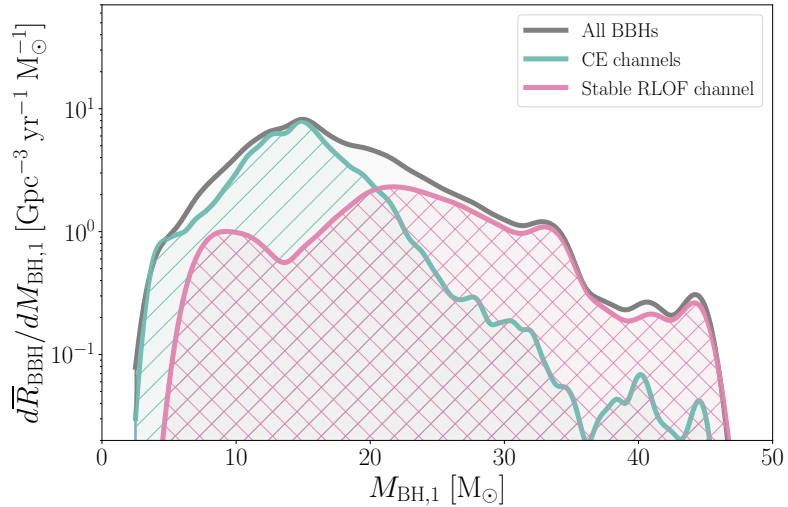


Figure 3.5: Distribution of primary BH masses $M_{\text{BH},1}$ split by formation channel, for merger redshifts between $0 \leq z < 0.5$.

3.5.2 The shape of the mass function at different redshifts.

In the top panel of Figure 3.6 we show the $M_{\text{BH},1}$ distribution for different redshift bins (again adopting the averaged intrinsic merger rate density $\bar{R}_{\text{BBH}}(z)$ for every redshift bin). We see that there are features of the mass distribution that persist in all redshift bins. Firstly, the peak of the distribution occurs at $\sim 18 \text{ M}_\odot$. From Figures 3.2 and 3.3 we find that this peak originates from the CE channel.

In every redshift bin, $\bar{R}_{\text{BBH}}(z)$ decays for BH masses above $\sim 18 M_{\odot}$. In part, the slope on the right side of $\sim 18 M_{\odot}$ is steepened due to the decay of the initial mass function towards higher mass stars. However, the primary driver behind the decay towards higher masses is the effect of metallicity: higher metallicities lead to more mass loss through stellar winds, and therefore shift the maximum possible $M_{\text{BH},1}$ to lower values. In Figure 3.7 we show this shift in the maximum BH mass by dissecting the $M_{\text{BH},1}$ distribution for $0 < z < 0.5$ into bins of different formation metallicities. This shows that the maximum BH mass is about $18 M_{\odot}$ in our simulations for the high metallicities ($Z \gtrsim 0.01$) that dominate the metallicity dependent star formation rate density, $\mathcal{S}(Z, z)$. For completeness, we show the $M_{\text{BH},1}$ distribution split by both formation channel and formation metallicity in appendix Figure 3.13. This shows that the stable RLOF channel dominates the higher mass end of the distribution at every metallicity.

The decay of the distribution for BH masses below $\sim 18 M_{\odot}$ in Figure 3.6, can be understood as a combination of our adopted SN kick and CE physics. Firstly, above carbon oxygen core masses of $M_{\text{CO}} = 11 M_{\odot}$, BHs are assumed to experience full fallback, and hence receive no kick. BHs from lower-mass progenitors are expected to receive higher SN kicks (given the adopted BH-kick prescription from Fryer et al., 2012). These higher SN kicks can unbind the binary system and thus prevent the formation of a merging BBH system (see also panels M, N and O in Figure 3.15).. Secondly, for the same change in orbital separation, lower-mass BHs can provide less orbital energy to help unbind the common envelope. This means that progressively lower-mass BHs will fail to eject their companion's envelope at a given CE efficiency α_{CE} . Increasing α_{CE} will allow successful CE ejection for lower-mass BHs, thus pushing the peak of the mass

distribution to lower-mass BHs (see also panels F-I Figure 3.15).

Apart from the peak in Figure 3.6, two other distinct features persist in all redshift bins. The first is the rise in $R_{\text{BBH}}(z)$ just before the edge of the distribution at $M_{\text{BH},1} \approx 45 M_{\odot}$. This feature is caused by the prescription for pair pulsations. Specifically, we adopted the prescriptions from Farmer et al. (2019) (see Section 3.2). This is also called the ‘pulsational pair-instability supernova’ (or PPISN) pile-up (e.g. Talbot & Thrane, 2018; Marchant et al., 2019). Secondly there is a bump at $M_{\text{BH},1} \sim 35 M_{\odot}$. This bump is an artefact of the transition between prescriptions for remnant masses from core collapse supernovae (CCSN, following Fryer et al., 2012), to remnant masses from pair pulsational instability supernovae (from Farmer et al., 2019). Though the bump in our results is an artificial feature, it is not clear that the transition between core-collapse supernovae and pair pulsational supernovae should be smooth. For example, Renzo et al. (2020b) argue that such a discontinuity can occur if convection is not efficient at carrying away energy for the lowest mass systems that experience pair pulsations. Furthermore, Abbott et al. (2021f) find evidence for an overdensity in the merger rate ($> 99\%$ credibility) at $M_{\text{BH},1} = 35^{+1.5}_{-3.1} M_{\odot}$. It is difficult to attribute this observed peak to the PPISN pile-up at the lower-edge of the PISN mass gap, since stellar models predict this pile-up to occur at masses of about $40 - 60 M_{\odot}$ (see e.g. Marchant et al., 2019; Farmer et al., 2019; Renzo et al., 2020a,b; Marchant & Moriya, 2020b; Woosley & Heger, 2021; Costa et al., 2021, and references therein).

To investigate redshift evolution of the primary BH mass distribution, in the bottom panel of Figure 3.6 we show the intrinsic distribution normalized by the peak rate for each redshift bin. We focus on redshifts in the range $0 < z \leq 2$, because a large absolute change in $R_{\text{BBH}}(z)$ is contained in this redshift range (see Figure 3.8), while the

contribution from different metallicities to $\mathcal{S}(Z, z)$ does not vary greatly up to $z \sim 1.5$. The bottom panel of Figure 3.6 shows that the high mass end ($M_{\text{BH},1} > 18 M_{\odot}$) decays faster at higher redshifts than the low mass end ($M_{\text{BH},1} \leq 18 M_{\odot}$) of the distribution. We find that the ratio of $M_{\text{BH},1} > 18 M_{\odot} / M_{\text{BH},1} \leq 18 M_{\odot}$ is about 0.7 in the redshift bin $0 - 0.5$, while it is about 0.45 in the redshift bin $1 - 1.5$. The steeper decay of the high mass end of the mass distribution for higher redshifts can be explained by the scarcer contribution of the stable RLOF channel (which is responsible for the high mass end of the mass distribution) towards higher redshifts, as discussed above in Section 3.5.1.

3.6 Prospects for observing trends with redshift in the intrinsic merger rate density

Third-generation detectors promise to probe BBH mergers across all redshifts of interest, but these instruments are still at least a decade away (e.g. Sathyaprakash et al., 2019a). Present-day detectors are, however, already beginning to probe the evolution at low redshift.

In the previous section we found evolution of the high-mass slope of the predicted $M_{\text{BH},1}$ distribution for redshifts in the range $0 - 2$. Since current ground based detectors already detect many systems with $M_{\text{BH},1} > 20 M_{\odot}$, it is possible to start probing this mass-specific redshift evolution of the merger rate $R_{\text{BBH}}(z)$ (Abbott et al., 2021e,f).

In this section we explore the possibility of probing trends of the rates separated by mass bin as a function of redshift. In Section 3.6.1 we show our predictions and in Section 3.6.2 we discuss whether these effects are observable in the second gravitational-wave transient catalogue (GWTC-2).

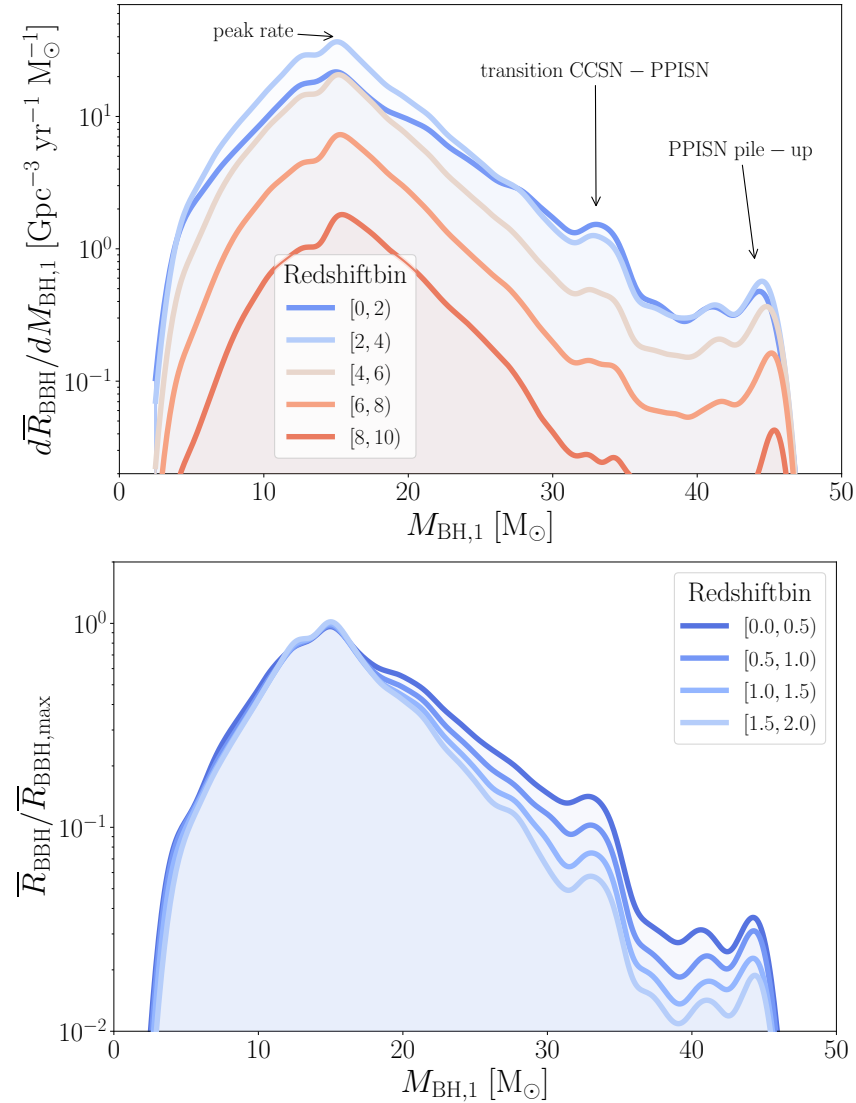


Figure 3.6: Distribution of primary BH masses $M_{\text{BH},1}$ for several redshift bins. The top panel shows the general trend for different redshift bins. The bottom panel shows the same distribution normalized by the peak rate value for the given redshift bin, with a focus on redshifts up to $z = 2$. Both distributions are shown down to $M_{\text{BH},1} = 2.5 M_{\odot}$, which is our minimum allowed BH mass. This shows that the distribution of primary BH masses evolves with redshift.

3.6.1 The slope of the intrinsic rates per mass bin at low redshift

In Fig. 3.8 we show how the intrinsic BBH merger rate density, $R_{\text{BBH}}(z)$, evolves as a function of redshift for four different $M_{\text{BH},1}$ mass bins. In each mass bin we have

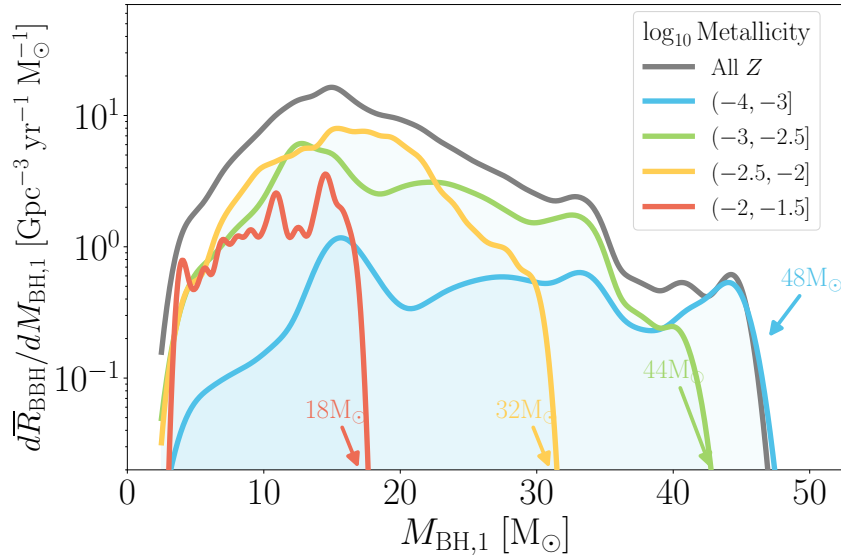


Figure 3.7: Breakdown of the $M_{\text{BH},1}$ mass distribution by birth metallicity for all BBH mergers between redshifts $0 \leq z < 0.5$. The maximum BH mass that contributes to each metallicity bin is annotated.

normalized the merger rate to the rate at redshift zero, to emphasize different trends at low redshifts. We see clear differences in the evolution of the rate at low redshift and the overall redshift evolution. These differences are highlighted by the orange lines, that show linear fits in the range $0 \leq z \leq 1$, with the slopes a_i provided in the legend.

For the lowest-mass BHs ($M_{\text{BH},1} \leq 10 M_{\odot}$ and $10 M_{\odot} \leq M_{\text{BH},1} \leq 20 M_{\odot}$), our models predict a steep increase of the BBH merger rate density with increasing redshift, with a slope that is very similar to the slope of $\text{SFRD}(z)/\text{SFRD}(z = 0)$. The peak of the merger rate of the lowest $M_{\text{BH},1}$ bin coincides with the peak of $\text{SFRD}(z)/\text{SFRD}(z = 0)$, as adopted in our models (at $z = 2.7$). The merger rate for slightly higher masses ($10 M_{\odot} \leq M_{\text{BH},1} \leq 20 M_{\odot}$), peaks at slightly higher redshifts, around $z = 2.8$. The redshift evolution of $R_{\text{BBH}}(z)/R_0$ follows the shape of $\text{SFRD}(z)/\text{SFRD}(z = 0)$ for these mass bins, because the lowest-mass events are formed predominantly through the CE channel, which produces short delay time systems. On top of this, these lower-mass

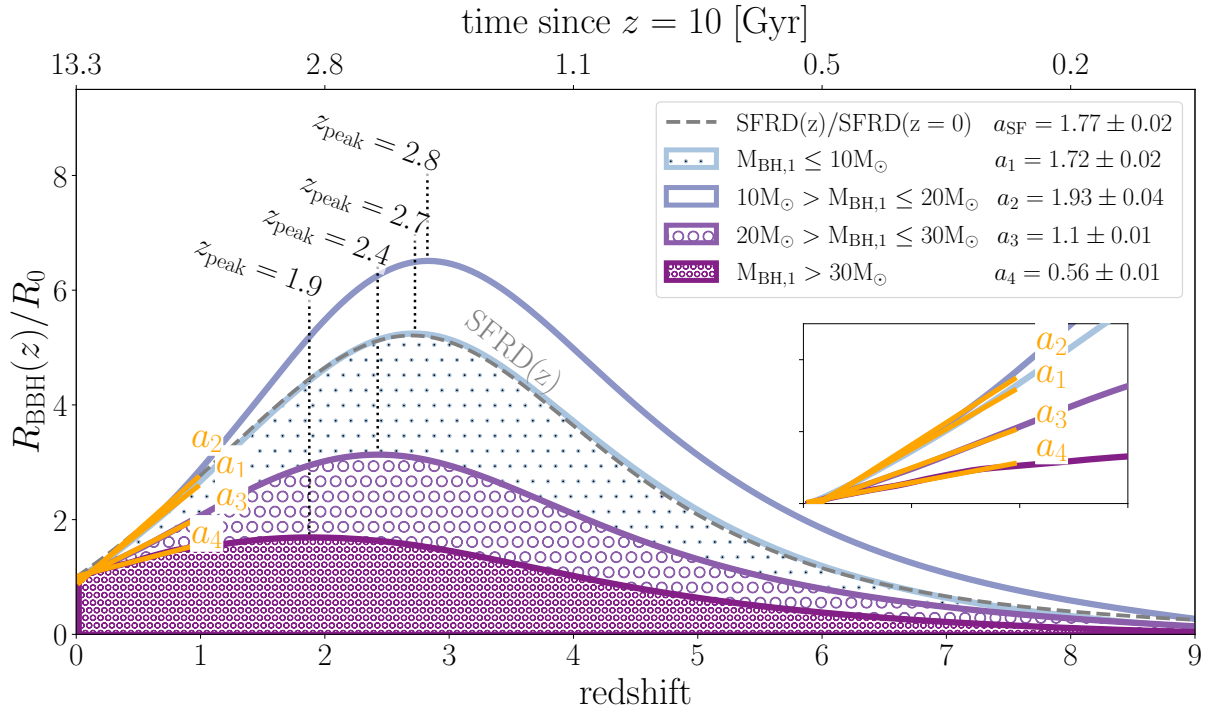


Figure 3.8: Intrinsic BBH merger rate density as a function of redshift, z ($R_{\text{BBH}}(z)$, Eq. 3.2), normalized by the rate at redshift zero (R_0), for several bins in primary BH mass. The top axis shows the time since $z = 10$, which we have chosen as the redshift of first star formation. The dashed grey line shows the star formation rate density as a function of redshift, $\text{SFRD}(z)$, normalized by the star formation rate density at redshift 0, $\text{SFRD}(z = 0)$. The redshift at which the merger rate density peaks is annotated with a dotted line for each mass bin. A linear fit to the merger rate density between $0 \leq z \leq 1$ is shown with an orange line for each mass bin (these are also highlighted in the inset). The respective slopes of these fits are annotated in the legend. This shows that, at low redshift, the slope of $R_{\text{BBH}}(z)$ is more shallow for higher $M_{\text{BH},1}$.

events can form from almost all metallicities, as opposed to the high-mass systems that only form from the lowest metallicities (see Figure 3.7).

In contrast, for BHs with masses in the range $20 M_{\odot} < M_{\text{BH},1} \leq 30 M_{\odot}$ we find that the evolution of the merger rate with redshift is much less steep in the low-redshift regime than the merger rate for lower-mass BHs. Moreover, the merger rate of these events starts to decline at redshift $z = 2.4$, lower than the redshift of peak SFRD(z). The rate density for the most massive BHs ($M_{\text{BH},1} > 30 M_{\odot}$) exhibits the flattest slope and peaks at the lowest redshift (at $z = 1.9$). In other words, in order to capture the peak of the BBH merger rate density for BHs with $M_{\text{BH},1} \gtrsim 30 M_{\odot}$ we need gravitational wave detectors that can observe out to redshift $z \sim 2$ (depending on the exact location of the peak of star formation). This peak at lower redshift can be understood from the characteristics of the stable RLOF channel, which is the primary producer of such massive events. As discussed in Sections 3.3 and 3.5, these events primarily form with long delay times. Hence, at progressively higher redshifts, the fraction of systems formed through the stable RLOF channel BBHs that can contribute to the merger rate decreases. The systems that don't contribute at higher redshift have not had sufficient time since the adopted moment of first star formation to merge as a BBH.

This implies that mergers of massive BHs are relatively less common at higher redshifts. This may at first sight seem counter intuitive, considering that at higher redshifts, the low metallicities that allow for the formation of massive BHs are more common (see Figure 3.7 and, e.g. Vink & de Koter, 2005; Belczynski et al., 2010; Spera et al., 2019b).

3.6.2 Observing the different slopes in GWTC-2

To test our prediction of a distinct redshift evolution for different $M_{\text{BH},1}$ as discussed in Section 3.6.1, we look for observational evidence of a different slope in $R_{\text{BBH}}(z)$ in the open data from the first, second, and half of the third observing runs of Advanced LIGO and Advanced Virgo (Abbott et al., 2021d), also presented in the gravitational-wave transient catalogues GWTC-2 (Abbott et al., 2021b) and GWTC-2.1 (Abbott et al., 2021g). To this end, we use the observed BBH mergers to hierarchically infer their underlying mass and spin distributions (e.g. Mandel et al., 2019).

Contrary to our predictions here, analyses of the BBH population typically assume that BBHs have independently distributed masses and redshifts, with $p(M_{\text{BH},1}, z) = p(M_{\text{BH},1})p(z)$. Here, we will explore several alternative models for the joint distribution $p(M_{\text{BH},1}, z)$ of BBH masses and redshifts. Our method closely follows that of Callister et al. (2021). We assume that the distribution of mass ratios $p(q|M_{\text{BH},1}, \gamma)$ follows a power-law with index γ and that the distribution of effective spins, $p(\chi_{\text{eff}}|\mu_\chi, \sigma_\chi)$, follows a Gaussian with mean μ_χ and variance σ_χ (Roulet & Zaldarriaga, 2019; Miller et al., 2020).

For primary masses and redshifts, we take as a baseline the POWERLAW + PEAK model from Abbott et al. (2021e), with an overall merger rate that is allowed to evolve as a function of z :

$$\frac{dN_{\text{BBH}}}{dt d M_{\text{BH},1} dz} = R_0 \frac{dV_c}{dz} (1+z)^\kappa \left[f_p P(M_{\text{BH},1} | \lambda, m_{\max}) + (1-f_p) N(M_{\text{BH},1} | \mu_m, \sigma_m, m_{\max}) \right]. \quad (3.7)$$

Here, the assumed primary mass distribution is a mixture between a power law $P(M_{\text{BH},1} | \lambda, m_{\max}) \propto M_{\text{BH},1}^\lambda$ (for $M_{\text{BH},1}$ between $5 M_\odot$ and m_{\max}) and a Gaussian peak

$N(M_{\text{BH},1} | \mu_m, \sigma_m, m_{\text{max}})$, with mean μ_m and variance σ_m , which is needed to fit an observed excess of BBHs with primary masses near $M_{\text{BH},1} \approx 35 M_\odot$. R_0 is the local rate of BBH mergers per co-moving volume at $z = 0$.

We inspect several variations of this model in an attempt to identify any relationship between BBH masses and their redshift distribution.

First, we expanded Eq. 3.7 such that the parameter κ , governing the BBH rate evolution, is a function of $M_{\text{BH},1}$. We considered several possibilities, including a piecewise function cut at $30 M_\odot$,

$$\kappa(M_{\text{BH},1}) = \begin{cases} \kappa_{\text{low}} & (M_{\text{BH},1} < 30 M_\odot) \\ \kappa_{\text{high}} & (M_{\text{BH},1} \geq 30 M_\odot), \end{cases} \quad (3.8)$$

a piecewise function in which the cut location m_{cut} itself varies as a free parameter,

$$\kappa(M_{\text{BH},1} | m_{\text{cut}}) = \begin{cases} \kappa_{\text{low}} & (M_{\text{BH},1} < m_{\text{cut}}) \\ \kappa_{\text{high}} & (M_{\text{BH},1} \geq m_{\text{cut}}), \end{cases} \quad (3.9)$$

and a case in which κ is a linear function of $M_{\text{BH},1}$:

$$\kappa(M_{\text{BH},1} | \kappa_0, \kappa') = \kappa_0 + \kappa' \left(\frac{M_{\text{BH},1}}{30 M_\odot} - 1 \right). \quad (3.10)$$

In Fig. 3.8, we also saw that dR_{BBH}/dz is not a strictly monotonic function of mass. Instead, this slope reaches a maximum in the range $10 M_\odot < M_{\text{BH},1} \leq 20 M_\odot$, below which it again decreases. To capture this possibility, we additionally considered a *three-bin* piecewise model,

$$\kappa(M_{\text{BH},1}) = \begin{cases} \kappa_{\text{low}} & (M_{\text{BH},1} < 10 M_\odot) \\ \kappa_{\text{mid}} & (10 M_\odot \geq M_{\text{BH},1} < 30 M_\odot) \\ \kappa_{\text{high}} & (M_{\text{BH},1} \geq 30 M_\odot), \end{cases} \quad (3.11)$$

We do not consider more complex models, given the relative scarcity of the data available at the time of writing. In all four cases above, we find no evidence for a varying redshift distribution as a function of mass.

As mentioned above, the BBH primary mass distribution in GWTC-2 is well-modelled as a mixture between a broad power law and an additional peak between 30 to $35 M_{\odot}$. As an alternative test, we allow the rates of BBHs comprising the broad power law and those situated in the peak to each evolve independently as a function of redshift:

$$\frac{dN_{\text{BBH}}}{dt d M_{\text{BH},1} dz} = \frac{dV_c}{dz} \left[R_0^{\text{pl}} (1+z)^{\kappa_{\text{pl}}} P(M_{\text{BH},1} | \lambda, m_{\max}) + R_0^{\text{peak}} (1+z)^{\kappa_{\text{peak}}} N(M_{\text{BH},1} | \mu_m, \sigma_m, m_{\max}) \right], \quad (3.12)$$

in which R_0^{pl} and R_0^{peak} are the local merger rate densities of BBHs in the power law and peak, respectively, with κ_{pl} and κ_{peak} governing the redshift evolution of each rate. We find very marginal evidence that the BBH mergers comprising these two components obey different redshift distributions; we measure $\kappa_{\text{pl}} = 2.7^{+3.2}_{-3.5}$ and $\kappa_{\text{peak}} = 0.7^{+4.0}_{-5.8}$, with $\kappa_{\text{peak}} < \kappa_{\text{pl}}$ for about 70% of the posterior samples. However, our large uncertainties mean we cannot draw any conclusions about differing rate evolution (or lack thereof).

We conclude that we find insufficient evidence in GWTC-2 ([Abbott et al., 2021b](#)) for a distinct redshift evolution of $R_{\text{BBH}}(z)$ for different $M_{\text{BH},1}$. This is consistent with [Fishbach et al. \(2021\)](#), who find no strong evidence in GWTC-2 that the BBH mass distribution evolves with redshift. Specifically, they find that the detections in GWTC-2 are consistent with a mass distribution that consists of a power law with a break that does *not* evolve with redshift, as well as with a mass distribution that includes a sharp maximum mass cutoff, if this cutoff *does* evolve with redshift. Furthermore, [Fishbach & Kalogera \(2021\)](#) found no strong evidence for the time delay distribution to evolve

with mass. They did find a mild preference for high mass ($M_{\text{BH},1} \sim 50 M_{\odot}$) BBH to prefer shorter delay times than the low mass ($M_{\text{BH},1} \sim 15 M_{\odot}$) BBH systems. However, they also argue that this preference could be an effect of higher mass BHs forming more strictly at the lowest metallicities (which is consistent with our findings in Figure 3.7). Alternatively, these high mass mergers with masses of about $50 M_{\odot}$ could be probing hierarchical mergers.

At the time of writing, finding evidence for a distinct redshift evolution in GWTC-2 is difficult, considering that observed BBHs with lower mass primary BH masses ($M_{\text{BH},1} \sim 10 M_{\odot}$) only probe the very local Universe ($z \lesssim 0.4$). As can be seen from Figure 3.8, this redshift range encompasses only a small fraction of the BBH merger rate evolution. Given the prospects of observing BBH mergers out to increasingly high redshifts with Advanced LIGO, Advanced Virgo and KAGRA (Abbott et al., 2018b), second- (Voyager Adhikari et al., 2020), and third-generation detectors like the Einstein telescope (Punturo et al., 2010; Hild et al., 2011; Sathyaprakash et al., 2019b; Maggiore et al., 2020) and the Cosmic Explorer (Abbott et al., 2017a; Reitze et al., 2019) we expect our predicted different evolution of the BBH merger rate to be either confirmed or disproven within the coming decades.

3.7 Discussion

In the previous sections we showed our prediction that the mass distribution of merging BBH systems varies with redshift. Specifically, we showed that the evolution of the merger rate with redshift, $R_{\text{BBH}}(z)$, is more shallow and peaks at lower redshifts for systems with higher primary BH masses compared to systems with lower primary BH masses. This difference is the result of the contribution of two different

formation channels. The CE channel predominantly forms lower mass BBH systems ($M_{\text{BH},1} \lesssim 30 M_{\odot}$) and allows for very short delay times ($t_{\text{delay}} < 1 \text{ Gyr}$). In contrast, the stable RLOF channel is the main source of massive systems ($M_{\text{BH},1} \gtrsim 30 M_{\odot}$) and primarily forms systems with longer delay times ($t_{\text{delay}} \gtrsim 1 \text{ Gyr}$).

The quantitative predictions presented in this work are subject to several major uncertainties and we discuss the key ones in the remainder of this section. Throughout this section we also argue why we expect our qualitative findings to be robust.

3.7.1 The relative contribution of the CE and stable RLOF channel

The prediction that merging BBHs can be formed through both the CE and stable RLOF channels has been reported by various groups (e.g. van den Heuvel et al., 2017; Bavera et al., 2021a; Marchant et al., 2021; Broekgaarden et al., 2021a; Gallegos-Garcia et al., 2021; Shao & Li, 2021; Olejak et al., 2021a). However, the relative contribution of both channels is uncertain. This is mainly due to uncertainties in the treatment of stability of mass transfer, and whether or not the ejection of a common envelope is successful (Ivanova et al. 2013b, Ivanova et al. 2020, and references therein).

Recent work by e.g. Pavlovskii et al. (2017), Klencki et al. (2021), Marchant et al. (2021) and Gallegos-Garcia et al. (2021) have questioned whether the CE channel plays a prominent role, based on results obtained with the 1D detailed binary evolutionary code MESA (Paxton et al., 2015). They argue that systems that are typically assumed to lead to successful CE ejection in rapid population synthesis simulations (such as ours), will instead fail to initiate and survive a common envelope phase. If true, this would potentially drastically reduce the relative contribution of the CE channel. This would

have major implications for the field and implies that the contribution of the CE channel is over estimated in our work.

Despite all off the above, it seems unlikely that the CE channel does not operate at all. Various compact binary systems containing double white dwarfs and double neutron stars exist, which are hard to all explain through other formation channels (Rebassa-Mansergas et al., 2007, 2012; Nebot Gómez-Morán et al., 2011; Ivanova et al., 2013b). As long as the CE channel plays a non-negligible role, we believe that at least our qualitative conclusions will hold.

3.7.2 Are the delay time and mass distributions of the two channels distinguishable?

Although the detailed shape of the delay time and mass distributions are uncertain, we believe that our finding that these two channels lead to distinct delay time distributions is robust for the following reasons.

The first reason is that the CE channel and stable RLOF channel lose angular momentum through intrinsically different mechanisms as explained in Section 3.3.2. Because of this, it is reasonable to expect a difference in the distributions of final separations and thus inspiral times. In fact, fine tuning would be required to avoid significant differences. Similar arguments can be made for the mass distribution (see e.g. Dominik et al., 2012; Eldridge & Stanway, 2016; Bavera et al., 2021a; Gallegos-Garcia et al., 2021).

To better understand the impact of our (uncertain) model assumptions on the resulting delay time and mass distributions we have analysed the suite of models

presented in Broekgaarden et al. (2021b) (see Appendix 3.14). A relative lack of high mass BHs with short delay times was found in all model variations. Furthermore, we find significant differences in the delay-time and mass distributions for the two channels for almost all variations.

Exceptions concern the models where we assume high values for the CE ejection efficiency α_{CE} (panels H and I in Figure 3.14). In these simulations the number of short delay-time systems resulting from the CE channel is reduced (for $\alpha_{\text{CE}} = 2$) or disappear entirely (for $\alpha_{\text{CE}} = 10$). The latter assumption results in delay-time distributions for the CE and RLOF channel that are practically indistinguishable, but we consider such high efficiencies unrealistic.

The distinction in the $M_{\text{BH},1}$ distribution diminishes in the models where a fixed accretion efficiency during stable Roche-lobe overflow involving two stellar companions is considered, $\beta = 0.25$ and $\beta = 0.5$, where β denotes the fraction of the mass lost by the donor that is accreted by the companion (see panels B and C in Figure 3.14). In these models, we find that the RLOF channel is less efficient in producing BBH mergers, especially in the case of systems with high-mass $M_{\text{BH},1}$. We still find significant differences in the delay times between the two channels, but the RLOF and CE channel can no longer be clearly distinguished in the $M_{\text{BH},1}$ distribution. While the mass accretion efficiency is an important uncertainty in our simulations, we do not believe that assuming a fixed accretion efficiency is realistic.

3.7.3 Alternative observables to distinguish the two channels

We are not able to directly observe whether a BBH was formed through the CE channel or the stable RLOF channel. Hence we need characteristic observable source

properties to expose the distinct rate evolution. In this work we have focused on BH mass as this can be inferred relatively well from observations. Possible other observables that could be used are the distribution of the BH spins, the secondary masses, and the mass ratio.

Mass ratios In the top panel of Figure 3.9 we show our predictions for the distribution of mass ratios as seen by a hypothetical perfect detector (equation 3.6), which are very different for both channels. The CE channel preferentially produces systems with unequal masses ($q_{\text{final}} \approx 0.3$) but the distribution is broad and spans from $0.2 \lesssim q_{\text{final}} \lesssim 1$. In contrast, we find that the stable RLOF channel predominantly forms merging binaries with $0.6 \lesssim q_{\text{final}} \lesssim 0.8$ in our simulation. The distinct shape of this distribution is the result of the requirement of the stability of mass transfer, the total-mass to core-mass relation, the mass transfer efficiency (see Appendix 3.9 for an analytical derivation of the low q_{final} end). The clear difference in the two distributions is promising, but we note that at the time of writing the mass ratios inferred for the detected systems are typically not well constrained (e.g. Abbott et al., 2021c).

Secondary masses The distribution of secondary masses, $M_{\text{BH},2}$, is shown in the bottom panel of Figure 3.9. The CE channel dominates the formation of low secondary BH masses $M_{\text{BH},2} < 15 M_{\odot}$, while the stable RLOF channel dominates in the range $15 M_{\odot} < M_{\text{BH},2} < 40 M_{\odot}$. The reason for this is the same as discussed in Section 3.3.1. The CE channel dominates again for the highest secondary mass BHs ($36 M_{\odot} < M_{\text{BH},2} < 46 M_{\odot}$). The contribution of the stable RLOF drops quickly here due to a lack of equal mass systems and the PISN mass limit of about $46 M_{\odot}$. We caution not to over interpret the features of the highest mass BHs as the uncertainties in the

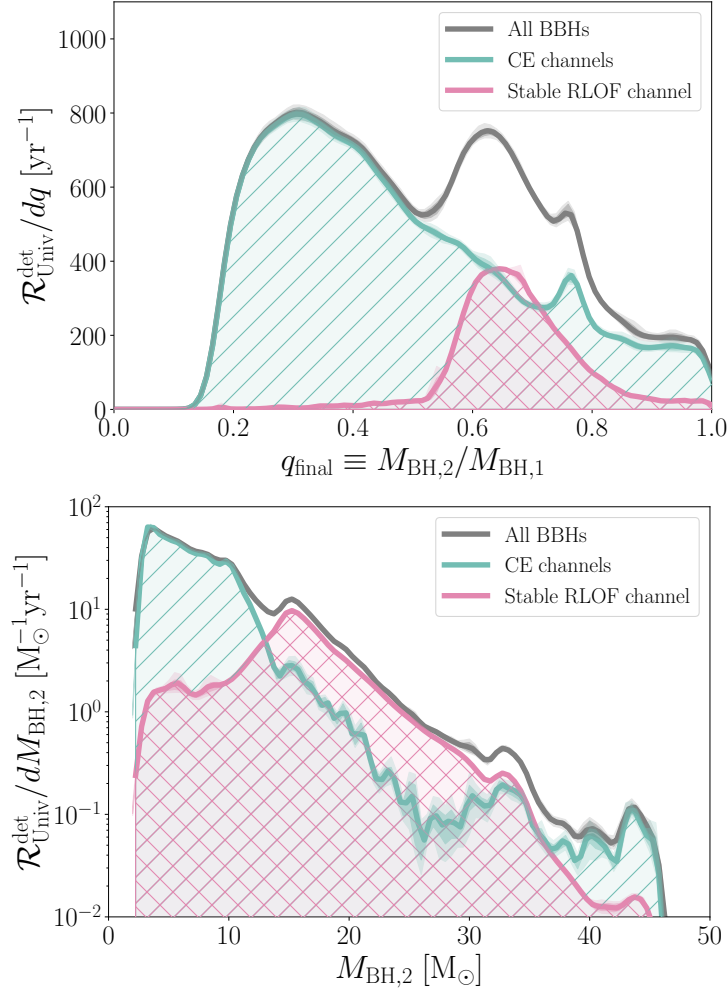


Figure 3.9: Distributions of mass ratios, q_{final} , and secondary masses, $M_{\text{BH},2}$, for BBHs seen by a hypothetical perfect detector ($\mathcal{R}_{\text{Univ}}^{\text{det}}(\zeta)$, equation 3.6). Each panel shows the distribution for all systems in grey, the stable RLOF channel in cross hatched pink, and the CE channel in line hatched green. The dark and light shaded areas shows the 1- and 2- σ sampling uncertainties respectively, obtained through bootstrapping.

evolution of the progenitor systems are the largest here.

Spins Gravitational wave observations provide constraints on the mass weighted effective spin, χ_{eff} and for some events on the individual spin magnitudes and their orientation. The constraints on the spin have been suggested as a promising diagnostic to distinguish formation scenarios (e.g. [Kushnir et al., 2016](#); [Hotokezaka & Piran, 2017](#); [Zaldarriaga et al., 2018](#))

Our simulations do not provide predictions for the spin, but [Bavera et al. \(2020\)](#) showed that, in case of the CE channel, the post-CE separation may well be small enough to allow for tidal spin up of the He core that is the progenitor of the second born BH (e.g. [Bavera et al., 2020](#); [Mandel & Fragos, 2020](#)). In the case of the stable RLOF channel, final separations are expected to be too wide for tidal spin-up (e.g. [Bavera et al., 2021a](#)), but one might expect spin-up of the first born BH through mass transfer (e.g. [Bardeen, 1970](#)), although this is matter of debate. In case of Eddington limited accretion, spin up may not be significant ([Bavera et al., 2021a](#)). In the case of super-Eddington accretion it remains unclear whether one can significantly spin up the accreting BH (e.g. [Tchekhovskoy et al., 2012](#)) and in this case the orbit widens preventing the formation of a GW source ([van Son et al., 2020](#)). Furthermore, large uncertainties remain in the angular momentum transport of massive stars, which makes it difficult to accurately translate stellar spins to BH spins (see e.g. [Fuller et al. 2015](#), [Olejak & Belczynski 2021](#) and [Steinle & Kesden 2021](#) for a discussion of possible pathways to spinning BHs from the isolated binary channel).

3.7.4 The uncertain metallicity dependent cosmic star formation history

In general, variations in the assumed $\mathcal{S}(Z, z)$ have a large impact on $R_{\text{BBH}}(z)$, and the shape of the BH mass distribution (e.g. Chruslinska et al., 2018a; Neijssel et al., 2019; Broekgaarden et al., 2021b; Briel et al., 2021). Because the highest mass BHs can only form from the lowest metallicities (see Figure 3.7), the stable RLOF channel will only play a significant role in the BBH merger rate if there is sufficient star formation at low metallicity, and the stable RLOF systems have had enough time to coalesce since this low metallicity star formation.

To test the effect of the $\mathcal{S}(Z, z)$ on our main results, we repeated our complete analysis while adopting the phenomenological model from Neijssel et al. (2019). This $\mathcal{S}(Z, z)$ forms fewer stars at low metallicity ($Z < 0.01$) for the majority of our simulated star-forming universe, but forms a significantly larger amount of low-metallicity stars at the highest redshifts. Because this model is very sharply peaked around the mean metallicity at each redshift there is almost no star formation at low metallicities for all redshifts lower than $z \approx 1$. In contrast, in our fiducial model we adopt a skewed distribution to capture the tail of low metallicity star formation at low redshifts.

With this $\mathcal{S}(Z, z)$, we still retrieve the distinct redshift evolution for different BH mass bins, similar to the trends discussed in Sections 3.5 and 3.6 . Specifically we find a steep positive slope for $R_{\text{BBH}}(z)$ between $0 < z < 1$ for BBHs with $M_{\text{BH},1} < 20 M_{\odot}$, and a more shallow slope for BBHs with $M_{\text{BH},1} \geq 20 M_{\odot}$. This causes the high mass end ($M_{\text{BH},1} \gtrsim 20 M_{\odot}$) of the $M_{\text{BH},1}$ mass distribution to decay faster at higher redshifts than the low-mass end ($M_{\text{BH},1} \lesssim 18 M_{\odot}$) of the distribution. This is in line with Neijssel

et al. (2019), who also found evidence for evolution of the BBH mass distribution with redshift.

Our estimate of the total intrinsic BBH merger rate is $R_0 = 73 \text{ Gpc}^{-3}\text{yr}^{-1}$ at redshift zero, and $R_{0.2} = 94 \text{ Gpc}^{-3}\text{yr}^{-1}$ at $z = 0.2$. Although this rate prediction is not an outlier in the recent review of local BBH merger rate predictions for isolated binaries from Mandel & Broekgaarden (2022), it is a factor 2-5 higher than the most recent estimates from the LIGO/Virgo/Kagra collaboration ($R_{0.2} = 17.3 - 45 \text{ Gpc}^{-3}\text{yr}^{-1}$, Abbott et al., 2021f). Our setup and binary physics assumptions are similar to those in Neijssel et al. (2019), who predict a local rate of $R_0 \approx 22 \text{ Gpc}^{-3}\text{yr}^{-1}$. The difference in our rate prediction stems from our updated prescription for the metallicity-dependent star-formation rate density as described above, $\mathcal{S}(Z, z)$ (see also Appendix 3.11).

Although we acknowledge the large uncertainties in $\mathcal{S}(Z, z)$, we note that if we are sufficiently confident in the delay time distributions of observed BBH mergers, the redshift evolution of the BBH merger rate can be used to measure the star formation rate with gravitational waves (Vitale et al., 2019a). Therefore, detecting evolution in the BH mass distribution as described in Section 3.6 could help us constrain $\mathcal{S}(Z, z)$ through gravitational waves.

3.7.5 Further caveats of rapid population synthesis

All uncertainties that apply to rapid population synthesis simulations also apply to this work (see e.g. Ablimit & Maeda, 2018; Belczynski et al., 2022a; Broekgaarden et al., 2021b). Above, we already discussed the main uncertainties related to mass transfer stability and the treatment of common envelope phases. Below, we highlight further known shortcomings and uncertainties that are expected to impact our quantitative

predictions

A major uncertainty for the evolution of massive stars concerns internal mixing and, specifically, mixing beyond the boundaries of the convectively unstable regions. This directly impacts the core masses. In our simulations we use prescriptions from [Hurley et al. \(2000\)](#) that are fitted against models by [Pols et al. \(1997\)](#). For stars with initial masses higher than $50 M_{\odot}$ these fits are extrapolated. The core masses in our simulations turn out to be substantially smaller than those predicted in more recent grids of detailed evolutionary models that were calibrated against observations (e.g. [Brott et al., 2011](#)). Overall, we expect that our core masses for high mass stars to be underestimated (as is true for all simulations that apply the original Hurley formulae). This will affect the quantitative predictions for the BH mass, and mass ratio distributions. This includes our predictions for the maximum BH mass that is efficiently formed through the CE channel ($\sim 30 M_{\odot}$ in this work).

The post-supernova remnant mass, including the amount of fallback, is uncertain. In particular, stars that retain a significant fraction of their envelope up to the moment of core collapse have been hypothesised to produce massive BHs if the envelope is assumed to entirely fall back onto the newly formed BH (e.g. [Fernández et al., 2018; Di Carlo et al., 2019, 2020a](#)). This way, relatively low mass stars ($M_{\text{ZAMS}} \lesssim 40 M_{\odot}$) that are expected to more easily lead to successful CE events (following our arguments as stated in Section 3.3.1), can still form high BH masses ($M_{\text{BH},1} \gtrsim 30 M_{\odot}$, [Di Carlo et al., 2019, 2020a,b; Kremer et al., 2020](#)). However, for red supergiant stars, the envelope is expected to be sufficiently loosely bound that the change in gravitational mass due to neutrino losses when a core collapses likely unbinds the envelope ([Nadezhin, 1980; Lovegrove & Woosley, 2013; Adams et al., 2017](#)). Complete fallback is expected only for blue and

yellow supergiants (Fernández et al., 2018; Ivanov & Fernández, 2021). Moreover, in this work we only study isolated binaries, which are not able to form BBH progenitors that merge within the age of the Universe without the system transferring or losing angular momentum as a consequence of mass transfer. Mass transfer, whether stable or unstable (CE) leads to significant mass loss in our simulations. Therefore, we find that forming merging BBHs with a massive primary BH through the fallback of a hydrogen envelope only works if there is an external mechanism that brings the BH progenitors closer together.

Lastly, in this work we have assumed a universal initial mass function (IMF). However, recent studies suggest that the IMF might be more top-heavy at low metallicity (e.g. Geha et al., 2013; Martín-Navarro et al., 2015; Schneider et al., 2018; Gennaro et al., 2018). Although uncertainties in the IMF can have a large impact on rate predictions (de Mink & Belczynski, 2015a; Chruścińska et al., 2021), to first order, we expect to still retrieve a distinct redshift evolution, $R_{\text{BBH}}(z)$ for low and high mass BHs because the existence of the CE channel and stable RLOF channel is not affected by IMF changes. A full study of the effect of a non-universal IMF is outside the scope of this paper.

3.7.6 Contribution from other formation channels

In this work, we focus on predictions from the isolated binary channel. However, the observed population of merging BBHs is most likely a mixture of several channels (Zevin et al., 2021; Wong et al., 2021a). The variety of physics involved is vast, and hence the span of predictions for merging BBH properties is equally large. See also Mapelli (2021) and Mandel & Farmer (2022a) for reviews of proposed formation channels, and Mandel &

Broekgaarden (2022) for a review of predictions for the merger rates from said formation channels. Below we summarise findings for other formation channels, with an emphasis on delay-time predictions, the slope of $R_{\text{BBH}}(z)$, and the predicted mass distribution (see also, Fishbach & Kalogera 2021 for an overview of delay time predictions from several different formation channels).

Two formation channels which exhibit a preference for the formation of more massive BBHs are chemically-homogeneous evolution (CHE; e.g. de Mink et al., 2009; Song et al., 2013, 2016b; Mandel & de Mink, 2016; Marchant et al., 2016; Riley et al., 2021) and Population III binaries (e.g. Marigo et al., 2001; Belczynski et al., 2004; Kinugawa et al., 2014; Inayoshi et al., 2017). Riley et al. (2021) find that CHE binaries have quite short delay times (between 0.1 – 1 Gyr), causing the redshift evolution of $R_{\text{BBH}}(z)$ to be fairly similar between CHE binaries and the full population of isolated binaries. du Buisson et al. (2020) furthermore find that the intrinsic BBH merger rate from CHE binaries evolves less steeply at low redshift than their adopted SFRD. Ng et al. (2021) compare the intrinsic BBH merger rate density from formation in isolated binaries and dynamical formation in globular clusters, to predictions for BBH mergers formed from Population III stars. They find that Population III remnants should result in a secondary peak of $R_{\text{BBH}}(z)$ around $z \approx 12$ (beyond what we have adopted as the redshift of first star formation).

Several formation channels have been proposed where the BBH merger is assisted by dynamical encounters. These include BBH formation in nuclear star clusters (e.g. Antonini et al., 2016; Petrovich & Antonini, 2017; Antonini et al., 2019b; Arca Sedda et al., 2020b; Arca Sedda, 2020; Fragione & Silk, 2020), globular clusters (e.g. Downing et al., 2010; Bae et al., 2014; Askar et al., 2017; Fragione & Kocsis, 2018; Rodriguez et al.,

2019b) and young stellar clusters (e.g. Portegies Zwart & McMillan, 2000b; Mapelli et al., 2013; Ziosi et al., 2014; Mapelli et al., 2017; Bouffanais et al., 2019; Fragione & Banerjee, 2021). For globular clusters, Choksi et al. (2019) find a merger rate that is weakly increasing out to $z = 1.5$ and drops at higher redshift. This behaviour is driven by dynamical processes within the cluster, which introduce a significant delay between cluster formation and BBH mergers.

Recent studies aim to compare the redshift evolution of the intrinsic BBH merger rate between different formation channels. Zevin et al. (2021) investigate the local source properties for the CE channel, stable RLOF channel, globular clusters and nuclear clusters. Their Figure 1 shows evidence that the stable RLOF channel preferentially forms higher chirp masses than the CE channel. Mapelli et al. (2022) compare the rate evolution of the intrinsic BBH merger rate from isolated binaries to the rate from nuclear star clusters, globular star clusters and young stellar clusters. They find that the primary BH mass function is more top heavy at high redshift for both globular and nuclear star clusters. In contrast to our work, they find that the mass distribution from isolated binaries does not vary greatly with redshift, because the majority of systems in their isolated binary channel is formed through CE, which results in short delay times. However, the mass distribution of isolated binaries in their Figure 5 appears to contain fewer primary BH masses of $\gtrsim 20 M_{\odot}$ at redshift 4 relative to redshift 0 (although this effect is smaller than the variation with redshift that they retrieve for nuclear and globular clusters).

Lastly, AGN disks (e.g. Baruteau et al., 2011; Bellovary et al., 2016; Leigh et al., 2018; Yang et al., 2019a; Secunda et al., 2019; McKernan et al., 2020), and mergers in hierarchical systems assisted by dynamical interactions (e.g. Kimpson et al., 2016;

(Antonini et al., 2017b; Rodriguez & Antonini, 2018; Hoang et al., 2018) have also been proposed as promising formation channels for BBH mergers.

At the time of writing, the estimates for the relative contribution of formation channels are highly uncertain. However, linking source properties to predictions for the rate evolution with redshift, such as in this work, could help distinguish between the many possible origins of merging BBH systems.

3.8 Conclusions and summary

We discuss the implications of relations between the delay time and BH mass for BBH systems that originate from isolated binaries. We explore the origin of these relations by dividing our simulations into two main formation channels: BBH systems that have experienced at least one common envelope (the ‘CE channel’) and systems that did not experience a CE, i.e. that only experienced stable Roche-lobe overflow (the ‘stable RLOF channel’). We discuss how our findings affect the redshift evolution of the BBH mass distribution. Specifically, we find a distinct redshift evolution of the BBH merger rate, $R_{\text{BBH}}(z)$, for different primary BH masses, $M_{\text{BH},1}$. Below we summarise our main findings.

The CE channel predominantly forms BBH systems with masses $M_{\text{BH},1} \lesssim 30 M_\odot$ and typically short delay times ($t_{\text{delay}} < 1 \text{ Gyr}$) The CE channel typically leads to shorter separations at BBH formation than the stable RLOF channel. This causes on average shorter inspiral times and thus shorter delay times (Figure 3.2). The CE channel does not form more massive BHs, because the massive progenitor stars required for these BH masses experience less radial expansion and stronger winds with respect to their lower mass counter parts. This results in conditions

that are ill-favoured for successful common-envelope initiation and ejection.

The stable RLOF channel generally forms BBH systems with longer delay times ($t_{\text{delay}} \gtrsim 1$ Gyr) and it is the main source of BBH systems with $M_{\text{BH},1} \gtrsim 30 M_{\odot}$. The stable RLOF channel primarily produces larger separations at BBH formation than the CE channel, which result in longer delay times. Because high mass stars are ill-favoured for successful common-envelope initiation and ejection, the highest mass BHs are almost exclusively formed through the stable RLOF channel.

The redshift evolution of the intrinsic BBH merger rate density is different for low and high $M_{\text{BH},1}$ Due to the relations between the delay time and BH mass, we find distinctly different slopes in the BBH merger rate density $R_{\text{BBH}}(z)$ for different mass ranges of $M_{\text{BH},1}$ (see Figure 3.8). The merger rate density of the lowest mass BHs ($M_{\text{BH},1} \leq 20 M_{\odot}$) is dominated by the CE channel. For these BH masses, the merger rate density has a slope at low redshift that is similar to the slope of the star formation rate. The merger rate density of the highest mass BHs ($M_{\text{BH},1} \geq 30 M_{\odot}$) is dominated by the stable RLOF channel. These higher mass systems have relatively longer delay times ($t_{\text{delay}} > 1$ Gyr), causing the rate density to peak at lower redshift than the peak of the star formation rate. We find that in the low-redshift regime that current detectors probe, the evolution of the merger rate density is less steep for higher-mass $M_{\text{BH},1}$ than for lower-mass BHs.

Although we cannot find significant evidence for this relation in the observed data at the time of writing, if isolated binaries contribute significantly to the BBH merger rate density, we expect that the distinct redshift evolution of the intrinsic merger rate density for different BH masses will be verifiable with near-future detectors (see Section 3.6.2).

The contribution of different formation channels to $R_{\text{BBH}}(z)$ varies with redshift. While the CE channel dominates the production of merging BBHs in the Universe, we predict that almost half of the systems we see merging at redshift 0 come from the stable RLOF channel (Figure 3.4). Conversely, in the high redshift Universe, the contribution to $R_{\text{BBH}}(z)$ from the stable RLOF channel will be negligible.

Acknowledgements

We thank Charlie Conroy and Eva Laplace for useful discussions and support. We thank Will Farr for his suggestion to investigate trends in the rate per mass bin and Maya Fishbach for discussing the impact of the results at an early stage. The authors thank Lokesh Khandelwal for his invaluable work on STROOPWAFEL. The authors are furthermore grateful for stimulating conversations with and Katie Breivik and members of the BinCosmos, COMPAS, CCA-GW and MPA stellar groups. LvS performed portions of this study as part of the remote pre-doctoral Program at the Center for Computational Astrophysics of the Flatiron Institute, supported by the Simons Foundation. LvS and SdM also acknowledge KITP for hospitality. The authors acknowledge partial financial support from the National Science Foundation under Grant No. (NSF grant number 2009131 and PHY-1748958).”, the Netherlands Organisation for Scientific Research (NWO) as part of the Vidi research program BinWaves with project number 639.042.728 and the European Union’s Horizon 2020 research and innovation program from the European Research Council (ERC, Grant agreement No. 715063). IM is partially supported by the Australian Research Council (ARC) Centre of Excellence for Gravitational-wave Discovery (OzGrav), project number CE170100004. IM is the recipient of the ARC Future Fellowship FT190100574. This research has made use of

NASA’s Astrophysics Data System Bibliographic Services.

Software and Data

The data used in this work is available on Zenodo under an open-source Creative Commons Attribution license at [doi:10.5281/zenodo.5544170](https://doi.org/10.5281/zenodo.5544170).

Simulations in this paper made use of the [COMPAS](#) rapid binary population synthesis code (v02.19.04), which is freely available at <http://github.com/TeamCOMPAS/COMPAS> (Riley et al., 2022b). The data used in Appendix 3.14 is described in Broekgaarden et al. (2021b) and is publically available at <https://zenodo.org/record/5651073>. The authors use the adaptive importance sampling tool STROOPWAFEL from Broekgaarden et al. (2019), publicly available at <https://github.com/lokiysh/stroopwafel>.

This research has made use of GW data provided by the Gravitational Wave Open Science Center (<https://www.gw-openscience.org/>), a service of LIGO Laboratory, the LIGO Scientific Collaboration and the Virgo Collaboration. LIGO Laboratory and Advanced LIGO are funded by the United States National Science Foundation (NSF) as well as the Science and Technology Facilities Council (STFC) of the United Kingdom, the Max-Planck-Society (MPS), and the State of Niedersachsen/Germany for support of the construction of Advanced LIGO and construction and operation of the GEO600 detector. Additional support for Advanced LIGO was provided by the Australian Research Council. Virgo is funded, through the European Gravitational Observatory (EGO), by the French Centre National de Recherche Scientifique (CNRS), the Italian Istituto Nazionale di Fisica Nucleare (INFN) and the Dutch Nikhef, with contributions by institutions from Belgium, Germany, Greece, Hungary, Ireland, Japan, Monaco, Poland, Portugal, Spain.

Further software used in this work: Python ([Van Rossum & Drake, 2009](#)), Astropy ([Astropy Collaboration et al., 2013a, 2018a](#)) Matplotlib ([Hunter, 2007](#)), NumPy ([Harris et al., 2020](#)), SciPy ([Virtanen et al., 2020](#)), `ipython/jupyter` ([Perez & Granger, 2007](#); [Kluyver et al., 2016](#)), Seaborn ([Waskom, 2021](#)) and hdf5 ([Collette et al., 2019](#)).

3.9 Appendix: Inspecting mass ratios

Below we derive the typical minimum mass ratio of a BBH that forms through the stable RLOF channel, as a function of the uncertain assumptions that go into our population synthesis. We will refer to the star that is more (less) massive at zero-age main sequence (ZAMS) as the primary (secondary) and with the subscript A (B). See Figure 3.1 for a cartoon example of a stable RLOF system, including a short definition of the symbols as used in this section.

3.9.1 First mass transfer: from the primary to the secondary

Since the primary star is more massive, it will evolve on a shorter timescale than the secondary and thus it will be the first to overflow its Roche Lobe. The donor (primary star) typically starts RLOF either at the end of its main sequence, or during H-shell burning, also known as Case A or early Case B mass transfer. We will focus on Case B mass transfer (post core H burning) because, due to the large radial expansion, this is most common case of mass transfer (e.g. [Sana et al., 2012](#)). During this phase of stable mass transfer, the primary star will donate at most its envelope to the secondary star. We neglect all mass loss due to winds in this simple approximation. We capture the mass transfer efficiency in the parameter β , where $\beta = 0$ implies no mass is accreted, while $\beta = 1$ implies the complete envelope of the primary is accreted by the secondary.

The mass of the secondary after completion of the first mass transfer phase becomes:

$$\begin{aligned}\tilde{M}_B &= M_{\text{ZAMS},B} + \beta M_{\text{env},A} = M_{\text{ZAMS},A} \cdot q_{\text{ZAMS}} + M_{\text{ZAMS},A} \cdot \beta(1 - f_{\text{core}}) \\ &= M_{\text{ZAMS},A} \cdot (q_{\text{ZAMS}} + \beta(1 - f_{\text{core}})),\end{aligned}\quad (3.13)$$

where $q_{\text{ZAMS}} \equiv M_{\text{ZAMS},B}/M_{\text{ZAMS},A}$, and we assume a fraction f_{core} of the stellar mass is used to form the He core. We implicitly assume the core mass fraction of star A and star B are similar, i.e. $f_{\text{core},A}/f_{\text{core},B} \approx 1$.

The primary star will continue to evolve and ultimately form a BH. For the purpose of this argument, we assume the complete core mass of the primary goes into forming the BH mass, i.e.

$$M_{\text{BH},a} = M_{\text{ZAMS},A} \cdot f_{\text{core}}. \quad (3.14)$$

3.9.2 Second mass transfer: from the secondary to the primary

When the secondary star ends core-H burning, it will swell up in size and, in our case, start stable mass transfer. The second phase of mass transfer is highly non-conservative, since accretion onto the BH is assumed to be Eddington limited. Therefore, $M_{\text{BH},a}$ remains approximately the same, and $M_{\text{BH},b}$ will be approximately;

$$M_{\text{BH},b} = \tilde{M}_B f_{\text{core}}, \quad (3.15)$$

where we again assume that the complete He core mass is used to form the BH mass.

3.9.3 Final mass ratio

We find that for the stable channel, $M_{\text{BH},b}$ typically forms the more massive BH, because in most cases star B accretes a significant fraction of its companion's envelope, making it more massive than the primary at ZAMS. Hence, we define the typical final mass ratio at BBH formation as:

$$q_{\text{final}} \equiv \frac{M_{\text{BH},a}}{M_{\text{BH},b}} \approx q_{\text{BBH}}. \quad (3.16)$$

Using Equations 3.14 and 3.15 we find

$$q_{\text{BBH}} = \frac{M_{\text{ZAMS,A}}}{\tilde{M}_B} = \frac{1}{(q_{\text{ZAMS}} + \beta(1 - f_{\text{core}}))}. \quad (3.17)$$

We find that in our simulations, core mass fractions range between about 0.33 and 0.43. To minimise equation 3.17 we further need to maximise $q_{\text{ZAMS}} = 1$ and $\beta = 1$. Hence we find $\min(q_{\text{final}}) \approx 0.60 - 0.64$. This agrees broadly with the location of the drop in the distribution of mass ratios that we find in our simulations below around $q_{\text{final}} \approx 0.6$, shown in Fig. 3.9. Understanding the right hand side of the mass ratio distribution is more involved. It is set in part by the requirement that the systems shrinks sufficiently during the second mass transfer, but also by mass transfer efficiency itself.

For illustration, we also show a typical example system in Figure 3.10. This system started with $M_{\text{ZAMS},1} \approx 90 M_\odot$ and $M_{\text{ZAMS},2} \approx 70 M_\odot$ and ends with $M_{\text{BH},a} = 36 M_\odot$ and $M_{\text{BH},b} = 43 M_\odot$, hence $q_{\text{final}} \approx 0.84$.

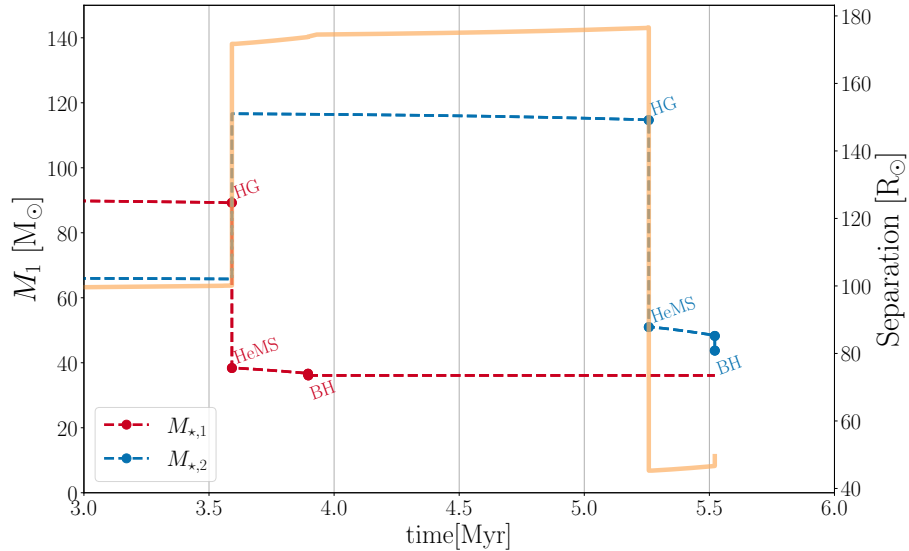


Figure 3.10: Masses (dashed lines, left y-axis) and binary orbital separation (solid yellow line, right y-axis) over time, for a typical BBH progenitor system that evolved through the stable RLOF channel. Transitions to different evolutionary stages are labelled with the following acronyms: HG for Hertzsprung Gap star, HeMS for He Main Sequence star and BH for Black Hole.

3.10 Appendix: Delay time distributions

We emphasize the bimodality in the delay time distribution by plotting the number of merging BBHs per $\log t_{\text{delay}}$ in the top panel of 3.11. This is similar to Figure 3.2, but integrated over all BH masses. For completeness, we also show the same distribution, but per t_{delay} (i.e. not in log space).

3.11 Appendix: Metallicity-dependent star formation rate $\mathcal{S}(Z, z)$

Several recent studies have highlighted the importance of the choice of the metallicity dependent cosmic starformation rate density $\mathcal{S}(Z, z)$ and the impact on the

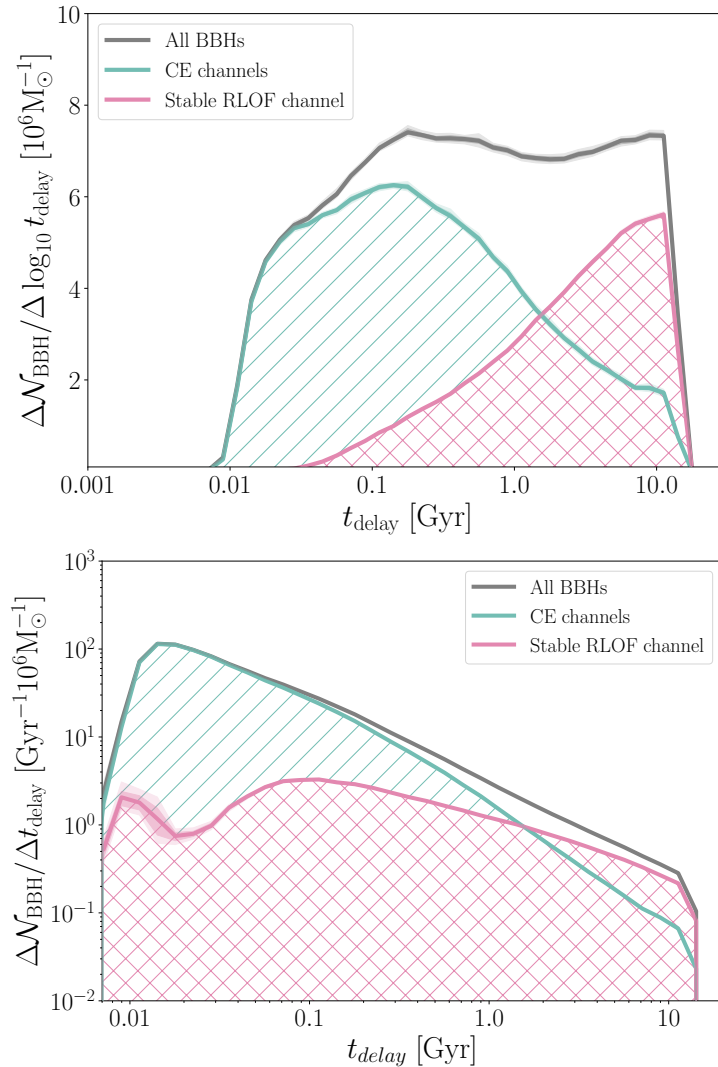


Figure 3.11: Similar to Figure 3.2, but integrated over $M_{\text{BH},1}$. The solid line shows the centres of the histogram per $d \log_{10} t_{\text{delay}}$ (top panel) versus the histogram per dt_{delay} (bottom panel), with bin sizes that are equal size in log-space ($d \log_{10} t_{\text{delay}} = 0.1$), and hence unequal size in t_{delay} . Both are normalized per $10^6 M_{\odot}$ of star forming mass. This histogram contains a mixture of birth metallicities, that were sampled uniformly in log. The dark and light shaded areas shows the 1- and 2- σ bootstrapping uncertainties respectively. We indicate the stable RLOF channel with pink cross hatched lines, and the CE channel with green line hatches.

final predictions (e.g. Chruścińska et al., 2019; Chruścińska & Nelemans, 2019a; Neijssel et al., 2019; Broekgaarden et al., 2021b; Briel et al., 2021).

For the metallicity dependent starformation history assumed in this work we use the

IllustrisTNG simulations. This is a suite of large magneto-hydrodynamical cosmological simulations computed with the moving-mesh code Arepo (Springel, 2010; Pakmor et al., 2016; Weinberger et al., 2020). The simulations follow the formation and evolution of galaxies from high redshift to the current time and solve for the evolution of dark matter and gas under the influence of feedback from star formation and supermassive blackholes (for details see Springel et al., 2018; Marinacci et al., 2018; Nelson et al., 2018; Pillepich et al., 2018a; Naiman et al., 2018).

The simulations were originally calibrated against the observed total cosmic star formation rate density and the stellar mass function of galaxies (Pillepich et al., 2018b). They reproduce the evolution of the sizes of galaxies with redshift (Genel et al., 2018) and with observational constraints on the mass-metallicity relation of galaxies up to $z = 2$ (Torrey et al., 2019) as well as iron abundances (Naiman et al., 2018) and the metallicity gradients within galaxies at low redshift (Hemler et al., 2021). These simulations have also already been used to make predictions for gravitational wave sources through pairing with predictions for the outcomes of binary evaluation obtained with the BPASS code Briel et al. (2021).

We extract the amount of starformation ongoing at each redshift and metallicity in the IllustrisTNG100 simulations and use this to derive the metallicity cosmic starformation rate density, $\mathcal{S}(Z, z)$. For this we make use of an analytical fit inspired by Neijssel et al. (2019), but adapted to better capture the asymmetry in the metallicity distribution as detailed in Van Son et al. (in prep.). For the simulations presented in

this work we use

$$S(Z, z) = \underbrace{a \frac{(1+z)^b}{1 + [(1+z)/c]^d}}_{(1) \text{ SFRD}(z)} \underbrace{\frac{2}{Z} \phi\left(\frac{\ln Z - \xi(z)}{\omega(z)}\right) \Phi\left(\alpha \frac{\ln Z - \xi(z)}{\omega(z)}\right)}_{(2) \text{ dP/dZ}(Z, z)} [\text{M}_\odot \text{yr}^{-1} \text{cMpc}^{-3}] \quad (3.18)$$

where the first term (1) governs the overall starformation rate density SFRD(z), as a function of redshift z (following the analytical form proposed by [Madau & Dickinson, 2014](#)). The second term (2) governs the metallicity distribution at each redshift, we approximate this with a skewed log-normal distribution written as the product of the standard log-normal distribution, ϕ , and the cumulative distribution function of the standard log-normal distribution, Φ ([O'Hagan & Leonard, 1976](#)). For the width of the distribution we assume $\omega(z) = \omega_0 \cdot 10^{\omega_z \cdot z}$. We furthermore ensure that mean of the metallicity distribution has the following simple dependence on redshift $\langle Z \rangle \equiv \mu(z) = \mu_0 \cdot 10^{\mu_z \cdot z}$ by setting

$$\xi(z) = \frac{-\omega(z)^2}{2} \ln\left(\frac{\mu_0 \cdot 10^{\mu_z \cdot z}}{2\Phi(\beta\omega(z))}\right) \quad \text{where} \quad \beta = \frac{\alpha}{\sqrt{1+\alpha^2}}. \quad (3.19)$$

This leaves us in total with nine free parameters which are fitted simultaneously. In this work we have used $a = 0.02$, $b = 1.48$, $c = 4.45$, $d = 5.9$, $\alpha = -1.77$, $\mu_0 = 0.025$, $\mu_z = -0.048$, $\omega_0 = 1.125$, and $\omega_z = 0.048$ (c.f. Van Son et al. in prep).

We note that our approach differs from the approach taken in some earlier studies that use observed scaling relations to construct a prescription for the metallicity dependent cosmic star formation history, for example as proposed by [Langer & Norman \(2006a\)](#). Unfortunately, the observational constraints are scarce at high redshift, where simple extrapolations may not be valid. This is problematic for gravitational wave sources, which preferentially form from low metallicity star formation which is most poorly constrained, especially at high redshift (cf. [Chruścińska et al., 2021](#)).

We have therefore opted instead to make use of current state-of-the-art cosmological simulations (see also [Briel et al., 2021](#), for a discussion). These provide physically motivated predictions at high redshift and have by now been extensively compared with observational constraints at lower redshift. Despite the large remaining uncertainties in these simulations, we believe this to be our best option at current times.

3.12 Appendix: The redshift dependence of the merger rate as a function of chirp mass

In Figure 3.12 we show the same evolution of $R_{\text{BBH}}(z)$ per primary BH mass, in the merger redshift – $M_{\text{BH},1}$ plane as displayed in Figure 3.3, but as a function of chirp mass, M_{chirp} . We observe similar trends in the BBH merger distribution when we investigate M_{chirp} instead of $M_{\text{BH},1}$. Specifically, BBH mergers with high chirp mass ($M_{\text{chirp}} > 20 M_{\odot}$) originate predominantly from the stable RLOF channel, while the CE channel dominates the BBH merger rate for low chirp mass ($M_{\text{chirp}} \leq 20 M_{\odot}$).

3.13 Appendix: Mass distribution split by formation channel and metallicity

In Figure 3.13 we show the $M_{\text{BH},1}$ distribution split by both formation channel and formation metallicity. We apply the same metallicity bins as those in Figure 3.7, but exclude the highest metallicity bin to focus on metallicities low enough to form BHs with masses above $20 M_{\odot}$. This shows that the stable RLOF channel dominates the high mass end of the distribution at every metallicity.

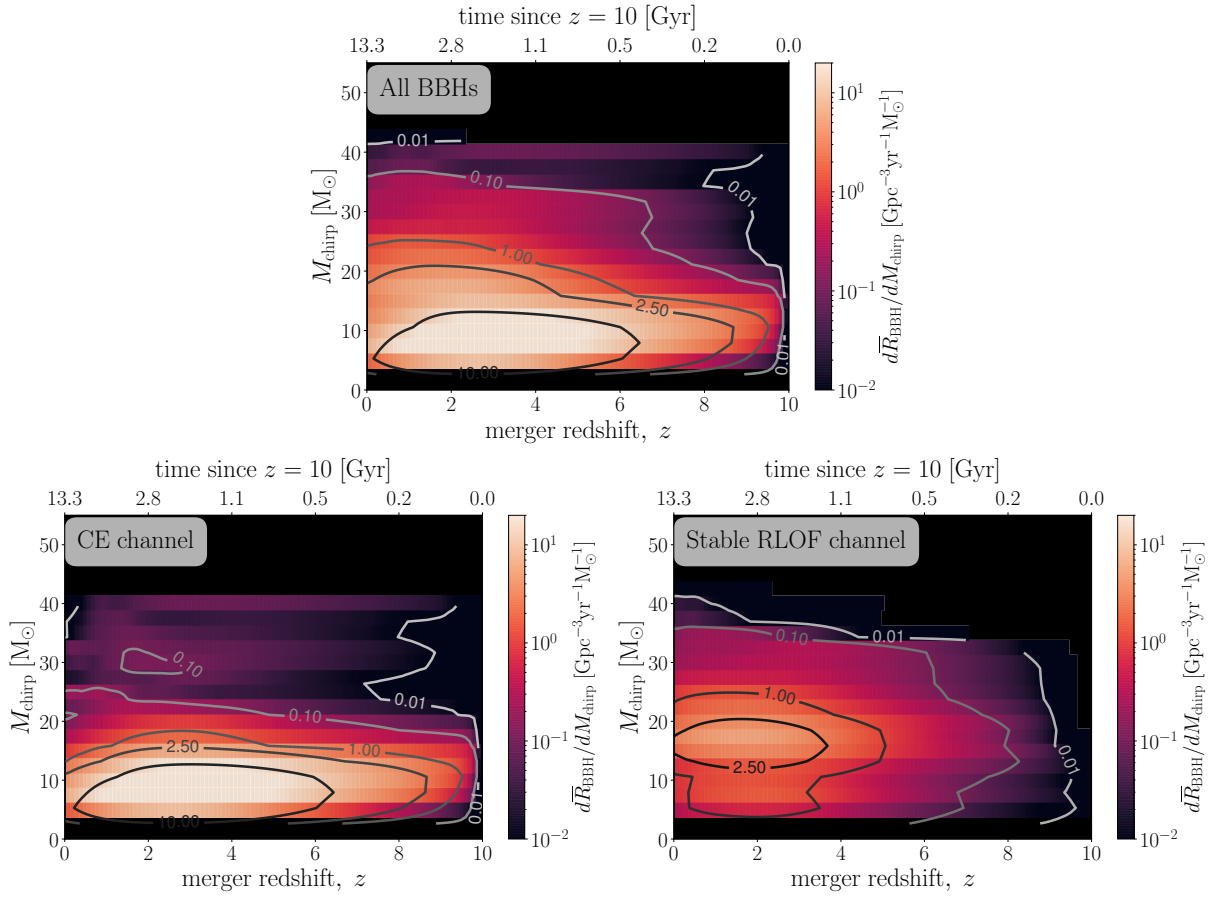


Figure 3.12: The averaged intrinsic merger rate density $\bar{R}_{\text{BBH}}(z)$, for redshift bins of $dz = 0.2$, and chirp mass bins of $dM_{\text{chirp}} = 2.5 M_{\odot}$. The colours and symbols are the same as in Figure 3.3.

3.14 Appendix: Physics variations

To test the robustness of our finding that the CE channel and stable RLOF channel lead to distinct distributions in delay time and primary BH mass, we use the grid of models presented in Broekgaarden et al. (2021a) and Broekgaarden et al. (2021b). These simulations were performed with a version of **COMPAS** that predates the publicly available code (most similar to version 02.13.01 of the publicly available code).

In Figures 3.14, 3.15, and 3.16, we show the distribution of primary BH mass

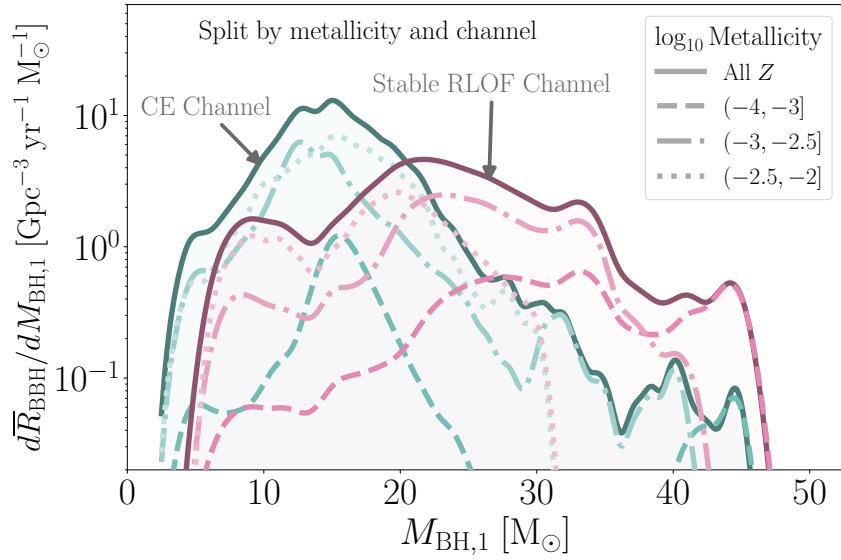


Figure 3.13: Distribution of primary BH masses $M_{\text{BH},1}$ split by formation channel and birth metallicity, for merger redshifts between $0 \leq z < 0.5$.

($M_{\text{BH},1}$) and delay time (t_{delay}) similar to Figure 3.2. Each panel in these Figures displays a separate simulation of 53×10^6 binaries. The fiducial model in this grid (panel A in Figure 3.14) adopts physics assumptions that are very similar to our model assumptions as described in Section 3.2. The exceptions are the PPISN prescription (which follows Marchant et al., 2019), the metallicity sampling (which uses a discrete grid of 53 metallicities between $10^{-4} - 0.03$), and the LBV wind prescription (LBV-type stars, that is, stars above the Humphreys-Davidson limit, are assumed to receive an *additional* wind mass loss of $10^{-4} \text{ M}_{\odot} \text{yr}^{-1}$, inspired by Belczynski et al., 2010).

Each panel in Figures 3.14, 3.15 and 3.16 considers a physics variation with respect to the fiducial model in panel A. The variations are summarised in the caption of each Figure, and for a full description of the physics assumptions we direct the reader to Broekgaarden et al. (2021a) and Broekgaarden et al. (2021b).

Figures 3.14, 3.15 and 3.16 show that the dearth of BBH systems with high mass

($M_{\text{BH},1} > 30 M_{\odot}$) and short delay time ($t_{\text{delay}} \lesssim 1 \text{ Gyr}$) is quite robust over numerous physics variations. Moreover, as discussed in Section 3.7, we retrieve distinct BH-mass and delay-time distributions for the two channels in almost all variations. The exceptions are the models which assume a fixed value for the accretion efficiency β of 0.25 and 0.5 for episodes of mass transfer with a non-compact accretor (panels B and C in Figure 3.14), and the model which assumes a high value for the CE “efficiency parameter” ($\alpha_{\text{CE}} = 2$ and $\alpha_{\text{CE}} = 10$; panels H and I in Figure 3.14). Those variations in the accretion efficiency β diminish the contribution of the stable RLOF channel, and specifically reduce the production of high-mass $M_{\text{BH},1}$. This removes the distinction between the channels in the $M_{\text{BH},1}$ distribution. Assuming $\alpha_{\text{CE}} = 10$ causes all the short delay-time systems from the CE channel to disappear. This is because at higher α_{CE} , a BH needs to inspiral less deeply into its companion’s envelope to achieve envelope ejection. This results in wider post-CE separations and hence more similar delay-time distributions for the two channels.

Figure 3.14 (following page): Same as Figure 3.2 but for several variations in the assumed model physics, based on models presented in Broekgaarden et al. (2021a) and Broekgaarden et al. (2021b). The models in each panel are as follows. Panel A: the fiducial model (see text). Panels B, C, and D: fixed mass-transfer efficiency of $\beta = 0.25, 0.5$, and 0.75 respectively. Panel E: case BB mass transfer is assumed to be always unstable. Panels F, G, H, I: the CE efficiency parameter, α_{CE} , is set to $0.1, 0.5, 2.0$, and 10.0 respectively.

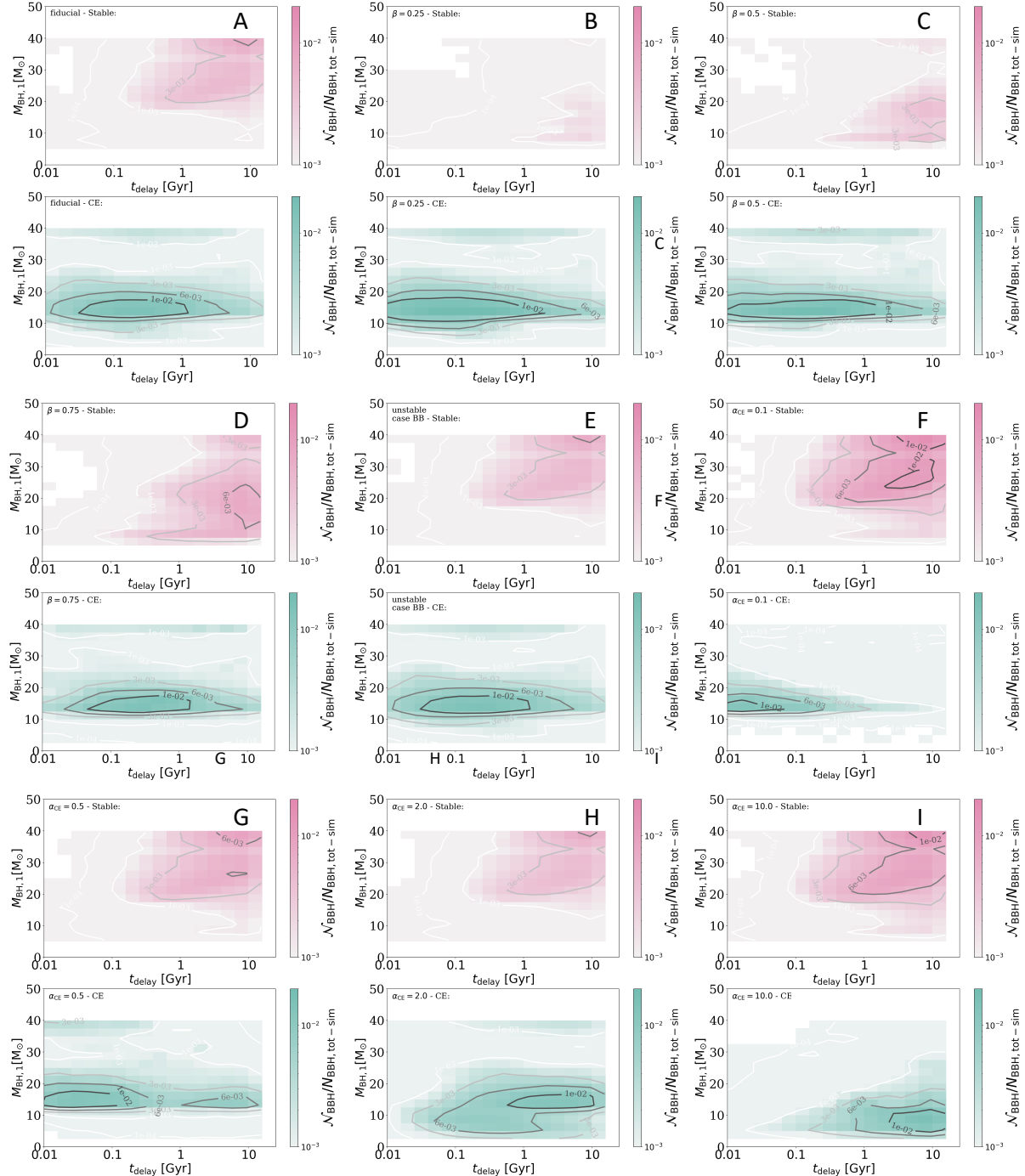
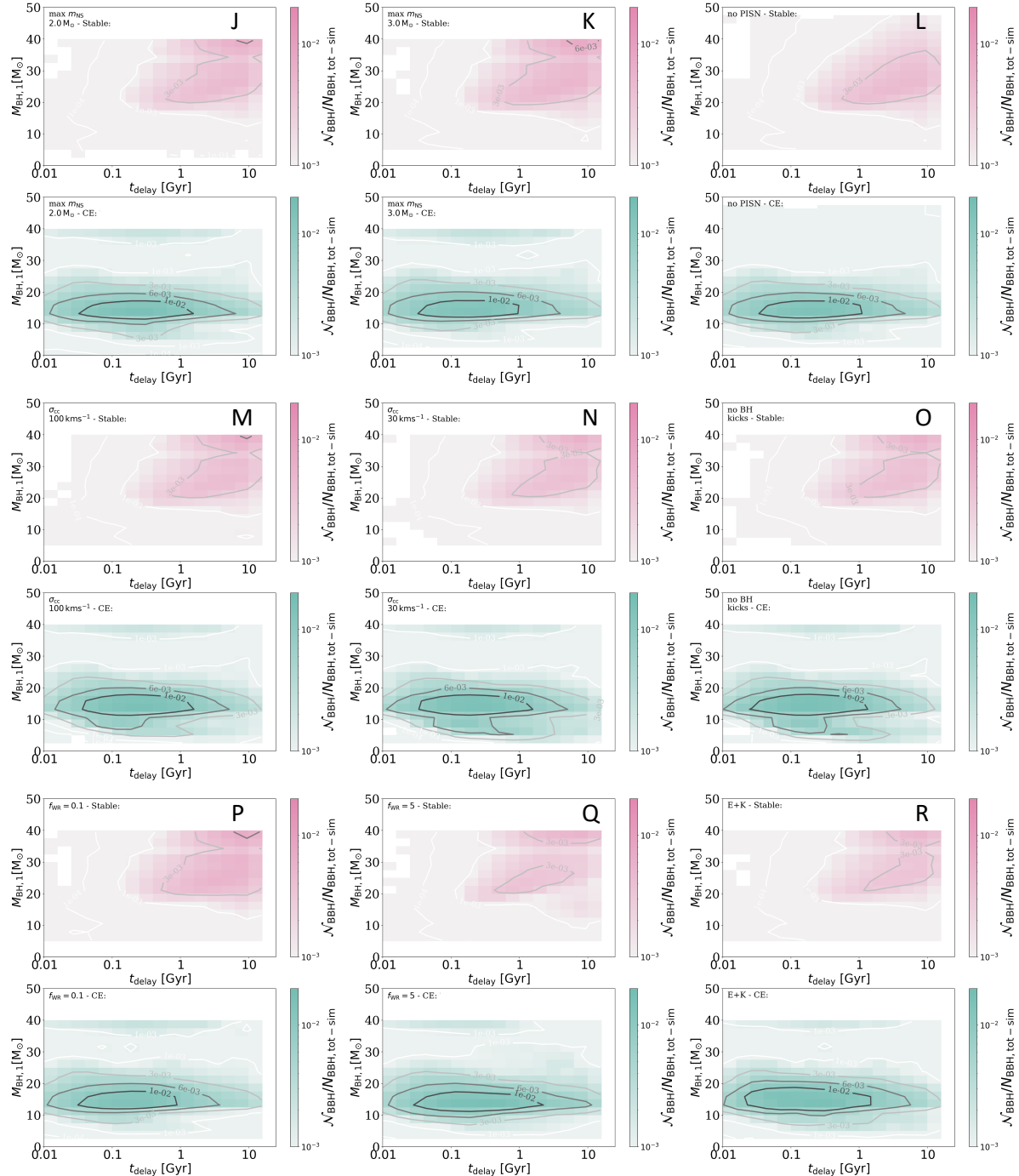


Figure 3.15 (following page): Same as Figure 3.14 but for the following model variations: Panels J and K: maximum neutron star mass is fixed to $2.0 M_{\odot}$ and $3.0 M_{\odot}$ respectively. Panel L: no PPISN or PISN implemented. Panels M and N: natal kicks are drawn from a Maxwellian velocity distribution with a one-dimensional root-mean-square velocity dispersion of $\sigma_{CC} = 100 \text{ km s}^{-1}$ and 30 km s^{-1} respectively. Panel O: BHs are assumed to receive no natal kick. Panels P and Q vary the strength of the Wolf-Rayet-like wind mass loss by a constant factor of $f_{\text{WR}} = 0.1$ and 5 respectively. Panel R combines the assumption that case BB mass transfer is always unstable with allowing Hertzsprung-gap donor stars which initiate a CE to survive the CE event (models E and S).



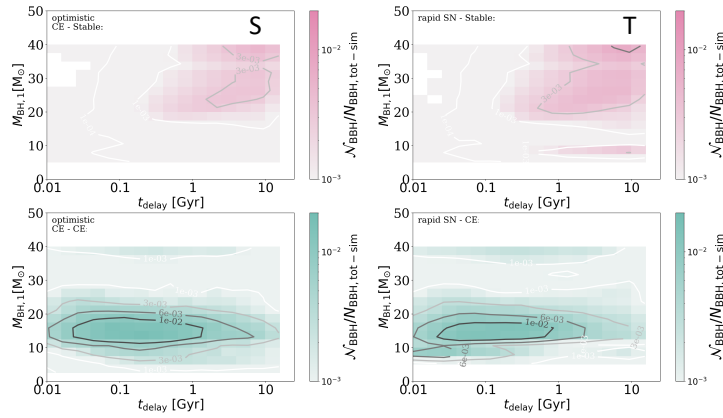
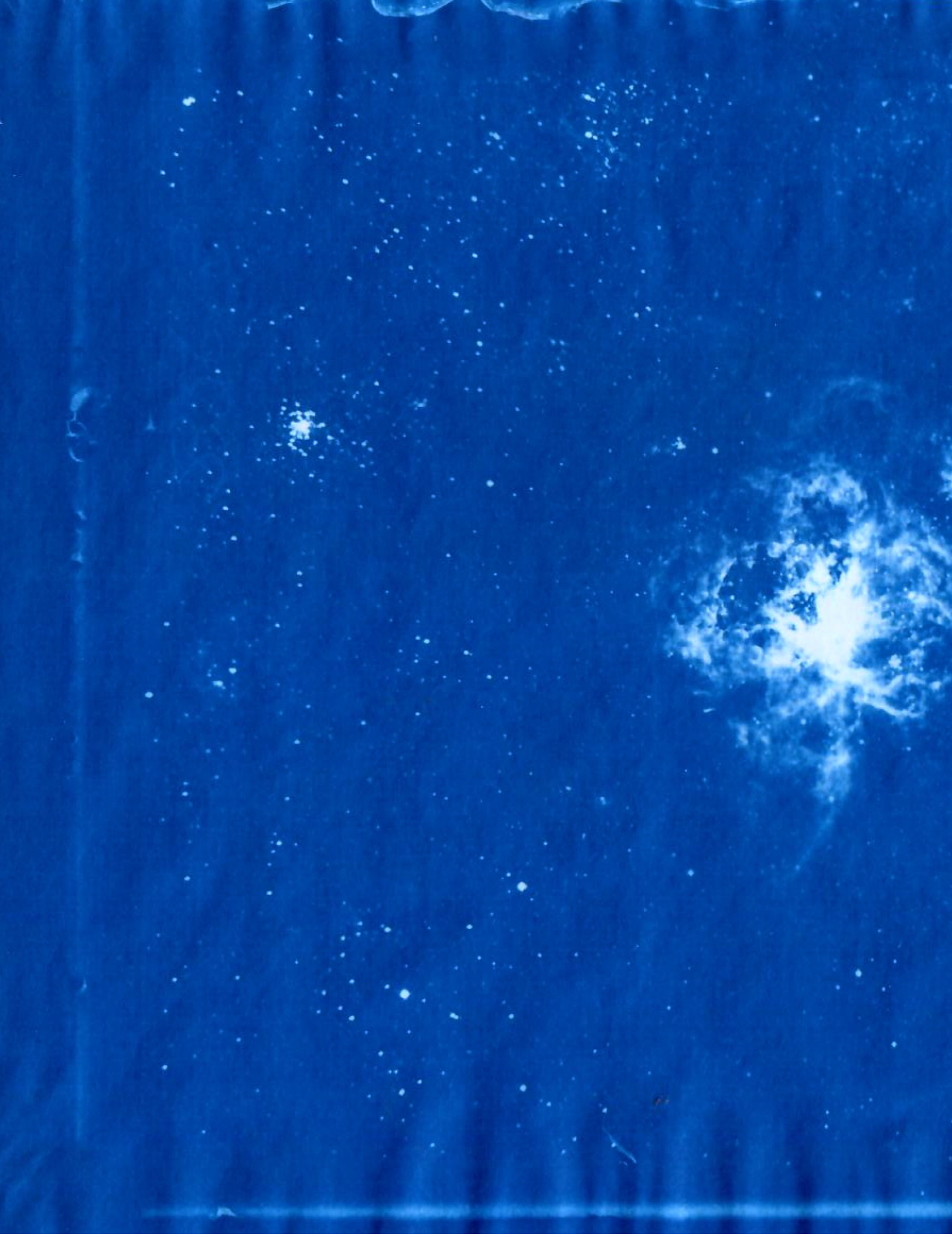


Figure 3.16: Same as Figure 3.14 but for the following model variations: Panel S: Hertzsprung-gap donor stars initiating a CE are allowed to survive this CE event. Panel T: adopts the Fryer et al. (2012) “rapid” supernova remnant-mass prescription.



Chapter 4

The locations of features in the mass distribution
of merging binary black holes are robust
against uncertainties in the metallicity-dependent
cosmic star formation history.

This thesis chapter originally appeared in the literature as

L.A.C. van Son, S. E. de Mink, M. Chru sli nska, C. Conroy, R. Pakmor, L Hernquist,
Accepted for publication in *The Astrophysical Journal*, 2023

Abstract

New observational facilities are probing astrophysical transients such as stellar explosions and gravitational-wave sources at ever-increasing redshifts, while also revealing new features in source property distributions. To interpret these observations, we need to compare them to predictions from stellar population models. Such models require the metallicity-dependent cosmic star formation history ($\mathcal{S}(Z, z)$) as an input. Large uncertainties remain in the shape and evolution of this function. In this work, we propose a simple analytical function for $\mathcal{S}(Z, z)$. Variations of this function can be easily interpreted, because the parameters link to its shape in an intuitive way. We fit our analytical function to the star-forming gas of the cosmological TNG100 simulation and find that it is able to capture the main behaviour well. As an example application, we investigate the effect of systematic variations in the $\mathcal{S}(Z, z)$ parameters on the predicted mass distribution of locally merging binary black holes (BBH). Our main findings are: I) the locations of features are remarkably robust against variations in the metallicity-dependent cosmic star formation history, and II) the low mass end is least affected by these variations. This is promising as it increases our chances to constrain the physics that governs the formation of these objects.

4.1 Introduction

A myriad of astrophysical phenomena depend critically on the rate of star formation throughout the cosmic history of the Universe. Exotic transient phenomena, including (pulsational) pair-instability supernovae, long gamma-ray bursts and gravitational wave (GW) events appear to be especially sensitive to the metallicity at which star formation occurs at different epochs throughout the Universe (e.g., Langer et al., 2007;

Fruchter et al., 2006; Abbott et al., 2016c). Gravitational astronomy in particular has seen explosive growth in the number of detections in the past decade (Abbott et al., 2018a, 2021b,c), while theoretical predictions vary greatly due to uncertainties in the aforementioned metallicity of star formation (e.g., Santoliquido et al., 2021b; Broekgaarden et al., 2021b). In order to correctly model and interpret these observations, it is thus fundamental to know the rate of star formation at different metallicities throughout cosmic history; i.e. the metallicity-dependent cosmic star formation history ($\mathcal{S}(Z, z)$, see also the recent review by Chruścińska, 2022). Throughout this work little z refers to the redshift and Z to the metallicity of star formation.

It is difficult to observationally constrain the shape of $\mathcal{S}(Z, z)$ – (see e.g., Chruścińska & Nelemans, 2019b; Boco et al., 2021, for discussion of relevant observational caveats). Even at low redshifts, the low metallicity part of the distribution is poorly constrained (Chruścińska et al., 2021). Nonetheless, several methods exist to estimate the metallicity-dependent cosmic star formation history.

The first method is based on empirical scaling relations, linking galaxy properties like stellar mass M_* , metallicity Z , and overall star-formation rate density SFRD(z), with the galaxy stellar mass function, GSMF (see e.g. Dominik et al., 2013b). However, the applied methods to infer galaxy properties and subsequently scaling relations such as the MZ-relation differ greatly, which makes it difficult to interpret these results in a consistent way (e.g., Kewley & Ellison, 2008; Maiolino & Mannucci, 2019; Cresci et al., 2019). Moreover, observations are generally incomplete at high redshifts and low galaxy luminosity (e.g., Chruścińska et al., 2021).

One can also directly extract the metallicity-dependent cosmic star formation history from cosmological simulations (e.g. Mapelli et al., 2017; Briel et al., 2022a).

However, these simulations currently lack the resolution to resolve the lowest mass galaxies, and their variations in $\mathcal{S}(Z, z)$ span a smaller range than those observed in observationally-based models (Pakmor et al., 2022).

Alternatively, one can combine analytical models for the observed overall star-formation rate density, $\text{SFRD}(z)$, like those from Madau & Dickinson (2014) or Madau & Fragos (2017), and convolve this with an assumed function for the shape of the cosmic metallicity density distribution, such as was done in e.g., Langer & Norman (2006b) and the phenomenological model in Neijssel et al. (2019).

In this work we follow the latter approach and propose a flexible analytical model for $\mathcal{S}(Z, z)$ that can be fit to the output of both cosmological simulations, and observational data constraints where available. In contrast to earlier work, we adopt a skewed-lognormal distribution of metallicities that can capture the asymmetry in the low and high metallicity tails.

The purpose of this proposed form is twofold. First of all, the form we propose allows for an intuitive interpretation of the free parameters. This allows us to get better insight of the impact of changes in these parameters on the inferred ranges of astrophysical transients (as we demonstrate in Section 4.4 using GW predictions as an example). By adopting an analytical, parametrized form for $\mathcal{S}(Z, z)$, the large uncertainties can be systematically explored. Secondly, both the large complications in observational constraints, and the many uncertainties in cosmological simulations call for a generalised form of $\mathcal{S}(Z, z)$ that can be easily updated when new information becomes available. In particular, the advent of observations with the James Webb Space Telescope promises a new era of high-redshift metallicity studies of previously unexplored regimes (e.g., Sanders et al., 2022). We hope that this form will facilitate the flexibility needed to keep

up with observations. The model described in this work is incorporated in the publicly available ‘Cosmic Integration’ suite of the **COMPAS** code.¹

We describe our model for $\mathcal{S}(Z, z)$ in Section 4.2. We fit our model to the star-forming gas in the Illustris TNG100 simulation in Section 4.3, and demonstrate an example application of our model by systematically varying the parameters that determine the shape of $\mathcal{S}(Z, z)$ and investigate their impact on the local distribution of merging BBH masses in Section 4.4. We summarise our findings in Section 4.5.

Throughout this work, we adopt a universal Kroupa initial mass function (Kroupa, 2001) with the mass limits $0.01 - 200 \text{ M}_\odot$ and a flat ΛCDM cosmology with $\Omega_M = 0.31$, $\Omega_\Lambda = 0.69$ and $H_0 = 67.7 \text{ km s}^{-1} \text{ Mpc}^{-1}$ (Planck Collaboration et al., 2020).

4.2 A convenient analytic expression for the metallicity-dependent cosmic star formation history

We write the metallicity-dependent cosmic star formation history as

$$\boxed{\mathcal{S}(Z, z) = \text{SFRD}(z) \times \frac{dP}{dZ}(Z, z)} \quad (4.1)$$

(similar to e.g., Langer & Norman 2006b). The first term is the star formation rate density, $\text{SFRD}(z)$, that is the amount of mass formed in stars per unit time and per unit comoving volume at each redshift, z . The second term, $dP/dZ(Z, z)$, is a probability density distribution that expresses what fraction of star formation occurs at which metallicity, Z , at each redshift.

¹<https://github.com/TeamCOMPAS/COMPAS/tree/dev/utils/CosmicIntegration>

4.2.1 The cosmic metallicity density distribution

For the probability distribution of metallicities we draw inspiration from the approach by e.g., Neijssel et al. (2019) who used a log-normal distribution for their phenomenological model. Unfortunately, a simple log-normal distribution cannot capture the asymmetry that we see in the cosmological simulations, which show an extended tail in $\log_{10} Z$ towards low metallicity, combined with a very limited tail towards higher metallicity. To capture this behaviour we adopt a skewed-log-normal distribution instead. This is an extension of the normal distribution that introduces an additional shape parameter, α , that regulates the skewness (first introduced by O'Hagan & Leonard, 1976).

The skewed-log-normal distribution of metallicities is defined as:

$$\begin{aligned}\frac{dP}{dZ}(Z, z) &= \frac{1}{Z} \times \frac{dP(Z, z)}{d \ln Z} \\ &= \frac{1}{Z} \times \underbrace{\frac{2}{\omega} \phi\left(\frac{\ln Z - \xi}{\omega}\right)}_{(a)} \underbrace{\Phi\left(\alpha \frac{\ln Z - \xi}{\omega}\right)}_{(b)},\end{aligned}\quad (4.2)$$

where (a) is the standard log-normal distribution, ϕ ,

$$\phi\left(\frac{\ln Z - \xi}{\omega}\right) \equiv \frac{1}{\sqrt{2\pi}} \exp\left\{-\frac{1}{2} \left(\frac{\ln Z - \xi}{\omega}\right)^2\right\} \quad (4.3)$$

and (b) is the new term that allows for asymmetry, which is equal to the cumulative of the log-normal distribution, Φ ,

$$\Phi\left(\alpha \frac{\ln Z - \xi}{\omega}\right) \equiv \frac{1}{2} \left[1 + \operatorname{erf}\left\{\alpha \frac{\ln Z - \xi}{\omega\sqrt{2}}\right\}\right]. \quad (4.4)$$

This introduces three parameters, α, ω and ξ , each of which may depend on redshift. The first parameter, α , is known as the “shape”. It affects the skewness of the distribution and thus allows for asymmetries between metallicities that are higher and lower than

the mean. The symmetric log-normal distribution is recovered for $\alpha = 0$. The second parameter, ω is known as the “scale”. It provides a measure of the spread in metallicities at each redshift. Finally, ξ , is known as the “location”, because this parameter plays a role in setting the mean of the distribution at each redshift.

The location and the mean of the metallicity distribution To obtain a useful expression for the redshift dependence of the “location” $\xi(z)$ we first express the expectation value or mean metallicity at a given redshift

$$\langle Z \rangle = 2 \exp \left(\xi + \frac{\omega^2}{2} \right) \Phi(\beta \omega) \quad (4.5)$$

where β is

$$\beta = \frac{\alpha}{\sqrt{1 + \alpha^2}}. \quad (4.6)$$

(For a more extended derivation of the moments of the skewed-log-normal, see e.g., [Wang et al. \(2019\)](#).)

For the evolution of the mean metallicity with redshift we follow [Langer & Norman \(2006b\)](#) and the phenomenological model from [Neijssel et al. \(2019\)](#) in assuming that the mean of the probability density function of metallicities evolves with redshift as:

$$\langle Z \rangle \equiv \mu(z) = \mu_0 \cdot 10^{\mu_z \cdot z}, \quad (4.7)$$

where μ_0 is the mean metallicity at redshift 0, and μ_z determines redshift evolution of the location. Equating this to Equation 4.5, we get an expression for $\xi(z)$,

$$\xi(z) = \ln \left(\frac{\mu_0 \cdot 10^{\mu_z \cdot z}}{2 \Phi(\beta \omega)} \right) - \frac{\omega^2}{2}. \quad (4.8)$$

The scale (and variance) of the metallicity distribution We will also allow the “scale” ω to evolve with redshift in a similar manner,

$$\omega(z) = \omega_0 \cdot 10^{\omega_z \cdot z}. \quad (4.9)$$

where ω_0 is the width of the metallicity distribution at $z = 0$, and ω_z the redshift evolution of the scale.

Note that the width, $w(z)$ is not the same as the variance. The variance, $\sigma^2(z)$, can be expressed as

$$\sigma^2(z) = \omega^2(z) \left(1 - \frac{2\beta^2}{\pi}\right) \quad (4.10)$$

Asymmetry of the metallicity distribution: α The skewness α could in principle also be allowed to evolve with redshift (e.g., $\alpha(z) = \alpha(z=0)10^{\alpha_z \cdot z}$). However, we find no significant improvement over the simpler assumption where alpha is kept constant. Note that the redshift evolution of the ‘scale’ (eq. 4.9), already captures similar behaviour in our current formalism. We therefore adopt $\alpha = \alpha(z=0)$ and $\alpha_z = 0$.

In summary, Equation 4.2 becomes:

$$\boxed{\frac{dP}{dZ}(Z, z) = \frac{2}{\omega(z)Z} \times \phi\left(\frac{\ln Z - \xi(z)}{\omega(z)}\right) \Phi\left(\alpha \frac{\ln Z - \xi(z)}{\omega(z)}\right)}, \quad (4.11)$$

where $\xi(z)$ and $\omega(z)$ are defined in Equations 4.8 and 4.9 respectively and we have assumed α to be constant.

4.2.2 The overall cosmic star formation rate density

For the star formation rate density, we assume the analytical form proposed by

Madau & Dickinson (2014),

$$\text{SFRD}(z) = \frac{d^2 M_{\text{SFR}}}{dt dV_c}(z) = a \frac{(1+z)^b}{1 + [(1+z)/c]^d} \quad (4.12)$$

in units of [$\text{M}_\odot \text{yr}^{-1} \text{cMpc}^{-3}$]. This introduces four parameters: a which sets the overall normalisation and which has the same units as $\text{SFRD}(z)$ and b, c and d which are unitless and which govern the shape of the overall cosmic star formation rate density with redshift.

Lastly, we combine equations 4.11 and 4.12 to form a full metallicity specific star formation rate density as described in equation 4.1.

4.3 Fit against Cosmological simulation

We fit our new functional form of $\mathcal{S}(Z, z)$ as defined by equations 4.1, 4.11 and 4.12 to the IllustrisTNG cosmological simulations. We simultaneously fit for the following nine free parameters $\alpha, \mu_0, \mu_z, \omega_0, \omega_z$, which govern the metallicity dependence and a, b, c and d , which set the overall star-formation rate density. Below we briefly discuss the IllustrisTNG simulations, and elaborate on our fitting procedure.

4.3.1 IllustrisTNG Cosmological simulations

Although here, we only fit our model to the TNG100 simulation, our prescription can be easily be used to fit other simulated or observational data of the metallicity-dependent

cosmic star formation history².

The IllustrisTNG-project (or TNG in short) considers galaxy formation and evolution through large-scale cosmological hydrodynamical simulations (Springel et al., 2018; Marinacci et al., 2018; Nelson et al., 2018; Pillepich et al., 2018a; Naiman et al., 2018; Nelson et al., 2019a; Pillepich et al., 2019). Such simulations provide the tools to study parts of the Universe that are not easily accessible by observations. In particular of interest for this work, they simulate the high redshift enrichment of galaxies and the tail of low metallicity star formation at low redshift.

The models implemented in the publicly available TNG simulations (Nelson et al., 2019b)³ have lead to many successes. These models where calibrated at the resolution of the TNG100 simulation, hence TNG100 is expected to provide the best overall agreement to global properties (like the star formation rate density). This is why we adopt the TNG100 simulation as our fiducial simulation. For a more extended discussion focused on the processes that govern the creation, distribution and mixing of metals in the TNG simulations, we refer to Pakmor et al. (2022). In short, star formation in the TNG simulations is calibrated against the Kennicutt–Schmidt relation (Schmidt, 1959; Kennicutt, 1989), using an effective equation of state (Springel & Hernquist, 2003). The stellar metallicity yields are an updated version of the original Illustris simulations as described in Pillepich et al. (2018b). Star particles deposit metals into the gas through type Ia and type II supernovae, as well as through asymptotic giant branch stars. The TNG simulations have been shown to match observational constraints on the

²We provide a Jupyter notebook to facilitate this fit here: https://github.com/LiekeVanSon/SFRD_fit/blob/main/src/scripts/Notebooks/Fit_model_to_sfrdzZ.ipynb

³<https://www.tng-project.org/>

mass-metallicity relation of galaxies up to $z = 2$ (Torrey et al., 2019), as well as iron abundances (Naiman et al., 2018), metallicity gradients within galaxies at low redshift (Hemler et al., 2021), and the reduction of star formation in the centers of star-forming galaxies (Nelson et al., 2021). Several studies have used the TNG simulations to make predictions for astronomical transient sources (e.g. Briel et al., 2022a; Bavera et al., 2022; van Son et al., 2022c). Out of the four $\mathcal{S}(Z, z)$ variations explored, Briel et al. (2022a) find that TNG provides one of the best agreements between observed and predicted cosmic rates for electromagnetic and gravitational-wave transients, when combined with their fiducial binary population synthesis model.

On the other hand, large uncertainties and crude approximations remain in all contemporary cosmological simulations, thus also in the TNG simulations. Generally, some of the chemical evolution of galaxies in cosmological simulations is unresolved, and thus depends strongly on the implemented ‘sub-grid physics’. A known uncertainty is that dust is not included in the TNG simulations, which could mean that metallicity of the star-forming gas is overestimated. Feedback from active galactic nuclei is not well understood theoretically and is described in an approximate manner (Springel et al., 2005; Weinberger et al., 2017). Furthermore, all stellar winds mass loss from massive stars, binary interactions and their ionising effects are ignored (e.g. Dray et al., 2003; Smith, 2014; Götberg et al., 2020; Doughty & Finlator, 2021; Farmer et al., 2021; Goswami et al., 2022). Moreover, the uniform ionising UV background is turned on abruptly at $z = 6$. This crucially impacts the amount of low metallicity star formation at high redshift as it allows small galaxies to produce more stars than what would be expected for a gradually increasing UV background that reaches full strength at $z = 6$. All these uncertainties underline the need for a flexible approximation of the $\mathcal{S}(Z, z)$,

that can be easily updated when cosmological models and sub-grid physics are updated.

4.3.2 Choices and binning of the data

We fit equation 4.1 to the metallicity-dependent star formation rate of the star-forming gas in the TNG100 simulation. For this we use a binned version of the TNG data $\mathcal{S}(Z, z)_{\text{sim}}$. We consider metallicities between $\log_{10} Z = -5$ to $\log_{10} Z = 0$ in 30 bins, where we use Z_i to refer to the logarithmic centres of the bins. We ignore star formation in metallicities $\log_{10} Z \leq -5$ as this accounts for less than 1% of the total cosmic star formation rate in these simulations. We consider bins in redshifts between $z = 0$ and $z = 10$, with a step size of $dz = 0.05$, where z_j refers to the centres of the bins.

4.3.3 Optimisation function

To find a solution we use a method based on the sum of the quadratic differences between the simulations and our fit function. Using a vanilla χ -squared approach does not serve our purposes very well as it does a poor job in fitting regions where the star formation is very low. Using a χ -squared approach on the logarithm of the function instead places far too much weight on trying to fit the star formation rate in regions where the rate is very low or not even significant. After experimenting, we find that the following approach gives us satisfactory results.

We first consider a given redshift z_j . For this redshift we compute the sum of the squared residuals between the cosmological simulation and our fit. This is effectively the square of the l^2 -norm:

$$\chi^2(z_j) \equiv \sum_{Z_i} (\mathcal{S}(Z_i, z_j)_{\text{sim}} - \mathcal{S}(Z_i, z_j)_{\text{fit}})^2. \quad (4.13)$$

Here, the variable Z_i runs over all metallicity bins. We are particularly interested in

properly fitting the low metallicity star formation at high redshifts. At high redshifts, the overall star-formation rate density is generally lower. To ensure that our fitting procedure gives sufficient weight to the behaviour at all redshifts, we introduce a penalisation factor to somewhat reduce the contribution of redshifts where the peak of cosmic star formation occurs, while increasing the weight at redshifts where the overall star-formation rate density is lower. To achieve this we divide $\chi^2(z_j)$ by the star formation $\sum_{Z_i} \mathcal{S}(Z_i, z_j)$ per redshift bin before adding the contribution of all redshifts. Our final expression for the cost function reads

$$\chi = \sum_{z_j} \frac{\chi^2(z_j)}{\sum_{Z_i} \mathcal{S}(Z_i, z_j)} \quad (4.14)$$

To minimize this cost function, we use `scipy.optimize.minimize` from SciPy v1.6.3 which implements the quasi-Newton method of Broyden, Fletcher, Goldfarb, and Shanno (BFGS, [Nocedal & Wright, 2006](#)).⁴

4.3.4 Resulting $\mathcal{S}(Z, z)$

Our best fitting parameters are listed in Table 4.1. With these fit parameters, $\chi^2(z_j)$ is smaller than $2 \cdot 10^{-4}$ at any given redshift. To evaluate our fit, we show the absolute residuals and relative errors in Appendix 4.6. We will refer to the $\mathcal{S}(Z, z)$ with the parameters listed in Table 4.1 as our fiducial model.

In Figure 4.1 we show our fiducial model at different redshifts and metallicities. We also show the overall star-formation rate density $\text{SFRD}(z)$ in Figure 4.2. In general, our analytical model captures the metallicity-dependent cosmic star formation history

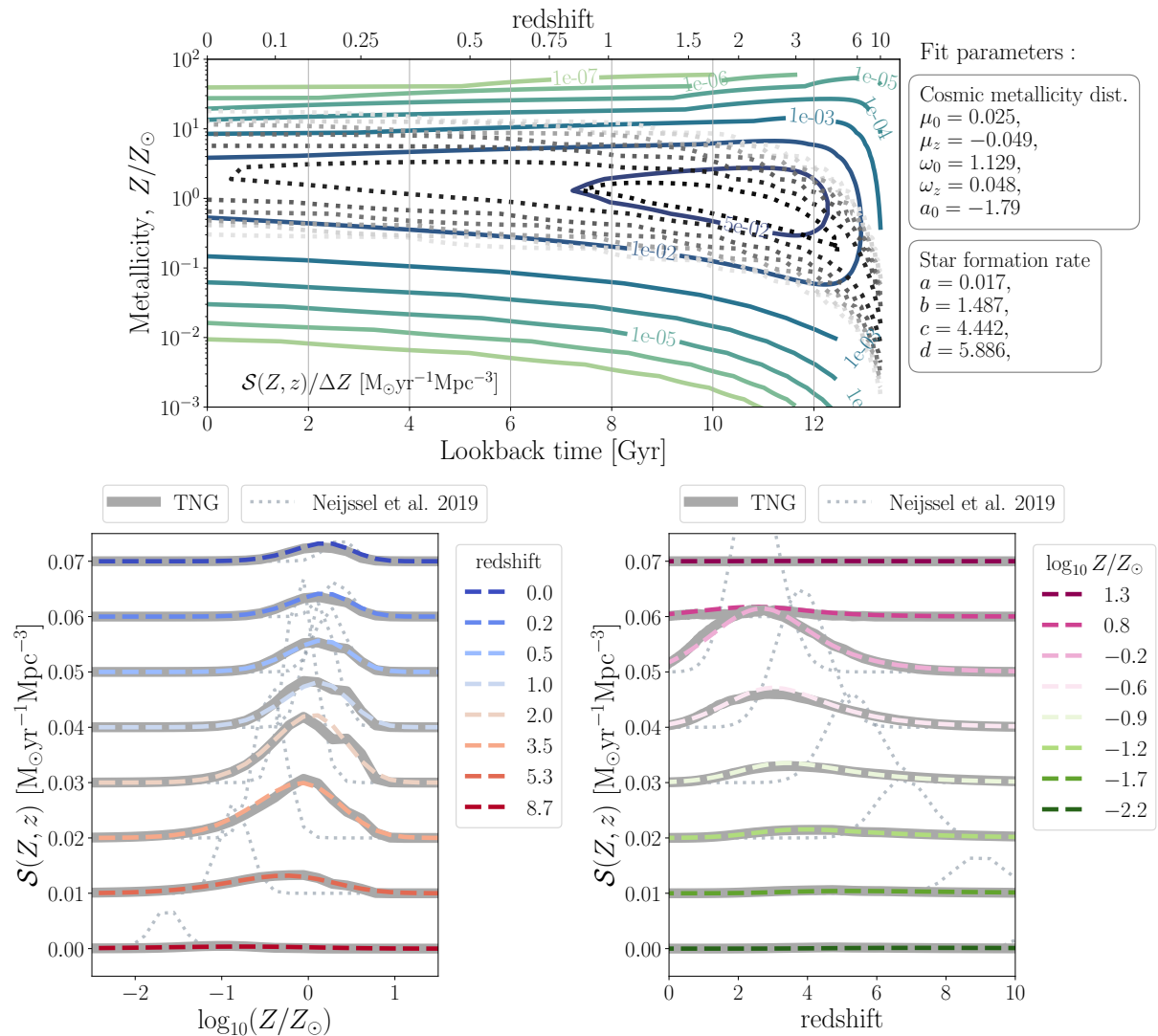
⁴http://www.apmath.spbu.ru/cnsa/pdf/monograf/Numerical_Optimization2006.pdf

Table 4.1.: Best fitting parameters for our $\mathcal{S}(Z, z)$ fit to TNG100 data. The $\text{SFRD}(z)$ parameters are in units of $M_{\odot} \text{yr}^{-1} \text{Mpc}^{-3}$.

$dP/dZ(Z, z)$	description	best fit	$\text{SFRD}(z)$	best fit
μ_0	mean metallicity at $z = 0$	0.025 ± 0.036	a	0.02 ± 0.072
μ_z	z -dependence of the mean	-0.049 ± 0.006	b	1.48 ± 0.002
α	shape (skewness)	-1.778 ± 0.002	c	4.44 ± 0.001
ω_0	scale at $z = 0$	1.122 ± 0.001	d	5.90 ± 0.002
ω_z	z -dependence of the scale	0.049 ± 0.009		

in the TNG100 simulations well (bottom panels of Figure 4.1). The skewed-log normal metallicity distribution is able to reproduce the overall behaviour that is observed in TNG100 (bottom left panel, but cf. [Pakmor et al., 2022](#), for an in-depth discussion of low metallicity star formation in the TNG50 simulation). Only minor features like the additional bump just above $\log_{10}(Z) = -2$ at redshift 2 are missed. However, for our purposes, it is more important to prioritise fitting the large scale trends, while we are

Figure 4.1 (following page): Our fiducial $\mathcal{S}(Z, z)$ model, adopting the best fitting parameters (listed on the top right) to fit the TNG100 simulations. The top panel shows the full two dimensional $\mathcal{S}(Z, z)$ linear in time. Contours range from $10^{-7} - 10^{-2} M_{\odot} \text{yr}^{-1} \text{Mpc}^{-3}$. The bottom left (right) panel shows slices of the distribution in redshift (metallicity). Each slice is displaced by $0.01 M_{\odot} \text{yr}^{-1} \text{Mpc}^{-3}$ (note the linear scale of $\mathcal{S}(Z, z)$ in the bottom panel). We show the TNG100 simulation data with thick gray lines. For comparison, we also show the phenomenological model from [Neijssel et al. \(2019\)](#) in all panels with grey dotted lines. The bottom panels show that our analytical model adequately captures the shape of the $\mathcal{S}(Z, z)$ from TNG100.



not so interested in smaller scale fluctuations.

Adopting a skewed-lognormal metallicity distribution allows for a tail of low metallicity star formation out to low redshifts. To emphasise the difference between a skewed-lognormal and a symmetric lognormal distribution, we show the phenomenological model from Neijssel et al. (2019) in dotted grey. Their model falls within the family of functions that is encompassed by our model described in Section 4.2, but we note that their model is distinctly different.⁵

Although our model preforms well at reproducing the large scale trends seen in TNG, we acknowledge that more complex features as suggested by some observational studies could be missed. One example is that the SFRD(z) shape we adopt from Madau & Dickinson (2014) does not account for starburst galaxies (see discussion in Chruścińska et al., 2021). Moreover, our model cannot capture inflection points in the mean metallicity, because we assume both μ_0 and μ_z are constants with redshift (equation 4.7). Contrarily, Chruścińska & Nelemans (2019b) find an upturn in the amount of low metallicity star formation above $z = 4$ if the power law of the GMSF is allowed to evolve with redshift. Hence, although our model is more broadly applicable than previous models, in it's current form, it does not capture the complete range of observationally-allowed variations. Incorporating more complex functional forms for our the mean metallicity could possibly capture such behaviour, but this analysis is beyond the scope of this paper.

⁵The phenomenological model from Neijssel et al. (2019) is recovered by adopting $\mu_0 = 0.035$, $\mu_z = -0.23$, $\omega_0 = 0.39$, $\omega_z = 0$, $\alpha = 0$, $a = 0.01$, $b = 2.77$, $c = 2.9$ and $d = 4.7$.

4.4 Application: systematic variations of $\mathcal{S}(Z, z)$ and the effect on the mass distribution of merging BHs

We will now demonstrate the application of our analytical model by systematically varying the parameters in our fiducial $\mathcal{S}(Z, z)$ model, and investigate their effect on the local mass distribution of BBH mergers originating from isolated binaries.

We use the publicly available rapid binary population synthesis simulations presented in van Son et al. (2022a).⁶ These simulations were run using version v02.26.03 of the open source **COMPAS** suite (Riley et al., 2022b)⁷. **COMPAS** is based on algorithms that model the evolution of massive binary stars following Hurley et al. (2000, 2002) using detailed evolutionary models by Pols et al. (1998). In particular, we use the simulations behind Figure 1 from van Son et al. (2022a), and we refer the reader to their methods section for a detailed description of the adopted physics parameters and assumptions.⁸ Metallicities of each binary system were sampled from a smooth probability distribution to avoid artificial peaks in the BH mass distribution (e.g. Dominik et al., 2015a; Kummer, 2020). These simulations provide us with an estimate of the yield of BBH mergers per unit of star-forming mass and metallicity.

⁶ Available for download at <https://zenodo.org/record/7612755>, see also the Software and Data section in the acknowledgements

⁷<https://github.com/TeamCOMPAS/COMPAS>

⁸We note that the rate in van Son et al. (2022a) is slightly higher than the fiducial rate presented in Figure 4.3 in this work. This difference is caused by the use of rounded parameter values of $\mathcal{S}(Z, z)$ in van Son et al. (2022a).

We combine the aforementioned yield with variations of the fiducial $\mathcal{S}(Z, z)$ model described in this work. By integrating over cosmic history, we obtain the local merger rates of BBH systems, which allow us to construct the distribution of source properties at every redshift. We use the cosmic integration scheme that is part of the publicly available [COMPAS](#) suite, which includes the $\mathcal{S}(Z, z)$ model described in this work. The details of this framework are described in [Neijssel et al. \(2019\)](#), but also in [van Son et al. \(2022c\)](#), where more similar settings to this work are used.

4.4.1 Determining reasonable variations of $\mathcal{S}(Z, z)$

We consider variations in both the shape of the cosmic metallicity density distribution $dP/dZ(Z, z)$, and the shape of the overall star-formation rate density, SFRD(z). To determine the range that is reasonably allowed by observations, we compare our variations to the observation-based $\mathcal{S}(Z, z)$ models described in [Chruścińska et al. \(2021\)](#). An overview of the explored variations is shown in Table 4.2. Below we explain how we arrive at these values.

Table 4.2.: Variations on $\mathcal{S}(Z, z)$. For every variation, we either swap the value of an individual $dP/dZ(Z, z)$ parameter, or exchange the set of four SFRD(z) parameters, and replace them by the the min/max values listed here. All other parameters are kept fixed at their fiducial value.

$dP/dZ(Z, z)$	min	fiducial	max	SFRD(z)	min	fiducial	max
μ_0	0.007	0.025	0.035	a	0.01	0.02	0.03
μ_z	0.0	-0.049	-0.5	b	2.60	1.48	2.6
α	-6.0	-1.778	0.0	c	3.20	4.44	3.3
ω_0	0.7	1.125	2.0	d	6.20	5.90	5.9
ω_z	0.0	0.048	0.1				

For the cosmic metallicity density distribution, we vary every parameter that determines the shape of $dP/dZ(Z, z)$ independently (three left-most columns of Table 4.1, and top of Table 4.2), while keeping all other parameters fixed at their fiducial value. For each variation, we inspect the fraction of stellar mass that is formed at low-metallicity ($Z < 0.1Z_{\odot}$) versus the fraction of stellar mass that is formed at high-metallicity ($Z > Z_{\odot}$), for all star formation that occurred below a certain threshold redshift. We compare this to the models from Chruślińska et al. (2021) in Figure 4.6 in Appendix 4.7. We have chosen our variations such that they span a reasonable range of cosmic metallicity density distributions as allowed by observation-based and cosmological simulations-based models. We use the models `214-f14SB-BiC_FMR270_FOH_z_dM.dat`, and `302-f14SB-Boco_FMR270_FOH_z_dM.dat` from Chruślińska et al. (2021)⁹ as a representation of a very low and high metallicity star formation realisation respectively. These models are the low and high metallicity extreme under their fiducial SFR–metallicity correlation, and so we will refer to them as `Chr21_lowZ` and `Chr21_highZ` respectively from hereon. The difference between these models lies in the assumptions in the underlying empirical galaxy relations. In general, low-mass galaxies contribute to low-metallicity star formation and shift the peak of $S(Z, z)$ to lower metallicities. `Chr21_lowZ` is characterised by a star formation–galaxy mass relation that is flat at high galaxy masses (reducing the star formation rate for the highest-mass galaxies), a galaxy stellar mass function that evolves with redshift (predicting an increasing number density of low-mass galaxies), and a local galaxy mass-metallicity relation as in Pettini & Pagel (2004). This model further approximates

⁹These models including a detailed description of their contents are publicly available at https://ftp.science.ru.nl/astro/mchruslinska/Chruslinska_et_al_2021/

the contribution of starburst galaxies following Bisigello et al. (2018) and Caputi et al. (2017). Assuming that starburst galaxies follow the empirical fundamental metallicity relation (leading to anti-correlation between the SFR and metallicity), their inclusion tends to shift the peak of $\mathcal{S}(Z, z)$ to lower metallicities and broadens the low-metallicity part of the distribution.

On the other hand, `Chr21_highZ` assumes the star formation–galaxy mass relation does not flatten towards higher galaxy masses, a galaxy stellar mass function where the slope for the low-mass end is constant over redshift, and a local galaxy mass-metallicity relation following Kobulnicky & Kewley (2004). Lastly, this model adopts the starburst prescription from Boco et al. (2021), which produces results that are similar to models without starburst galaxies.

For every variation of our model, we inspect both the full $\mathcal{S}(Z, z)$ and slices at redshifts $z = 0, 0.5, 3.0$ and 6 by eye. At each slice we compare our model variation to `Chr21_lowZ` and `Chr21_highZ`, and ensure that none of our variations significantly exceeds these extremes in $\mathcal{S}(Z, z)$. This also serves as a sanity check for the overall star-formation rate density.

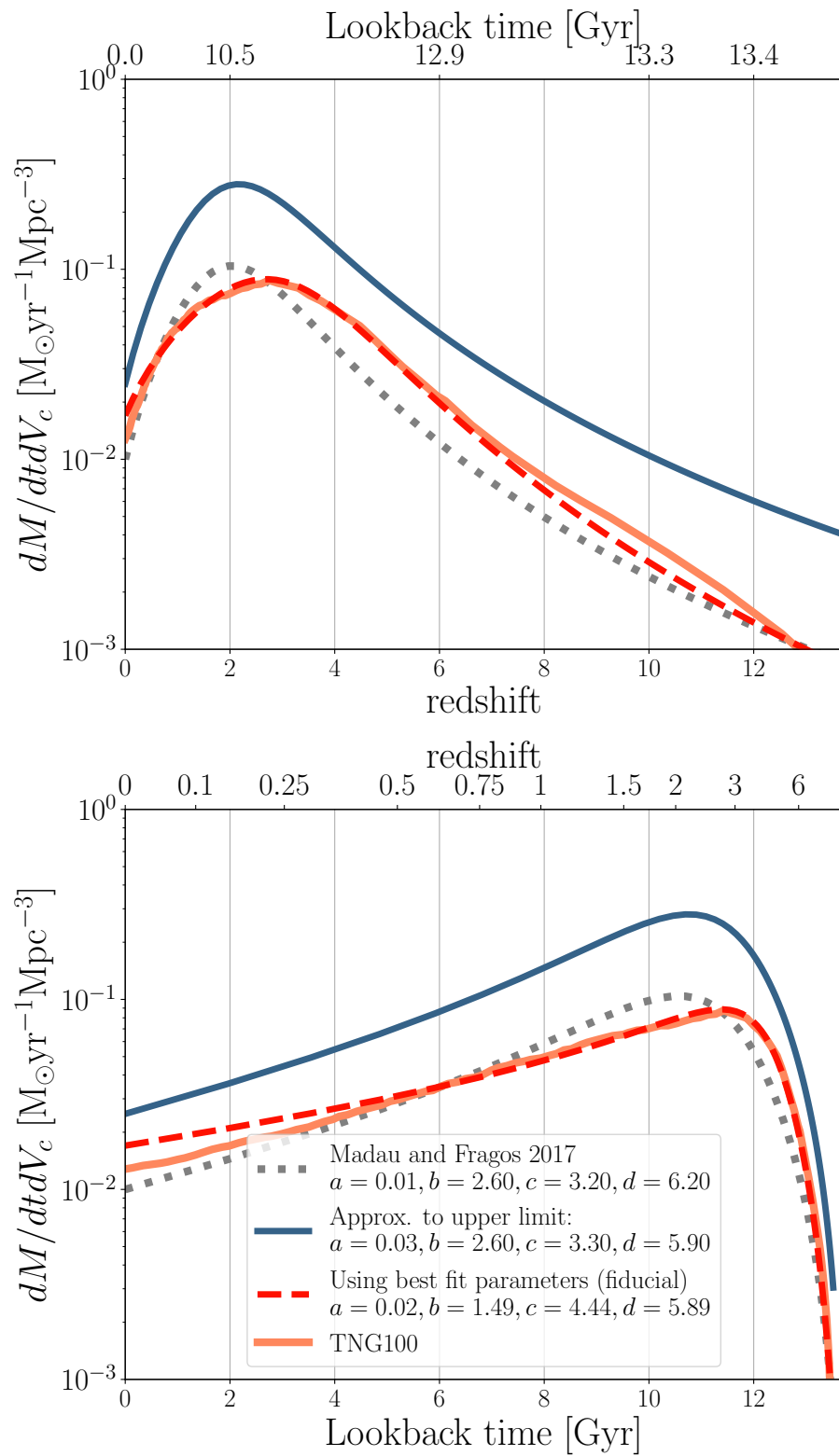
We also consider two variations of the overall star-formation rate density, $\text{SFRD}(z)$, where we keep the metallicity distribution $dP/dZ(Z, z)$ fixed, but vary all four $\text{SFRD}(z)$ parameters at once (right two columns of Table 4.1, and bottom of Table 4.2). We use Figure 11 from Chruścińska et al. (2021) to determine approximate upper and lower bounds to the overall star-formation rate density. We choose Madau & Fragos (2017) as an approximation of the lower limit. For the upper limit, we use the upper edge of models that adopt starbursts following Bisigello et al. (2018) and Caputi et al. (2017) (SB: B18/C17), combined with a non-evolving low-mass end of the

galaxy stellar mass function (shown as a thick brown line in Fig. 11 of Chruścińska et al., 2021, and described in their table B1). To approximate these models, we fit equation 4.12 by eye to the broken power law description of this model as presented in appendix B1 of Chruścińska et al. (2021). We show all $\text{SFRD}(z)$ variations in Figure 4.2.

4.4.2 The effect of the $\mathcal{S}(Z, z)$ on the primary masses of merging BBH

To isolate the effect of the $\mathcal{S}(Z, z)$ from the effects of different formation channels, we split the data from van Son et al. (2022c) between the stable mass transfer channel (e.g., van den Heuvel et al., 2017; Inayoshi et al., 2017; Bavera et al., 2021a; Marchant et al., 2021; Gallegos-Garcia et al., 2021; van Son et al., 2022c), and the ‘classical’ common-envelope channel (or CE channel, e.g., Belczynski et al., 2007b; Postnov & Yungelson, 2014b; Belczynski et al., 2016b; Vigna-Gómez et al., 2018b). These channels

Figure 4.2 (following page): Comparison of several overall star-formation rate densities, $\text{SFRD}(z)$, with redshift (top panel) and with lookback time (bottom panel). The solid orange and dashed red lines respectively show the star formation data from TNG100 and our corresponding fit adopting eq. 4.12 (fiducial model). The dotted gray and solid blue lines are variations of eq. 4.12 used to approximate the lower and upper edge of possible star-formation histories. The dotted gray line shows the model from Madau & Fragos (2017), while the solid blue line mimics the behaviour of the powerlaw-fit to the SB:B18/C17 variations with a non-evolving low-mass end of the galaxy stellar mass function from Chruścińska et al. (2021).

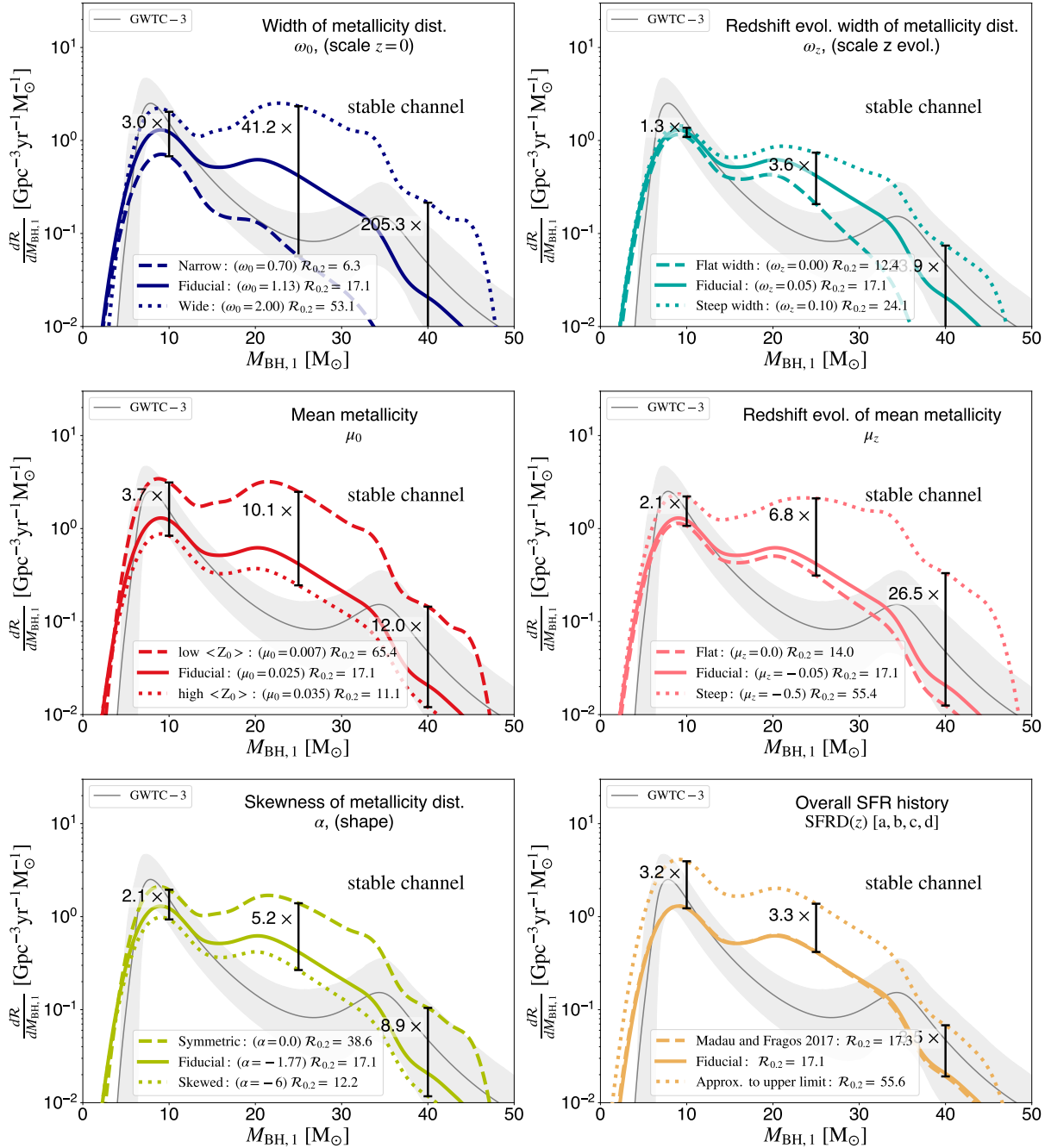


are distinguished based on whether the binary system has experienced a common envelope phase (CE channel) or only stable mass transfer (stable channel in short from now on).

In Figures 4.3 and 4.4, we show the resulting primary mass distribution of merging BBHs from the stable channel and CE channel respectively. The primary (secondary) component refers to the more (less) massive component of merging BBHs. Each panel varies one aspect of the $\mathcal{S}(Z, z)$. In the first five panels of Figures 4.3 and 4.4, we vary one of the parameters that determine the shape of the probability density distribution of metallicities, while keeping all other values fixed at their fiducial values. In the last panel of Figures 4.3 and 4.4, we vary the shape of the overall star-formation rate densities, $SFRD(z)$, to one of the variations shown in Figure 4.2, while keeping the probability density distribution of metallicities fixed.

The first thing we note is that the location of the features in the primary mass distribution are robust against variations in $\mathcal{S}(Z, z)$. For the stable channel, two features

Figure 4.3 (following page): The primary mass distribution of merging BBH systems from the stable mass transfer channel for several variations in $\mathcal{S}(Z, z)$ (see Table 4.2). The first five panels show variations of $dP/dZ(Z, z)$, eq. 4.11, where we vary one parameter at a time while keeping the rest fixed at their fiducial value. The bottom right panel shows variations in $SFRD(z)$, where we vary the four parameters of $SFRD(z)$ simultaneously. All panels are shown at redshift $z = 0.2$, with the corresponding BBH merger rate indicated in the legend. We show the power-law + peak model from Abbott et al. (2021f) in gray. We annotate the relative change in the rate at three reference masses: $10 M_{\odot}$, $25 M_{\odot}$ and $40 M_{\odot}$.



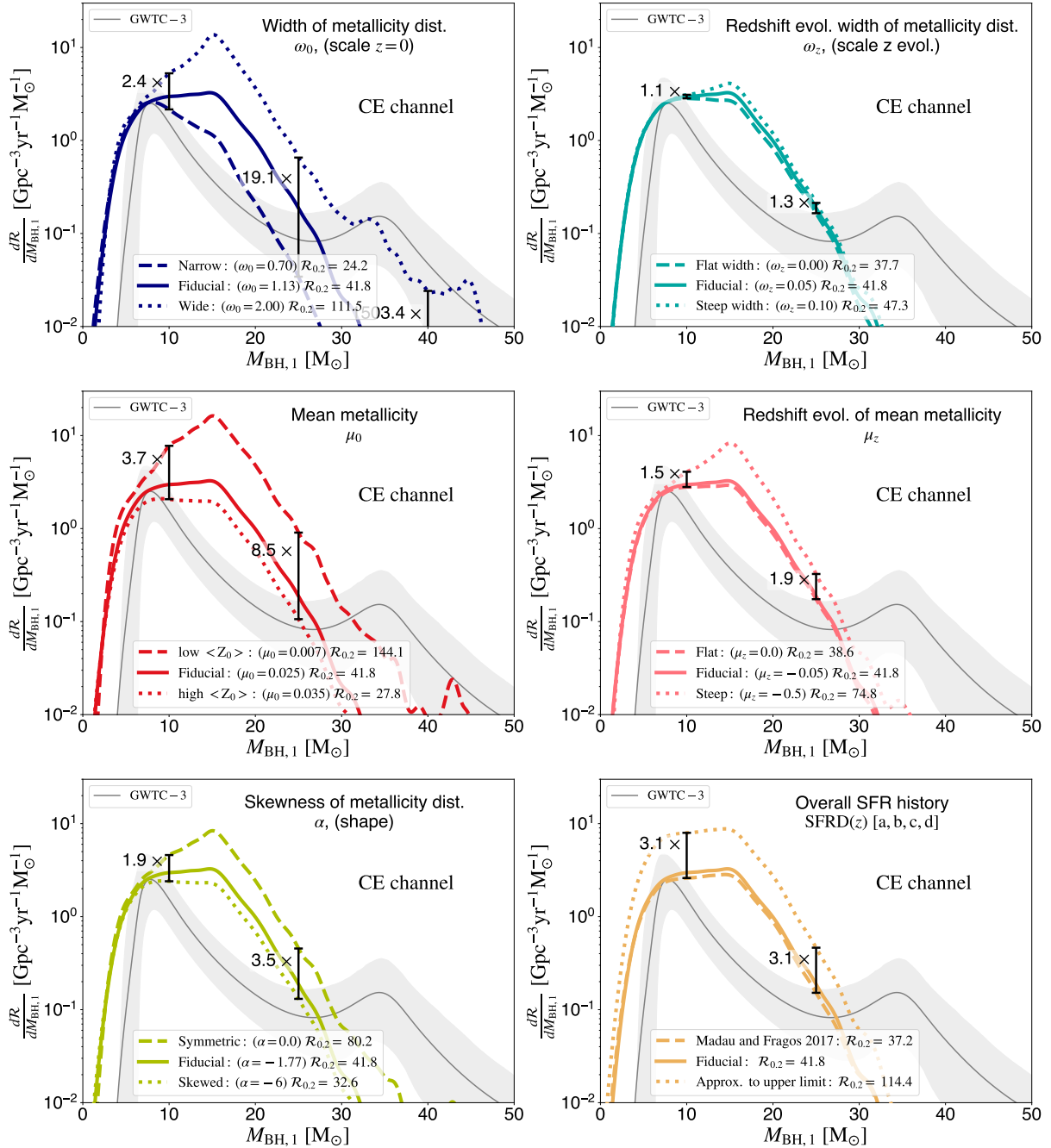
are visible in all variations: a peak at $M_{\text{BH},1} \approx 9 M_{\odot}$ and a bump at $M_{\text{BH},1} \approx 22 M_{\odot}$.

Two more features are visible in at the high mass end for almost all $\mathcal{S}(Z, z)$; a knee at $M_{\text{BH},1} \approx 35 M_{\odot}$ and another bump at $M_{\text{BH},1} \approx 45 M_{\odot}$. Although the locations of these features are constant, the features themselves can disappear for variations that suppress the rate of high mass BHs (e.g., dashed lines in the top panels of Fig. 4.3).

Similarly, the CE channel displays a kink in the distribution at about $9 M_{\odot}$, and a peak at approximately $M_{\text{BH},1} \approx 17 M_{\odot}$ for all variations. The latter peak is the global peak of the mass distribution in almost all variations.

The finding that the locations of features in the mass distribution do not change for different $\mathcal{S}(Z, z)$ is consistent with earlier work. Recent work by Chruścińska (2022) showed that, when comparing two very different models of $\mathcal{S}(Z, z)$ (their Figure 5), the location of the peaks remains the same, even though the normalisation between the two BBH merger rates is completely different. Furthermore, Broekgaarden et al. (2021b) show the probability distribution of chirp masses for BBHs in their Fig. 4. Although features can disappear when the $\mathcal{S}(Z, z)$ prohibits the formation of certain (typically higher) mass BHs, the *location* of features remains the same. This implies that the locations of features in the mass distribution of BBHs are determined by the formation channel and its underlying stellar and binary physics. The locations of features could therefore serve as sign posts of the underlying physics.

Figure 4.4 (following page): Same as Figure 4.3, but for the Common Envelope channel. These figures show that the low mass end of the primary mass distribution is least affected by the adopted $\mathcal{S}(Z, z)$. Moreover, the *location* of features in the mass distribution are robust against all explored variations.



Second, we see that the low mass end of the primary mass distribution is relatively robust against variations in $\mathcal{S}(Z, z)$. To quantify this, we annotate the ratio between the maximum and minimum rate at three reference masses; $M_{\text{BH},1} = 10, 25$, and 40 M_\odot . At $M_{\text{BH},1} = 10 \text{ M}_\odot$, we find that the rate changes by at most a factor of about 3.7 for the stable channel, and at most about a factor of 3.8 for the CE channel. On the other hand, the change in rate at $M_{\text{BH},1} = 40 \text{ M}_\odot$ can be as high as a factor of about 200 and 150 for the stable and CE channels, respectively. The lowest mass BHs are least affected by the $\mathcal{S}(Z, z)$ because they can be formed from all metallicities above $Z \gtrsim 10^{-3}$ (see e.g., Figures 7 and 13 from [van Son et al., 2022c](#)). The rate of star formation at metallicities above $\gtrsim 10^{-3}$ is observationally relatively well constrained for redshifts below 0.5 (which comprises the past 5 Gyr of star formation). This is reflected in the top panel of Figure 4.6: all models show that 10% or less of the stellar mass was formed at a metallicity below $Z/10 \approx 0.0014$, or in other words, about 90% or more of the stellar mass was formed at a metallicity above $Z/10$. Hence the lowest mass BHs derive from the least uncertain parts of the $\mathcal{S}(Z, z)$. The low-mass end of the mass distribution of merging double compact objects will also provide a particularly powerful cosmological constraint in the era of third generation gravitational wave telescopes ([María Ezquiaga & Holz, 2022](#)). Our finding that the low mass end is more robust against variations in $\mathcal{S}(Z, z)$ supports this claim.

Parameter variations that affect shape of $\mathcal{S}(Z, z)$ at low redshift primarily change the normalisation of the mass distribution. This is the case for variations of the width of the cosmic metallicity density distribution at $z = 0$ (ω_0), the mean metallicity of the cosmic metallicity density distribution at $z = 0$ (μ_0), and the skewness of the cosmic metallicity

density distribution (α , left columns of Figures 4.3 and 4.4). To emphasise this point, we annotate the total BBH merger rate at redshift 0.2, $\mathcal{R}_{0.2}$, in the legends of Figures 4.3 and 4.4 (0.2 is the redshift where the observations are best constrained Abbott et al. 2021f). Variations that increase the amount of star formation at low metallicity (i.e. for a low mean metallicity $\mu_0 = 0.007$ and a wide metallicity distribution $\omega_0 = 2.0$) increase the predicted BBH merger rate. This is consistent with other work that finds merging BBHs form more efficiently at low metallicities (e.g. Belczynski et al., 2010b; Stevenson et al., 2017; Mapelli et al., 2017; Chruścińska et al., 2019; Broekgaarden et al., 2021b). A more skewed cosmic metallicity density distribution pushes the peak of the distribution to higher metallicities and thus forms more stars at high metallicity when compared to a symmetric distribution. Hence, the local rate of BBH mergers is lower for the skewed distribution ($\alpha = -6$) with respect to the symmetric variation ($\alpha = 0.0$).

Changing the overall star-formation rate density (SFRD(z), bottom right panels of Figures 4.3 and 4.4) also affects the normalisation of the mass distribution, but has a smaller effect than the width and the mean of the cosmic metallicity density distribution at $z = 0$ (ω_0 and μ_0). This underlines the importance of the amount of low-metallicity star formation (e.g., Chruścińska, 2022), and is furthermore in line with findings from Tang et al. (2020). As discussed in Section 4.4.1, we use Madau & Fragos (2017) and the solid blue line in Figure 4.2 as an approximate lower and upper bound to the SFRD(z) respectively. The overall cosmic star formation rate density from Madau & Fragos (2017) is very similar to our fiducial model (Figure 4.2), and the differences between the resulting mass distributions are correspondingly small. Our approximation of the upper limit to the allowed SFRD(z) leads to an overall increase of the BBH merger rate by a factor of about 3.

Parameters that change the evolution of the metallicity distribution $dP/dZ(Z, z)$ with redshift, such as the redshift dependence of the width and mean; ω_z and μ_z (top right and centre right panels of Figures 4.3 and 4.4) primarily affect the high mass end of the stable channel. We understand this as an effect of the different delay time distributions for both formation channels. Since both, ω_z and μ_z influence the amount of low metallicity stellar mass formed at high redshifts they will mostly affect systems with longer delay times. The stable channel has been shown to produce more high mass BHs with longer delay times when compared to the CE channel (van Son et al., 2022c; Briel et al., 2022b). Hence we find these variations affect the slope of the high mass end of the BBH mass distribution for the stable channel, while they have a relatively small impact on the CE channel.

4.5 Discussion & Summary

We present a flexible analytic expression for the metallicity-dependent cosmic star formation history, $S(Z, z)$ (equations 4.1, 4.11 and 4.12). An analytical expression allows for controlled experiments of the effect of $S(Z, z)$ on dependent values, such as the rate and mass distribution of merging BBHs. The model presented in this work adopts a skewed-lognormal for the distribution of metallicities at every redshift ($dP/dZ(Z, z)$).

The model can capture the general behaviour of cosmological simulations, such as TNG100 Our analytical expression for $S(Z, z)$ is composed of a cosmic metallicity density distribution that is determined by a mean, scale and skewness and their redshift dependence, as well as parameters governing the overall star-formation rate density. We fit our analytical expression for $S(Z, z)$ to the star-forming gas in the TNG100 simulation, and provide the best fit parameters in Table 4.1. We show that

our model captures the shape and general behaviour of the cosmological simulations well (Figure 4.1). Although our model is more broadly applicable than previous models, we acknowledge that it does not capture the *complete* range of observationally-allowed variations in its current form. Incorporating more complex functions for the redshift evolution of the metallicity could solve this issue, but this is left for future research.

The model allows for a controlled experiment on the effect of $\mathcal{S}(Z, z)$ on the local distribution of merging BBH As an example, we use our model to calculate the local rate and mass distribution of the more massive components from merging BBHs ($M_{\text{BH},1}$) in Figures 4.3 and 4.4. We systematically vary all five parameters that shape the cosmic metallicity density distribution, and explore two additional variations of the overall star-formation rate density $\text{SFRD}(z)$. Our main findings are as follows:

- The locations of features in the distribution of primary BH masses are robust against variations in $\mathcal{S}(Z, z)$. The location of features in the mass distribution of BHs could thus be used as sign posts of their formation channel.
- For all variations, the low mass end of the mass distribution is least influenced by changes in the $\mathcal{S}(Z, z)$. This is because the lowest mass BHs can be formed from all metallicities above $Z \gtrsim 10^{-3}$, for which the star formation rate is relatively well constrained in the recent Universe. This suggests that the lower end of the BH mass distribution (component masses of $\leq 15 M_\odot$) is potentially very powerful for constraining the physics of the formation channels, irrespective of the cosmic star formation rate uncertainties.
- The metallicity distribution of star formation at low redshift primarily impacts the normalisation of the BBH merger rate. Changing the overall star-formation

rate density, SFRD(z) also affects the rate, but to a lesser degree. This shows that low-metallicity star formation at low redshifts dominates the overall normalisation of the BBH merger rate.

- Parameters that influence the redshift evolution of the mean and the width of the metallicity distribution affect the slope of the high mass end of the primary BH mass distribution for the stable channel. This reflects the longer delay times of the stable channel with respect to the CE channel.

The flexibility of the model presented in this work can capture the large uncertainties that remain in the shape and normalisation of the metallicity-dependent cosmic star formation history. Our hope is that this expression will provide a useful starting point for making predictions and comparisons with observations.

Acknowledgments

The authors acknowledge partial financial support from the National Science Foundation under Grant No. (NSF grant number 2009131 and PHY-1748958).”, the Netherlands Organisation for Scientific Research (NWO) as part of the Vidi research program BinWaves with project number 639.042.728 and the European Union’s Horizon 2020 research and innovation program from the European Research Council (ERC, Grant agreement No. 715063). This research was supported in part by the National Science Foundation under Grant No. NSF PHY-1748958.

Software and Data

All code associated to reproduce the data and plots in this paper is publicly available at https://github.com/LiekeVanSon/SFRD_fit. The data used in this work

is available on Zenodo under an open-source Creative Commons Attribution license at [10.5281/zenodo.7612755](https://zenodo.10.5281/zenodo.7612755). All observationally constrained models of the $\mathcal{S}(Z, z)$ from Chruścińska et al. (2021) can be found online at: https://ftp.science.ru.nl/astro/mchruslinska/Chruslinska_et_al_2021/.

This research has made use of GW data provided by the Gravitational Wave Open Science Center (<https://www.gw-openscience.org/>), a service of LIGO Laboratory, the LIGO Scientific Collaboration and the Virgo Collaboration. Further software used in this work: Python (Van Rossum & Drake, 2009), Astropy (Astropy Collaboration et al., 2013a, 2018a) Matplotlib (Hunter, 2007), NumPy (Harris et al., 2020), SciPy (Virtanen et al., 2020), ipython/jupyter (Perez & Granger, 2007; Kluyver et al., 2016), Seaborn (Waskom, 2021) and hdf5 (Collette et al., 2019).

4.6 Appendix: Evaluating our fit; the squared residuals

In the top panel of Figure 4.5, we show the log of the absolute residuals. The *square* of the residuals is used in the cost function, equation 4.14, to optimize our fit. We observe that the maximum residuals appear near the peak of star formation at high metallicities. The log of the relative errors (defined as $\frac{|\mathcal{S}_{\text{sim}} - \mathcal{S}_{\text{fit}}|}{\mathcal{S}_{\text{fit}}}$), is shown in the bottom panel of Figure 4.5. The relative errors generally exhibit an opposite trend with respect to the residuals. The relative errors are largest in regions of very low-metallicity star formation at low redshift. This occurs due to the very low star-formation rate in this regime (of the order $10^{-8} M_{\odot} \text{yr}^{-1} \text{Mpc}^{-3}$ for the TNG simulations and $10^{-11} M_{\odot} \text{yr}^{-1} \text{Mpc}^{-3}$ in our model fit). Another regime where the relative error becomes large is at very high

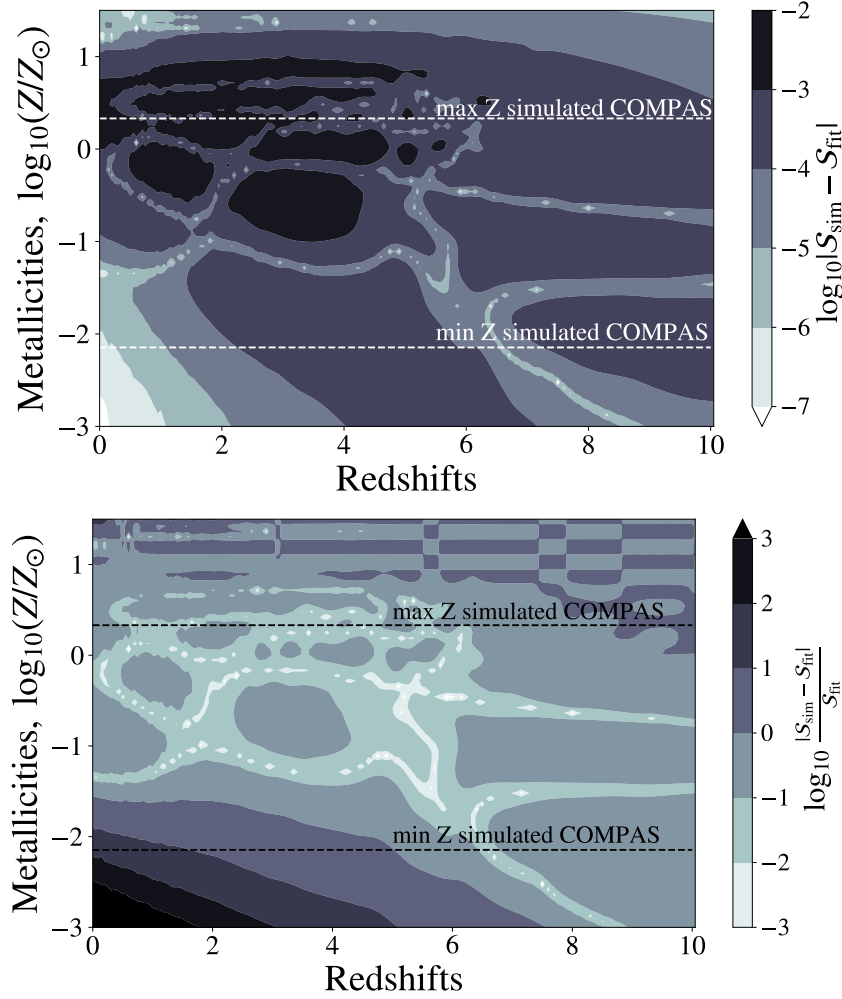


Figure 4.5: log of the residuals (top), and log of the relative error (bottom) between the TNG100 data and our best-fitting model. We show the minimum and maximum metallicity used in [COMPAS](#) simulations with dashed lines in each plot.

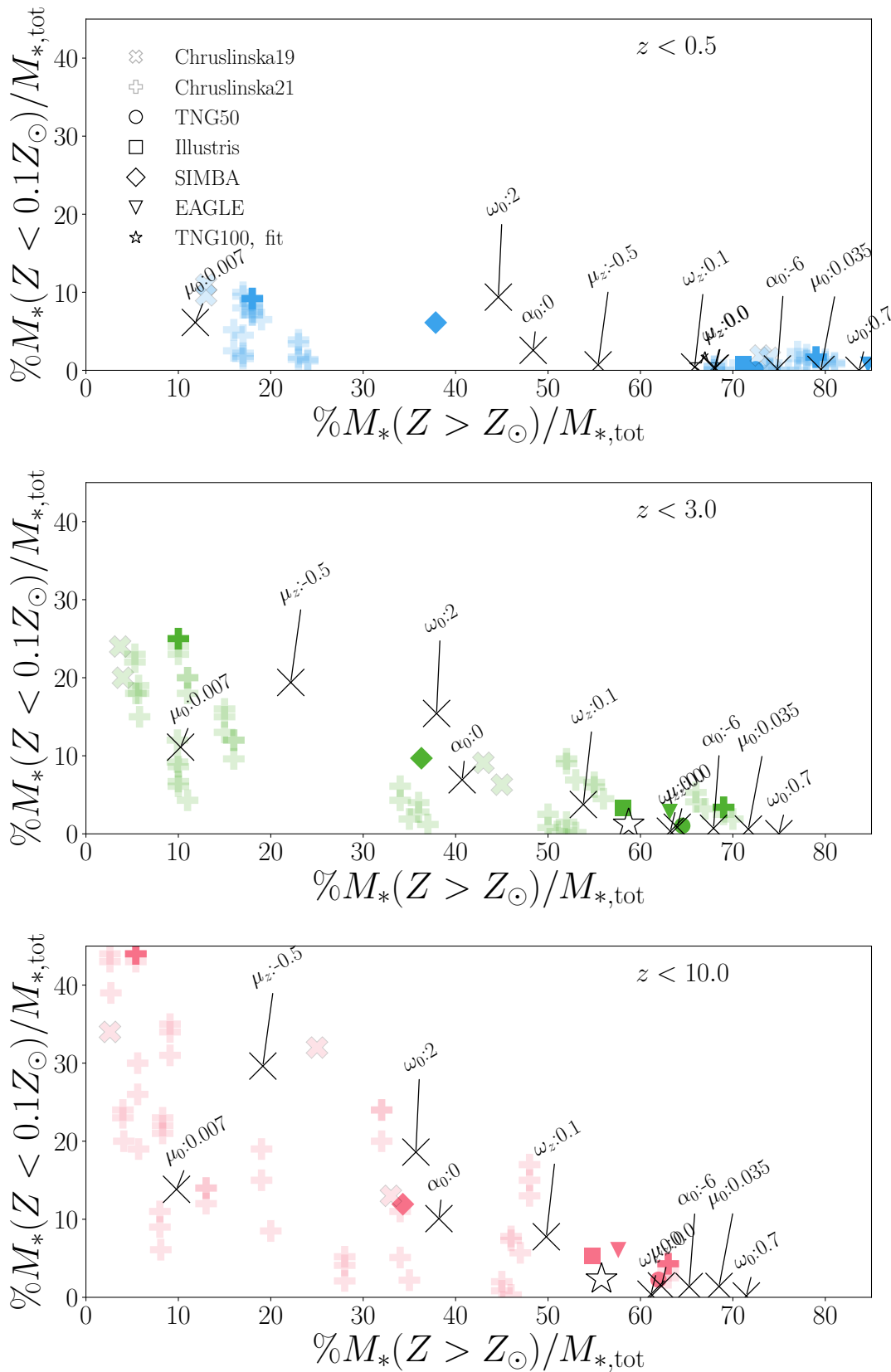
metallicities (about 10 times Z_\odot). This is because in this regime, the TNG data is very sparse and contains regions where the rate abruptly drops to zero. To avoid sharp features in the data, we use interpolated TNG data to produce the fit. We note that we chose to minimize the squared residuals (which is similar to minimizing the mean squared error) in favour of minimizing, for example, the relative error, to prevent overfitting such regions of very low star-formation rate. For the illustration purposes in this work, we are most interested in closely fitting the $\mathcal{S}(Z, z)$ between the minimum (10^{-4}) and maximum

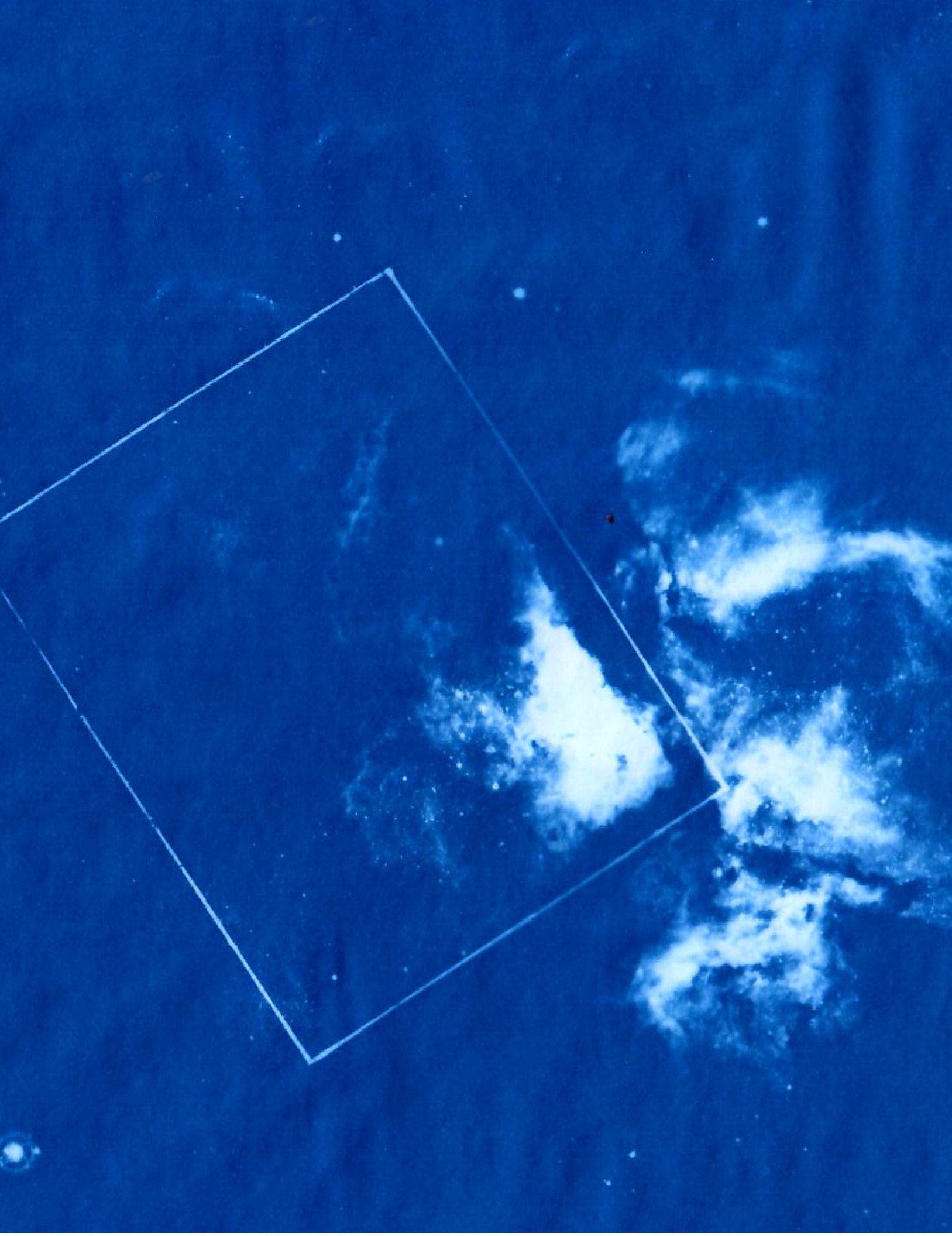
(0.03) metallicities that can be simulated with [COMPAS](#). For applications that focus on extremely low ($< 0.01Z_{\odot}$) or extremely high ($\sim 10 \times Z_{\odot}$) metallicity star formation, a different cost function would be more appropriate.

4.7 Appendix: Determining reasonable variations of the $\mathcal{S}(Z, z)$

To determine reasonable variations of our fiducial model for $\mathcal{S}(Z, z)$, we compute the fraction of low and high metallicity stellar mass formed for redshifts below $z < 0.5$, $z < 3.0$ and $z < 10$. We show the results in Figure 4.6, which is an adaptation of Fig. 2 in [Pakmor et al. \(2022\)](#), which in turn builds on Fig. 9 from [Chruślińska & Nelemans \(2019b\)](#).

Figure 4.6 (following page): Percentage of stellar mass formed at low metallicity ($Z < 0.1Z_{\odot}$), versus high metallicity ($Z > Z_{\odot}$) for all star formation below a certain threshold redshift: $z < 0.5$ (top), $z < 3.0$ (middle) and $z < 10$ (bottom). Data from observation-based variations are shown with semi-transparent thick crosses and plus signs (Chruścińska & Nelemans, 2019b; Chruścińska et al., 2021), the low- and high-metallicity extremes are indicated with opaque symbols. For data from cosmological simulations, we follow Pakmor et al. (2022) and show Illustris (Vogelsberger et al., 2014, squares), Simba (Davé et al., 2019, diamonds), EAGLE (Schaye et al., 2015, triangles), TNG50 and TNG100 (Springel et al., 2018, filled and open circles respectively). Black thin crosses display variations of $\mathcal{S}(Z, z)$ explored in this work. The parameter that is varied with respect to the fiducial is annotated. This shows that our $\mathcal{S}(Z, z)$ variations span the range of reasonable cosmic metallicity density distributions as determined by observation-based and cosmological simulations-based models.





Chapter 5

No peaks without valleys: The stable mass transfer channel for gravitational-wave sources in light of the neutron star–black hole mass gap.

This thesis chapter originally appeared in the literature as

L.A.C. van Son, S. E. de Mink, M. Renzo, S. Justham, E. Zapartas, K. Breivik, T. Callister, W. M. Farr, C. Conroy,
The Astrophysical Journal, 2022, Vol. 940, Issue 2, Article id. 184, 17 pp.

Abstract

Gravitational-wave (GW) detections are starting to reveal features in the mass distribution of double compact objects. The lower end of the black hole (BH) mass distribution is especially interesting as few formation channels contribute here and because it is more robust against variations in the cosmic star formation than the high mass end. In this work we explore the stable mass transfer channel for the formation of GW sources with a focus on the low-mass end of the mass distribution. We conduct an extensive exploration of the uncertain physical processes that impact this channel. We note that, for fiducial assumptions, this channel reproduces the peak at $\sim 9 M_\odot$ in the GW-observed binary BH mass distribution remarkably well, and predicts a cutoff mass that coincides with the upper edge of the purported neutron star BH mass gap. The peak and cutoff mass are a consequence of unique properties of this channel, namely (1) the requirement of stability during the mass transfer phases, and (2) the complex way in which the final compact object masses scale with the initial mass. We provide an analytical expression for the cutoff in the primary component mass and show that this adequately matches our numerical results. Our results imply that selection effects resulting from the formation channel alone can provide an explanation for the purported neutron star –BH mass gap in GW detections. This provides an alternative to the commonly adopted view that the gap emerges during BH formation.

5.1 Introduction

Gravitational-wave (GW) events are revealing substructure in the mass distribution of merging double compact objects (Abbott et al. 2021e, Abbott et al. 2021f, cf. Fishbach et al. 2020, Tiwari & Fairhurst 2021 and Tiwari 2022). Understanding the origin of

these features provides insight into the physics of binary formation and evolution (e.g., Stevenson et al., 2015; Fishbach et al., 2017; Barrett et al., 2018; Wysocki et al., 2019; Fishbach et al., 2020; Vitale et al., 2020; Doctor et al., 2020; Belczynski et al., 2020; Romero-Shaw et al., 2021; Wong et al., 2021b). A better understanding of features in the mass distribution may enable us to break the degeneracy between the observed source mass and redshift from GW sources, which would provide a powerful cosmological probe (also known as ‘dark sirens’ or ‘spectral sirens’, e.g., Schutz, 1986; Farr et al., 2019a; Farmer et al., 2019; María Ezquiaga & Holz, 2022). Additionally, redshift evolution of different parts of the mass distribution can provide constraints on the cosmic star formation rate from a completely new perspective (e.g., Vitale et al., 2019b; van Son et al., 2022d; Chruścińska, 2022).

At present it is difficult to take full advantage of the information that is contained within the mass distribution due to the uncertain origin of the compact object mergers. Many channels have been proposed to explain the formation of double compact objects (see the reviews from Mapelli 2020 and Mandel & Farmer 2022b, and references therein). The mixing fraction between these formation channels is unclear (e.g., Zevin et al., 2021; Wong et al., 2021b). Moreover, large uncertainties in the evolution of massive stellar binaries lead to significant uncertainties in the predictions for the formation of GW sources, this is especially true for predictions from binary population synthesis models (e.g., Abadie et al., 2010; Dominik et al., 2015b; de Mink & Belczynski, 2015b; Giacobbo & Mapelli, 2018; Tang et al., 2020; Broekgaarden et al., 2021a; Bavera et al., 2021b; Belczynski et al., 2022b) It is therefore crucial to find predicted features in the source property distributions that are characteristic and unique to a single formation channel.

The lower end of the BH mass distribution (component masses of $\leq 15 M_{\odot}$) is the most promising site to reveal the origin of double compact objects for two reasons. First, the low mass end of the binary black hole (BBH) mass distribution is least affected by the uncertainties in the metallicity-dependent star formation rate (van Son et al., 2022c). Second, only a few formation channels are relevant at the low-mass regime. Only isolated binary evolution channels have been suggested to produce a global peak of the BH mass distribution at the low mass end (Belczynski et al., 2016b; Giacobbo & Mapelli, 2018; Giacobbo et al., 2018; Wiktorowicz et al., 2019; Belczynski et al., 2020; Tanikawa et al., 2022). The mass distributions from other channels, such as hierarchical formation (Askar et al., 2017; Rodriguez et al., 2019b; Antonini et al., 2019b; Fragione et al., 2020; Fragione & Silk, 2020; Antonini & Gieles, 2020), chemically-homogeneous evolution (CHE; e.g. de Mink et al., 2009; Mandel & de Mink, 2016; Marchant et al., 2016; Riley et al., 2021), population III binaries (e.g. Marigo et al., 2001; Belczynski et al., 2004; Kinugawa et al., 2014; Inayoshi et al., 2017) and binaries merging in the disks of active galactic nuclei (e.g. Baruteau et al., 2011; Bellovary et al., 2016; Leigh et al., 2018; Yang et al., 2019c; Secunda et al., 2019; McKernan et al., 2020) are expected to peak at masses above $20 M_{\odot}$. Antonini et al. (2022) furthermore show that the globular cluster channel under-predicts the observed rate of BBH mergers at the low mas end (around $10 M_{\odot}$) by about two orders of magnitude. Less confusion about the dominant formation channel also makes the low mass end one of the most promising sites to distinguish any astrophysical redshift evolution of the mass distribution from cosmological evolution (e.g., María Ezquiaga & Holz, 2022).

The latest catalogue of GW events has revealed two new features at the low end of

the mass distribution of merging binary black holes (BBH). We expect that these findings are most likely two sides of the same coin and hence need to be jointly investigated. First, the distribution of more massive components of merging BBH systems peaks at approximately $9 M_{\odot}$ (Abbott et al., 2021f; Li et al., 2021; Veske et al., 2021; Tiwari, 2022; Edelman et al., 2022). From hereon, we will use ‘primary’ (secondary) to describe the more (less) massive component of double compact objects. This feature at $9 M_{\odot}$ forms the *global* peak in the primary BH mass distribution (Tanikawa et al., 2022), which implies that the merger rate of $3 M_{\odot}$ BHs is lower than the rate of $9 M_{\odot}$ BHs. This is surprising, because lower mass BHs are expected to form from lower-mass progenitor stars (cf. Woosley et al., 2002b; Spera et al., 2015; Woosley et al., 2020), which are heavily favoured by the initial mass function (e.g., Kroupa, 2001). Second, there is tentative evidence for a relative dearth of merging BBH observations with component masses between $3 M_{\odot}$ and $5 M_{\odot}$. Although at the time of writing, definitive statements about this dearth are hindered by the scarcity of detections in this mass range, Farah et al. (2022), Ye & Fishbach (2022) and Biscoveanu et al. (2022) find that models for the mass distribution as observed in GW *with* a gap are preferred over models *without* a gap. If such a gap is allowed in the model, Farah et al. (2022) find that a ‘rise’ from this gap is expected between about 4.5 and $8.5 M_{\odot}$ (see the blue band in Figure 5.1). Future detectors will decisively probe the existence and location of a low-mass gap in the observations (e.g., Baibhav et al., 2019).

Several works have suggested a gap in the remnant mass distribution between the most massive neutron stars (NSs) and the least massive BHs as an explanation of the dearth of low-mass BHs observed in gravitational waves (e.g., Zevin et al., 2020; Farah et al., 2022; Olejak et al., 2022). This notion of a ‘NS–BH mass gap’ was originally

inspired by observations of X-ray binaries, and has been a topic of active debate for over a decade (e.g., Bailyn et al., 1998; Özel et al., 2010; Farr et al., 2011; Kreidberg et al., 2012; Casares et al., 2017; Wyrzykowski & Mandel, 2020). The discussion ranges from the observational selection biases that could create the *appearance* of a mass gap (e.g., Jonker et al., 2021; Siegel et al., 2022; Liotine et al., 2022), to the theoretical explanation under the assumption that the mass-gap is real (e.g., a fallback mechanism as proposed by Fryer et al. 2012, Fryer et al. 2022, or failed supernova as proposed by Kochanek 2014, Kochanek 2015).

Alternatively, it could be that there is an *evolutionary* selection bias at play that excludes the formation of merging double compact objects with component masses of about $3\text{--}5 M_{\odot}$. In this case, features in the mass distribution could be a telltale sign of the dominant formation channel.

The channels that are expected to dominate BBH formation with low component masses are the stable mass transfer channel (e.g., van den Heuvel et al., 2017; Inayoshi et al., 2017; Bavera et al., 2021b; Marchant et al., 2021; Gallegos-Garcia et al., 2021; van Son et al., 2022d), and the ‘classical’ common-envelope channel (or CE channel, e.g. Belczynski et al., 2007b; Postnov & Yungelson, 2014b; Belczynski et al., 2016b; Vigna-Gómez et al., 2018b). These channels are both forms of isolated binary evolution, and are distinguished based on whether the binary experiences common envelope evolution (CE channel) or only stable mass transfer (stable channel in short from now on). Recent work suggests that the contribution of the CE channel to the BBH merger rate might be overestimated in rapid population synthesis simulations (e.g., Pavlovskii et al., 2017; Klencki et al., 2021; Marchant et al., 2021; Gallegos-Garcia et al., 2021; Olejak et al., 2021b). They argue that many of the systems that are assumed to lead

to successful CE ejection in rapid population synthesis codes should instead either lead to stable mass transfer or a stellar merger. This has caused the stable mass transfer channel to receive renewed attention as a plausible dominant channel for the formation of merging BBHs (e.g., Shao & Li, 2022; Briel et al., 2022b).

5.1.1 Motivation for this work

The inspiration for the work in this paper is shown in Figure 5.1. This Figure was produced shortly after the release of the third GW catalogue (GWTC-3 Abbott et al., 2021c,f), using `COMPAS` version v02.26.03 with the exact same settings as the fiducial model for isolated binary formation from van Son et al. (2022d), i.e., this is not optimised to match the observations. In pink we show the fiducial predictions from the stable channel. The characteristic of this channel is that every mass transfer episode throughout the binary evolution is dynamically stable, and no common envelope occurs. The main reason for the orbit to shrink in this channel is loss of mass with high specific angular momentum from the vicinity of the lower mass companion.

There is a striking similarity between the GW inferred BBH mass distribution and our predictions for the stable channel, shown in Figure 5.1. This model reproduces both a) the dearth of merging primary BH masses between $2.5\text{--}6 M_{\odot}$, and b) a peak around $8\text{--}10 M_{\odot}$. It also matches the local intrinsic rate of BBH mergers. As shown in van Son et al. (2022c), the *location* of features could in particular serve as sign posts of the underlying physics. However, at present, it is not clear whether this resemblance is coincidental given the uncertainties that plague population synthesis modeling (see e.g., Dominik et al., 2015b; de Mink & Belczynski, 2015b; Giacobbo & Mapelli, 2018; Broekgaarden et al., 2021a; Belczynski et al., 2022b) and the significant model

dependence involved in the GW-inference of the mass distribution (e.g., Abbott et al., 2021f). That is, it could be that we are getting the right result for the wrong reasons.

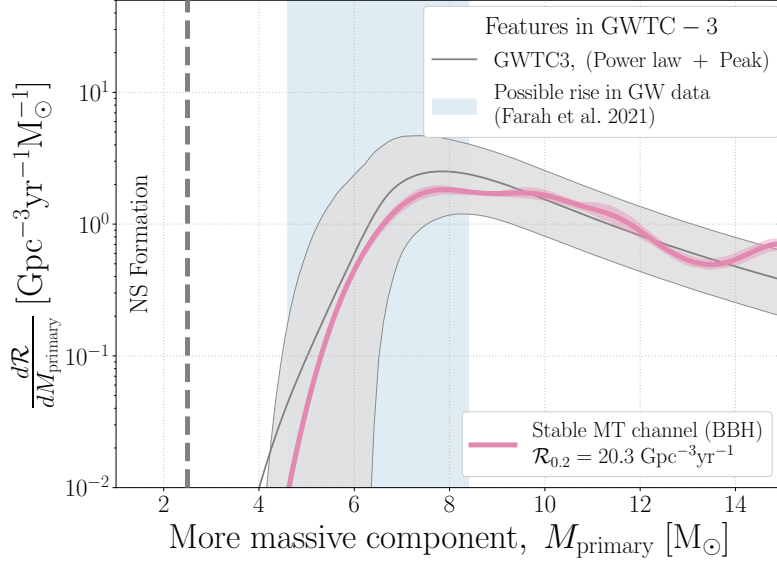


Figure 5.1: Intrinsic distribution of primary masses from BBH merging at redshift 0.2. We show the fiducial predictions for the stable channel in the pink kernel density distributions. The light-shaded area shows the 90% sampling uncertainty as obtained from bootstrapping. The total merger rate of BBHs at $z = 0.2$ is annotated in the legend. The power law + peak model from Abbott et al. (2021f) is shown in grey, light grey bands show the 90% credible intervals. We indicate a tentative rise observed in the GW data with filled blue (see text). We see that the local rate and the location of the peak at the low mass end of the primary BH mass distribution can be explained remarkably well by the stable channel under our fiducial assumptions.

To better understand *why* this model provides a good fit, we investigate the stable mass transfer channel in more detail in this work. In particular, we set out to explore 1) why the stable channel experiences a sharp rise that turns into a peak around $6 M_\odot$, 2) the physical processes that dominate the shape of the mass distribution, and 3) how robust this feature is against variations. We find that the stable channel leads to a cutoff in the primary mass, M_{primary} for BBH and BHNS systems. Adopting a set of simplifying assumptions, we analytically express this minimum mass as a function of birth mass ratio, and determine the main uncertainties in the physical

assumptions that dictate the minimum value of M_{primary} . We discuss how this cutoff mass affects the location of the peak of the BBH mass distribution, while it could also lead to a decrease or even a gap in the mass distribution of M_{primary} that follows from GW events, without the need for a gap in the supernova remnant mass function.

The remainder of this paper is structured as follows: we define the key parameters and assumptions needed to describe typical evolution through the stable channel, and show how these lead to a cutoff mass in Section 5.2. In Section 5.3 we compare our analytically derived minimum to numerical simulations and confirm that the physics variations considered lead to a comprehensive understanding of the minimum mass. We furthermore compute the corresponding mass distribution for every variation considered. We explore the effect of a more complex supernova remnant mass function and of mass loss into a circumbinary disc in Section 5.3.3. Finally, we discuss implications of constraints on the primary mass as expected for the ‘stable mass transfer channel’ in Section 5.4, and we summarise our findings in Section 5.5.

5.2 Analytic approximation of the stable mass transfer channel

In Section 5.2.1 we describe the typical evolution of a binary through the stable channel in chronological order. We describe the key evolutionary steps in terms of uncertain physics parameters and explain our adopted analytical assumptions. The parameters discussed throughout this section are shown in Figure 5.2, which depicts the key evolutionary steps of the stable channel. In Section 5.2.2 we investigate constraints

on the masses that follow from this channel.

5.2.1 The evolutionary steps of the stable channel

At the zero age main sequence (ZAMS, step A in Figure 5.2) we define masses $M_{\text{ZAMS},a}$ and $M_{\text{ZAMS},b}$ for the respectively more and less massive binary component at the onset of H-burning. Throughout this work, we will refer to these components using the subscripts a and b accordingly.

The more massive star evolves on a shorter timescale and will typically overflow its Roche lobe first. We will refer to this as the first mass transfer event (step B in Figure 5.2). We assume that the donor star loses its complete envelope, which implicitly assumes a well defined core-envelope structure, typical for post main sequence mass transfer. The relevant type of mass transfer is known as Case B mass transfer, which is the most common type of binary interaction especially for increasing metallicity (e.g., van den Heuvel, 1969; de Mink et al., 2008; Renzo et al., 2019). We will discuss the effects of this assumption in Section 5.4.5.

We define the core mass fraction, f_{core} , as the fraction of the ZAMS mass that ends up in the He core mass (M_{core}) at the end of the main sequence, i.e., $f_{\text{core}} = M_{\text{core}}/M_{\text{ZAMS}}$. The fraction of mass lost by the donor star will be $1 - f_{\text{core}}$. We assume a fraction β_{acc} of the transferred mass will be accreted by the companion star. We will refer to this as the mass transfer efficiency. We assume that any mass lost from the system during a stable mass transfer event will carry away the specific angular momentum of the accretor (also known as isotropic reemission; e.g., Soberman et al., 1997).

At step C in Figure 5.2, the initially more massive star has become a helium star, and the initially less massive star is still a main sequence star with new mass

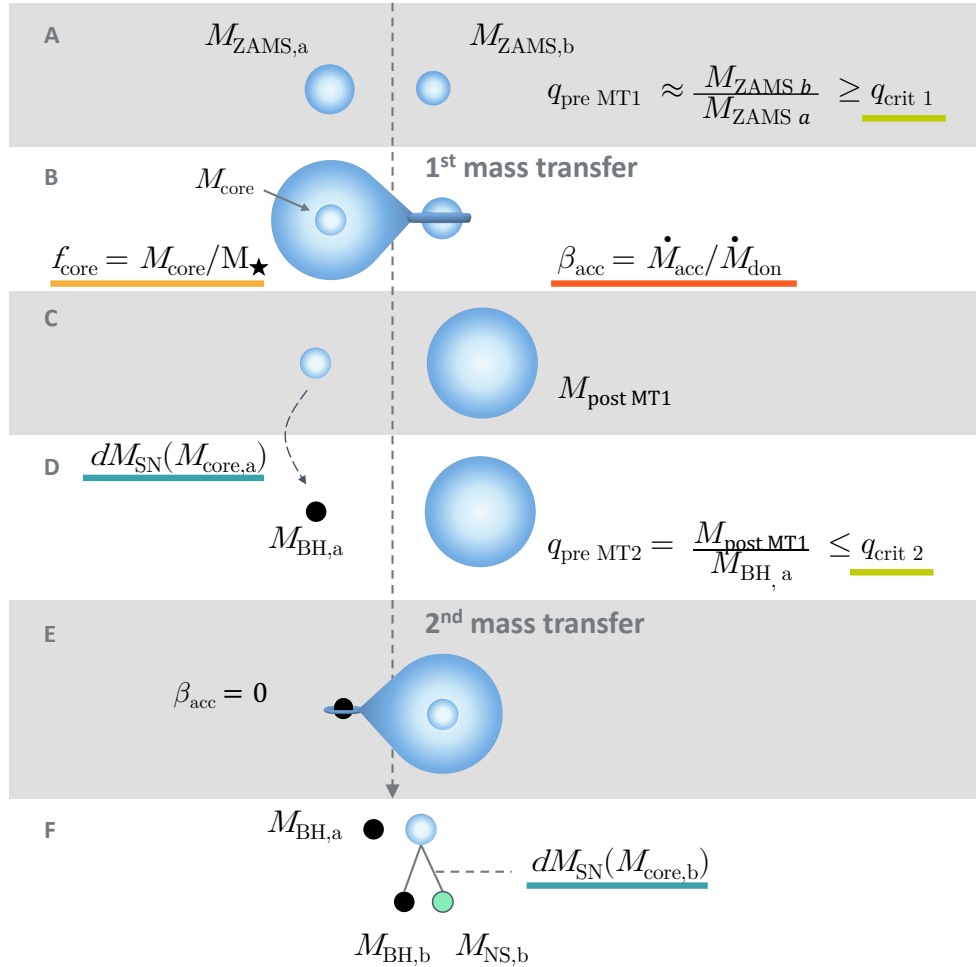


Figure 5.2: Cartoon depiction of the stable mass transfer channel, including the most relevant parameters. See Section 5.2.1 and Table 5.1 for an explanation of the parameters.

$M_{\text{post,MT1}} = M_{\text{ZAMS},b} + \beta_{\text{acc}} M_{\text{ZAMS},a}(1 - f_{\text{core}})$. In the latter approximation we neglect wind mass loss. We assume that the initially more massive star will collapse to form a compact object (step D). This is typically a BH for the systems we consider and we denote its mass as $M_{\text{BH},a}$. Note that this will not necessarily be the more massive compact object. Not all the mass of the core will end up in $M_{\text{BH},a}$. Part could be lost during the supernova (SN), and part will be lost to stellar winds. The SN mass loss

is expected to become particularly important for low-mass BHs. We parameterize this mass loss as $dM_{\text{SN}} \equiv M_{\text{core},1} - M_{\text{BH,a}}$ (cf. “top down” approach in Renzo et al., 2022). Because both winds and SN mass loss are expected to be mass dependent, dM_{SN} is also mass dependent. Here, we assume mass lost from the system carries away the specific angular momentum of the donor (i.e. ‘Jeans mode’).

A second mass transfer phase occurs as the initially less massive star evolves off the main sequence and overflows its Roche lobe (step E). Typically accretion on BHs is limited by radiation pressure in the accretion flow, which leads to very low accretion rates (i.e., Eddington limited accretion). Hence we adopt $\beta_{\text{acc}} = 0$ during the second mass transfer phase. Finally, the initially less massive component collapses to form either a BH or a NS. We again parametrise the difference between the core mass and final remnant mass with dM_{SN} (step F).

In this work, unless stated otherwise we define mass ratios as the initially less massive over the initially more massive binary component. Hence $q_{\text{ZAMS}} \equiv M_{\text{ZAMS,b}}/M_{\text{ZAMS,a}}$. The mass ratios right before the first and second mass mass transfer phases are thus respectively $q_{\text{preMT,1}} = M_{\text{ZAMS,b}}/M_{\text{ZAMS,a}}$ and $q_{\text{preMT,2}} = M_{\text{post,MT1}}/M_{\text{BH,a}}$.

To determine the dynamical stability of mass transfer, we approximate the response of the Roche radius to mass lost, $\zeta_{\text{RL}} \equiv d \ln R_{\text{RL}} / d \ln M_{\star}$, and compare this to an approximation of the adiabatic response of the donor star to mass loss, $\zeta_{\star} \equiv d \ln R_{\star} / d \ln_{\star}$ (see e.g., Soberman et al., 1997; Riley et al., 2022b). Mass transfer is assumed to be stable as long as $\zeta_{\text{RL}} \leq \zeta_{\star}$. The value of ζ_{\star} is determined by the stellar structure of the donor in the adiabatic approximation (e.g., Ge et al., 2015, 2020). Throughout the rest of this work, we adopt $\zeta_{\star} = \zeta_{\text{eff}} = 6.0$ as our reference value for Hertzsprung-gap donor stars (these are subject to the delayed dynamical instability, for which see Hjellming &

Webbink 1987a). ζ_{RL} is a function of β_{acc} , and the mass ratio between the accretor and donor ($q = M_d/M_a$). The dependence of ζ_{eff} on β_{acc} , and the mass ratio between the accretor and the donor, is shown in Figure 4 of Soberman et al. (1997). For clarity, we also show this dependence for different values of β_{acc} in Appendix 5.6.

The requirement of mass-transfer stability leads to a limit on the mass ratio between the accretor and donor. We will refer to these critical mass ratios as $q_{\text{crit},1}$ and $q_{\text{crit},2}$ for the first and second mass transfer phase, with $\beta_{\text{acc}} = 0.5$ and $\beta_{\text{acc}} = 0$ respectively. The mass ratio right before the first mass transfer phase is $q_{\text{preMT},1} = M_b/M_a$, which we approximate with $q_{\text{preMT},1} = M_{\text{ZAMS,b}}/M_{\text{ZAMS,a}}$ in our analytical approximation. Since, at this point, the initially more massive star is overflowing its Roche-lobe, mass transfer will be dynamically stable as long as $M_{\text{ZAMS,b}}/M_{\text{ZAMS,a}} = M_{\text{accretor}}/M_{\text{donor}} \geq q_{\text{crit},1}$. Similarly, right before the second mass transfer, the mass ratio is defined as

$$q_{\text{preMT},2} = M_b/M_a = M_{\text{postMT1}}/M_{\text{BH,a}} = M_{\text{donor}}/M_{\text{accretor}} \leq q_{\text{crit},2}.$$

5.2.2 Derivation of low-mass cutoff for primary components

The main objective of this work is to understand constraints on the allowed compact-object masses at the low end of the mass distribution for the stable mass transfer channel. The characteristic constraint of the stable mass transfer channel is that both the first and the second mass transfer phases must be stable. We start from the constraint on the second mass transfer phase, as we find that it is particularly decisive for the final masses involved. This leads to an inequality between the mass ratio of the system at the onset of the second mass transfer phase and $q_{\text{crit},2}$,

$$q_{\text{preMT},2} = \frac{M_{\text{post,MT1}}}{M_{\text{BH,a}}} \leq q_{\text{crit},2}, \quad (5.1)$$

where $q_{\text{crit},2}$ is the critical mass ratio during the second mass transfer phase (i.e. assuming $\beta_{\text{acc}} = 0$, see Section 5.2.1). $M_{\text{post,MT1}}$ is the mass of the initially less massive star post mass accretion from the first mass transfer event. We can approximate this as

$$M_{\text{post,MT1}} = M_{\text{ZAMS,b}} + M_{\text{ZAMS,a}}\beta_{\text{acc}}(1 - f_{\text{core}}), \quad (5.2)$$

and $M_{\text{BH,a}}$ as

$$M_{\text{BH,a}} = f_{\text{core}}M_{\text{ZAMS,a}} - dM_{\text{SN}}. \quad (5.3)$$

Rewriting Equation 5.1 using Equations 5.2, 5.3 and $q_{\text{ZAMS}} = M_{\text{ZAMS,b}}/M_{\text{ZAMS,a}}$ gives:

$$\frac{q_{\text{ZAMS}} + \beta_{\text{acc}}(1 - f_{\text{core}})}{f_{\text{core}} - \frac{dM_{\text{SN}}}{M_{\text{ZAMS,a}}}} \leq q_{\text{crit},2}. \quad (5.4)$$

In this work, we are specifically interested in placing a lower bound on the possible masses of BBH and BHNS systems formed through the stable mass transfer channel. At this point, the only explicit mass dependence left is $M_{\text{ZAMS,a}}$. However, both f_{core} , and dM_{SN} implicitly depend on $M_{\text{ZAMS,a}}$. In order to find a lower bound on $M_{\text{ZAMS,a}}$, we would like to make these dependencies explicit.

In general, f_{core} is expected to increase with mass. It is however reasonable to adopt an approximately constant value for f_{core} as long as the $M_{\text{ZAMS,a}}$ range of interest is not too large. This is the case for the range of ZAMS masses relevant for producing the lowest mass BHs in our simulations. For $M_{\text{ZAMS,a}} \approx 20 - 40 \text{ M}_{\odot}$, stellar evolution tracks in **COMPAS** lead to core mass fractions of effectively $f_{\text{core}} \approx 0.3 - 0.34$ (which is a result of the assumptions in [Pols et al., 1998](#), on which the **COMPAS** code was based). Hence from

here on we continue using the simplification that is constant at $f_{\text{core}} = 0.34$ (though see appendix 5.7 for an alternative scenario).

In reality, dM_{SN} is a complicated function that depends on both the structure of the core at the moment of core collapse, as well as on the dynamics of the collapse, bounce and shock propagation. However, in general we expect that lower mass cores more easily lead to a successful explosion, and hence lead to more mass loss, than higher mass cores (e.g., Fryer et al., 2012; Müller et al., 2018). For our reference model we adopt the ‘Delayed’ model from Fryer et al. (2012), which is a continuous function that maps CO core masses to final remnant masses. This allows us to express dM_{SN} as a linear function of the core mass;

$$dM_{\text{SN}}(M_{\text{core}}) = \begin{cases} a_{\text{SN}} M_{\text{core}} + b_{\text{SN}} & M_{\text{core}} \leq M_{\text{thresh}} \\ 0 & M_{\text{core}} > M_{\text{thresh}}. \end{cases} \quad (5.5)$$

Here $M_{\text{thresh}} = 14.8 M_{\odot}$ is the threshold core mass above which we assume full fallback occurs, and $a_{\text{SN}} = -0.9$ and $b_{\text{SN}} = 13.9$ are obtained through a linear fit to our reference model (see also in Table 5.1). For dM_{SN} we approximate the core mass as $M_{\text{core}} = f_{\text{core}} M_{\text{ZAMS,a}}$, with f_{core} constant.

Going back to Equation 5.4, we can now explicitly write all terms that depend on $M_{\text{ZAMS,a}}$ on one side of the equation

$$\frac{q_{\text{crit},2} f_{\text{core}} - \beta_{\text{acc}}(1 - f_{\text{core}}) - q_{\text{ZAMS}}}{q_{\text{crit},2}} \geq \frac{dM_{\text{SN}}(M_{\text{core}})}{M_{\text{ZAMS,a}}}, \quad (5.6)$$

which we can re-write to

$$M_{\text{ZAMS,a}} \geq \frac{b_{\text{SN}} q_{\text{crit},2}}{q_{\text{crit},2} f_{\text{core}}(1 - a_{\text{SN}}) - \beta_{\text{acc}}(1 - f_{\text{core}}) - q_{\text{ZAMS}}}. \quad (5.7)$$

So far, we have only used the mass transfer stability constraint from the second mass transfer phase. The requirement that the first mass transfer must be stable also places a constraint on the minimum allowed value for $q_{\text{ZAMS}} \in [q_{\text{crit},1}, 1]$. Hence, we can derive a cut-off mass for $M_{\text{ZAMS,a}}$ by adopting $q_{\text{ZAMS}} = q_{\text{crit},1}$.

Equation 5.7 implies that the minimum ZAMS mass that can lead to double compacts objects through the stable channel, is determined by the physics parameters that are relevant to mass transfer stability at the first and second mass transfer phase. These parameters include $q_{\text{crit},1}$ and $q_{\text{crit},2}$, but also parameters determining the mass ratio at mass transfer, namely β_{acc} , f_{core} and $dM_{\text{SN}}(a_{\text{SN}}, b_{\text{SN}})$.

We can use Equation 5.7 to further derive a minimum mass for each of the final compact objects. For the remnant from the initially more massive star:

$$\min(M_{\text{BH,a}}) = f_{\text{core}} \min(M_{\text{ZAMS,a}}) - dM_{\text{SN}}(M_{\text{core,a}}), \quad (5.8)$$

where $dM_{\text{SN}}(M_{\text{core,a}})$ is a shorthand for Equation 5.5 at $M_{\text{core,a}} = M_{\text{ZAMS,a}} f_{\text{core}}$.

Similarly, for the remnant from the initially less massive star;

$$\min(M_{\text{BH,b}}) = f_{\text{core}} \min(M_{\text{post,MT1}}) - dM_{\text{SN}}(M_{\text{core,b}}), \quad (5.9)$$

where $dM_{\text{SN}}(M_{\text{core,b}})$ is Equation 5.5 at $M_{\text{core,b}} = M_{\text{post,MT1}} f_{\text{core}}$.

Using Equation 5.1, we can constrain $\min(M_{\text{post,MT1}})$ as

$$\min(M_{\text{post,MT1}}) = q_{\text{crit},2} \min(M_{\text{BH,a}}).$$

Finally, to compare with GW observations, we are interested in the BH that will form the more massive (primary) component of the double compact objects, since we cannot infer from GW if the primary descends from the initially more or less massive star. Therefore we consider

$$\min(M_{\text{primary}}) = \max \{\min(M_{\text{BH,a}}), \min(M_{\text{BH,b}})\}. \quad (5.10)$$

Equation 5.10 sets a minimum to the primary mass that can originate from the stable channel. It is an analytical function that depends on the initial condition q_{ZAMS} , and the uncertain physics parameters $q_{\text{crit},2}$, β_{acc} , f_{core} and dM_{SN} ($a_{\text{SN}}, b_{\text{SN}}$). See Table 5.1 for the reference values of these parameters as used in this work.

Table 5.1.: Physics parameters and their reference values.

Variable	Description	Ref. value	Explored variations
β_{acc}	Mass transfer efficiency: fraction of donated mass accreted by the companion star	0.5	[0.0, 0.25, 0.5, 0.75, 1.0]
ζ_{eff}	Response of donor star to mass loss $\zeta_{\text{eff}} \equiv d \ln R_{\star} / d \ln M_{\star}$	6.0	[3.5, 4.5, 5.5, 6.0, 6.5]
$(q_{\text{crit},1}, q_{\text{crit},2})$	Effective critical mass ratio for stable mass transfer, using $\beta_{\text{acc}} = 0.5$ and 0 respectively (first and second mass transfer phase)	(0.25, 4.32)	[(0.41, 3.03), (0.35, 3.55), (0.30, 4.06), (0.28, 4.32), (0.26, 4.58)]
f_{core}	Core mass fraction.	0.34	[0.28, 0.31, 0.34, 0.38, 0.41]
$a_{\text{SN}}, b_{\text{SN}}$	Fit parameters for supernova mass loss dM_{SN} (eq. 5.5)	$-0.9, 13.9 M_{\odot}$	varied prescription to Fryer et al. (2022)
M_{thresh}	Boundary mass for full fallback (eq. 5.5)	$14.8 M_{\odot}$	varied prescription to Fryer et al. (2022)

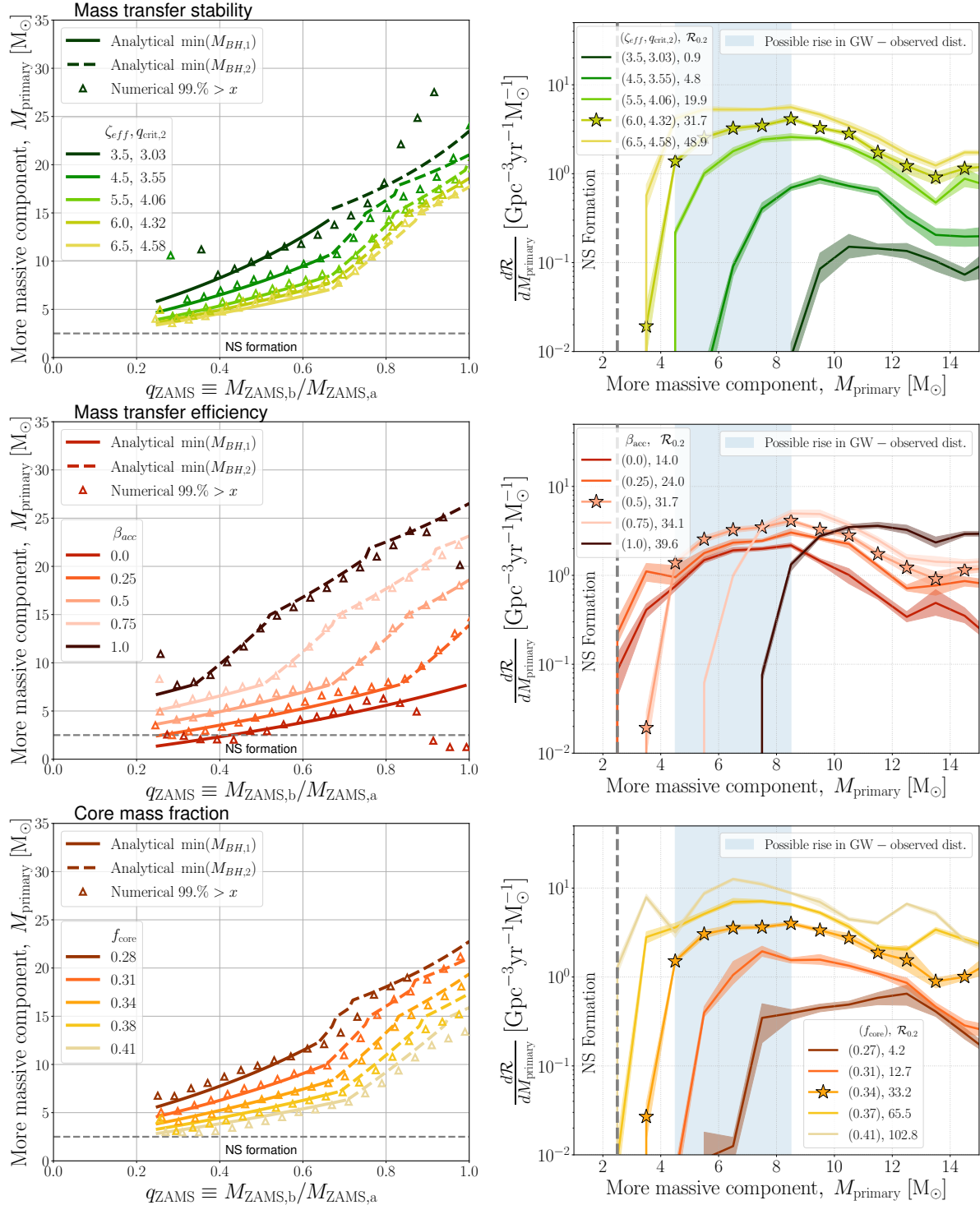
5.3 Results: Effect of the minimum mass for the stable channel

In this section we discuss a comparison of our analytical results presented in Section 5.2 with numerical simulations. For this we adopt a reference model that is very similar

to the fiducial model in van Son et al. (2022d), presented also in Figure 5.1. Below, we will shortly describe the differences. We refer the reader to methods section of van Son et al. (2022d) for a more detailed description of the remainder of adopted physics parameters.

Motivated by the variables in our analytical expression, we explore variations in the stability of the second mass transfer $q_{\text{crit},2}$, the mass transfer efficiency β_{acc} and the core mass fraction f_{core} . We discuss direct changes to the supernova remnant mass function in Section 5.3.3. The varied physics parameters and their reference values are listed in Table 5.1. In contrast to the model in van Son et al. (2022d), we adopt a fixed mass

Figure 5.3 (following page): Model predictions for the masses of BBH and BHNS systems formed through the stable channel. **Left column:** $\min(M_{\text{primary}})$ as a function of the ZAMS mass ratio q_{ZAMS} . Lines show our analytical prediction from Eq. 5.10. Solid (dashed) lines indicate that M_{primary} comes from $M_{\text{BH,a}}$ ($M_{\text{BH,b}}$), described by Eq. 5.8 (5.9). Triangles show results from numerical simulations; 99% of the simulation has a mass M_{primary} larger than that value for bins in q_{ZAMS} of 0.02. **Right column:** Histogram of M_{primary} for BBH and BHNS from the stable channel for bins in M_{primary} of $1 M_{\odot}$. The total rate at redshift 0.2 is annotated in the legend. Star markers indicate the reference model (Table 5.1). Light-shaded areas show the 90% sampling uncertainty, obtained by bootstrapping. We show variations in the stability criteria (ζ_{eff} and $q_{\text{crit},2}$, top), the mass transfer efficiency (β_{acc} , middle), and the core mass fraction (f_{core} , bottom). This shows that the analytically derived minimum can explain the numerical results well. It furthermore displays how the cutoff mass in the stable channel leads to a dearth of BBH and BHNS systems with low primary masses for most variations.



transfer efficiency value of $\beta_{\text{acc}} = 0.5$ as our reference value (Meurs & van den Heuvel, 1989; Belczynski et al., 2008), to enable a clear illustration of the effect described in Section 5.2. The effect of adopting a mass transfer efficiency that varies with accretor properties is discussed in Section 5.4.5. We adopt $\zeta_{\text{eff}} = 6.0$ as our reference for radiative envelope donors with a clear core-envelope structure, compared to $\zeta_{\text{eff}} = 6.5$ in van Son et al. (2022d). For $\zeta_{\text{eff}} = 6.0$, the maximum mass ratio that leads to stable mass transfer $q_{\text{crit},2} \approx 4.32$ for fully non-conservative mass transfer, compared to 4.6 for $\zeta_{\text{eff}} = 6.5$. Both values of ζ_{eff} are in agreement with the work of Ge et al. (2015). The value of $f_{\text{core}} = 0.34$ is chosen as the best fit to our reference simulation. Similarly, the values for a_{SN} and b_{SN} are obtained from a fit to the difference between the pre-SN core mass and remnant mass as a function of the pre-SN core mass for our reference simulation.

In total we ran 25 variations on our reference model. Each simulation set contains 10^7 binaries run with version v.02.26.03 of the COMPAS suite (Riley et al., 2022b). To reduce sampling noise, we have sampled binaries using adaptive importance sampling (Broekgaarden et al., 2019) optimising for BBH and BHNS mergers.

5.3.1 Comparison to numerical data

For this analysis, we include all BBH and BHNS that have experienced exclusively stable mass transfer (i.e. we do not include chemically homogeneously evolving systems). We choose to show both BBH and BHNS, because our analytical prescription in Equation 5.10 does not require the outcome to be either a BBH or BHNS. We furthermore exclude binaries that never interact, or experience only one phase of mass transfer, since such systems are not expected to obey to our derived $\min(M_{\text{primary}})$, and because such systems are much too wide to form GW events.

We compare Equation 5.10 to our grid of numerical simulations in the left column of Figure 5.3. Triangles show where 99% of each simulation has a mass M_{primary} larger than that value, for bins in q_{ZAMS} of width 0.02. We do not include bins with less than 10 samples. Lines show our analytical prediction from Equation 5.10. Solid (dashed) lines indicate that M_{primary} comes from $M_{\text{BH,a}}$ ($M_{\text{BH,b}}$) and is described by Equation 5.8 (5.9). Figure 5.3 shows that our analytical prediction of $\min(M_{\text{primary}})$, described by Equation 5.10, is in good agreement with the numerical data at almost every q_{ZAMS} for all physics variation explored here.

The strongest deviations occur at two points. For $\zeta_{\text{eff}} = 3.53$ (dark green line top right panel) we see that our prescription under-predicts the minimum primary mass from numerical simulations. This is effectively sampling noise: at low ζ_{eff} , we heavily reduce the window for stable mass transfer. Hence, for this variation, we barely sample any systems with high q_{ZAMS} that do not experience unstable mass transfer. Furthermore, at $\beta_{\text{acc}} = 0$ and $q_{\text{ZAMS}} \approx 1$ (bright red line middle right panel), we over-predict the minimum primary mass. We find that this is caused by nearly equal life-time of the two stars: in these cases, the initially more massive star has not yet finished the He-core burning phase when the initially less massive star evolves off the main sequence and overflows its Roche Lobe. This means that $q_{\text{preMT,2}} = M_{\text{ZAMS,b}}/(f_{\text{core}}M_{\text{ZAMS,a}})$, which will be smaller than the assumed $q_{\text{preMT,2}} = M_{\text{ZAMS,b}}/M_{\text{BH,a}}$ in our analytical formula. Hence, the second mass transfer phase is more stable than our analytical formula predicts, and lower primary masses can be formed.

We note that for all variations, $\min(M_{\text{primary}})$ increases with q_{ZAMS} . If there is a relation between q_{ZAMS} and the final double compact object mass ratio q_{final} , then this implies a relation between $\min(M_{\text{primary}})$ and the observed q_{final} .

The absolute minimum M_{primary} formed through the stable channel is found at $q_{\text{ZAMS}} = q_{\text{crit},1}$. In other words, the stable channel will only contribute significantly to systems with $q_{\text{ZAMS}} \geq q_{\text{crit},1}$. Because $q_{\text{crit},1}$ is a function of both β_{acc} and ζ_{eff} (see Appendix 5.6), we expect that the minimum q_{ZAMS} at which the stable channel contributes significantly will also depend on β_{acc} and ζ_{eff} . We see this effect in the top-left and middle-left panels of Figure 5.3. For lower ζ_{eff} , the minimum q_{ZAMS} shifts to higher values because $q_{\text{crit},1}$ increases. That is, we only find systems with $q_{\text{ZAMS}} \geq 0.25$ for $\zeta_{\text{eff}} = 6.5$, while for $\zeta_{\text{eff}} = 3.5$, this shifts to $q_{\text{ZAMS}} \geq 0.4$. Similarly, for $\beta_{\text{acc}} = 0.0$ systems with $q_{\text{ZAMS}} \gtrsim 0.25$ contribute to the distribution while for $\beta_{\text{acc}} = 1.0$, $q_{\text{ZAMS}} \gtrsim 0.33$.

5.3.2 Effect of minimum mass on mass distributions

We show the distribution of M_{primary} for merging BBH and BHNS in the right column of Figure 5.3. Note that this is different from Figure 5.1, where we show only merging BBH. The reason for showing both BBHs and BHNSs is twofold. Firstly, we would like to confirm if the stable channel could lead to a dearth of low mass BHs that could be interpreted as a NS-BH mass gap (see Section 5.1). Excluding BHNS systems could unintentionally create an artificial dearth of low mass BHs. Second, we aim to explore and explain the behaviour of the stable channel. Hence, in order to investigate the effect of the minimum M_{primary} on the resulting mass distribution, we integrate each of the physics variations as shown in the left hand panels of Figure 5.3, over the metallicity-dependent star formation rate density as described in [van Son et al. \(2022d\)](#) and [van Son et al. \(2022c\)](#) (which is based on the approach of earlier work, e.g., [Dominik et al. 2013a, 2015b](#); [Belczynski et al. 2016d](#); [Neijssel et al. 2019](#); [Broekgaarden et al. 2021b](#)). To emphasise the steep features in the mass distribution, we use a histogram instead of a kernel density distribution to display the distribution of primary masses.

We see that a higher cutoff mass can move the minimum primary mass to values that are significantly higher than the maximum NS mass. This affects the location of the peak of the mass distribution, while also potentially opening up a gap between the most massive NS and the least massive BH. Whether such a gap occurs is determined by the adopted physics variations. For many of our physics variations, the stable mass transfer channel is unable to form BBH or BHNS mergers with primary masses $M_{\text{primary}} \sim 3\text{--}4 M_{\odot}$. Below we consider the effect of each physics variation on the primary mass in more detail. For completeness, we also show the chirp mass and final mass ratio distributions in Appendix 5.8. Throughout this section, we will refer to the combined rate of BBH and BHNS as $\mathcal{R}_{0.2}$. We include an overview of the individual BBH and BHNS rates as predicted by the stable channel in Appendix 5.9.

Variations in the mass transfer stability ζ_{eff} Lower values of ζ_{eff} , and equivalently lower values of $q_{\text{crit},2}$, leave less room for stable mass transfer and severely restrict the window for stable mass transfer. Lower values of ζ_{eff} (darker green), lead to higher cutoff masses in M_{primary} . A higher cutoff mass also shifts the peak of the mass distribution towards higher masses. Less room for stable mass transfer furthermore significantly reduces the total merger rate for the stable channel (from $\mathcal{R}_{0.2} \approx 49 \text{ Gpc}^{-3} \text{ yr}^{-1}$ for $\zeta_{\text{eff}} = 6.5$ to $\mathcal{R}_{0.2} \approx 0.9 \text{ Gpc}^{-3} \text{ yr}^{-1}$ for $\zeta_{\text{eff}} = 3.5$). For $\zeta_{\text{eff}} = 6.5$ the stable mass transfer channel can form almost all primary BH masses, though primary black hole masses of about $3 M_{\odot}$ are still much less common than $M_{\text{primary}} \sim 8 M_{\odot}$. For $\zeta_{\text{eff}} = 3.5$, the stable mass transfer only produces BHNSs and BBHs with primary masses above about $9 M_{\odot}$. We further note how M_{primary} derives from the initially more massive component ($M_{\text{BH,a}}$), for systems with $q_{\text{ZAMS}} \lesssim 0.65$, while it derives from the initially less massive component ($M_{\text{BH,b}}$) for $q_{\text{ZAMS}} \gtrsim 0.65$, for every variation of ζ_{eff} (as can be seen in the

upper left panel of Figure 5.3).

Variations in the accreted mass β_{acc} Higher values of β_{acc} significantly raise the minimum value of M_{primary} at constant q_{ZAMS} . Moreover, the slope of $\min(M_{\text{primary}})$ with q_{ZAMS} increases for higher β_{acc} . We understand this through the change in M_{postMT1} . For larger β_{acc} , M_{postMT1} will be larger, leading to larger $q_{\text{preMT},2}$, which leaves less room for stable mass transfer. This effect is more severe for $q_{\text{ZAMS}} \sim 1$, since this implies a more massive companion star at ZAMS. β_{acc} influences whether M_{primary} derives from $M_{\text{BH,a}}$ versus $M_{\text{BH,b}}$. For $\beta_{\text{acc}} = 1.0$, M_{primary} almost always derives from the initially less massive star (except for $q_{\text{ZAMS}} < 0.35$, light pink line). For $\beta_{\text{acc}} = 0.0$, M_{primary} is always $M_{\text{BH,a}}$ (cf. Broekgaarden et al., 2022; Zevin & Bavera, 2022). For $\beta_{\text{acc}} = 1$, the distribution in M_{primary} drops off steeply below about $8 M_{\odot}$, while for $\beta_{\text{acc}} = 0$ there no real gap left in the mass distribution. We again note how the location of the peak of the mass distribution is determined by the cutoff mass in M_{primary} .

Variations in the core mass fraction f_{core} The general behaviour of the core-mass fraction is similar to the effect of variations in the mass transfer stability: the peak of the primary mass distribution shifts to higher masses while the overall rate decreases. Increasing the core mass fraction makes the second mass transfer phase more stable for constant values of q_{ZAMS} . This is because for higher f_{core} , $q_{\text{preMT},2}$ is lower and thus less likely to exceed $q_{\text{crit},2}$. $q_{\text{preMT},2} = M_{\text{post,MT1}}/M_{\text{BH,a}}$ is lower for higher f_{core} both because $M_{\text{BH,a}}$ is more massive due to the higher core mass of the initially more massive star, and because M_{postMT1} is reduced since there is less envelope left to be accreted during the first mass transfer phase. Hence, higher core mass fractions allow lower M_{primary} to contribute to the stable mass transfer channel. Increasing the core mass fraction by 20%

($f_{\text{core}} \sim 0.41$) with respect to our fiducial simulation causes the stable mass transfer channel to produce M_{primary} with masses down to the NS limit of $2.5 M_{\odot}$. Moreover, this increases the rate to about $103 \text{ Gpc}^{-3} \text{ yr}^{-1}$. Conversely, lowering the core mass fraction by 20% to $f_{\text{core}} \sim 0.27$ lowers the rate to about $4 \text{ Gpc}^{-3} \text{ yr}^{-1}$, while only allowing $M_{\text{primary}} \geq 7 M_{\odot}$.

5.3.3 Variations in the SN mass loss and angular momentum loss

In this section we explore two further variations that are not captured by our simplified analytical model, while they are expected to significantly impact the mass distribution of merging double compact objects resulting from the stable channel.

Supernova remnant mass function

In Section 5.3.2 we explore variations on all variables that appear in our analytical expression Equation 5.10, except for the supernova mass loss dM_{SN} (Equation 5.5). The supernova mass loss is special, because variations in this function can cause a gap between BH and NS masses even in single stars, regardless of whether a double compact object forms (see also Section 5.1).

Here, we explore variations in the supernova remnant mass function by applying the new prescription from Fryer et al. (2022). In this prescription the remnant mass is a function of the carbon oxygen core mass at core-collapse, $M_{\text{crit}} = 5.75 M_{\odot}$; the lower boundary on the carbon oxygen core mass for BH formation (lower mass cores will form a NS) and f_{mix} , which describes the mixing growth time; higher f_{mix} corresponds to a more rapid growth of the convection. Similar to Fryer et al. (2022) and Olejak et al.

(2022) we explore variations between $f_{\text{mix}} = 0.5$, which is closest to the ‘DELAYED’ model in Fryer et al. (2012), and $f_{\text{mix}} = 4.0$ which is most similar to the ‘RAPID’ model in Fryer et al. (2012). We apply BH kicks according to the ‘fallback’ model from Fryer et al. (2012), where we adopt the proto-NS masses (M_{proto}) from the DELAYED model.

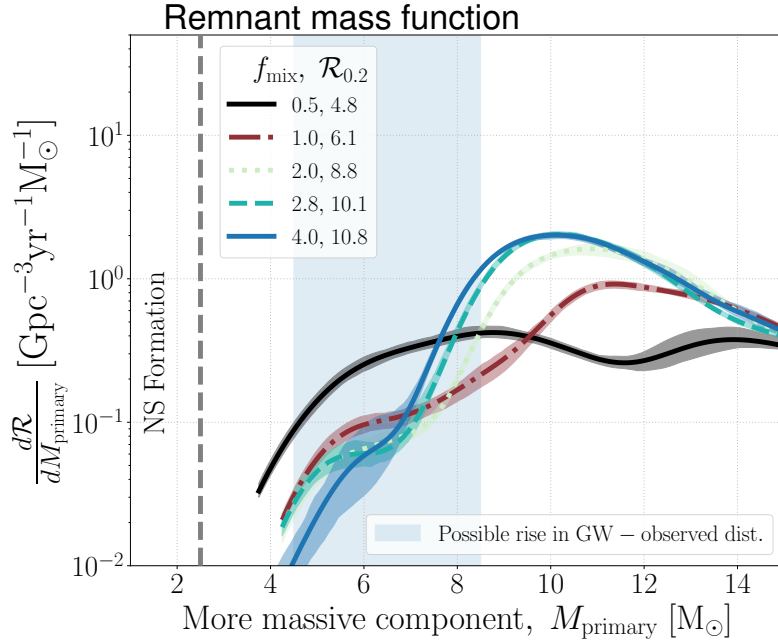


Figure 5.4: Mass distributions in M_{primary} for BBH and BHNS from the stable channel. We show variations in the supernova remnant mass function using the prescription from Fryer et al. (2022). Similar to the right column of Fig. 5.3, but using a kernel density distribution. To prevent the kernel to smooth over the cutoff mass in M_{primary} , we only draw the distribution for M_{primary} values where the corresponding histogram predicts a rate above $10^{-5} \text{ Gpc}^{-3} \text{ yr}^{-1} \text{ M}_{\odot}^{-1}$.

We show the resulting M_{primary} distribution of merging BBH and BHNS for the stable channel in Figure 5.4. All models predict the rate of systems with M_{primary} below about 4 M_{\odot} to be less than $10^{-5} \text{ Gpc}^{-3} \text{ yr}^{-1}$. In other words, all of these models predict a lack of BHs with masses below 4 M_{\odot} . This is not surprising since our fiducial model was chosen such that it is most efficient in forming low mass BHs. The variations in Figure 5.4 are only expected to increase the gap between NS and BH masses. We

furthermore see that the overall merger rate density varies by a factor of about 2 between $f_{\text{mix}} = 0.5$ ($\mathcal{R}_{0.2} \approx 5 \text{ Gpc}^{-3} \text{ yr}^{-1}$) and $f_{\text{mix}} = 4.0$ ($\mathcal{R}_{0.2} \approx 11 \text{ Gpc}^{-3} \text{ yr}^{-1}$). Low f_{mix} causes a shallow rise in the mass distribution with no clear peak. For higher values in f_{mix} , a peak starts to occur around $11 M_{\odot}$. This peak becomes more pronounced and moves to lower M_{primary} for increasing f_{mix} . For $f_{\text{mix}} = 4.0$ the distribution peaks strongly at $M_{\text{primary}} = 9.5 M_{\odot}$, below which it decays steeply towards $M_{\text{primary}} = 6 M_{\odot}$.

The shape of the mass distribution is similar to the results from [Olejak et al. \(2022\)](#) (top right panel of their Figure 5). In line with their results, we find the rate of $M_{\text{primary}} = 6 M_{\odot}$ is much higher for $f_{\text{mix}} = 0.5$ with respect to $f_{\text{mix}} = 4.0$. However, in contrast to [Olejak et al. \(2022\)](#) we only show the contribution of the stable channel. We speculate that this explains why the merger rate density between $3 M_{\odot}$ and $15 M_{\odot}$ is an order of magnitude higher in [Olejak et al. \(2022\)](#) with respect to our results.

Loss of orbital angular momentum through a circumbinary disk.

A key ingredient determining the population of merging double compact objects is the orbital angular momentum loss during mass transfer that is not fully conservative. In order to form a binary compact enough to merge within a Hubble time through GW emission, it is generally crucial for the binary to shrink to a tight orbit during the second mass transfer phase. Which binaries manage to lose enough orbital angular momentum during this mass transfer phase will thus determine the shape of the mass distribution.

In our fiducial model we assume ‘isotropic re-emission’ of matter during non-conservative stable mass transfer. This means that mass lost from the donor star is assumed to be transported to the vicinity of the accretor (in the form of e.g., an accretion disk), from where it is then ejected as a fast isotropic wind. Hence, the mass lost from

the binary system carries the specific angular momentum of the accretor (e.g., Soberman et al., 1997). When mass is transferred at high rates, it is conceivable that some of the mass is lost through the L2 Lagrange point (see e.g., discussion in Marchant et al., 2021). This mass can end up in a circumbinary ring which removes angular momentum much faster than mass lost through isotropic-reemission (e.g., Artymowicz & Lubow, 1994c; Soberman et al., 1997; Renzo et al., 2019; Lu et al., 2022). An observational example of a system that has been argued to experience mass loss through L2 is SS433 (Fabrika, 1993, 2004). One explanation of the observational outflow signatures of this system is mass loss through a circumbinary disc, see for example Cherepashchuk et al. (2020) and references therein (for an alternative explanation to L2 mass loss see e.g., Blundell et al., 2001).

We explore the effect of the specific angular momentum of mass lost from the system by assuming that a fraction f_{disk} of the mass lost during every stable mass transfer event will be lost with the specific angular momentum of a circumbinary disk. We assume the circumbinary ring to be located at twice the orbital separation (as first suggested by Tutukov & Yungelson, 1979). In Figure 5.5 we show variations of f_{disk} ranging from $f_{\text{disk}} = 0$ (all mass is lost though isotropic-reemission, our fiducial model) to $f_{\text{disk}} = 1$ (all mass is lost from a circumbinary disk).

Variations in f_{disk} have a significant impact on both the rate and the shape of the mass distribution (bottom panel of Figure 5.5). Both the location and the peak of the mass distribution change. Moreover, for $f_{\text{disk}} = 0.75$ and 1.0 , the stable mass transfer channel is effectively killed; the total local merger rate density is decreased to $0.5 \text{ Gpc}^{-3} \text{ yr}^{-1}$ and $0.3 \text{ Gpc}^{-3} \text{ yr}^{-1}$ respectively. We find this is mainly due to an increased number of stellar mergers. This result is in line with previous work that

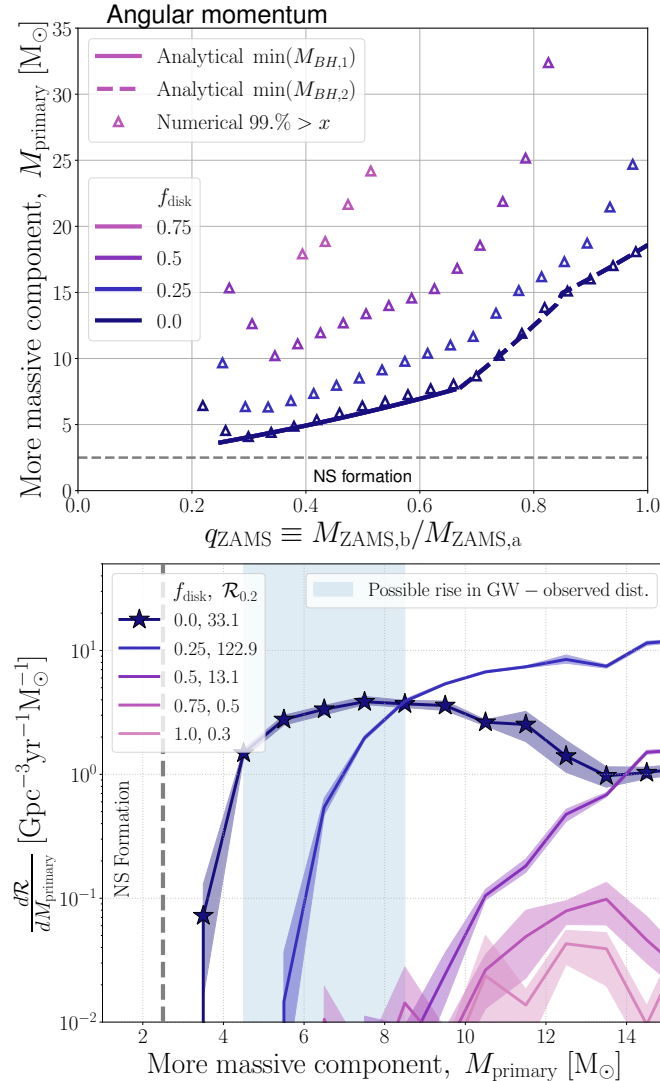


Figure 5.5: Same as Figure 5.3, but for variations in the fraction of the mass that is assumed to be lost from a circumbinary disk, f_{disk} . Because Equation 5.10 does not capture variations in the orbital angular momentum loss, we only show the analytical solution for $f_{\text{disk}} = 0.0$ in the top panel. Furthermore, we do not show $f_{\text{disk}} = 1.0$ in the top panel because it contains too few samples to properly bin the distribution.

studied the effect of a circumbinary ring on the population of Be X-ray binaries and gravitational wave sources (e.g., Portegies Zwart, 1995; De Donder & Vanbeveren, 2004; Mennekens & Vanbeveren, 2014b; Vinciguerra et al., 2020).

Furthermore, the local merger rate density rises to about $141 \text{ Gpc}^{-3} \text{ yr}^{-1}$ for

$f_{\text{disk}} = 0.25$. This is higher than the fiducial merger rate from the CE channel in van Son et al. (2022d). For $f_{\text{disk}} = 0.5$ the rate has dropped back down to about $16 \text{ Gpc}^{-3} \text{ yr}^{-1}$, which implies that the contribution of the stable mass transfer channel experiences some maximum in the local merger rate density between $f_{\text{disk}} = 0$ and $f_{\text{disk}} = 0.5$. The actual value of f_{disk} most likely depends on the mass transfer rate (see Lu et al., 2022, for a detailed analysis). Lu et al. (2022) find that for non-extreme mass ratios (not much less, or much greater than one), f_{disk} can become of order unity for rates $\gtrsim \text{few} \times 10^{-4} M_{\odot} \text{ yr}^{-1}$.

Finally, the minimum primary mass from the stable channel increases as a larger fraction of the mass is lost through a circumbinary disk. In other words, higher f_{disk} correspond to a higher value of $\min(M_{\text{primary}})$ at constant q_{ZAMS} . This can be seen in the top panel of Figure 5.5. This figure also shows that $\min(M_{\text{primary}})$ increases with q_{ZAMS} , following a similar trend as that described by Equations 5.8, 5.9 and 5.10.

5.4 Discussion

In this work, we investigate the low-mass end of the primary mass distribution (M_{primary}) for BBHs and BHNS systems as predicted from the stable mass transfer channel. We find that the stable mass transfer channel leads to a sharp cut-off at the low-mass end of the primary mass distribution. This feature is a consequence of the requirement of stable mass transfer, which is a characteristic property of the channel. We analytically express the minimum allowed primary mass, $\min(M_{\text{primary}})$, as a function of the ZAMS mass ratio q_{ZAMS} . We identify the key physical processes that determine the value of $\min(M_{\text{primary}})$, and discuss the robustness of this minimum against variations. Depending on the adopted physics, we find that $\min(M_{\text{primary}})$ leads to a low-mass cut-off

in the primary masses between $2.5 - 9 M_{\odot}$. Our main results as presented in Figure 5.3 provide several direct predictions.

5.4.1 Remnant mass function or binary physics effect?

Many of the physics variations explored in this work lead to a dearth of merging BBH and BHNS systems with low primary masses. This lack of low-mass BHs also dictates the location of the peak of the BBH primary mass distribution. In this case, the shape of the mass distribution at the low-mass end is thus determined by binary physics.

Alternatively, adopting a remnant mass function with a low-mass gap can also cause the models to predict a pile up just above the upper edge of this gap. Several isolated binary evolution models predict a peak near $10 M_{\odot}$ when adopting the ‘RAPID’ SN engine prescription from Fryer et al. (2012) (see e.g., Belczynski et al., 2016b; Giacobbo & Mapelli, 2018; Giacobbo et al., 2018; Wiktorowicz et al., 2019; Belczynski et al., 2020; Tanikawa et al., 2022). In this case, the remnant mass function determines the shape of the low mass end of the mass distribution.

The crucial difference between these two scenarios is that the remnant mass distribution is expected to affect *all BH and NS formation*, while we expect the constraints discussed in this work to affect *only those systems that evolve through the stable channel* i.e., that have experienced two phases of stable mass transfer.

A smoking gun to determine whether the stable mass transfer channel dominates the low-mass end of the BH mass distribution observed in GW would thus be if the dearth of low-mass BHs persists in the distribution of primary BH masses observed in GW, while a significant number of low-mass BHs are detected as part of systems that are not expected to have evolved through the stable mass transfer channel. Examples of

the latter are low-mass XRB (see the discussion on XRB below in Section 5.4.3)

5.4.2 NSNS and binary white dwarf mergers

In principle, the arguments presented in this work should hold for all binary systems that have experienced stable mass transfer from the initially more massive to the initially less massive star, and vice versa. This implies that the stable mass transfer channel is inefficient at producing lower mass systems like NSNS. This finding agrees with earlier work that suggests the formation of NSNS mergers is dominated by the CE channel (e.g., Vigna-Gómez et al., 2018b; Chruslinska et al., 2018b). Earlier work has also found that different channels dominate the formation of NSNS mergers with respect to BBH mergers (see the appendix of Wagg et al. 2022 and the discussion in Broekgaarden et al. 2021b). If we assume that the CE channel dominates the formation of NSNS systems, while the stable mass transfer channel dominates the shape of the primary mass distribution around the peak at $9 M_{\odot}$, then the transition between these two channels happens within a narrow range of remnant masses. This would have large implications on the efficiency of CE for different donor masses, as it suggests that successful CE ejection is only possible for lower mass stars that produce NS (see also Klencki et al., 2020, 2021).

A similar constraint on the primary mass could be explored for binary White Dwarf (WD) formation, however, many of our assumptions (such as supernova mass loss, and an approximately constant core mass fraction $f_{\text{core}} \approx 0.34$, see also Appendix 5.7) cannot simply be directly adopted for WD progenitors. In the context of the formation of double WDs, Woods et al. (2012) emphasized the importance of systems in which the first phase of mass transfer is stable but the second mass transfer phase is unstable. Numerous works investigate formation channels in which the last mass transfer phase

(which resulted in the double WD) is stable (e.g., Nelson et al., 2004; Kalomeni et al., 2016; Sun & Arras, 2018; Chen et al., 2022). An analysis similar to the one in this paper might be used to study the potential population of double WDs formed following only stable mass transfer in both directions.

5.4.3 Results in context of X-ray binary observations

In this work, we have discussed a potential dearth of BHs with low masses as observed in GW events. The original proposal for a gap in the mass distribution between NS and BHs was based on the detection of X-ray binaries (XRB, Bailyn et al., 1998; Özel et al., 2010; Farr et al., 2011). One might therefore wonder if the stability criteria discussed in this work could also lead to a dearth of low-mass BHs in observed XRBs. However, it is unclear whether XRB systems and GW progenitors belong to the same astrophysical population (see e.g. Fishbach & Kalogera, 2021; Belczynski et al., 2022a). It is difficult to resolve this issue because the observed population of XRB represents a wide variety of binary star evolutionary stages. In order to understand our results in context of XRB observation, we take a closer look at the XRB populations that were used to infer a NS-BH mass gap in the first place.

The population of XRB is commonly subdivided into two classes, characterised by the mass of the donor star. First, there are low-mass XRB, where the compact objects accretes from low-mass donor stars below about $2\text{--}3 M_{\odot}$ through Roche-lobe overflow. The origin of short period low-mass XRB is unknown, but it is most commonly assumed that they are the outcome of a CE event (e.g., Podsiadlowski et al., 2003, for a discussion on plausible evolutionary origins). However, many different evolutionary pathways have been proposed (e.g. Eggleton & Verbunt, 1986; Ivanova, 2006; Michaely & Perets, 2016;

Klencki et al., 2017). Due to the extreme ZAMS mass ratios required to form a compact object + a low-mass companion, we *do not* expect the first mass transfer phase to be stable, and thus we do not expect the stable mass transfer channel to contribute to the population of low-mass XRB. Hence, if there is truly a dearth of low-mass BHs in low-mass XRB, this would not be caused by the stability requirements discussed in this work.

Secondly, there are high-mass XRB, which accrete from a typically higher-mass ($\gtrsim 5 M_{\odot}$) companion star. Due to the longer timescales involved, these systems are often expected to be wind fed as opposed to experiencing stable RLOF (possibly occurs in phase D of Figure 5.2). In this work, we have found that the stability of the *second* mass transfer phase is a crucial element in $\min(M_{\text{primary}})$. Hence we also do not expect the mechanisms as discussed in this work to lead to any dearth of low-mass BHs in high-mass XRB.

There is third population of XRB systems; Wolf-Rayet X-ray binaries (or WR-XRB in short), which are expected to be the direct descendants of high-mass XRB. They are composed of a (stripped) helium star and a compact object and exist on the He burning nuclear timescale. One would thus expect the birthrate of WR-XRB systems to be approximately equal to the birthrate of high-mass XRB. However, while there are hundreds of Galactic high-mass XRB (see Liu et al., 2006, for the most recent review), there is only one known WR-XRB system in the Milky Way (Cygnus X-3 van Kerkwijk et al., 1992). This is known as the ‘missing WR-XRB’ problem (e.g., Lommen et al., 2005). van den Heuvel et al. (2017) argue that this problem can be explained based on arguments of mass transfer stability in the same way as we explain a lack of low-mass BHs in the population of GW sources: only when the mass ratio at the second mass

transfer phase is in the right regime for stable mass transfer, can the system avoid CE evolution. Although the results in our work do not explain a dearth in low or high-mass XRB, they *can* provide an explanation for the missing WR-XRB problem as well as an explanation for a dearth of primary BHs with low masses, inferred from GW events.

As mentioned above, if the dearth of low-mass BHs persists in the distribution of primary BH masses observed in GW while a significant number of low-mass BHs are detected as the less massive components of GW events or as part of low- and high-mass XRB, this could serve as a smoking gun to determine whether the stable mass transfer channel dominates the low-mass end of the mass distribution observed in GW. On the other hand, if a dearth of low-mass BHs remains in *all* mass-observations of BHs, we argue that a gap in the remnant mass distribution is a more likely explanation. A rapidly increasing number of recent detections through various observational methods already seem to challenge whether the NS-BH mass gap is empty (e.g., Thompson et al., 2019; Giesers et al., 2019; Breivik et al., 2019; Rivinius et al., 2020; Wyrzykowski & Mandel, 2020; Gomez & Grindlay, 2021; Sahu et al., 2022; Lam et al., 2022; van der Meij et al., 2021; Jayasinghe et al., 2021, 2022; Andrews et al., 2022). At the same time, many of these candidates are controversial (see El-Badry et al., 2022, and references therein), and the existence of a gap in the remnant mass distribution remains an open question to this day. A large increase in BH mass measurements is expected from both GW observations (Abbott et al., 2018c), as well as from detections of BH + main sequence systems in the Gaia data release 3 (e.g., Breivik et al., 2017; Mashian & Loeb, 2017; Andrews et al., 2019; Langer et al., 2020; Andrews et al., 2021; Chawla et al., 2022; Janssens et al., 2022; Halbwachs et al., 2022). Hence we are hopeful that near future detection surveys will provide evidence in favour or against the existence of a NS-BH mass gap.

5.4.4 Filling the low-mass gap from below

Several works investigated if it is possible to populate the lower mass gap between $3\text{--}5 M_{\odot}$ through hierarchical mergers. [Samsing & Hotokezaka \(2021\)](#) considered NSNS merger products in dense cluster environments. They conclude that populating the low-mass gap through in-cluster mergers of NSs is a much too slow process to be relevant, even for a highly idealised case. In response to the detection of GW190814 (a compact binary coalescence involving a less massive component with a mass of $2.50\text{--}2.67 M_{\odot}$) [Abbott et al., 2020](#)), [Lu et al. \(2021\)](#) propose that GW190814 was a second-generation merger from a hierarchical triple system. They anticipate that this scenario would lead to a narrow peak in the mass distribution of the less massive component masses between 2.5 and $3.5 M_{\odot}$. They find that it is plausible, but rare for a NSNS merger to give rise to a second-generation merger and estimate that 0.1 to 1 per cent of NSNS mergers occurring in triples could contribute to this channel. Similarly [Hamers et al. \(2021\)](#) consider repeated mergers of NSs and BHs in stellar 2+2 quadruple systems and find that second generation mergers are about ten million times less common than first generation counterparts. Hence we do not expect hierarchical mergers to ‘fill the gap from below’, nor cause a peak at about $9 M_{\odot}$.

5.4.5 Caveats

Adopting a fixed value for the accretion efficiency In the model variations presented in Section 5.3, we have adopted a fixed value for $\beta_{\text{acc}} = 0.5$ ([Meurs & van den Heuvel, 1989](#); [Belczynski et al., 2008](#); [Dominik et al., 2012](#)). In contrast, in the model shown in Figure 5.1 we adopt an accretion rate that is limited to the thermal timescale of the accretor to simulate accretors that remain in thermal equilibrium. This

limits the accretion rate to $\dot{M}_a = C \times M_a/t_{KH,a}$, where M_a and $t_{KH,a}$ are the mass and Kelvin-Helmholz time of the accretor, and $C=10$ is a constant factor assumed to take into account the expansion of the accreting star due to mass transfer (Paczyński & Sienkiewicz, 1972; Neo et al., 1977; Hurley et al., 2002; Schneider et al., 2015). Adopting this accretion rate will cause β_{acc} to be effectively zero for binary systems with low $q_{\text{ZAMS}} \sim 0.3$ (see e.g. the top panels of Figures 19 and 20 from Schneider et al., 2015). The value of $\min(M_{\text{primary}})$ is lowest at low values of β_{acc} and q_{ZAMS} (Figure 5.3), and such systems will thus pollute any dearth in the mass range $M_{\text{primary}} = 2.5 - 6 \text{ M}_{\odot}$.

It is hard to say what the real accretion rate will be, since this depends critically on the response of the accretor which is here merely encompassed in the constant C . A more realistic treatment of the expanding accretor could also affect mass-transfer stability, since this expansion may lead to a contact phase and subsequent CE evolution (see e.g., Pols, 1994; Langer & Heger, 1998; Justham et al., 2014). On top of this, the post-mass-transfer properties of the accreting star are not captured by single-star models (Renzo & Götberg, 2021), and will further influence the details of the second mass-transfer phase (Renzo et al., 2022).

Treatment of Case A mass transfer Mass transfer where the donor star overflows its Roche lobe while still on the main sequence is known as ‘Case A’ mass transfer. In general, rapid population synthesis simulations oversimplify the processes involved in a mass transfer episode, but the outcome of Case A mass transfer is particularly difficult to predict (e.g., Pols, 1994; Sen et al., 2022). In this work, we adopt a set value of $\zeta_{MS} = 2$ to determine the stability of mass transfer for donor stars on the main sequence (see Section 5.2). In our simulations, Case A mass transfer is thus more prone to unstable mass transfer, which in part explains why we find that Case A mass transfer is

subdominant in the stable mass transfer channel. Our simulations under-predict the size of the donor’s core following case-A mass transfer. Nonetheless Case A mass transfer is generally assumed to lead to smaller core masses and to be more conservative than Case B mass transfer (e.g., Schneider et al., 2015; Sen et al., 2022), and we expect the former prediction to hold even when core masses are corrected since both smaller cores and more conservative mass transfer lead to higher values of $\min(M_{\text{primary}})$ (see Figure 5.3). Hence we find that systems from Case A mass transfer are not dominant in determining the cut-off mass in M_{primary} .

5.5 Conclusions

We explore the low-mass end of the primary mass distribution of BBH and BHNS systems that can lead to GW sources. We argue that a dearth of BHs with masses between $3\text{--}5 M_{\odot}$, as observed in the GW-inferred mass distribution, should be jointly investigated with the observed peak of primary masses at about $9 M_{\odot}$. With this in mind, we investigate the stable mass transfer channel to GW emitters. We make predictions for the expected merger rates and mass distributions that follow from this channel, and explain their origins. Our main findings are listed below:

1. *The low mass end of the primary BH mass distribution inferred from GW detections can be explained remarkably well by the stable mass transfer channel alone.* For our fiducial assumptions, we naturally match the local rate ($20 \text{ Gpc}^{-3} \text{ yr}^{-1}$ at redshift 0.2) and key features of BBH mass distribution (the dearth of primary masses between $2.5\text{--}6 M_{\odot}$, and the subsequent peak around $8\text{--}10 M_{\odot}$) without need for additional channels (see Figure 5.1).
2. *A unique prediction of the stable channel is that it is unable to produce GW events*

with primary BH masses below a certain cut-off mass. The reason for the existence of the cut-off is (1) the requirement of stability during the mass transfer phases, which imposes constraints on the mass ratios, and (2) the fact that the final BH masses do not simply scale with the initial mass. Specifically, at the onset of the second mass transfer phase, the masses of the binary components can be expressed as a function of the initial masses. This places a bound on the zero-age mass of the initially most massive star and consequently the mass of the BH it gives rise to. Similarly, the requirement of stability during the second mass transfer phase places bounds on the mass of the compact object resulting from secondary star (see Section 5.2).

3. *Our results imply that the binary physics involved in the stable channel alone can provide an explanation for the purported NS–BH mass gap in GW detections.* This is an alternative explanation to the common assertion that the gap results from supernova physics. This also implies that GW detections may not directly reflect the remnant mass function, as selection effects of the formation channels can not be neglected.
4. *We provide an analytical expression for the lower limit for the cut-off mass* We find expressions for the binary components at all relevant stages using parameterised assumptions for the dominant physical processes (see Figure 5.2), namely, the mass transfer efficiency, the core mass fraction, the mass transfer stability and the difference between the core mass and final remnant mass (Equations 5.8, 5.9 and 5.10).
5. *Using numerical simulations, we conduct an extensive exploration of the uncertain*

physical processes that impact the stable channel. We show these impact the shape of the low end of the mass distribution and location of the peak. (Figure 5.3, 5.4 and 5.5).

6. *The difference between the remnant mass function inferred from electromagnetic observations and the mass distribution from GW observations may serve as a smoking gun.* Specifically, if the NS-BH gap fills in for electromagnetic observations but remains for GW observations, this would be a telltale sign of a dominant contribution by the stable channel in this mass range.

acknowledgments

LvS would like to thank Eric Burns, Chris Fryer and David Hendriks useful comments and informative discussions on the impact of the supernova remnant mass prescriptions. LvS performed portions of this study as part of the pre-doctoral Program at the Center for Computational Astrophysics of the Flatiron Institute, supported by the Simons Foundation. The authors thank the anonymous reviewer for helpful comments that improved this work. The authors acknowledge partial financial support from the National Science Foundation under Grant No. (NSF grant number 2009131 and PHY-1748958), the Netherlands Organisation for Scientific Research (NWO) as part of the Vidi research program BinWaves with project number 639.042.728 and the European Union’s Horizon 2020 research and innovation program from the European Research Council (ERC, Grant agreement No. 715063). EZ acknowledges funding support from the European Research Council (ERC) under the European Union’s Horizon 2020 research and innovation programme (Grant agreement No. 772086).

Software and data

All code associated to reproduce the data and plots in this paper is publicly available at https://github.com/LiekeVanSon/LowMBH_and_StableChannel. The data used in this work is available on Zenodo under an open-source Creative Commons Attribution license at [10.5281/zenodo.7080725](https://doi.org/10.5281/zenodo.7080725), and [10.5281/zenodo.7080164](https://doi.org/10.5281/zenodo.7080164). Simulations in this paper made use of the **COMPAS** rapid binary population synthesis code (v02.26.03), which is freely available at <http://github.com/TeamCOMPAS/COMPAS> (Riley et al., 2022b). This research has made use of GW data provided by the GW Open Science Center (<https://www.gw-openscience.org/>), a service of LIGO Laboratory, the LIGO Scientific Collaboration and the Virgo Collaboration. Further software used: astropy (Astropy Collaboration et al., 2013b, 2018b), Python (Van Rossum & Drake, 2009), Matplotlib (Hunter, 2007), NumPy (Harris et al., 2020), SciPy (Virtanen et al., 2020), ipython/jupyter (Perez & Granger, 2007; Kluyver et al., 2016), Seaborn (Waskom, 2021) and hdf5 (Collette et al., 2019).

5.6 Appendix: The dependence of mass transfer stability on the mass ratio and the mass transfer accretion fraction

In Figure 5.6 we show ζ_{RL} as a function of q_{ZAMS} .¹ Mass transfer is dynamically stable as long as $\zeta_{\text{RL}} \leq \zeta_{\text{eff}}$. The intersection of the coloured lines with the adopted value

¹The full functional form of ζ_{RL} can be found at https://github.com/LiekeVanSon/LowMBH_and_StableChannel/blob/master/Code/AppendixFig6_zeta_q_beta_relations.ipynb, where we closely follow Soberman et al. (1997).

of ζ_{eff} (grey horizontal lines) lead to a value of q_{crit} . For example, if we assume $\beta_{\text{acc}} = 0.0$ for the second mass transfer, and $\zeta_{\text{eff}} = 6.0$, we can see $q_{\text{crit},2} = m_{\text{donor}}/m_{\text{accretor}} \approx 4.4$ for this mass transfer phase. Note that we define $q_{\text{crit},1} = M_{\text{ZAMS,b}}/M_{\text{ZAMS,a}}$ which is the inverse of $m_{\text{donor}}/m_{\text{accretor}}$.

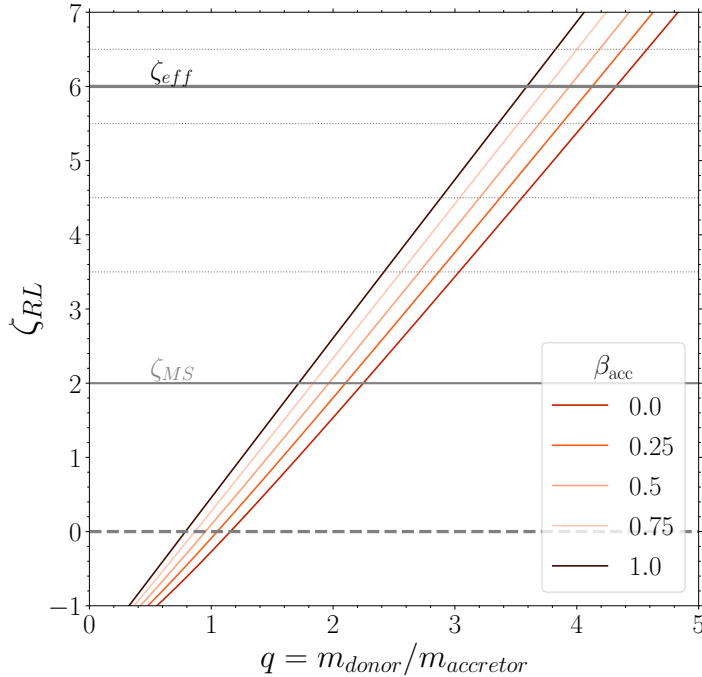


Figure 5.6: ζ_{RL} as a function of mass ratio of between the donor and accretor star. Mass transfer is dynamically stable as long as $\zeta_{\text{RL}} \leq \zeta_{\text{eff}}$. The intersections of ζ_{RL} and ζ_{eff} reveal different values of $q_{\text{crit},1}$ and $q_{\text{crit},2}$. Our default value of $\zeta_{\text{eff}} = 6.0$ for a star with a clear core-envelope structure is annotated. $\zeta_{\text{MS}} = 2$ shows the adopted stability criteria assumed for main-sequence stars (Ge et al., 2015)

5.7 Appendix: Mass dependent core mass fraction

Throughout this work we have assumed that the difference in mass between the core post mass transfer and the final remnant mass is nonzero (i.e., $dM_{\text{SN}} \neq 0$). Note that we use dM_{SN} as a shorthand for *all* mass lost between the core mass post mass transfer

and the final remnant mass, i.e. including stellar winds such as Wolf-Rayet-like winds. We have adopted this because we find that this leads to a more stringent constraint on the BH and NS masses that form from the stable channel. However, in some cases such as the formation of double WDs through stable (early) Case B mass transfer, assuming $dM_{\text{SN}} = 0$ may be closer to the truth.

In this section we thus look at an alternative to Equation 5.7, by assuming $dM_{\text{SN}} = 0$, but f_{core} is a function of the ZAMS mass;

$$f_{\text{core}1} = a_f M_{\text{TAMS}} + b_f, \quad (5.11)$$

where M_{TAMS} refers to the mass at the terminal age main sequence (TAMS). We approximate $M_{\text{TAMS},1} = M_{\text{ZAMS,a}}$ and $M_{\text{TAMS},2} = M_{\text{post,MT1}}$. Applying this to Equation 5.4, we get

$$\frac{q_{\text{ZAMS}} + \beta_{\text{acc}}}{q_{\text{crit},2} + \beta_{\text{acc}}} \leq f_{\text{core}} = a_f M_{\text{ZAMS,a}} + b_f \quad (5.12)$$

Note that we define all mass ratios (including $q_{\text{crit},1}$ and $q_{\text{crit},2}$) as the ratio between the initially less massive component over the initially more massive component. This means that for the first mass transfer phase, mass transfer will be dynamically stable as long as $M_{\text{ZAMS,b}}/M_{\text{ZAMS,a}} = q_{\text{ZAMS}} = M_{\text{accretor}}/M_{\text{donor}} \geq q_{\text{crit},1}$. While for the second mass transfer $q_{\text{preMT},2} = M_b/M_a = M_{\text{postMT1}}/M_{\text{BH,a}} = M_{\text{donor}}/M_{\text{accretor}} \leq q_{\text{crit},2}$.

And thus

$$M_{\text{ZAMS,a}} \geq \frac{1}{a_f} \left[\frac{q_{\text{ZAMS}} + \beta_{\text{acc}}}{q_{\text{crit},2} + \beta_{\text{acc}}} - b_f \right] \quad (5.13)$$

The minimum cut-off mass is reached for $q_{\text{ZAMS}} = q_{\text{crit},1}$, which leads to:

$$M_{\text{ZAMS,a}} \geq \frac{1}{a_f} \left[\frac{q_{\text{crit},1} + \beta_{\text{acc}}}{q_{\text{crit},2} + \beta_{\text{acc}}} - b_f \right] \quad (5.14)$$

Applying this to equations 5.8, 5.9 we get a different relation for $\min(M_{\text{primary}})$ from Equation 5.10.

5.8 Appendix: Chirp mass and final mass ratios

In the left column of Figure 5.7 we show the mass distributions for the chirp masses, M_{Chirp} , for merging BBH and BHNS from the stable mass transfer channel. This shows that the less massive components can form masses low enough for NS formation for most variations. Only for the more extreme assumptions of $\zeta_{\text{eff}} = 3.5$ and $\beta_{\text{acc}} = 1.0$ does a significant gap remain between the lowest chirp mass and the upper boundary for NS formation (set to $2.5 M_{\odot}$ in this work). For almost all variations explored, the distribution of component masses (individual BH and NS masses) does not display an empty ‘gap’ between the most massive NS and the least massive BH.

In the right column of Figure 5.7 we show the final mass ratio $q_{\text{final}} = M_{\text{secondary}}/M_{\text{primary}}$. The mass ratio distributions are all rather flat but display a slight bi-modality with a first peak around $q_{\text{final}} \sim 0.35$ and a second peak around $q_{\text{final}} \sim 0.75$. This bimodality disappears for $\beta_{\text{acc}} = 0.75$ and $\beta_{\text{acc}} = 1.0$ because for these mass transfer efficiencies the lower values of q_{final} are excluded. Similarly, $\zeta_{\text{eff}} = 3.5$ does not produce any q_{final} near one. For all physics variations, the mass ratio distribution drops off steeply below $q_{\text{final}} \approx 0.2$, i.e., the stable mass transfer channel is very inefficient at creating the most extreme mass ratio systems.

5.9 Appendix: Overview of rates

In Tables 5.2 and 5.3 we split $\mathcal{R}_{0.2}$, as shown in Figures 5.3, 5.4 and 5.5 into the individual contributions from the BBH and BHNS merger rate.

Table 5.2.: Merger rates of BBH, BHNS and their combined rate at redshift 0.2, for the core mass fraction, mass transfer stability and mass transfer efficiency variations of the stable channel (as described in Section 5.3.1).

[Gpc $^{-3}$ yr $^{-1}$]	Core mass fraction (f_{core})					Mass transfer stability (ζ_{eff})					Mass transfer efficiency (β_{acc})				
Variations	0.27	0.31	0.34	0.374	0.408	3.5	4.5	5.5	6	6.5	0	0.25	0.5	0.75	1
$\mathcal{R}_{\text{BHNS},0.2}$	0.7	2.7	7.4	11.7	15.5	0	0.3	3.3	6.5	13	3.9	6.6	6.5	0.1	0
$\mathcal{R}_{\text{BBH},0.2}$	3.5	10	25.8	53.9	87.3	0.9	4.6	16.7	25.3	35.9	10.1	17.4	25.3	34	39.6
$\mathcal{R}_{0.2}$	4.2	12.7	33.2	65.5	102.8	0.9	4.8	19.9	31.7	48.9	14	24	31.7	34.1	39.6

Table 5.3.: Merger rates of BBH, BHNS and their combined rate at redshift 0.2, for the supernova prescription and angular momentum variations of the stable channel (as described in Section 5.3.3).

[Gpc $^{-3}$ yr $^{-1}$]	Supernova prescription (f_{mix})							Angular momentum (f_{disk})				
Variations	0.5	0.7	1	1.4	2	2.8	4	0	0.25	0.5	0.75	1
$\mathcal{R}_{\text{BHNS},0.2}$	0.6	0.6	0.7	0.9	0.8	0.9	1.1	7.1	4.5	1.1	0.4	0.3
$\mathcal{R}_{\text{BBH},0.2}$	4.2	4.1	5.5	6.8	8	9.2	9.7	26	118.4	12	0.1	0
$\mathcal{R}_{0.2}$	4.8	4.7	6.1	7.8	8.8	10.1	10.8	33.1	122.9	13.1	0.5	0.3

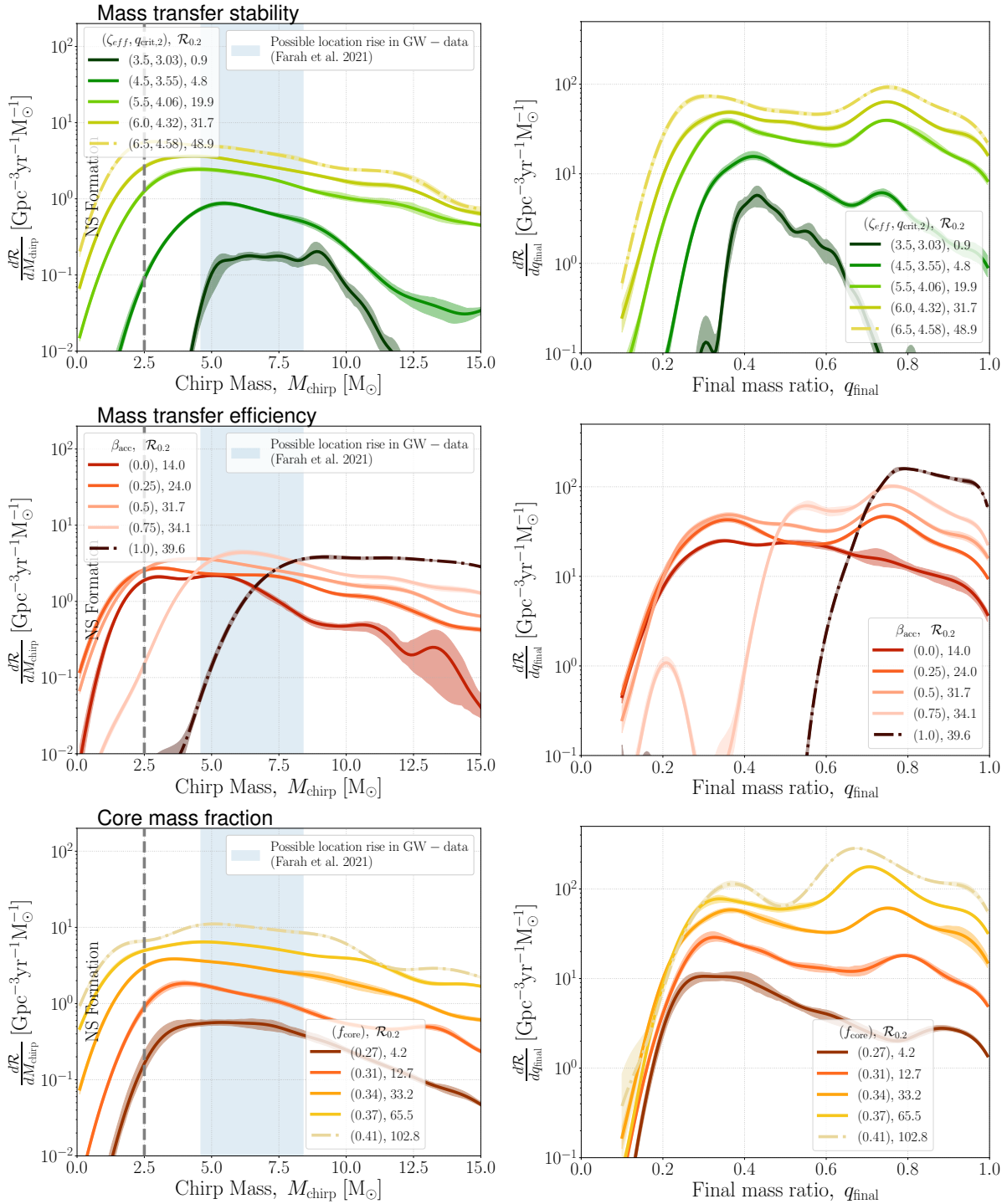
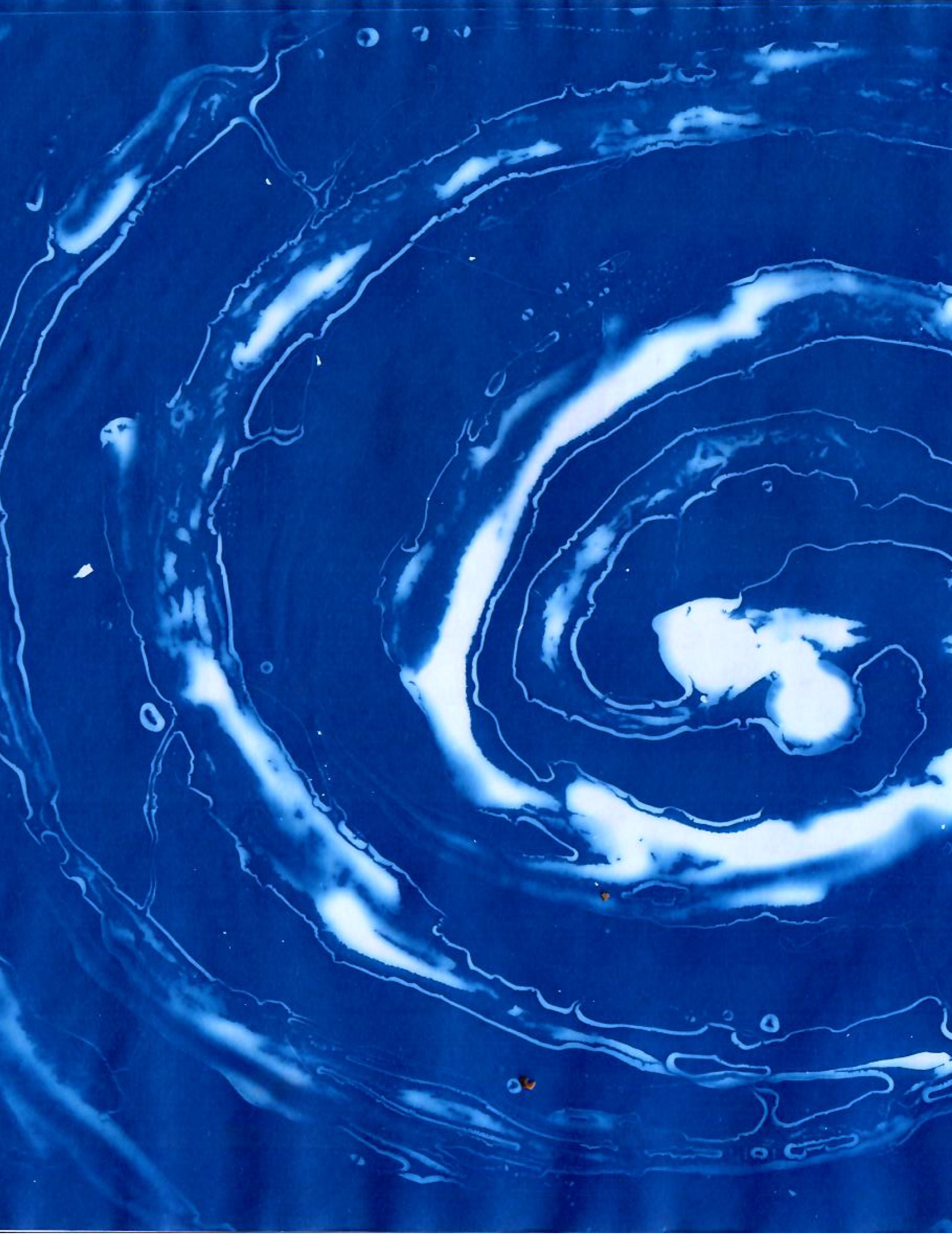


Figure 5.7: The distributions for the chirp mass M_{Chirp} , and the final mass ratio $q_{\text{final}} = M_{\text{secondary}}/M_{\text{primary}}$ for merging BBH and BHNS. Colours and symbols are the same as the right hand panels of Figure 5.3. This shows that the less massive components can form NS masses, often closing any gap between the most massive NS and the least massive BH.



Chapter 6

Summary and Outlook

6.1 Summary of this thesis

At the start of this thesis in 2019, the Gravitational-Wave Transient catalog 1 (GWTC1) featured 10 BBH mergers and the first NSNS merger ever detected (Abbott et al., 2018a). Today the most recent catalog (GWTC3, Abbott et al., 2021c), contains about 90 confident detections of merging double compact objects (namely, 84 BBH, 2 NSNS, and 4 tentative BHNS).¹ This increase in numbers enabled, for the first time, properties of the entire population to be inferred, rather than just those of individual sources. The observed population properties serve as the initial building blocks of the progenitor population puzzle, that provides new insight into the question: ‘how do merging double compact objects form?’ In this thesis, we set out to use the first pieces of this puzzle to form a picture of the massive stellar progenitors that give rise to these double compact objects.

Piece 1: a dearth of high-mass BHs Early GW catalogs indicated a lack of BH mergers with component masses over $45 M_{\odot}$, attributed to the theoretical prediction of Pair Instability Supernovae (PISN). We investigated this prediction in context of binary accretion using rapid population synthesis models ([COMPAS](#)). Our study, detailed in Chapter 2, examined the effect of super-Eddington accretion physics, and confirms that even under extreme assumptions isolated binaries will not pollute the theoretically predicted PISN-mass gap.

Piece 2: the redshift evolution of the rate The redshift evolution of the BBH merger rate is related to the delay-time distribution of the progenitor population. In

¹Notably, the defense of this thesis will roughly coincide with the start of the fourth observing run O4, planned to start on May 24 2023. This run is expected to triple the size of the catalog (see Fig 1.1).

CHAPTER 6. SUMMARY AND OUTLOOK

Chapter 3, identify unique relations between the delay times and masses of BBH systems formed through the two main isolated binary formation channels: the stable Roche-lobe overflow (RLOF) channel and the common-envelope (CE) channel. We predict a distinct redshift evolution for the BBH merger rates in each channel. Our findings indicate that the CE channel will dominate the low-mass systems and follow the star formation rate, while the stable RLOF channel will dominate the high-mass mergers and exhibit a less steep redshift evolution due to longer delay times. These predictions will be testable with near future GW observing runs.

The rate evolution with redshift is also related to the metallicity-dependent cosmic star formation history, $\mathcal{S}(Z, z)$. In chapter 4 we present a new flexible functional form for $\mathcal{S}(Z, z)$, and find that the *locations* of peaks in the mass distributions of merging BBHs are not sensitive to $\mathcal{S}(Z, z)$. Therefore, such features have great potential for revealing the underlying binary physics of stellar progenitors.

Piece 3: The global maximum of the BBH mass distribution, and the ‘NS-BH mass gap’ In our follow-up work (Chapter 5), we aim to understand the *location* of the global peak of the BBH mass distribution and identify a new characteristic of the stable RLOF channel: it cannot form the lowest mass BBHs. Depending on the physics assumed, this may result in a lack of low-mass BHs, which creates a gap in the mass distribution. This gap resembles the debated mass gap between the most massive NSs and the least massive BHs. Our findings provide an alternative explanation for a low-mass gap observed in GW sources and highlight the contribution of the stable RLOF channel.

6.2 The observational landscape of the next 20 years

While the focus of this thesis has largely been on constraints from GW observations, significant advances have also been made in the observations of the electromagnetic (EM) spectrum. Moreover, the “alive” population of binary stars will result in much more broadly applicable constraints than GW-sources, since the latter only make up a very small sub-population of all massive stars.² Both current and future observational facilities and large survey programs are expected to shed new light on different aspects of the lives of massive stars and their unseen companions.

Figure 6.1 (top panel) highlights some of the upcoming surveys.³ The Square Kilometre Array (SKA, [Dewdney et al., 2009](#)) will observe many radio pulsars, thereby also contributing to Pulsar timing arrays (see below) and providing a unique opportunity for multi-messenger astrophysics with LISA (see e.g., [Wagg et al., 2022](#)). The James Webb Space Telescope (JWST [Gardner et al., 2006](#)) promises to provide measurements of low-metallicity star formation at redshifts that were previously inaccessible (see e.g., [Sanders et al., 2022](#)). Large ground-base telescopes like the Extremely Large Telescope (ELT, <https://elt.eso.org/>), the Thirty Meter Telescope (TMT, www.tmt.org), and the Giant Magellan Telescope (GMT www.gmto.org) will allow for massive star surveys in low-metallicity dwarf galaxies. Stellar surveys such as SDSS-V, and Gaia are revealing new insights into the multiplicity of stars (e.g., [Halbwachs et al., 2022](#)),

²At low metallicities ($< 0.01 Z_{\odot}$), we expect about 1 system to successfully form a merging double compact object per $10^5 M_{\odot}$ of stellar mass formed. This rate rapidly declines towards higher metallicities.

³The data and code to reproduce this Figure can be found: <https://github.com/LiekeVanSon/ThesisFigures>

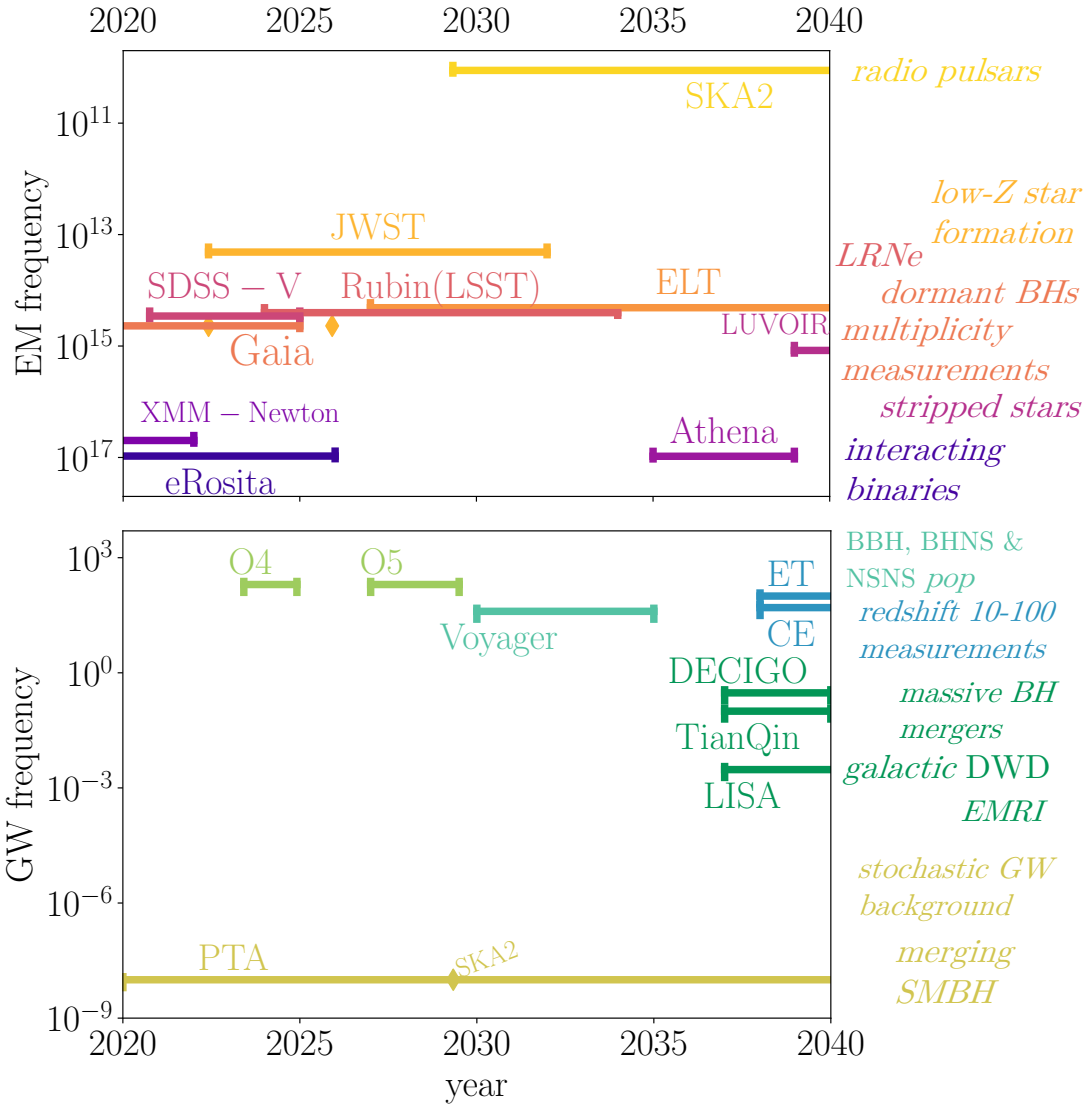


Figure 6.1: A sample of the observational landscape in the next two decades in both EM (top) and GW (bottom) frequencies. Examples of relevant observational constraints that follow from each observing mission are annotated on the right hand side of the plot. Each mission is indicated at either the center of its frequency band, or at the frequency of maximum sensitivity, though some have been slightly shifted for clarity purposes. Diamond symbols indicate either a data release or upgrade to the facility. The dates for third generation GW-missions (2030 and beyond) are very rough estimates. See the text for references and an explanation of the acronyms.

while at the same time revealing dormant (non-accreting) companion BHs (e.g., Shenar et al., 2022). Luminous red novae (LRNe), a class of observed transients linked to

CHAPTER 6. SUMMARY AND OUTLOOK

stellar mergers (e.g., Tylenda et al., 2011), will have their galactic rate measured by the Rubin observatory (previously referred to as the Large Synoptic Survey Telescope, LSST Science Collaboration et al., 2009; Walton et al., 2022), providing an observational constraint on the rates of common envelopes and stellar mergers (e.g., Howitt et al., 2020). The near-UV part of the Large UV/Optical/Infrared Surveyor (LUVOIR Bolcar et al., 2017) will help observe stars stripped in binaries (see Götberg et al., 2018; Goetberg et al., 2022). Lastly, interacting systems are visible as X-ray binaries. They are currently probed by XMM-Newton (Jansen et al., 2001) and eRosita (Predehl et al., 2021), but will be further studied by the European flagship mission Athena (Barcons et al., 2012).

Near future and next generation of GW observations The fourth GW observing run (O4) is set to start in one month, (and it will be succeeded eventually by O5 in 2027). The event catalog is expected to grow by a factor $f_{\text{catalog}} \approx 3$ between O3 and O4, (or $f_{\text{catalog}} \approx 30$ for O5, see Figure 1.1, and Abbott et al., 2018b; Petrov et al., 2022), which will reduce the population-level error by a factor of $\sim 1/\sqrt{f_{\text{catalog}}}$. Moreover, about $1/f_{\text{catalog}}$ of the new detections will fall within the horizon of O3, and consequently be loud events with high S/N, allowing for better constraints on the source properties. This will be particularly valuable in constraining the shape of the distributions of source parameters that leave weaker imprints on the waveform, such as the mass ratio and spin. O4 and O5 will furthermore help us answer questions like: ‘is there a gap in the mass distribution between NSNS and BBH mergers?’ (see predictions in Piece 3 above), and ‘does the mass distribution of BBHs evolve with redshift?’ (allowing to test the predictions laid out in Piece 2 above).

The next generation of ground-based GW detectors, such as the Einstein telescope

CHAPTER 6. SUMMARY AND OUTLOOK

(ET, [Maggiore et al., 2020](#)) and Cosmic explorer (CE, [Reitze et al., 2019](#)) will extend the observing band down from 10Hz to about 3Hz, improve the sensitivity by an order of magnitude, and extend the detector horizons out to cosmological scales. These improvements are expected to be ground-breaking in three ways.

First, the increased sensitivities promise millions to billions of new detections (see Figure 1.1). In particular the population of stellar-mass mergers (with total masses $10 - 1000 M_{\odot}$) is expect to be *complete* out to redshift 2. This will reveal how source-property distributions evolve with redshift, and furthermore opens up exciting possibilities for multidimensional constraints within this population. Second, these detections will include many “golden events” with high S/N, providing precise measurements of source properties such as masses, mass ratios, and spins (see e.g., [Krishnendu et al., 2019](#)). Third, they will probe the extremely high-redshift Universe. Specifically, for BBH mergers of about $20 M_{\odot}$ they will probe merger events out to redshift ~ 100 ([Maggiore et al., 2020](#); [Sathyaprakash et al., 2019b](#)), providing an opportunity to learn about I) the first generation of stars (pop III stars, e.g., [Ng et al., 2021](#)), II) primordial BHs (e.g., [Caldwell et al., 2022](#)), and III) provide an in-situ measurement of the star-formation rate extending far beyond the reach of even the most advanced EM telescopes ([Vitale et al., 2019b](#); [van Son et al., 2022b](#); [Singh et al., 2023](#)).

Currently, we have only scratched the surface of the GW spectrum. Planned GW detections will broaden our horizons to lower frequencies and uncover the rest of the spectrum (bottom panel of Figure 6.1). Space-based interferometers like LISA ([Robson et al., 2019](#)), TianQin ([Luo et al., 2016](#)), and DECIGO ([Kawamura, 2006](#)) will expand the frequency reach from the ground-based detectors down to 10^{-5}Hz . These instruments will allow for eccentricity measurements, detect galactic double white dwarf

CHAPTER 6. SUMMARY AND OUTLOOK

(DWD) binaries, extreme mass ratio inspirals (EMRI), and massive BH mergers (of the order $10^4 - 10^7 M_\odot$, as early as $z = 10$ [Amaro-Seoane et al., 2023](#)). Pulsar Timing Arrays will further open up the nano-hertz frequency range, revealing the stochastic GW background, and mergers of supermassive BH binaries which will help unravel their origin and co-evolution with early galaxies ([Moore et al., 2015](#); [Hazboun et al., 2019](#)).

With the help of new GW detectors and facilities in the EM spectrum, the next two decades promise to be exceptionally bright, especially in GWs!

Chapter A

Cover and Chapter Images

The cover and chapter title pages of this thesis were created using cyanotype printing: a photographic technique invented around 1840. The images are a mixture of impressions of relevant physical processes discussed in this thesis and reproductions of glass plate photographs taken by Harvard's pioneering women astronomical computers during the nineteenth century. They symbolically represent the technological and societal progress made over the past 200 years, uniting a historical technique from a time when humanity first endeavored to capture light on paper, with the present-day advancements, in particular the detection of gravitational waves. Moreover, nearly 100 years after Cecilia Payne-Gaposchkin was the first woman to receive a Ph.D. in astronomy in 1925 it is heartening to note that today, about 60% of the graduate students at the Harvard & Smithsonian Center for Astrophysics are women.

Below we list each of the cyanotype images in this thesis, what they represent, and/or how they connect to the work in this thesis.

Cover *Artist's impression of Merging BBH*

Chapter 1 *Eta Carinae and Notes of Williamina Fleming* - Eta Carinae is a well-known binary system consisting of two very massive stars that has undergone

APPENDIX A. COVER AND CHAPTERS

eruptive mass-loss episodes. The overlaid text are historical notes on double stars and stellar parallax by Williamina Fleming ([Fleming, 1893](#)).

Chapter 2 *Artist’s Impression of Accreting BH in Binary* - This impression reflects the heavily super-Eddington accreting sources discussed in Chapter 2.

Chapter 3 *Orion Nebula and Notes of Williamina Fleming* - Orion is a star-forming region that is relatively close to Earth. We combined this again with notes by Flemming ([Fleming, 1893](#)).

Chapter 4 *Tarantula Nebula* - The Tarantula Nebula, or 30 Doradus, is an icon of massive star formation, such as discussed in Chapter 4. It is the brightest star-forming region in the Local Group and it hosts some of the most massive stars known to date.

Chapter 5 *Close-up of Eta Carinae* - One possible explanation for the eruptions of Eta Carinae is that it has undergone a stellar merger (e.g., [Hirai et al., 2021](#)). As discussed in Chapter 5, unstable mass transfer leading to stellar mergers instead of merging double compact objects could plausibly explain a lack of low-mass BHs in the GW-source population.

Chapter 6 *Artist’s Impression of NSNS Merger*

References

- Abadie, J., et al. 2010, Classical and Quantum Gravity, 27, 173001
- Abbott, B., et al. 2019a, Physical Review X, 9
- Abbott, B. P., et al. 2016a, ApJ, 818, L22
- . 2016b, ApJ, 818, L22
- . 2016c, ApJ, 818, L22
- Abbott, B. P., et al. 2016, Phys. Rev. Lett., 116, 241102
- Abbott, B. P., et al. 2016, Phys. Rev. Lett., 116, 241102
- Abbott, B. P., et al. 2016, ApJ, 833, L1
- Abbott, B. P., et al. 2017a, Classical and Quantum Gravity, 34, 044001
- . 2017b, Phys. Rev. Lett., 119, 161101
- . 2017c, ApJ, 848, L12
- . 2018a, Phys. Rev.
- . 2018b, Living Reviews in Relativity, 21, 3
- . 2018c, Living Reviews in Relativity, 21, 3
- Abbott, B. P., et al. 2019b, The Astrophysical Journal, 882, L24
- . 2019c, Astrophys. J., 882, L24
- Abbott, R., et al. 2020, GW190412: Observation of a Binary-Black-Hole Coalescence with Asymmetric Masses
- Abbott, R., et al. 2020, ApJ, 896, L44
- . 2021a, arXiv e-prints, arXiv:2111.03604
- . 2021b, Physical Review X, 11, 021053
- . 2021c, arXiv e-prints, arXiv:2111.03606
- . 2021d, SoftwareX, 13, 100658
- . 2021e, ApJ, 913, L7

REFERENCES

- . 2021f, arXiv e-prints, arXiv:2111.03634
- Abbott, T. D., et al. 2021g, arXiv e-prints, arXiv:2108.01045
- Ablimit, I., & Maeda, K. 2018, ApJ, 866, 151
- Abramowicz, M. A., Czerny, B., Lasota, J. P., & Szuszkiewicz, E. 1988, ApJ, 332, 646
- Acernese, F., et al. 2015, Classical and Quantum Gravity, 32, 024001
- Adams, S. M., Kochanek, C. S., Gerke, J. R., Stanek, K. Z., & Dai, X. 2017, MNRAS, 468, 4968
- Adhikari, R. X., et al. 2020, Classical and Quantum Gravity, 37, 165003
- Agrawal, P., Hurley, J., Stevenson, S., Rodriguez, C. L., Szecsi, D., & Kemp, A. 2023, arXiv e-prints, arXiv:2303.10187
- Agrawal, P., Hurley, J., Stevenson, S., Szécsi, D., & Flynn, C. 2020, MNRAS, 497, 4549
- Aguirre, A., Hernquist, L., Schaye, J., Katz, N., Weinberg, D. H., & Gardner, J. 2001, ApJ, 561, 521
- Akutsu, T., et al. 2021, Progress of Theoretical and Experimental Physics, 2021, 05A101
- Almeida, L. A., et al. 2017, A&A, 598, A84
- Amaro-Seoane, P., et al. 2023, Living Reviews in Relativity, 26, 2
- Andrews, J. J., Breivik, K., & Chatterjee, S. 2019, ApJ, 886, 68
- Andrews, J. J., Breivik, K., Chawla, C., Rodriguez, C., & Chatterjee, S. 2021, arXiv e-prints, arXiv:2110.05549
- Andrews, J. J., Taggart, K., & Foley, R. 2022, arXiv e-prints, arXiv:2207.00680
- Antonini, F., Chatterjee, S., Rodriguez, C. L., Morscher, M., Pattabiraman, B., Kalogera, V., & Rasio, F. A. 2016, ApJ, 816, 65
- Antonini, F., & Gieles, M. 2020, Phys. Rev. D, 102, 123016
- Antonini, F., Gieles, M., Dosopoulou, F., & Chattopadhyay, D. 2022, arXiv e-prints, arXiv:2208.01081

REFERENCES

- Antonini, F., Gieles, M., & Gualandris, A. 2019a, MNRAS, 486, 5008
—. 2019b, MNRAS, 486, 5008
- Antonini, F., & Perets, H. B. 2012, ApJ, 757, 27
- Antonini, F., Toonen, S., & Hamers, A. S. 2017a, ApJ, 841, 77
—. 2017b, ApJ, 841, 77
- Arca Sedda, M. 2020, ApJ, 891, 47
- Arca Sedda, M., Mapelli, M., Spera, M., Benacquista, M., & Giacobbo, N. 2020a, ApJ, 894, 133
—. 2020b, ApJ, 894, 133
- Arcones, A., & Thielemann, F.-K. 2023, A&A Rev., 31, 1
- Artymowicz, P., & Lubow, S. H. 1994a, ApJ, 421, 651
—. 1994b, ApJ, 421, 651
—. 1994c, ApJ, 421, 651
- Askar, A., Szkudlarek, M., Gondek-Rosińska, D., Giersz, M., & Bulik, T. 2017, MNRAS, 464, L36
- Asplund, M., Grevesse, N., Sauval, A. J., & Scott, P. 2009, ARA&A, 47, 481
- Astropy Collaboration et al. 2013a, A&A, 558, A33
—. 2013b, A&A, 558, A33
—. 2018a, AJ, 156, 123
—. 2018b, AJ, 156, 123
- Bachetti, M., et al. 2014, Nature, 514, 202
- Bae, Y.-B., Kim, C., & Lee, H. M. 2014, MNRAS, 440, 2714
- Baibhav, V., Berti, E., Gerosa, D., Mapelli, M., Giacobbo, N., Bouffanais, Y., & Di Carlo, U. N. 2019, Phys. Rev. D, 100, 064060
- Baibhav, V., Gerosa, D., Berti, E., Wong, K. W. K., Helper, T., & Mould, M. 2020, The mass gap, the spin gap, and the origin of merging binary black holes

REFERENCES

- Bailyn, C. D., Jain, R. K., Coppi, P., & Orosz, J. A. 1998, ApJ, 499, 367
- Baird, E., Fairhurst, S., Hannam, M., & Murphy, P. 2013, Phys. Rev. D, 87, 024035
- Baker, J. G., Boggs, W. D., Centrella, J., Kelly, B. J., McWilliams, S. T., Miller, M. C., & van Meter, J. R. 2007, ApJ, 668, 1140
- Bambi, C. 2018, Annalen der Physik, 530, 1700430
- Banerjee, S. 2021, MNRAS, 503, 3371
- Banerjee, S., Baumgardt, H., & Kroupa, P. 2010, MNRAS, 402, 371
- Barcons, X., et al. 2012, arXiv e-prints, arXiv:1207.2745
- Bardeen, J. M. 1970, Nature, 226, 64
- Barkana, R., & Loeb, A. 2001, Phys. Rep., 349, 125
- Barkat, Z., Rakavy, G., & Sack, N. 1967, Phys. Rev. Lett., 18, 379
- Barrett, J. W., Gaebel, S. M., Neijssel, C. J., Vigna-Gómez, A., Stevenson, S., Berry, C. P. L., Farr, W. M., & Mandel, I. 2018, MNRAS, 477, 4685
- Bartos, I., Kocsis, B., Haiman, Z., & Márka, S. 2017, ApJ, 835, 165
- Baruteau, C., Cuadra, J., & Lin, D. N. C. 2011, ApJ, 726, 28
- Bavera, S. S., et al. 2020, A&A, 635, A97
- . 2021a, A&A, 647, A153
- . 2021b, A&A, 647, A153
- . 2022, A&A, 657, L8
- Begelman, M. C., Volonteri, M., & Rees, M. J. 2006, MNRAS, 370, 289
- Belczynski, K., Bulik, T., Fryer, C. L., Ruiter, A., Valsecchi, F., Vink, J. S., & Hurley, J. R. 2010a, ApJ, 714, 1217
- . 2010b, ApJ, 714, 1217
- Belczynski, K., Bulik, T., & Rudak, B. 2004, ApJ, 608, L45
- Belczynski, K., Dominik, M., Bulik, T., O'Shaughnessy, R., Fryer, C., & Holz, D. E. 2010, The Astrophysical Journal, 715, L138–L141

REFERENCES

- Belczynski, K., Holz, D. E., Bulik, T., & O'Shaughnessy, R. 2016a, *Nature*, 534, 512
- . 2016b, *Nature*, 534, 512
- Belczynski, K., Kalogera, V., & Bulik, T. 2002, *ApJ*, 572, 407
- Belczynski, K., Kalogera, V., Rasio, F. A., Taam, R. E., Zezas, A., Bulik, T., Maccarone, T. J., & Ivanova, N. 2008, *ApJS*, 174, 223
- Belczynski, K., Repetto, S., Holz, D. E., O'Shaughnessy, R., Bulik, T., Berti, E., Fryer, C., & Dominik, M. 2016c, *ApJ*, 819, 108
- . 2016d, *ApJ*, 819, 108
- Belczynski, K., Taam, R. E., Kalogera, V., Rasio, F. A., & Bulik, T. 2007a, *ApJ*, 662, 504
- . 2007b, *ApJ*, 662, 504
- Belczynski, K., Taam, R. E., Rantsiou, E., & van der Sluys, M. 2008, *The Astrophysical Journal*, 682, 474–486
- Belczynski, K., et al. 2016e, *A&A*, 594, A97
- . 2020, *A&A*, 636, A104
- Belczynski, K., et al. 2020, Evolutionary roads leading to low effective spins, high black hole masses, and O1/O2 rates for LIGO/Virgo binary black holes
- Belczynski, K., et al. 2022a, *ApJ*, 925, 69
- . 2022b, *ApJ*, 925, 69
- Bellovary, J. M., Mac Low, M.-M., McKernan, B., & Ford, K. E. S. 2016, *ApJ*, 819, L17
- Bestenlehner, J. M., et al. 2011, *A&A*, 530, L14
- Bethe, H. A., & Brown, G. E. 1998, *ApJ*, 506, 780
- Bird, S., Cholis, I., Muñoz, J. B., Ali-Haïmoud, Y., Kamionkowski, M., Kovetz, E. D., Raccanelli, A., & Riess, A. G. 2016, *Physical Review Letters*, 116, 201301
- Biscoveanu, S., Landry, P., & Vitale, S. 2022, *MNRAS*
- Bisigello, L., Caputi, K. I., Grogin, N., & Koekemoer, A. 2018, *A&A*, 609, A82

REFERENCES

- Blundell, K. M., & Bowler, M. G. 2005, ApJ, 622, L129
- Blundell, K. M., Mioduszewski, A. J., Muxlow, T. W. B., Podsiadlowski, P., & Rupen, M. P. 2001, ApJ, 562, L79
- Boco, L., Lapi, A., Chruslinska, M., Donevski, D., Sicilia, A., & Danese, L. 2021, ApJ, 907, 110
- Bolcar, M. R., et al. 2017, in Society of Photo-Optical Instrumentation Engineers (SPIE) Conference Series, Vol. 10398, Society of Photo-Optical Instrumentation Engineers (SPIE) Conference Series, ed. H. A. MacEwen & J. B. Breckinridge, 1039809
- Bond, J. R., Arnett, W. D., & Carr, B. J. 1982, in NATO Advanced Science Institutes (ASI) Series C, Vol. 90, NATO Advanced Science Institutes (ASI) Series C, ed. M. J. Rees & R. J. Stoneham, 303–311
- Borhanian, S., & Sathyaprakash, B. S. 2022, arXiv e-prints, arXiv:2202.11048
- Bouffanais, Y., Mapelli, M., Gerosa, D., Di Carlo, U. N., Giacobbo, N., Berti, E., & Baibhav, V. 2019, ApJ, 886, 25
- Bouffanais, Y., Mapelli, M., Santoliquido, F., Giacobbo, N., Di Carlo, U. N., Rastello, S., Artale, M. C., & Iorio, G. 2021, MNRAS, 507, 5224
- Brands, S. A., et al. 2022, A&A, 663, A36
- Breivik, K., Chatterjee, S., & Andrews, J. J. 2019, ApJ, 878, L4
- Breivik, K., Chatterjee, S., & Larson, S. L. 2017, ApJ, 850, L13
- Breivik, K., et al. 2020, ApJ, 898, 71
- Briel, M. M., Eldridge, J. J., Stanway, E. R., Stevance, H. F., & Chrimes, A. A. 2021, arXiv e-prints, arXiv:2111.08124
- . 2022a, MNRAS, 514, 1315
- Briel, M. M., Stevance, H. F., & Eldridge, J. J. 2022b, arXiv e-prints, arXiv:2206.13842
- Broekgaarden, F. S., Stevenson, S., & Thrane, E. 2022, ApJ, 938, 45
- Broekgaarden, F. S., et al. 2019, Monthly Notices of the Royal Astronomical Society, 490, 5228–5248

REFERENCES

- Broekgaarden, F. S., et al. 2021a, MNRAS, 508, 5028
- . 2021b, arXiv e-prints, arXiv:2112.05763
- Bromm, V., & Larson, R. B. 2004, ARA&A, 42, 79
- Brott, I., et al. 2011, A&A, 530, A115
- Brown, G. E. 1995, ApJ, 440, 270
- Burrows, A., & Vartanyan, D. 2021, Nature, 589, 29
- Caldwell, R., et al. 2022, General Relativity and Gravitation, 54, 156
- Callister, T., Fishbach, M., Holz, D. E., & Farr, W. M. 2020, ApJ, 896, L32
- Callister, T. A., Haster, C.-J., Ng, K. K. Y., Vitale, S., & Farr, W. M. 2021, ApJ, 922, L5
- Caputi, K. I., et al. 2017, ApJ, 849, 45
- Carr, B. J. 1975, ApJ, 201, 1
- Casares, J., Jonker, P. G., & Israelian, G. 2017, in Handbook of Supernovae, ed. A. W. Alsabti & P. Murdin (Cham: Springer International Publishing), 1499–1526
- Chawla, C., Chatterjee, S., Breivik, K., Moorthy, C. K., Andrews, J. J., & Sanderson, R. E. 2022, ApJ, 931, 107
- Chen, H.-L., Tauris, T. M., Chen, X., & Han, Z. 2022, ApJ, 925, 89
- Cherepashchuk, A., Postnov, K., Molkov, S., Antokhina, E., & Belinski, A. 2020, NewAR, 89, 101542
- Chevalier, R. A. 1993, ApJ, 411, L33
- Chini, R., Hoffmeister, V. H., Nasseri, A., Stahl, O., & Zinnecker, H. 2012, MNRAS, 424, 1925
- Choksi, N., Volonteri, M., Colpi, M., Gnedin, O. Y., & Li, H. 2019, ApJ, 873, 100
- Chruścińska, M. 2022, arXiv e-prints, arXiv:2206.10622
- Chruslinska, M., Belczynski, K., Klencki, J., & Benacquista, M. 2018a, MNRAS, 474, 2937
- . 2018b, MNRAS, 474, 2937

REFERENCES

- Chruścińska, M., & Nelemans, G. 2019a, MNRAS, 488, 5300
- . 2019b, MNRAS, 488, 5300
- Chruścińska, M., Nelemans, G., & Belczynski, K. 2019, MNRAS, 482, 5012
- Chruścińska, M., Nelemans, G., Boco, L., & Lapi, A. 2021, MNRAS, 508, 4994
- Collette, A., et al. 2019, h5py/h5py: 2.10.0, Zenodo
- Costa, G., Bressan, A., Mapelli, M., Marigo, P., Iorio, G., & Spera, M. 2021, MNRAS, 501, 4514
- Cresci, G., Mannucci, F., & Curti, M. 2019, A&A, 627, A42
- Crowther, P. A., Schnurr, O., Hirschi, R., Yusof, N., Parker, R. J., Goodwin, S. P., & Kassim, H. A. 2010, MNRAS, 408, 731
- Daher, C. M., et al. 2022, MNRAS, 512, 2051
- D'Avanzo, P. 2015, Journal of High Energy Astrophysics, 7, 73
- Davé, R., Anglés-Alcázar, D., Narayanan, D., Li, Q., Rafieferantsoa, M. H., & Appleby, S. 2019, MNRAS, 486, 2827
- Davies, B., & Beasor, E. R. 2020, MNRAS, 493, 468
- Davies, B., Crowther, P. A., & Beasor, E. R. 2018, MNRAS, 478, 3138
- De Donder, E., & Vanbeveren, D. 2004, NewA, 9, 1
- de Kool, M. 1990, ApJ, 358, 189
- de Mink, S. E., & Belczynski, K. 2015a, ApJ, 814, 58
- . 2015b, ApJ, 814, 58
- de Mink, S. E., Cantiello, M., Langer, N., Pols, O. R., Brott, I., & Yoon, S. C. 2009, A&A, 497, 243
- de Mink, S. E., & Mandel, I. 2016, MNRAS, 460, 3545
- de Mink, S. E., Pols, O. R., & Yoon, S. C. 2008, in American Institute of Physics Conference Series, Vol. 990, First Stars III, ed. B. W. O'Shea & A. Heger, 230–232
- Dekel, A., & Silk, J. 1986, ApJ, 303, 39

REFERENCES

- Dewdney, P. E., Hall, P. J., Schilizzi, R. T., & Lazio, T. J. L. W. 2009, IEEE Proceedings, 97, 1482
- Di Carlo, U. N., Giacobbo, N., Mapelli, M., Pasquato, M., Spera, M., Wang, L., & Haardt, F. 2019, MNRAS, 487, 2947
- Di Carlo, U. N., Mapelli, M., Bouffanais, Y., Giacobbo, N., Santoliquido, F., Bressan, A., Spera, M., & Haardt, F. 2020a, MNRAS, 497, 1043
- . 2020b, MNRAS, 497, 1043
- Doctor, Z., Wysocki, D., O'Shaughnessy, R., Holz, D. E., & Farr, B. 2020, ApJ, 893, 35
- Dominik, M., Belczynski, K., Fryer, C., Holz, D. E., Berti, E., Bulik, T., Mandel, I., & O'Shaughnessy, R. 2013a, ApJ, 779, 72
- Dominik, M., Belczynski, K., Fryer, C., Holz, D. E., Berti, E., Bulik, T., Mandel, I., & O'Shaughnessy, R. 2012, ApJ, 759, 52
- . 2013b, ApJ, 779, 72
- Dominik, M., et al. 2015a, ApJ, 806, 263
- . 2015b, ApJ, 806, 263
- Doughty, C., & Finlator, K. 2021, MNRAS, 505, 2207
- Downing, J. M. B., Benacquista, M. J., Giersz, M., & Spurzem, R. 2010, MNRAS, 407, 1946
- . 2011, MNRAS, 416, 133
- Dray, L. M., Tout, C. A., Karakas, A. I., & Lattanzio, J. C. 2003, MNRAS, 338, 973
- du Buisson, L., et al. 2020, MNRAS, 499, 5941
- Dvorkin, I., Uzan, J.-P., Vangioni, E., & Silk, J. 2018, MNRAS, 479, 121
- Eddington, A. S. 1926, The Internal Constitution of the Stars (Cambridge University Press)
- Edelman, B., Doctor, Z., Godfrey, J., & Farr, B. 2022, ApJ, 924, 101
- Edelman, B., Farr, B., & Doctor, Z. 2023, ApJ, 946, 16

REFERENCES

- Eggleton, P. P. 1971, MNRAS, 151, 351
- . 1983, ApJ, 268, 368
- Eggleton, P. P., & Verbunt, F. 1986, MNRAS, 220, 13P
- El-Badry, K., Seeburger, R., Jayasinghe, T., Rix, H.-W., Almada, S., Conroy, C., Price-Whelan, A. M., & Burdge, K. 2022, MNRAS, 512, 5620
- Eldridge, J. J., & Maund, J. R. 2016, MNRAS, 461, L117
- Eldridge, J. J., & Stanway, E. R. 2016, MNRAS, 462, 3302
- Eldridge, J. J., Stanway, E. R., Xiao, L., McClelland, L. A. S., Taylor, G., Ng, M., Greis, S. M. L., & Bray, J. C. 2017, PASA, 34, e058
- Eldridge, J. J., & Tout, C. A. 2004, MNRAS, 353, 87
- Fabrika, S. 2004, Astrophys. Space Phys. Res., 12, 1
- Fabrika, S. N. 1993, MNRAS, 261, 241
- Farag, E., Renzo, M., Farmer, R., Chidester, M. T., & Timmes, F. X. 2022, ApJ, 937, 112
- Farah, A., Fishbach, M., Essick, R., Holz, D. E., & Galauadage, S. 2022, ApJ, 931, 108
- Farmer, R., Laplace, E., de Mink, S. E., & Justham, S. 2021, ApJ, 923, 214
- Farmer, R., Renzo, M., de Mink, S. E., Fishbach, M., & Justham, S. 2020, ApJ, 902, L36
- Farmer, R., Renzo, M., de Mink, S. E., Marchant, P., & Justham, S. 2019, The Astrophysical Journal, 887, 53
- Farr, W. M., Fishbach, M., Ye, J., & Holz, D. E. 2019a, ApJ, 883, L42
- . 2019b, ApJ, 883, L42
- Farr, W. M., Sravan, N., Cantrell, A., Kreidberg, L., Bailyn, C. D., Mandel, I., & Kalogera, V. 2011, ApJ, 741, 103
- Faucher-Giguère, C.-A., Kereš, D., & Ma, C.-P. 2011, MNRAS, 417, 2982
- Fernández, R., Quataert, E., Kashiyama, K., & Coughlin, E. R. 2018, MNRAS, 476, 2366

REFERENCES

- Fielding, D., Quataert, E., McCourt, M., & Thompson, T. A. 2017, MNRAS, 466, 3810
- Fishbach, M., Essick, R., & Holz, D. E. 2020, ApJ, 899, L8
- Fishbach, M., Farr, W. M., & Holz, D. E. 2020, The Astrophysical Journal, 891, L31
- Fishbach, M., Farr, W. M., & Holz, D. E. 2020, ApJ, 891, L31
- Fishbach, M., & Holz, D. E. 2017, ApJ, 851, L25
- Fishbach, M., Holz, D. E., & Farr, B. 2017, ApJ, 840, L24
- Fishbach, M., Holz, D. E., & Farr, W. M. 2018, ApJ, 863, L41
- Fishbach, M., & Kalogera, V. 2021, ApJ, 914, L30
- Fishbach, M., et al. 2021, ApJ, 912, 98
- Flannery, B. P., & van den Heuvel, E. P. J. 1975, A&A, 39, 61
- Fleming, W. P. 1893, Project PHAEDRA: Preserving Harvard's Early Data and Research in Astronomy (<https://library.cfa.harvard.edu/project-phaedra>). Harvard College Observatory observations, 891
- Flynn, C., Holmberg, J., Portinari, L., Fuchs, B., & Jahreiß, H. 2006, MNRAS, 372, 1149
- Fowler, W. A., & Hoyle, F. 1964, ApJS, 9, 201
- Fragione, G., & Banerjee, S. 2021, ApJ, 913, L29
- Fragione, G., & Kocsis, B. 2018, Phys. Rev. Lett., 121, 161103
- Fragione, G., Loeb, A., & Rasio, F. A. 2020, ApJ, 902, L26
- Fragione, G., & Silk, J. 2020, MNRAS, 498, 4591
- Fragos, T., et al. 2022, POSYDON: Single and binary star population synthesis code, Astrophysics Source Code Library, record ascl:2210.019
- Fraley, G. S. 1968, Ap&SS, 2, 96
- Frank, J., King, A., & Raine, D. J. 2002, Accretion Power in Astrophysics: Third Edition (Cambridge University Press), 398
- Fruchter, A. S., et al. 2006, Nature, 441, 463

REFERENCES

- Fryer, C. L., Belczynski, K., Wiktorowicz, G., Dominik, M., Kalogera, V., & Holz, D. E. 2012, ApJ, 749, 91
- Fryer, C. L., Benz, W., & Herant, M. 1996, ApJ, 460, 801
- Fryer, C. L., & Kalogera, V. 2001, ApJ, 554, 548
- Fryer, C. L., Olejak, A., & Belczynski, K. 2022, ApJ, 931, 94
- Fuller, J., Cantiello, M., Lecoanet, D., & Quataert, E. 2015, ApJ, 810, 101
- Gallegos-Garcia, M., Berry, C. P. L., Marchant, P., & Kalogera, V. 2021, arXiv e-prints, arXiv:2107.05702
- Gardner, J. P., et al. 2006, Space Sci. Rev., 123, 485
- Ge, H., Webbink, R. F., Chen, X., & Han, Z. 2015, ApJ, 812, 40
- . 2020, ApJ, 899, 132
- Geha, M., et al. 2013, ApJ, 771, 29
- Genel, S., et al. 2018, MNRAS, 474, 3976
- Gennaro, M., et al. 2018, ApJ, 855, 20
- Gerosa, D., & Berti, E. 2019, Phys. Rev. D, 100, 041301
- Giacobbo, N., & Mapelli, M. 2018, MNRAS, 480, 2011
- Giacobbo, N., Mapelli, M., & Spera, M. 2018, MNRAS, 474, 2959
- Giesers, B., et al. 2019, A&A, 632, A3
- Gilkis, A., Shenar, T., Ramachandran, V., Jermyn, A. S., Mahy, L., Oskinova, L. M., Arcavi, I., & Sana, H. 2021, MNRAS, 503, 1884
- Godfrey, J., Edelman, B., & Farr, B. 2023, arXiv e-prints, arXiv:2304.01288
- Goetberg, Y., Drout, M., Farrell, E., Groh, J., Ludwig, B. A., Smith, N., & de Mink, S. E. 2022, Characterizing four massive post-interaction binaries with HST/COS, HST Proposal. Cycle 30, ID. #17123
- Gomez, S., & Grindlay, J. E. 2021, ApJ, 913, 48
- Goswami, S., et al. 2022, A&A, 663, A1

REFERENCES

- Götberg, Y., de Mink, S. E., Groh, J. H., Kupfer, T., Crowther, P. A., Zapartas, E., & Renzo, M. 2018, *A&A*, 615, A78
- Götberg, Y., de Mink, S. E., McQuinn, M., Zapartas, E., Groh, J. H., & Norman, C. 2020, *A&A*, 634, A134
- Gräfener, G., & Hamann, W. R. 2008, *A&A*, 482, 945
- Gupta, I., Borhanian, S., Dhani, A., Chattopadhyay, D., Kashyap, R., Villar, V. A., & Sathyaprakash, B. S. 2023, arXiv e-prints, arXiv:2301.08763
- Halbwachs, J.-L., et al. 2022, arXiv e-prints, arXiv:2206.05726
- Hamann, W. R., & Koesterke, L. 1998, *A&A*, 335, 1003
- Hamers, A. S., Fragione, G., Neunteufel, P., & Kocsis, B. 2021, *MNRAS*, 506, 5345
- Harris, C. R., et al. 2020, *Nature*, 585, 357–362
- Hawking, S. 1971, *MNRAS*, 152, 75
- Hazboun, J. S., Romano, J. D., & Smith, T. L. 2019, *Phys. Rev. D*, 100, 104028
- Heger, A., & Woosley, S. E. 2002, *ApJ*, 567, 532
- Heger, A., Woosley, S. E., & Spruit, H. C. 2005, *ApJ*, 626, 350
- Hemler, Z. S., et al. 2021, *MNRAS*, 506, 3024
- Higgins, E. R., & Vink, J. S. 2020, *A&A*, 635, A175
- Hild, S., et al. 2011, *Classical and Quantum Gravity*, 28, 094013
- Hinshaw, G., et al. 2013, *ApJS*, 208, 19
- Hirai, R., Podsiadlowski, P., Owocki, S. P., Schneider, F. R. N., & Smith, N. 2021, *MNRAS*, 503, 4276
- Hjellming, M. S., & Webbink, R. F. 1987a, *ApJ*, 318, 794
- . 1987b, *ApJ*, 318, 794
- Hoang, B.-M., Naoz, S., Kocsis, B., Rasio, F. A., & Dosopoulou, F. 2018, *ApJ*, 856, 140
- Hobbs, G., Lorimer, D. R., Lyne, A. G., & Kramer, M. 2005, *MNRAS*, 360, 974
- Holz, D. E., & Hughes, S. A. 2005, *ApJ*, 629, 15

REFERENCES

- Hotokezaka, K., & Piran, T. 2017, ApJ, 842, 111
- Houck, J. C., & Chevalier, R. A. 1991, ApJ, 376, 234
- Howitt, G., Stevenson, S., Vigna-Gómez, A., Justham, S., Ivanova, N., Woods, T. E., Neijssel, C. J., & Mandel, I. 2020, MNRAS, 492, 3229
- Humphreys, R. M., & Davidson, K. 1979, ApJ, 232, 409
- Hunter, J. D. 2007, Computing in Science and Engineering, 9, 90
- Hurley, J. R., Pols, O. R., & Tout, C. A. 2000, MNRAS, 315, 543
- Hurley, J. R., Tout, C. A., & Pols, O. R. 2002, MNRAS, 329, 897
- Iben, Icko, J., & Livio, M. 1993, PASP, 105, 1373
- Inayoshi, K., Haiman, Z., & Ostriker, J. P. 2016, MNRAS, 459, 3738
- Inayoshi, K., Hirai, R., Kinugawa, T., & Hotokezaka, K. 2017, MNRAS, 468, 5020
- Iorio, G., et al. 2022, arXiv e-prints, arXiv:2211.11774
- Israel, G. L., et al. 2017, Science, 355, 817
- Ivanov, M., & Fernández, R. 2021, ApJ, 911, 6
- Ivanova, N. 2006, ApJ, 653, L137
- Ivanova, N., Justham, S., & Ricker, P. 2020, Common Envelope Evolution, 2514-3433 (IOP Publishing)
- Ivanova, N., et al. 2013a, A&A Rev., 21, 59
- . 2013b, A&A Rev., 21, 59
- Izzard, R. G., Dray, L. M., Karakas, A. I., Lugaro, M., & Tout, C. A. 2006, A&A, 460, 565
- Izzard, R. G., Glebbeek, E., Stancliffe, R. J., & Pols, O. R. 2009, A&A, 508, 1359
- Izzard, R. G., Tout, C. A., Karakas, A. I., & Pols, O. R. 2004, MNRAS, 350, 407
- Janka, H.-T. 2012, Annual Review of Nuclear and Particle Science, 62, 407
- Jansen, F., et al. 2001, A&A, 365, L1
- Janssens, S., et al. 2022, A&A, 658, A129

REFERENCES

- Jayasinghe, T., et al. 2021, MNRAS, 504, 2577
- . 2022, arXiv e-prints, arXiv:2201.11131
- Jiang, Y.-F., Cantiello, M., Bildsten, L., Quataert, E., & Blaes, O. 2015, ApJ, 813, 74
- Jiang, Y.-F., Cantiello, M., Bildsten, L., Quataert, E., Blaes, O., & Stone, J. 2018, Nature, 561, 498
- Jiang, Y.-F., Stone, J. M., & Davis, S. W. 2014, ApJ, 796, 106
- Johnson, J. L., & Haardt, F. 2016, PASA, 33, e007
- Jonker, P. G., Kaur, K., Stone, N., & Torres, M. A. P. 2021, ApJ, 921, 131
- Justham, S., Podsiadlowski, P., & Vink, J. S. 2014, ApJ, 796, 121
- Kalari, V. M., Vink, J. S., Dufton, P. L., & Fraser, M. 2018, A&A, 618, A17
- Kalomeni, B., Nelson, L., Rappaport, S., Molnar, M., Quintin, J., & Yakut, K. 2016, ApJ, 833, 83
- Kawamura, S. 2006, Astronomical Herald, 99, 490
- Kennicutt, Robert C., J. 1989, ApJ, 344, 685
- Kewley, L. J., & Ellison, S. L. 2008, ApJ, 681, 1183
- Kimpson, T. O., Spera, M., Mapelli, M., & Ziosi, B. M. 2016, MNRAS, 463, 2443
- King, A. R., & Kolb, U. 1999, Monthly Notices of the Royal Astronomical Society, 305, 654
- Kinugawa, T., Inayoshi, K., Hotokezaka, K., Nakauchi, D., & Nakamura, T. 2014, MNRAS, 442, 2963
- Klencki, J., Nelemans, G., Istrate, A. G., & Chruścińska, M. 2021, A&A, 645, A54
- Klencki, J., Nelemans, G., Istrate, A. G., & Pols, O. 2020, A&A, 638, A55
- Klencki, J., Wiktorowicz, G., Gladysz, W., & Belczynski, K. 2017, MNRAS, 469, 3088
- Kluyver, T., et al. 2016, in ELPUB, 87–90
- Knee, A. M., McIver, J., & Cabero, M. 2022, ApJ, 928, 21

REFERENCES

- Kobulnicky, H. A., & Kewley, L. J. 2004, ApJ, 617, 240
- Kobulnicky, H. A., et al. 2014, ApJS, 213, 34
- Kochanek, C. S. 2014, ApJ, 785, 28
- . 2015, MNRAS, 446, 1213
- Kopparapu, R. K., Hanna, C., Kalogera, V., O'Shaughnessy, R., González, G., Brady, P. R., & Fairhurst, S. 2008, ApJ, 675, 1459
- Kounkel, M., et al. 2021, AJ, 162, 184
- Kreidberg, L., Bailyn, C. D., Farr, W. M., & Kalogera, V. 2012, ApJ, 757, 36
- Kremer, K., et al. 2020, ApJ, 903, 45
- Krishnendu, N. V., Mishra, C. K., & Arun, K. G. 2019, Phys. Rev. D, 99, 064008
- Krishnendu, N. V., & Ohme, F. 2021, Universe, 7, 497
- Kroupa, P. 2001, MNRAS, 322, 231
- Kruckow, M. U., Tauris, T. M., Langer, N., Kramer, M., & Izzard, R. G. 2018, MNRAS, 481, 1908
- Kudritzki, R. P., Pauldrach, A., Puls, J., & Abbott, D. C. 1989, A&A, 219, 205
- Kudritzki, R. P., & Reimers, D. 1978, A&A, 70, 227
- Kulkarni, S. R., Hut, P., & McMillan, S. 1993, Nature, 364, 421
- Kummer, F. 2020, MSc thesis, University of Amsterdam
- Kushnir, D., Zaldarriaga, M., Kollmeier, J. A., & Waldman, R. 2016, MNRAS, 462, 844
- Lam, C. Y., et al. 2022, ApJ, 933, L23
- Langer, N., Baade, D., Bodensteiner, J., Greiner, J., Rivinius, T., Martayan, C., & Borre, C. C. 2020, Astronomy & Astrophysics, 633, A40
- Langer, N., & Heger, A. 1998, in Astrophysics and Space Science Library, Vol. 233, B[e] stars, ed. A. M. Hubert & C. Jaschek, 235
- Langer, N., & Norman, C. A. 2006a, ApJ, 638, L63
- . 2006b, ApJ, 638, L63

REFERENCES

- Langer, N., Norman, C. A., de Koter, A., Vink, J. S., Cantiello, M., & Yoon, S. C. 2007, A&A, 475, L19
- Langer, N., et al. 2020, A&A, 638, A39
- Lattimer, J. M., & Prakash, M. 2004, Science, 304, 536
- Lauterborn, D. 1970, A&A, 7, 150
- Leigh, N. W. C., Böker, T., Maccarone, T. J., & Perets, H. B. 2013, MNRAS, 429, 2997
- Leigh, N. W. C., et al. 2018, MNRAS, 474, 5672
- Li, Y.-J., Wang, Y.-Z., Han, M.-Z., Tang, S.-P., Yuan, Q., Fan, Y.-Z., & Wei, D.-M. 2021, ApJ, 917, 33
- LIGO Scientific Collaboration et al. 2015, Classical and Quantum Gravity, 32, 074001
- Liotine, C., Zevin, M., Berry, C., Doctor, Z., & Kalogera, V. 2022, arXiv e-prints, arXiv:2210.01825
- Lipunov, V. M., Kornilov, V., Gorbovskoy, E., Tiurina, N., Balanutsa, P., & Kuznetsov, A. 2017, NewA, 51, 122
- Lipunov, V. M., Ozernoy, L. M., Popov, S. B., Postnov, K. A., & Prokhorov, M. E. 1996a, ApJ, 466, 234
- Lipunov, V. M., Postnov, K. A., & Prokhorov, M. E. 1996b, A&A, 310, 489
- . 1997, MNRAS, 288, 245
- Lipunov, V. M., Postnov, K. A., Prokhorov, M. E., & Bogomazov, A. I. 2009, Astronomy Reports, 53, 915
- Liu, Q. Z., van Paradijs, J., & van den Heuvel, E. P. J. 2006, A&A, 455, 1165
- Loeb, A., & Barkana, R. 2001, ARA&A, 39, 19
- Lommen, D., Yungelson, L., van den Heuvel, E., Nelemans, G., & Portegies Zwart, S. 2005, A&A, 443, 231
- Lovegrove, E., & Woosley, S. E. 2013, ApJ, 769, 109
- LSST Science Collaboration et al. 2009, arXiv e-prints, arXiv:0912.0201

REFERENCES

- Lu, W., Beniamini, P., & Bonnerot, C. 2021, MNRAS, 500, 1817
- Lu, W., Fuller, J., Quataert, E., & Bonnerot, C. 2022, arXiv e-prints, arXiv:2204.00847
- Luca, V. D., Desjacques, V., Franciolini, G., Malhotra, A., & Riotto, A. 2019, Journal of Cosmology and Astroparticle Physics, 2019, 018–018
- Luo, J., et al. 2016, Classical and Quantum Gravity, 33, 035010
- MacLeod, M., & Ramirez-Ruiz, E. 2015, ApJ, 798, L19
- Madau, P., & Dickinson, M. 2014, ARA&A, 52, 415
- Madau, P., & Fragos, T. 2017, ApJ, 840, 39
- Madau, P., Haardt, F., & Dotti, M. 2014, ApJ, 784, L38
- Maeder, A. 1992, A&A, 264, 105
- Maeder, A., & Meynet, G. 2000, A&A, 361, 159
- Maggiore, M., et al. 2020, JCAP, 2020, 050
- Maiolino, R., & Mannucci, F. 2019, A&A Rev., 27, 3
- Mandel, I. 2021, Research Notes of the American Astronomical Society, 5, 223
- Mandel, I., & Broekgaarden, F. S. 2022, Living Reviews in Relativity, 25, 1
- Mandel, I., & de Mink, S. E. 2016, MNRAS, 458, 2634
- Mandel, I., & Farmer, A. 2022a, Phys. Rep., 955, 1
- . 2022b, Phys. Rep., 955, 1
- Mandel, I., Farr, W. M., & Gair, J. R. 2019, MNRAS, 486, 1086
- Mandel, I., & Fragos, T. 2020, ApJ, 895, L28
- Mandic, V., Bird, S., & Cholis, I. 2016, Phys. Rev. Lett., 117, 201102
- Mapelli, M. 2020, Frontiers in Astronomy and Space Sciences, 7, 38
- Mapelli, M. 2020, in Handbook of Gravitational Wave Astronomy, ed. C. Bambi, S. Katsanevas, & K. D. Kokkotas (Singapore: Springer Singapore), 1–65
- . 2021, in Handbook of Gravitational Wave Astronomy (Springer, Singapore), 4

REFERENCES

- Mapelli, M., Bouffanais, Y., Santoliquido, F., Arca Sedda, M., & Artale, M. C. 2022, MNRAS, 511, 5797
- Mapelli, M., & Giacobbo, N. 2018, MNRAS, 479, 4391
- Mapelli, M., Giacobbo, N., Ripamonti, E., & Spera, M. 2017, MNRAS, 472, 2422
- Mapelli, M., Giacobbo, N., Santoliquido, F., & Artale, M. C. 2019, MNRAS, 487, 2
- Mapelli, M., Ripamonti, E., Zampieri, L., Colpi, M., & Bressan, A. 2010, MNRAS, 408, 234
- Mapelli, M., Spera, M., Montanari, E., Limongi, M., Chieffi, A., Giacobbo, N., Bressan, A., & Bouffanais, Y. 2020, The Astrophysical Journal, 888, 76
- Mapelli, M., Zampieri, L., Ripamonti, E., & Bressan, A. 2013, MNRAS, 429, 2298
- Marchant, P., Langer, N., Podsiadlowski, P., Tauris, T. M., & Moriya, T. J. 2016, A&A, 588, A50
- Marchant, P., & Moriya, T. J. 2020a, A&A, 640, L18
- . 2020b, A&A, 640, L18
- Marchant, P., Pappas, K. M. W., Gallegos-Garcia, M., Berry, C. P. L., Taam, R. E., Kalogera, V., & Podsiadlowski, P. 2021, A&A, 650, A107
- Marchant, P., Renzo, M., Farmer, R., Pappas, K. M. W., Taam, R. E., de Mink, S. E., & Kalogera, V. 2019, ApJ, 882, 36
- María Ezquiaga, J., & Holz, D. E. 2022, arXiv e-prints, arXiv:2202.08240
- Marigo, P., Girardi, L., Chiosi, C., & Wood, P. R. 2001, A&A, 371, 152
- Marinacci, F., et al. 2018, MNRAS, 480, 5113
- Martín-Navarro, I., La Barbera, F., Vazdekis, A., Falcón-Barroso, J., & Ferreras, I. 2015, MNRAS, 447, 1033
- Mashian, N., & Loeb, A. 2017, MNRAS, 470, 2611
- McKernan, B., Ford, K. E. S., Kocsis, B., Lyra, W., & Winter, L. M. 2014a, MNRAS, 441, 900
- . 2014b, MNRAS, 441, 900
- McKernan, B., Ford, K. E. S., Lyra, W., & Perets, H. B. 2012, MNRAS, 425, 460

REFERENCES

- McKernan, B., Ford, K. E. S., & O'Shaughnessy, R. 2020, MNRAS, 498, 4088
- McKernan, B., Ford, K. E. S., & O'Shaughnessy, R. 2020a, Black hole, neutron star and white dwarf merger rates in AGN disks
- McKernan, B., Ford, K. E. S., O'Shaugnessy, R., & Wysocki, D. 2020b, Monthly Notices of the Royal Astronomical Society, 494, 1203–1216
- McKernan, B., et al. 2018a, ApJ, 866, 66
- . 2018b, ApJ, 866, 66
- McMillan, P. J. 2011, MNRAS, 414, 2446
- Mehta, A. K., Buonanno, A., Gair, J., Miller, M. C., Farag, E., deBoer, R. J., Wiescher, M., & Timmes, F. X. 2021, arXiv e-prints, arXiv:2105.06366
- Mennekens, N., & Vanbeveren, D. 2014a, A&A, 564, A134
- . 2014b, A&A, 564, A134
- Menon, A., & Heger, A. 2017, MNRAS, 469, 4649
- Mészáros, P. 2019, Mem. Soc. Astron. Italiana, 90, 57
- Meurs, E. J. A., & van den Heuvel, E. P. J. 1989, A&A, 226, 88
- Mezzacappa, A. 2023, IAU Symposium, 362, 215
- Michaely, E., & Perets, H. B. 2016, MNRAS, 458, 4188
- Miller, S., Callister, T. A., & Farr, W. M. 2020, ApJ, 895, 128
- Mirbabayi, M., Gruzinov, A., & Noreña, J. 2020, Spin of primordial black holes
- Moe, M., & Di Stefano, R. 2017, ApJS, 230, 15
- Mokiem, M. R., et al. 2007, A&A, 473, 603
- Mondal, S., Belczyński, K., Wiktorowicz, G., Lasota, J.-P., & King, A. R. 2019, Monthly Notices of the Royal Astronomical Society
- Moore, C. J., Cole, R. H., & Berry, C. P. L. 2015, Classical and Quantum Gravity, 32, 015014
- Morscher, M., Pattabiraman, B., Rodriguez, C., Rasio, F. A., & Umbreit, S. 2015, ApJ, 800, 9

REFERENCES

- Müller, B., Gay, D. W., Heger, A., Tauris, T. M., & Sim, S. A. 2018, MNRAS, 479, 3675
- Nadezhin, D. K. 1980, Ap&SS, 69, 115
- Naiman, J. P., et al. 2018, MNRAS, 477, 1206
- Naoz, S., Noter, S., & Barkana, R. 2006, MNRAS, 373, L98
- Nebot Gómez-Morán, A., et al. 2011, A&A, 536, A43
- Neijssel, C. J., et al. 2019, MNRAS, 490, 3740
- Nelemans, G., Yungelson, L. R., & Portegies Zwart, S. F. 2001a, A&A, 375, 890
- Nelemans, G., Yungelson, L. R., Portegies Zwart, S. F., & Verbunt, F. 2001b, A&A, 365, 491
- Nelson, D., et al. 2018, MNRAS, 475, 624
- . 2019a, MNRAS, 490, 3234
- . 2019b, Computational Astrophysics and Cosmology, 6, 2
- Nelson, E. J., et al. 2021, MNRAS, 508, 219
- Nelson, L. A., Dubeau, E., & MacCannell, K. A. 2004, ApJ, 616, 1124
- Neo, S., Miyaji, S., Nomoto, K., & Sugimoto, D. 1977, PASJ, 29, 249
- Ng, K. K. Y., Vitale, S., Farr, W. M., & Rodriguez, C. L. 2021, ApJ, 913, L5
- Ni, W.-T. 2018, in European Physical Journal Web of Conferences, Vol. 168, European Physical Journal Web of Conferences, 01004
- Nieuwenhuijzen, H., & de Jager, C. 1990, A&A, 231, 134
- Nocedal, J., & Wright, S. 2006, Numerical optimization, 2nd edn., Springer series in operations research and financial engineering (New York, NY: Springer)
- Offner, S. S. R., Moe, M., Kratter, K. M., Sadavoy, S. I., Jensen, E. L. N., & Tobin, J. J. 2022, arXiv e-prints, arXiv:2203.10066
- O'Hagan, A., & Leonard, T. 1976, Biometrika, 63, 201
- O'Leary, R. M., Rasio, F. A., Fregeau, J. M., Ivanova, N., & O'Shaughnessy, R. 2006, ApJ, 637, 937

REFERENCES

- Olejak, A., & Belczynski, K. 2021, ApJ, 921, L2
- Olejak, A., Belczynski, K., & Ivanova, N. 2021a, A&A, 651, A100
- . 2021b, A&A, 651, A100
- Olejak, A., Fryer, C. L., Belczynski, K., & Baibhav, V. 2022, MNRAS, 516, 2252
- Öpik, E. 1924, Tartu Obs. Publ., 25, 6
- Oppenheimer, B. D., & Davé, R. 2006, MNRAS, 373, 1265
- O’Shaughnessy, R., Belczynski, K., & Kalogera, V. 2008, ApJ, 675, 566
- Özel, F., Psaltis, D., Narayan, R., & McClintock, J. E. 2010, ApJ, 725, 1918
- Paczynski, B. 1970, AcA, 20, 47
- Paczynski, B. 1976, in IAU Symposium, Vol. 73, Structure and Evolution of Close Binary Systems, ed. P. Eggleton, S. Mitton, & J. Whelan, 75–+
- Paczynski, B., & Sienkiewicz, R. 1972, AcA, 22, 73
- Pakmor, R., Springel, V., Bauer, A., Mocz, P., Munoz, D. J., Ohlmann, S. T., Schaal, K., & Zhu, C. 2016, MNRAS, 455, 1134
- Pakmor, R., et al. 2022, MNRAS, 512, 3602
- Pavlovskii, K., & Ivanova, N. 2015, Monthly Notices of the Royal Astronomical Society, 449, 4415–4427
- Pavlovskii, K., & Ivanova, N. 2015, MNRAS, 449, 4415
- Pavlovskii, K., Ivanova, N., Belczynski, K., & Van, K. X. 2016, Monthly Notices of the Royal Astronomical Society, 465, 2092–2100
- Pavlovskii, K., Ivanova, N., Belczynski, K., & Van, K. X. 2017, MNRAS, 465, 2092
- Paxton, B., et al. 2015, ApJS, 220, 15
- Perez, F., & Granger, B. E. 2007, Computing in Science and Engineering, 9, 21
- Peters, P. C. 1964, Physical Review, 136, 1224
- Petrov, P., et al. 2022, ApJ, 924, 54
- Petrovich, C., & Antonini, F. 2017, ApJ, 846, 146

REFERENCES

- Pettini, M., & Pagel, B. E. J. 2004, MNRAS, 348, L59
- Pezzulli, E., Valiante, R., & Schneider, R. 2016, MNRAS, 458, 3047
- Pillepich, A., et al. 2018a, MNRAS, 475, 648
- . 2018b, MNRAS, 473, 4077
- . 2019, MNRAS, 490, 3196
- Planck Collaboration et al. 2020, A&A, 641, A6
- Podsiadlowski, P., Rappaport, S., & Han, Z. 2003, MNRAS, 341, 385
- Pols, O. R. 1994, A&A, 290, 119
- . 2011, lecture notes: Stellar Structure and Evolution (Utrecht University), 199
- Pols, O. R., Schröder, K.-P., Hurley, J. R., Tout, C. A., & Eggleton, P. P. 1998, MNRAS, 298, 525
- Pols, O. R., Tout, C. A., Eggleton, P. P., & Han, Z. 1995, MNRAS, 274, 964
- Pols, O. R., Tout, C. A., Schroder, K.-P., Eggleton, P. P., & Manners, J. 1997, MNRAS, 289, 869
- Popham, R., Woosley, S. E., & Fryer, C. 1999, ApJ, 518, 356
- Portegies Zwart, S. F. 1995, A&A, 296, 691
- Portegies Zwart, S. F., & McMillan, S. L. W. 2000a, ApJ, 528, L17
- . 2000b, ApJ, 528, L17
- Portegies Zwart, S. F., & Verbunt, F. 1996, A&A, 309, 179
- Portegies Zwart, S. F., & Yungelson, L. R. 1998, A&A, 332, 173
- Postnov, K. A., & Yungelson, L. R. 2014a, Living Reviews in Relativity, 17, 3
- . 2014b, Living Reviews in Relativity, 17, 3
- Predehl, P., et al. 2021, A&A, 647, A1
- Price-Whelan, A. M., et al. 2020, ApJ, 895, 2
- Punturo, M., et al. 2010, Classical and Quantum Gravity, 27, 084007
- Raidal, M., Vaskonen, V., & Veermäe, H. 2017, JCAP, 2017, 037

REFERENCES

- Raihel, C. A. 2019, European Physical Journal A, 55, 80
- Rakavy, G., & Shaviv, G. 1967, ApJ, 148, 803
- Ramírez-Tannus, M. C., et al. 2021, A&A, 645, L10
- Rebassa-Mansergas, A., Gänsicke, B. T., Rodríguez-Gil, P., Schreiber, M. R., & Koester, D. 2007, MNRAS, 382, 1377
- Rebassa-Mansergas, A., Nebot Gómez-Morán, A., Schreiber, M. R., Gänsicke, B. T., Schwope, A., Gallardo, J., & Koester, D. 2012, MNRAS, 419, 806
- Reitze, D., et al. 2019, in Bulletin of the American Astronomical Society, Vol. 51, 35
- Remillard, R. A., & McClintock, J. E. 2006, ARA&A, 44, 49
- Renzo, M., Farmer, R., Justham, S., Götberg, Y., de Mink, S. E., Zapartas, E., Marchant, P., & Smith, N. 2020a, A&A, 640, A56
- Renzo, M., Farmer, R. J., Justham, S., de Mink, S. E., Götberg, Y., & Marchant, P. 2020b, MNRAS, 493, 4333
- Renzo, M., Farmer, R. J., Justham, S., de Mink, S. E., Götberg, Y., & Marchant, P. 2020, Sensitivity of the lower edge of the pair-instability black hole mass gap to the treatment of time-dependent convection
- Renzo, M., & Götberg, Y. 2021, ApJ, 923, 277
- Renzo, M., Hendriks, D. D., van Son, L. A. C., & Farmer, R. 2022, Research Notes of the American Astronomical Society, 6, 25
- Renzo, M., Ott, C. D., Shore, S. N., & de Mink, S. E. 2017, A&A, 603, A118
- Renzo, M., et al. 2019, A&A, 624, A66
- Riley, J., Mandel, I., Marchant, P., Butler, E., Nathaniel, K., Neijssel, C., Shortt, S., & Vigna-Gómez, A. 2021, MNRAS
- Riley, J., et al. 2022a, ApJS, 258, 34
- . 2022b, ApJS, 258, 34
- Rivinius, T., Baade, D., Hadrava, P., Heida, M., & Klement, R. 2020, A&A, 637, L3

REFERENCES

- Robson, T., Cornish, N. J., & Liu, C. 2019, Classical and Quantum Gravity, 36, 105011
- Rodriguez, C. L., & Antonini, F. 2018, ApJ, 863, 7
- Rodriguez, C. L., Haster, C.-J., Chatterjee, S., Kalogera, V., & Rasio, F. A. 2016, ApJ, 824, L8
- Rodriguez, C. L., & Loeb, A. 2018, ApJ, 866, L5
- Rodriguez, C. L., Zevin, M., Amaro-Seoane, P., Chatterjee, S., Kremer, K., Rasio, F. A., & Ye, C. S. 2019a, Physical Review D, 100
- . 2019b, Phys. Rev., D100, 043027
- Rodriguez, C. L., Zevin, M., Pankow, C., Kalogera, V., & Rasio, F. A. 2016, The Astrophysical Journal, 832, L2
- Romero-Shaw, I. M., Kremer, K., Lasky, P. D., Thrane, E., & Samsing, J. 2021, MNRAS, 506, 2362
- Roulet, J., & Zaldarriaga, M. 2019, MNRAS, 484, 4216
- Roupas, Z., & Kazanas, D. 2019, A&A, 632, L8
- Sabbahit, G. N., Vink, J. S., Higgins, E. R., & Sander, A. A. C. 2021, MNRAS, 506, 4473
- Sadowski, A., & Narayan, R. 2015, MNRAS, 453, 3213
- Sahu, K. C., et al. 2022, arXiv e-prints, arXiv:2201.13296
- Samsing, J., & Hotokezaka, K. 2021, ApJ, 923, 126
- Sana, H., et al. 2012, Science, 337, 444
- Sana, H., et al. 2013, A&A, 550, A107
- . 2014, ApJS, 215, 15
- Sanders, R. L., et al. 2022, arXiv e-prints, arXiv:2207.12430
- Santoliquido, F., Mapelli, M., Giacobbo, N., Bouffanais, Y., & Artale, M. C. 2021a, MNRAS, 502, 4877
- . 2021b, MNRAS, 502, 4877
- Sanyal, D., Grassitelli, L., Langer, N., & Bestenlehner, J. M. 2015, A&A, 580, A20

REFERENCES

- Sanyal, D., Langer, N., Szécsi, D., -C Yoon, S., & Grassitelli, L. 2017, A&A, 597, A71
- Sasaki, M., Suyama, T., Tanaka, T., & Yokoyama, S. 2016, Physical Review Letters, 117
- Sathyaprakash, B., et al. 2019a, BAAS, 51, 248
- . 2019b, BAAS, 51, 276
- Schaye, J., et al. 2015, MNRAS, 446, 521
- Schmidt, M. 1959, ApJ, 129, 243
- Schneider, F. R. N., Izzard, R. G., Langer, N., & de Mink, S. E. 2015, ApJ, 805, 20
- Schneider, F. R. N., Ohlmann, S. T., Podsiadlowski, P., Röpke, F. K., Balbus, S. A., Pakmor, R., & Springel, V. 2019, Nature, 574, 211–214
- Schneider, F. R. N., et al. 2018, Science, 361, aat7032
- Schnittman, J. D., & Buonanno, A. 2007, The Astrophysical Journal, 662, L63
- Schutz, B. F. 1986, Nature, 323, 310
- Secunda, A., Bellovary, J., Mac Low, M.-M., Ford, K. E. S., McKernan, B., Leigh, N. W. C., Lyra, W., & Sándor, Z. 2019, ApJ, 878, 85
- Secunda, A., et al. 2020, Orbital Migration of Interacting Stellar Mass Black Holes in Disks around Supermassive Black Holes II. Spins and Incoming Objects
- Sedda, M. A. 2020, Birth, Life, and Death of Black Hole Binaries around Supermassive Black Holes: Dynamical Evolution of Gravitational Wave Sources
- Sen, K., et al. 2022, A&A, 659, A98
- Shao, Y., & Li, X.-D. 2021, ApJ, 920, 81
- . 2022, ApJ, 930, 26
- Shen, Y., et al. 2023, ApJ, 945, 41
- Shenar, T., et al. 2022, Nature Astronomy, 6, 1085
- Siegel, J. C., et al. 2022, arXiv e-prints, arXiv:2209.06844
- Sigurdsson, S., & Hernquist, L. 1993, Nature, 364, 423

REFERENCES

- Singh, N., Bulik, T., Belczynski, K., Cieslar, M., & Calore, F. 2023, arXiv e-prints, arXiv:2304.01341
- Smarr, L. L., & Blandford, R. 1976, ApJ, 207, 574
- Smith, N. 2014, ARA&A, 52, 487
- . 2017, Philosophical Transactions of the Royal Society of London Series A, 375, 20160268
- Soberman, G. E., Phinney, E. S., & van den Heuvel, E. P. J. 1997, A&A, 327, 620
- Song, H. F., Maeder, A., Meynet, G., Huang, R. Q., Ekström, S., & Granada, A. 2013, A&A, 556, A100
- Song, H. F., Meynet, G., Maeder, A., Ekström, S., & Eggenberger, P. 2016a, A&A, 585, A120
- . 2016b, A&A, 585, A120
- Spera, M., Mapelli, M., & Bressan, A. 2015, MNRAS, 451, 4086
- Spera, M., Mapelli, M., Giacobbo, N., Trani, A. A., Bressan, A., & Costa, G. 2019a, MNRAS, 485, 889
- . 2019b, MNRAS, 485, 889
- Springel, V. 2010, MNRAS, 401, 791
- Springel, V., Di Matteo, T., & Hernquist, L. 2005, MNRAS, 361, 776
- Springel, V., & Hernquist, L. 2003, MNRAS, 339, 289
- Springel, V., et al. 2018, MNRAS, 475, 676
- Stanway, E. R., & Eldridge, J. J. 2018, MNRAS, 479, 75
- Stegmann, J., Antonini, F., Schneider, F. R. N., Tiwari, V., & Chattopadhyay, D. 2022, Phys. Rev. D, 106, 023014
- Steinle, N., & Kesden, M. 2021, Phys. Rev. D, 103, 063032
- Stevenson, S., & Clarke, T. A. 2022, MNRAS, 517, 4034
- Stevenson, S., Ohme, F., & Fairhurst, S. 2015, ApJ, 810, 58
- Stevenson, S., Sampson, M., Powell, J., Vigna-Gómez, A., Neijssel, C. J., Szécsi, D., & Mandel, I. 2019, The Astrophysical Journal, 882, 121

REFERENCES

- Stevenson, S., Vigna-Gómez, A., Mandel, I., Barrett, J. W., Neijssel, C. J., Perkins, D., & de Mink, S. E. 2017, *Nature Communications*, 8, 14906
- Stone, N. C., Metzger, B. D., & Haiman, Z. 2017, *MNRAS*, 464, 946
- Stoop, M., Kaper, L., de Koter, A., Guo, D., Lamers, H. J. G. L. M., & Rieder, S. 2023, *A&A*, 670, A108
- Sun, M., & Arras, P. 2018, *ApJ*, 858, 14
- Tagawa, H., Haiman, Z., & Kocsis, B. 2020, *ApJ*, 898, 25
- Takahashi, K., Yoshida, T., & Umeda, H. 2018, *ApJ*, 857, 111
- Talbot, C., & Thrane, E. 2018, *Astrophys. J.*, 856, 173
- Tang, P. N., Eldridge, J. J., Stanway, E. R., & Bray, J. C. 2020, *MNRAS*, 493, L6
- Tanikawa, A., Yoshida, T., Kinugawa, T., Trani, A. A., Hosokawa, T., Susa, H., & Omukai, K. 2022, *ApJ*, 926, 83
- Tchekhovskoy, A., McKinney, J. C., & Narayan, R. 2012, in *Journal of Physics Conference Series*, Vol. 372, *Journal of Physics Conference Series*, 012040
- Thompson, T. A. 2011, *ApJ*, 741, 82
- Thompson, T. A., et al. 2019, *Science*, 366, 637
- Tiwari, V. 2022, *ApJ*, 928, 155
- Tiwari, V., & Fairhurst, S. 2021, *ApJ*, 913, L19
- Toonen, S., Hamers, A., & Portegies Zwart, S. 2016, *Computational Astrophysics and Cosmology*, 3, 6
- Toonen, S., Nelemans, G., & Portegies Zwart, S. 2012, *A&A*, 546, A70
- Torrey, P., et al. 2019, *MNRAS*, 484, 5587
- Tutukov, A., & Yungelson, L. 1996, *MNRAS*, 280, 1035
- Tutukov, A. V., & Yungelson, L. R. 1979, *AcA*, 29, 665
- . 1993, *MNRAS*, 260, 675
- Tylenda, R., et al. 2011, *A&A*, 528, A114
- van den Heuvel, E. P. J. 1969, *AJ*, 74, 1095

REFERENCES

- van den Heuvel, E. P. J. 1994, in Saas-Fee Advanced Course 22: Interacting Binaries, ed. S. N. Shore, M. Livio, E. P. J. van den Heuvel, H. Nussbaumer, & A. Orr, 263–474
- van den Heuvel, E. P. J., Portegies Zwart, S. F., & de Mink, S. E. 2017, MNRAS, 471, 4256
- van der Meij, V., Guo, D., Kaper, L., & Renzo, M. 2021, A&A, 655, A31
- van Kerkwijk, M. H., et al. 1992, Nature, 355, 703
- Van Rossum, G., & Drake, F. L. 2009, Python 3 Reference Manual (Scotts Valley, CA: CreateSpace)
- van Son, L. A. C., et al. 2020, ApJ, 897, 100
- . 2022a, ApJ, 940, 184
- . 2022b, ApJ, 931, 17
- . 2022c, ApJ, 931, 17
- . 2022d, ApJ, 931, 17
- Vanbeveren, D., De Donder, E., Van Bever, J., Van Rensbergen, W., & De Loore, C. 1998, NewA, 3, 443
- Vassiliadis, E., & Wood, P. R. 1993, ApJ, 413, 641
- Veske, D., Bartos, I., Márka, Z., & Márka, S. 2021, ApJ, 922, 258
- Vidaña, I. 2018, European Physical Journal Plus, 133, 445
- Vigna-Gómez, A., Justham, S., Mandel, I., de Mink, S. E., & Podsiadlowski, P. 2019, ApJ, 876, L29
- Vigna-Gómez, A., et al. 2018a, MNRAS, 481, 4009
- . 2018b, MNRAS, 481, 4009
- . 2020, PASA, 37, e038
- Vinciguerra, S., et al. 2020, MNRAS, 498, 4705
- Vink, J. S., & de Koter, A. 2005, A&A, 442, 587
- Vink, J. S., de Koter, A., & Lamers, H. J. G. L. M. 2000, A&A, 362, 295

REFERENCES

- . 2001a, A&A, 369, 574
- . 2001b, A&A, 369, 574
- Vink, J. S., & Sander, A. A. C. 2021, MNRAS, 504, 2051
- Virtanen, P., et al. 2020, Nature Methods, 17, 261
- Vitale, S. 2016, Phys. Rev. D, 94, 121501
- Vitale, S., Farr, W. M., Ng, K. K. Y., & Rodriguez, C. L. 2019a, ApJ, 886, L1
- . 2019b, ApJ, 886, L1
- Vitale, S., Gerosa, D., Farr, W. M., & Taylor, S. R. 2020, Inferring the Properties of a Population of Compact Binaries in Presence of Selection Effects (Singapore: Springer Singapore), 1–60
- Vitale, S., Lynch, R., Raymond, V., Sturani, R., Veitch, J., & Graff, P. 2017, Phys. Rev. D, 95, 064053
- Vitale, S., Lynch, R., Veitch, J., Raymond, V., & Sturani, R. 2014, Phys. Rev. Lett., 112, 251101
- Vogelsberger, M., et al. 2014, MNRAS, 444, 1518
- Volonteri, M., & Rees, M. J. 2005, ApJ, 633, 624
- Volonteri, M., Silk, J., & Dubus, G. 2015, ApJ, 804, 148
- Voss, R., & Tauris, T. M. 2003, MNRAS, 342, 1169
- Vynatheya, P., & Hamers, A. S. 2022, ApJ, 926, 195
- Wagg, T., Broekgaarden, F. S., de Mink, S. E., Frankel, N., van Son, L. A. C., & Justham, S. 2022, ApJ, 937, 118
- Walton, D. J., Mackenzie, A. D. A., Gully, H., Patel, N. R., Roberts, T. P., Earnshaw, H. P., & Mateos, S. 2022, MNRAS, 509, 1587
- Wang, K., Yu, S., & Peng, W. 2019, Journal of Aerosol Science, 134, 95
- Wang, S., Wang, Y.-F., Huang, Q.-G., & Li, T. G. F. 2018, Phys. Rev. Lett., 120, 191102
- Waskom, M. L. 2021, Journal of Open Source Software, 6, 3021
- Webbink, R. F. 1984, ApJ, 277, 355

REFERENCES

- Weinberger, R., Springel, V., & Pakmor, R. 2020, ApJS, 248, 32
- Weinberger, R., et al. 2017, MNRAS, 465, 3291
- Weis, K., & Bomans, D. J. 2020, Galaxies, 8, 20
- Wen, L. 2003, ApJ, 598, 419
- Wiktorowicz, G., Wyrzykowski, Ł., Chruslinska, M., Klencki, J., Rybicki, K. A., & Belczynski, K. 2019, ApJ, 885, 1
- Wong, K. W. K., Breivik, K., Kremer, K., & Callister, T. 2021a, Phys. Rev. D, 103, 083021
- . 2021b, Phys. Rev. D, 103, 083021
- Woods, T. E., & Ivanova, N. 2011, ApJ, 739, L48
- Woods, T. E., Ivanova, N., van der Sluys, M. V., & Chaichenets, S. 2012, ApJ, 744, 12
- Woosley, S. E. 2017, ApJ, 836, 244
- Woosley, S. E., Blinnikov, S., & Heger, A. 2007, Nature, 450, 390
- Woosley, S. E., & Heger, A. 2021, ApJ, 912, L31
- Woosley, S. E., Heger, A., & Weaver, T. A. 2002a, Reviews of Modern Physics, 74, 1015
- . 2002b, Reviews of Modern Physics, 74, 1015
- Woosley, S. E., Sukhbold, T., & Janka, H. T. 2020, ApJ, 896, 56
- Wu, S., Coughlin, E. R., & Nixon, C. 2018, Monthly Notices of the Royal Astronomical Society, 478, 3016–3024
- Wyithe, J. S. B., & Loeb, A. 2012, MNRAS, 425, 2892
- Wyrzykowski, Ł., & Mandel, I. 2020, A&A, 636, A20
- Wysocki, D., Lange, J., & O’Shaughnessy, R. 2019, Phys. Rev. D, 100, 043012
- Xu, X.-J., & Li, X.-D. 2010a, ApJ, 722, 1985
- . 2010b, ApJ, 716, 114

REFERENCES

- Yang, Y., Bartos, I., Haiman, Z., Kocsis, B., Márka, Z., Stone, N. C., & Márka, S. 2019a, ApJ, 876, 122
- Yang, Y., et al. 2019b, Phys. Rev. Lett., 123, 181101
- . 2019c, Phys. Rev. Lett., 123, 181101
- Ye, C., & Fishbach, M. 2022, ApJ, 937, 73
- Zaldarriaga, M., Kushnir, D., & Kollmeier, J. A. 2018, MNRAS, 473, 4174
- Zel'dovich, Y. B., & Novikov, I. D. 1966, AZh, 43, 758
- Zevin, M., & Bavera, S. S. 2022, ApJ, 933, 86
- Zevin, M., Spera, M., Berry, C. P. L., & Kalogera, V. 2020, ApJ, 899, L1
- Zevin, M., et al. 2021, ApJ, 910, 152
- Ziosi, B. M., Mapelli, M., Branchesi, M., & Tormen, G. 2014, MNRAS, 441, 3703